



ugr

Universidad  
de Granada

Programa de doctorado en física y matemáticas

# Estudio experimental y teórico de la matriz de scattering de análogos de polvo de Marte

## Experimental and theoretical study of scattering matrices of Martian dust analogs

Dissertation presented by:  
**Dominika Dabrowska**

**Supervisors:** Dr. Olga Muñoz Gómez

Dr. Fernando Moreno Danvila



Granada, 2014

Editor: Editorial de la Universidad de Granada  
Autor: Dominika Dabrowska  
D.L.: GR 2270-2014  
ISBN: 978-84-9083-331-5



## Contents

Acknowledgments	v
Resumen	vii
1. Introduction	1
1.1 Martian Atmosphere.....	6
1.2 Atmospheric dust.....	8
1.2.1 Size.....	11
1.2.2 Composition.....	16
2. Objectives	23
3. Methodology	25
3.1 Theoretical description of the light scattering phenomenon: The scattering matrix.....	25
3.2 The IAA COsmic Dust LABoratory (IAA-CODULAB).....	28
3.3 Test measurements.....	33
3.4 Single or multiple scattering .....	37
3.5 Simulations .....	39
3.6 Photophoresis: theory and experiment .....	39
Bibliography to Chapters 1-3	43
4. Scattering matrices of Martian dust analogs at 488 nm and 647 nm	49
4.1 Introduction.....	50
4.2 Physical properties of Martian dust and its terrestrial analogues.....	50
4.2.1 Martian dust properties.....	50
4.2.2 Martian dust analogs.....	51
4.3 Experimental Apparatus.....	54
4.4 Results.....	56
4.4.1 Measured scattering matrices.....	56
4.4.2 Lorenz-Mie calculations versus measured scattering matrices.....	58
4.4.3 Synthetic scattering matrices.....	58
4.5 Comparison with derived phase functions and degree of linear polarization in the Martian atmosphere.....	62
4.6 Conclusions.....	63
Bibliography to Chapter 4	67
5. Effect of the orientation of the optic axis on simulated scattering matrix elements of small birefringent particles	72
Bibliography to Chapter 5	77
6. Experimental and simulated scattering matrices of small calcite particles at 647 nm	78
6.1 Introduction.....	79
6.2 The calcite sample.....	79

6.2.1 Origin of the calcite sample and size distribution.....	79
6.2.2 Refractive index.....	80
6.2.3 Shapes.....	81
6.3 Experimental data.....	81
6.3.1 Experiment apparatus.....	81
6.3.2 Experimental scattering matrix.....	82
6.3.3 Synthetic scattering matrix for the calcite sample.....	84
6.4 Computations for calcite particles.....	85
6.4.1 DDSCAT 7.1.....	85
6.4.2 Simulations of calcite particles.....	85
6.4.3 Flake particles.....	88
6.4.4 Rhomboid-like particles.....	90
6.4.5 Combination of flake-like and rhomboid-like particles.....	91
6.5 Summary and conclusions.....	93
Appendix A.....	96
 Bibliography to Chapter 6.....	 99
 7. The Amsterdam-Granada Light Scattering Database.....	 102
7.1 Introduction.....	103
7.2 Amsterdam-Granada Light Scattering Database.....	103
7.2.1 Samples.....	104
7.2.2 Measured scattering matrix elements.....	106
7.2.3 Average and synthetic matrices.....	107
7.3 Applications.....	107
7.3.1 An example: Martian atmosphere.....	107
7.4 Discussion and conclusion.....	108
 Bibliography to Chapter 7.....	 115
 8. The photophoresis experiment for Martian dust analogs at 655 nm – work in progress.....	 119
 Bibliography to Chapter 8.....	 125
 9. Conclusions and future work.....	 126
 Bibliography to Chapter 9.....	 129

# Acknowledgements

*".. is a journey, not the destination"*

"Life's a journey not the destination", was Aerosmith, one of my favorite bands singing in their song "Amazing".

I would sing "Writing the Thesis is a journey, not the destination". In this journey, I was not alone. I really could not travel alone...

First of all, I need to give special thanks to my supervisors, Olga Muñoz and Fernando Moreno, for the patience and help, without whom this Thesis would not have been possible. Thanks for all I have learned from you and for the efforts you did for me, especially at the end of the Thesis. I could not forget to mention Gerhard Wurm and his fantastic group at "Duisburg-Essen University". The short time I spent in Germany re-filled me with motivation. My scientific work in Granada would not have been possible without José-Juan López Moreno, Dani Guirado, José-Luis Ramos... Thank you for so many things.. In particular, I want to give special thanks to José Luis for his energy and the ideas he put in the development of COsmic DUSt LABoratory, CODULAB at our Institute, where I performed majority of the experiments included my Thesis. Special thanks go to all co-authors of the publications in which I participated, especially for Evgenij Zubko and Timo Nousiainen for their crucial participation in these works, which were very important for me at the beginning of my scientific career. Thanks to the whole scientific community at IAA, particularly to Matilde Fernández and Carlos Barceló, the Computing Centre department, mainly Juanjo & Manolo, and the administration staff, especially Francisco Tapia.

During my studies, in Poland and France I met a bunch of scientists, without whom I would not have started my scientific career. Among many great people, I want to mention in particular Jan Masny, Arek Wójs, Andrzej Radosz, and Arnaud Siebert.

Also I want to thank to my parents, Ewa, Wlodek and my grandmas, Stasia and Marta just for being there for me and supporting me in my all choices. And to my brother Przemek and his family for wishing me all the best. For Sascha and Rumpel for staying by me virtually, and as much as possible, in person. And for Azorek, who unfortunately, is not with us anymore.

Maybe it is strange but thanks to my motorbike, that during last few years nearly everyday took me to my work, did not break so often, did not have many accidents and was wonderful when there was the need to make quick and effective paper-work in Granada.

The order of people below is completely random. And I am sorry if I have forgotten someone, it was completely unintentional. Thanks for the small things you people did for me during the most difficult time.

Thanks to Ana from security staff for being like my older sister and taking care of me when I needed. Thanks to Juan, her work-mate for so clever advices and good words, especially at 3 or 5 am at reception hall at IAA. Thanks to Aza, Albert, Javi and Alex, my flat-mates, you have done big things for me. You know what. And last but not least, thanks to Alex for going to the police for me, paying my fine for bad parking.

Thank you for all the things we did together. It was wonderful to share the "space-time" with you :-)

---

Thank you Audrey, Teresa and Maite for all the information you gave to me. You were like a guide and thanks for all the good and motivating words. Angela, Caro D., Ana C. Victor and Walter, thank you for coming to me in the most difficult moments and asking how I am. Thanks to you, I never felt alone. Being surrounded by people like you just made me stronger. I am glad and honored to know you.

Clarita, you understand me more than anyone else, thanks for the kind words "Maybe doing the PhD will be good for something. We do not know."

Thanks go to all the other people that I liked so much, my colleagues for the Institute: so good and warm Isabel B., Sandra and Sarita, always fair Marta, the always-ready-to-coffee Alicia, positively-crazy couple: my black-slope ski-parachuting-companion José Ramón and his wonderful wife María (indeed they made me overcome some fears...), the music-sister-souls Aytami and Fran P., incredible Miriana, who is inspiring me, and Gabi G., your thesis and your fight shown me that many things are possible.

I cannot forget about Monica B. and her cats, Caro K., Pablo, Christina T., Emilio, Sol, Ruben H., Zaira, Alba and Dario...

Before I mentioned Ana C. and Alex, but could not forget about the entire Volley-Lovers-Zaidin team, i.e., Monica R., Ana P., Jesus and Emilia, Antonio-s, Istoni, Juan-Carlos, Rubén S., etc and some ex-players.

During my short stay in Germany, I was playing volleyball as well and I want to thank the players of the teams who welcomed me in their midst as a friend.

Caro de B., Johannes and Jens. Apart I was playing with Andreas. Guys, do not forget that we have a beer-agreement. Special thanks goes to Jens Theiser, we have done some great work together and some other things. My stay in Germany was awesome and I want to thank people like Guillem for this, who made me feel like home. Thanks as well to Christoph and Thorsten, my other office-mates and Thorben, Tim, Markus and Rosa that additionally put the laboratory to work in such a great manner.

And people from my earlier past, the ones that have not forgotten me during long years, and were support me till now, i.e. Magda, Karol and Lidka.

The People from OSN, Observatorio de Sierra Nevada, you know I was there as much as I could, I like you so much, in particular the great popularizer of science Victor Costa, and Alfredo, Fran A., Jose-Antonio, Jose-Luis (J-L. Ramos again, special thanks for the IAA Scattering Laboratory help!!!), and the entire team.

Outside from the scientific world I would like to thank the swimmers Julieta, Ingrid, Dani L. and Beata J., and Dr Jose Manuel Muñoz at the emergency for very quick attendance, when I have explained my situation:-) I promised to include him in these acknowledgments. It is extremely funny what I did.. When working on my PhD, I used the earplugs, one broke, and made it impossible to take away. He helped me.

And thanks to other, still not mentioned, the most fantastic people I ever met, Olga, Lanard and Matthias, Garard, Djamil, Cristian, Timo, Reme, Alex L., and Flo.

*Dominika*

# Resumen

La presente Tesis se centra en el estudio experimental de la matriz de scattering de distintas muestras de análogos de polvo de Marte a dos longitudes de onda, 488 y 647 nm. El principal objetivo de la Tesis es el producir una base de datos con las propiedades de scattering de distintas muestras análogas en sus propiedades físicas a las existentes en la atmósfera marciana. Dicha base de datos estará disponible para la comunidad astronómica internacional en la Amsterdam-Granada Light Scattering Database [1] ([www.iaa.es/scattering](http://www.iaa.es/scattering)). Las muestras consideradas en este estudio son palagonita (JSC MARS-1 NASA simulant), montmorillonita, basalto y calcita. Las observaciones realizadas durante las últimas décadas en un amplio rango espectral han demostrado que la palagonita es un análogo espectral mejor que la montmorillonita. Además, considerando la pasada actividad volcánica en Marte, se estudia también una muestra de basalto, y, aunque no sea un componente mayoritario en Marte, se estudia también una muestra de calcita. La calcita, aparte de su interés por la relación con la existencia pasada de agua en Marte tiene un gran interés desde el punto de vista teórico por su carácter birrefringente. Algunas de las muestras han sido procesadas para obtener la distribución de tamaños que nos permita hacer los experimentos. En particular, la calcita ha sido pulverizada en un molino de bolas de ágata, y la palagonita (JSC MARS-1) ha sido tamizada con un tamiz de 200 micras de diámetro. Además, una parte de la muestra de palagonita ha sido calentada a 200°C durante 24 horas para eliminar el agua y otros componentes volátiles. Las muestras están caracterizadas por diferentes distribuciones de tamaño, con radios efectivos que van desde unas pocas micras hasta las decenas de micras. Además de las medidas de las distribuciones de tamaños, la caracterización de las muestras se ha completado con la realización de imágenes de microscopio electrónico (SEM). Las imágenes SEM han dejado patente la variedad de geometrías que presentan las partículas de las muestras naturales de polvo.

Las medidas de las matrices de scattering han sido realizadas en el COsmic DUst LABoratory (CODULAB) ubicado en Instituto de Astrofísica de Andalucía, en Granada, España. Las medidas se han realizado cubriendo un rango de ángulos de scattering desde 3 grados hasta 177 grados. Se ha verificado que todas las medidas pasan el test de coherencia de Cloude [2] dentro de las barras de error. Posteriormente, para facilitar el uso de las medidas como datos de entrada de los modelos de balance radiativo, la matrices experimentales se han extrapolado en el rango de ángulos a los que no son posibles las medidas, es decir,  $[0^\circ, 3^\circ]$  y  $[177^\circ, 180^\circ]$ . El método de extrapolación se presenta en el Capítulo 4 de esta Tesis.

Las medidas experimentales se han complementado con la simulación computacional de las matrices de scattering de la muestra de calcita. Se ha elegido dicha muestra por dos razones. En primer lugar, por el carácter birrefringente de la muestra. En segundo lugar, por la geometría característica de las partículas de dicha muestra, los cuales son discos y romboides con estructura de capas. Para llevar a cabo las simulaciones numéricas, hemos construido dichas formas computacionalmente, y hemos estudiado el efecto de la birrefringencia en los distintos elementos de la matriz de scattering. Las simulaciones se han llevado a cabo con el código DDSCAT 7.1 [3].

El trabajo viene complementado por experimentos de fotoforesis a 655 nm. La fotoforesis podría ser responsable de inyectar grandes cantidades de polvo en la atmósfera marciana. Dado que este trabajo está desarrollándose actualmente, en el manuscrito se presentan resultados preliminares, pero estos resultados están considerados para su publicación en breve. En el experimento se obtuvo la fuerza fotoforética para los análogos de polvo de Marte estudiados en esta Tesis. El principal objetivo del estudio es saber, bajo qué condiciones tanto de las partículas de polvo (tamaño, e índice de refracción) como atmosféricas (presión), la fuerza fotoforética es responsable del levantamiento de las partículas desde la superficie marciana.



---

El estudio se ha centrado en las muestras de palagonita (JSC MARS-1), basalto y calcita en un rango de presiones de 0.5 a 100 mbar. La dependencia de la fuerza fotoforética con la presión ha sido ajustada a la fórmula de Rohatschek, 1995 [4]. Gracias a ello se obtuvieron parámetros físicos adicionales para las muestras. En particular, el coeficiente de acomodación y el parámetro de asimetría dividido por el coeficiente de conductividad térmica. Se ha utilizado un novedoso método para obtener dichos parámetros, cuya derivación era, hasta ahora, bastante problemática para partículas irregulares.

La Tesis consiste en una introducción donde se trata, brevemente, la exploración de Marte, junto con la descripción del planeta, en particular su atmósfera. Se describe separadamente el polvo como constituyente muy importante de la atmósfera, y se exponen sus propiedades físicas, tales como su forma, tamaño y composición. En el capítulo 2 se presentan los objetivos de la Tesis. En el capítulo 3 se describe la metodología utilizada. La bibliografía de los capítulos se presenta conjuntamente, al finalizar el capítulo 3. A partir del capítulo 4 la bibliografía se presenta después cada capítulo. El capítulo 4, "Scattering matrices of Martian dust analogs at 488 and 647 nm", corresponde al artículo recientemente enviado a *Astronomy & Astrophysics* [5] con la doctoranda como primera autora. Los capítulos 5, 6 y 7 son los artículos previamente publicados, cuyos títulos respectivos son: "Effect of the orientation of the optic axis of simulated scattering matrix elements of small birefringent particles" [6], "Experimental and simulated scattering matrices of small calcite at 647 nm" [7], and "The Amsterdam-Granada Light Scattering Database" [1]. En el capítulo 8 se presentan los resultados preliminares del experimento de fotoforesis. La Tesis finaliza con las conclusiones.

# Introduction

From Ancient Egypt to Babylon, from China to India, from Greece to Rome, Mars has inspired the imagination of men throughout all of time. The planet's rusty-red color was associated with the conflagration of war what is often echoed in the names given to it in different languages. Moreover, in some cultures The Red Planet was identified with a god. In Ancient Egypt, Mars was Har Deched, "The Red One", in India, Lohitanga, "Red-Bodied". It was Nergal, the god of the underworld, death and war for the ancient Babylonians, for the Greeks and the Romans it was the god of war Ares and Mars, respectively. The Norse called it Tyr, the God of Law, and the Aztecs, Huitzilopotchli, the destroyer of men and cities. Huoxing, the fire-star, it was called by the ancient Chinese. Mars was a true companion for our imagination from the discovery of astronomy down to the present day. We drew pictures of it, Fig. 1.1 and even wrote novels about Martian lifeforms, little green creatures with antennas on the head. The Audio-play of the famous novel: *War of the Worlds* from H.G Wells even caused a mass-panic in New York and New Jersey, in 1938, Fig. 1.2. This has shown us how deep we are connected to The Red Planet.

Even until quite recently, the 1960s, we had a totally different concept of Mars. It was of general acceptance that the atmosphere of Mars consisted of nitrogen, not very different from that in the Earth's atmosphere. Astronomers based their opinions on precise measurements, but had not considered the presence of dust which creates the optical illusion of a dense Martian atmosphere. The effective exploration of Mars began on 14 July 1965, when Mariner 4 passed over the planet at an altitude of 9.850 km. The probe transmitted signals through the atmosphere as it passed behind the planet, revealing that the mean surface pressure on Mars was around 6-7 mbar (the value on Earth at an altitude of about 30 km). Mariner 4 was not the first space vehicle to approach Mars. The soviet probe, Mars 1, had already flown by the planet, but Mariner 4 was the first in transmitting images to Earth (e.g. Fig. 1.3). These 22 images proved that the climate on Mars was much harsher than expected. There were no canals, firstly observed and described by the Italian astronomer Giovanni Schiaparelli in 1877 (Fig. 1.1, [8]) and the observations indicated a very tenuous atmosphere.

The Golden Age of exploration of Mars began. In 1969 the Mariner 6 and 7 sent back hundreds of photos of Mars, and made the first observations of the surface and the atmosphere in the infrared and ultraviolet, confirming the hostile conditions for life. At the beginning of the 70s Mariner 9 reached the orbit of Mars and became the first Martian artificial satellite. The data from Mariner 9 revolted our understanding of the Red Planet. When Mariner 9 arrived at Mars on 14 November 1974, the planet was in the clutches of the greatest dust storm ever observed. The whole surface was obscured. Once the dust had settled, the probe carried out a complete photographic survey of the Martian surface, consisting of more than seven thousand images. Volcanoes, canyons, craters, river beds and spreading glaciers were discovered. During the northern winter and part of the spring, Mariner 9 examined the surface, the atmosphere, the polar caps and the clouds (e.g. Fig. 1.4) in ultraviolet, visible and infrared.

In the meantime the Soviet Union sent Mars 5. It successfully entered orbit around Mars in 1974. But unfortunately, it failed a few days later. Despite its very short mission, the spacecraft was able to perform very important and unique polarization measurements of Mars at large phase angles [9, 10, 11].

Lately, on 9 September 1975, two identical spacecrafts, Viking 1 and Viking 2 were launched. They consisted of a Mariner-type orbiter, coupled with a lander. This was one of the most complex and costly explorations ever undertaken by NASA. After 10 months of journey, Viking 1 entered to

Mars orbit on 19 June 1976. It was very important to find an ideal landing site, which was not too high, not too dusty, not too windy, not too sloping, not too rocky and not too near the poles. After difficulties in finding the perfect landing site Viking 1 lander touched the Martian surface, at Chryse Planitia, on 20 July. The lander carried instruments to achieve the primary scientific objectives of the lander mission (so did Viking 2 lander): to study the biology, chemical composition (organic and inorganic), meteorology, seismology, magnetic properties, appearance, and physical properties of the Martian surface and atmosphere. The primary object of the mission was to search for life. The official conclusion was "No life". The sister-ship Viking 2 landed on the other side of the planet on the plain of Utopia. The results of the experiment were the same. No life. Nevertheless, the Viking mission was counted as a success: the expecting working lifetime of the module was 90 days, but they rendered service for more than 6 years.

After the two Viking missions, many years elapsed before another spacecraft, successfully reached the Martian orbit. In 1988 Phobos 2 entered the orbit and sent back some data. However, sadly, it lost contact just before deployment of its two landers. Later, Mars Global Surveyor, MGS, was successfully launched, in November 1996, and reached Martian orbit in September 1997. The main scientific goals of the mission were: characterization the surface features and geological processes on Mars, to determine the composition, distribution and physical properties of surface minerals, rocks and ice, and to determine the global topography, planet shape, and gravitational field. Moreover, MGS was used to study the magnetic field, monitor global weather and the thermal structure of the atmosphere.

During the period 1997-2011 many arrivals to Mars took place. Mars Pathfinder with Sojourner, the first wheeled robotic Mars rover successfully landed on the Martian surface on 4 July 1997. The aim of the mission was to analyze the Martian atmosphere, climate, geology and the composition of its rocks and soil. With 2001 came Mars Odyssey orbiter. At the moment the spacecraft is operating for 13 years, 2 months and 1 day (from the launch). Its mission is to detect evidence of past or present water and volcanic activity on Mars. The Mars Express, MEx, is operating now for 11 years and 6 days (since launch in 2003). MEx is the first planetary mission attempted by the ESA agency and it is dedicated to the orbital (and originally in-situ) study of the interior, subsurface, surface and atmosphere, and environment of the planet Mars. In 2004, the twins Martian Exploration Rovers (MERs), MER A-Spirit, MER B- Opportunity safely landed on Martian surface. The mission's scientific objective was to search for and characterize a wide range of rocks and soils that hold clues to past water activity on Mars.

In 2006, Mars Reconnaissance Orbiter, MRO, joined the other five active spacecraft which were either in orbit or on the planet surface: MGS, MEx, Mars Odyssey, and two MERs. MRO was destined to analyze the landforms, stratigraphy, minerals, and ice of Mars. It paves the way for future spacecraft by monitoring Mars' daily weather and surface conditions, studying potential landing sites, and hosting a new telecommunications system.

Other very successful mission, Phoenix, landed in 2008 in the high latitudes of Northern hemisphere to study in situ one of the regions where the Mars Odyssey probe discovered an ice rich layer beneath a few centimeters of soil. Mission scientists used instruments on-board the lander to search for environments suitable for microbial life on Mars, and to research the history of water there.

Recently the Mars Science Laboratory, MSL, with rover Curiosity landed successfully on Mars at 6 August 2011. The MSL mission has four scientific goals: determine the landing site's habitability including the role of water, the study of the climate and the geology of Mars. It is also useful preparation for a future manned mission to Mars.

The long list of successes in the exploration of Mars is unfortunately accompanied with a longer list of unsuccessful missions. Especially the former Soviet Union lost a large amount of space probes, among others Mars-2 and Mars-3, the twin probes, which arrived to Mars in 1971. After Mars 2 crash-landed on the Martian surface, Mars 3 lander became the first spacecraft to attain soft landing on Mars. However, the contact was lost soon. By coincidence, as shown by Mariner 9, a particularly large dust storm rose up on Mars, that seriously affected the mission. Mariner 9 arrived and successfully orbited Mars on 14 November 1971. It was just two weeks prior to Mars 2 and Mars 3 and planetary scientists were surprised to find the atmosphere so thin but full of dust. It was "the largest storm ever observed" and the surface was totally obscured. Unable to reprogram the mission computers, both Mars 2 and Mars 3 dispatched their landers immediately, and the orbiters used up a significant portion of their available data resources in snapping images of the featureless dust clouds below, rather than the surface mapping.

After losing some missions the Soviets finally directed their main interest into Venus investigation. Some recent NASA equipment failed as well: Mars Observer (1992), Mars Climate Orbiter (1998), Mars Polar Lander and Deep Space 2a, 2b (1998). British/European Beagle 2 failed in landing in 2003, Japanese Nozomi, failed in 1998 entering the orbit and Chinese Yinghuo-1 failed leaving the Earth in

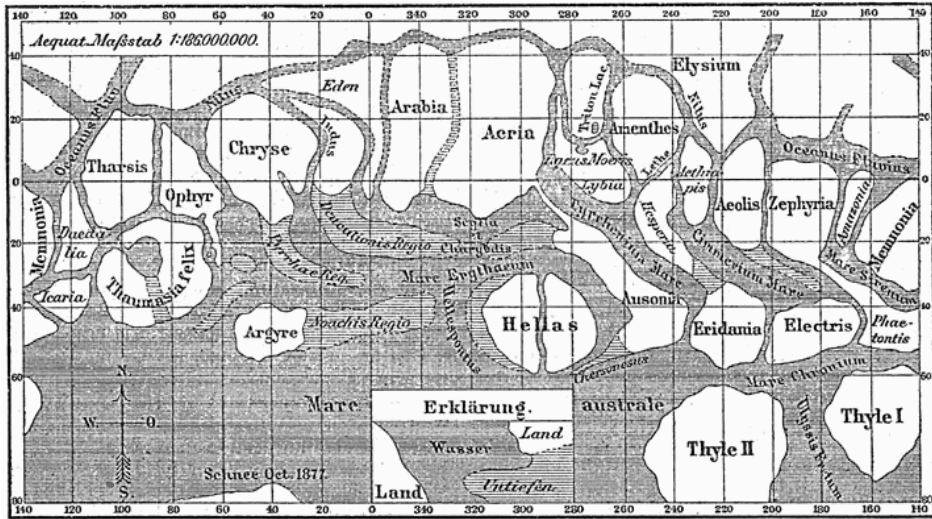


Figure 1.1: The map of Mars as sketched by Schiaparelli in 1877.

2011. In Fig. 1.5 one can see the number of successful and unsuccessful missions year by year.

On image-map shown in Fig. 1.6 are presented landing places of the successful landing missions (landers and rovers).

Nowadays, although during 50 years after successful Mariner 4 mission, orbiter and lander missions to Mars have clearly disproved the more fanciful theories of early observers, the images and data returned have only added to our fascination. They have shown us:

- the largest volcano in the Solar System, Olympus Mons, 600 km in diameter and 20 km in high,
- a huge rift valley (Valles Marineris, 4000 km long, up to 600 km wide and 8 km deep) created by massive uplifting of the mantle (Tharsis bulge),
- a remarkable global dichotomy where the northern hemisphere is, on average, 3 km below the average height of the southern hemisphere,
- evidence for liquid water in Mars past in the channels, valleys, and stream lined islands (e.g. Ares Vallis),
- a dry, rocky surface covered with dust, dominated with iron oxides, and
- the dusty atmosphere, the season variations, climate diversity and sometimes extremely changing weather conditions.

Although Mars is a beautiful place, the missions have shown that this planet has a vary harsh climate and it is not particularly hospitable towards man. As observed by Thermal Emission Spectrometer, TES, an instrument on board MGS, maximum surface temperatures during the Martian day under clear conditions are in general, below 250 K and during the polar nights temperatures can drop even below 140 K ([12], Fig. 2 therein). The thin atmosphere provides no protection from solar UV radiation. Ice water is presented at polar cups but probably only in the form of a permafrost layer and under the surface over the rest of the planet. However, the fact that liquid water was once present on the surface (albeit in Noachian, over 3 billion years ago, e.g. [13]) triggered imaginations and missions to Mars were and are designed to search for evidence of past water and life.

Our knowledge of Mars is now very extensive. Many very complete books (e.g. [14, 15, 16]) and reviews were published compiling information about the planet. Therefore, in this Thesis we restrict to discussion of the Martian atmosphere and in particular its dust component. Dust plays an important role in the dynamics of the atmosphere and in the illumination of the surface. Dust acts as a heat source for atmospheric gases, it can act as a nucleation site for condensates, it coats the surface via sedimentation, and it scatters incoming radiation to provide a diffuse illumination at the surface. Its atmospheric number density is also highly time variable. The role of dust is discussed in more details in Sections 1.1 and 1.2.



Figure 1.2: The Martian tripod attacking Earth from the 1906 French edition of H.G. Wells' *The War of the Worlds*, by Henrique Alves Correa.

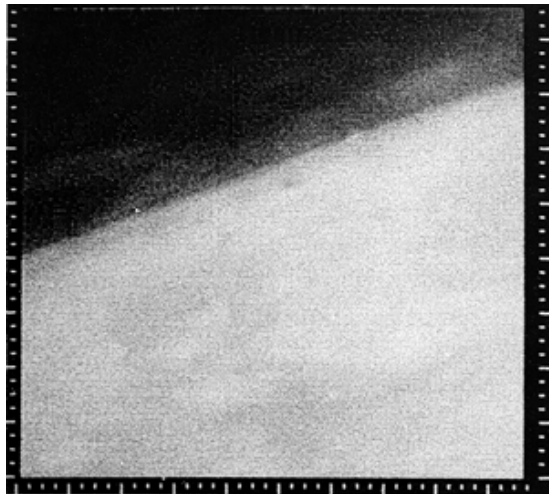


Figure 1.3: Mariner 4 image, the first close-up image ever taken of Mars. This shows an area about 330 km across by 1200 km from limb to bottom of frame, centered at 37°N, 187°W. The area is near the boundary of Elysium Planitia to the west and Arcadia Planitia to the east. The hazy area above the limb may be clouds. This image has been enhanced to bring out some of the details of this haze-like portion of the image, at the expense of resolution of the surface features. The resolution of this image is about 5 km. Credits: NASA.

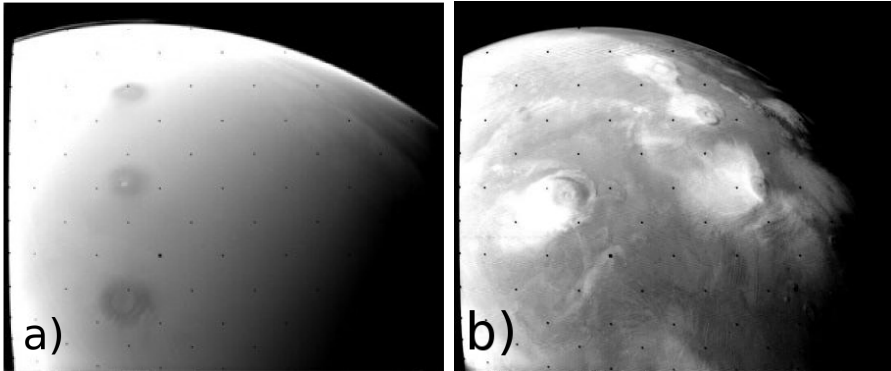


Figure 1.4: a) An early image of Mars after Mariner 9's arrival in November 1971 revealing a high opacity caused by atmospheric dust, leaving visible only a few mountains tops. b) A later Clearing skies revealed not only the Tharsis Montes (upper right) but the great bulk of Olympus Mons (mid-left). Credits: NASA.

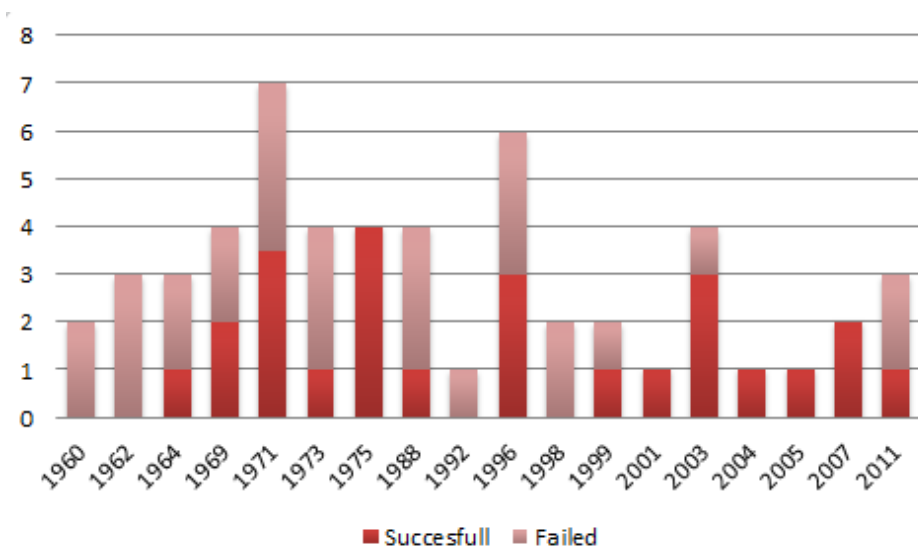


Figure 1.5: The successful and failed missions to Mars during five decades of exploration. At this graph the orbiters and landers/rovers are considered two different missions, e.g. Viking 1 Orbiter and Viking 1 Lander or MEx and Beagle.

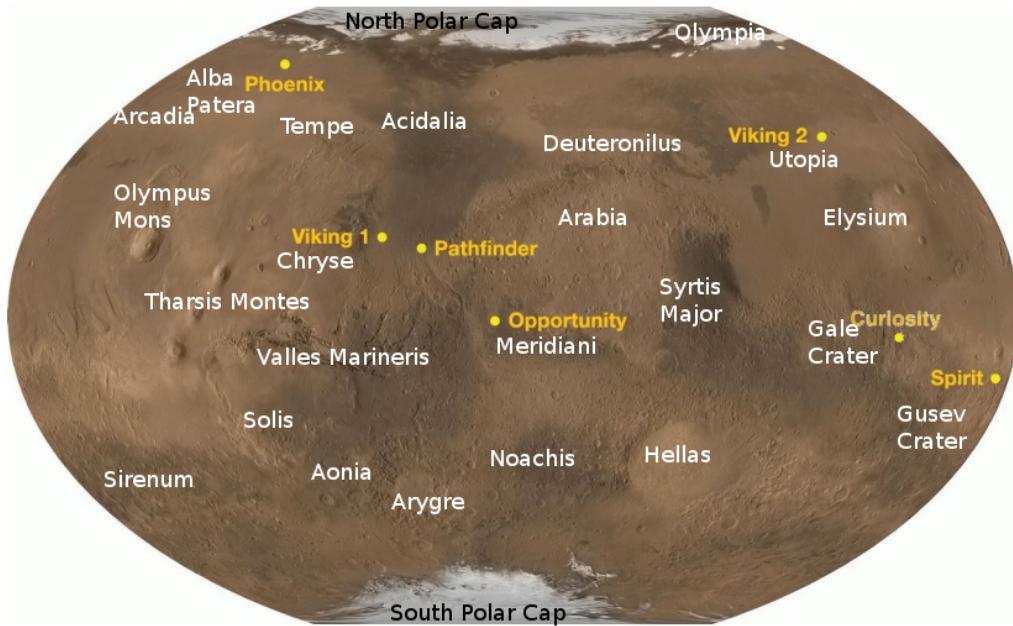


Figure 1.6: The photo-map of Mars with some geographical regions and landing sites of successful landing missions indicated.

## 1.1 Martian Atmosphere

The huge amount of data collected by the spacecrafts has displayed very valuable information about Martian geology and its atmosphere.

Mars has shared with the other rocky planets the history at the beginning of our Solar System. The Solar System planets evolved depending on their physical characteristics. Their masses and distance to the Sun have in particular affected their atmospheres. In Tab. 1.1, we present the basic physical and orbital parameters of Mars compared with those of Venus and the Earth. The listed values are from the IAV/IAG Working Group Report, 2006 (see <http://nssdc.gsfc.nasa.gov/planetary/planetfact.html>).

The distance from the Sun (approx. 1.5 AU) makes Mars a cold planet. According to NASA Mars Fact Sheet web page the global average temperature at the surface is  $\sim 210$  K ( $-63^{\circ}\text{C}$ ). However, the diurnal temperature range is from 184 K to 242 K ( $-89^{\circ}$  to  $-31^{\circ}\text{C}$ ) (at Viking 1 Lander site). The large temperature difference is a consequence of the lack of substantial cloud layers or a thick atmosphere that would reflect back radiation coming from the surface. In Fig. 1.7, some examples of summer temperature profiles at Tharsis region derived from MGS radio occultation measurements are presented [12]. In this case the day-night differences are about 40-80 K depending strongly on the atmospheric conditions.

Mars is much smaller than Earth or Venus. Its density is much lower and its mass is about 10 times smaller than Earth's. The low mass of Mars did not permit light atmospheric components as nitrogen or oxygen to stay in the atmosphere in large amounts. The main gas component of Martian atmosphere is carbon dioxide. The gas composition of the much heavier atmosphere is similar to that of Venus. However, the similarity ends there because the surface pressure of Mars is only about 6 mbar compared to 92 bars on Venus. Due to its thin atmosphere, there is virtually no greenhouse effect as is the case of Venus.

Mars has an axial tilt and a rotation period similar to those of Earth, Fig. 1.8 (top). Thereby, it experiences the same seasons as the Earth. Moreover, its day is about the same length. Its year, however, is almost twice as long as Earth's. A convention used by spacecraft lander projects to date has been to keep track of local solar time using a 24 hour "Mars clock" on which the hours, minutes and seconds are 2.7% longer than their standard (Earth) durations. The mean Martian day, named "sol", equals 24 hours, 39 minutes, and 35.244 seconds.

The track of the Martian seasons is described by solar longitude,  $L_s$ , which determines the position of Mars in its orbit around the Sun.  $L_s$  is defined as the angle described by the line connecting the Sun to the position of Mars in its orbit, Fig. 1.8 (bottom), relative to the planet position at northern hemisphere spring equinox.  $L_s$  is therefore 0 degrees at the Martian northward spring equinox, 90 degrees at the Martian northern summer solstice, 180 at the Martian northern autumn equinox, and 270 degrees at the Martian northern winter solstice.

	Venus	Earth	Mars
Distance to Sun [AU]	0.723	1	1.527
Min. distance from the Earth ( $10^6$ km)	38.2	-	55.7
Max. distance from the Earth ( $10^6$ km)	261.0	-	401.3
Min. apparent diameter from Earth (sec. of arc)	9.7	-	3.5
Max. apparent diameter from Earth (sec. of arc)	66.0	-	25.1
Orbit eccentricity	0.0067	0.0167	0.0935
Obliquity (deg)	177.36	23.45	25.19
Equatorial Radius (km)	6052	6378	3398
Polar radius (km)	6051.8	6356.8	3376.2
Mass ( $10^{24}$ kg)	4.87	5.98	0.642
Mean density ( $kg/m^3$ )	5243	5515	3933
Surface gravity ( $m/s^2$ )	8.87	9.80	3.71
Escape velocity (km/s)	10.36	11.19	5.03
Number of natural satellites	0	1	2
Length of the day (h)	2802	24	24.65
Mean Albedo	0.59	0.39	0.15
Solar irradiance ( $W/m^2$ )	2613.9	1367.6	589.2
Surface Temperature(K)	740	288	223
Surface pressure(bar)	92	1	0.006
Surface density ( $kg/m^2$ )	6.58E+01	1.21E+00	1.42E-02
Main atmospheric composition	$CO_2$	$N_2, O_2$	$CO_2$

Table 1.1: Venus, Earth and Mars comparison of basic physical and orbital parameters. Credits: NASA website (<http://nssdc.gsfc.nasa.gov/planetary>).

Table 1.2 lists the gases composing the Martian atmosphere, as measured by space probes [16]. As mentioned, the atmosphere is very thin with a mean value of about 6 mbar at the surface. However, this value is extremely variable, due not only to the great topographic differences observed on the surface, but also because of the temperature, that during polar night, may fall below the condensation temperature of  $CO_2$  which is a significant fraction of the atmospheric mass. Fig. 1.9 shows the daily averaged surface pressure recorded by the two Viking Landers [12]. The offset between the two curves is caused by the elevation difference (1.2 km) between the two landing sites. Over the course of a Martian year, the surface pressure varies by roughly 30%, decreasing as  $CO_2$  condenses on the seasonal ice cap at the winter pole, and then increasing as  $CO_2$  sublimates from the seasonal ice cap at the summer pole.

The dynamics of Martian atmosphere is complex. Winds on Mars are driven by gas pressure differences, which are created by temperature variations. The temperature and pressure of the atmosphere changes diurnally and along the year. Those occur on many scales at different regions and epochs on the planet. There are dust devils - micro scale eddies (mechanical and thermal turbulence, especially near the ground), small local wind systems (especially on mountainous regions), moving storms, stationary and seasonal large-scale weather patterns and planetary-scale waves. In Fig. 1.8, we present the circulation corresponding to northern hemisphere midsummer [17]. The image illustrates the complexity of circulation system: circulation cells, different types of wind and flows. The details about dynamics of the Martian atmosphere can be found in e.g. [16, 17].

As seen, on Mars, the dust activity is wide spread. Dust devils occur at a rate of 100 per year on the surface. Moreover, regional, local, and global dust storms occur. During such events the whole planet can be covered by dust for months. As an example, in Fig. 1.10 we show an image of the planet taken by the Hubble Space Telescope before and during the 2001 global dust storm. With those winds,



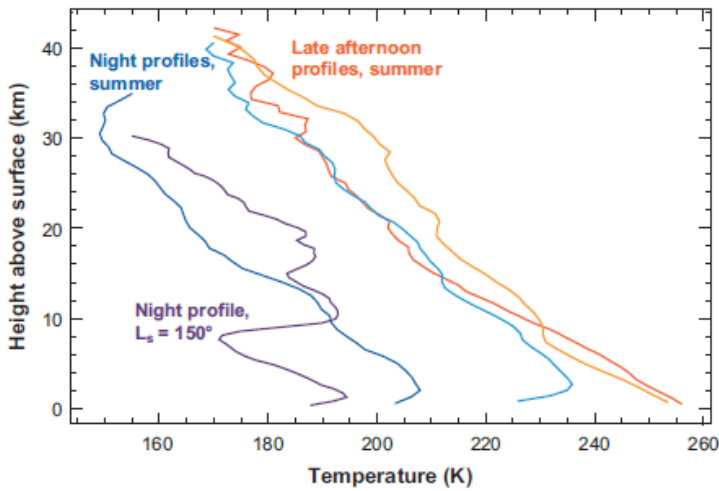


Figure 1.7: Temperature profiles as a function of height as derived from MGS radio occultation data. Late-afternoon temperatures are shown from southern mid-latitudes during summer. Nighttime temperatures are also shown from mid-latitudes during summer. A nighttime profile is shown with large waves taken near the Tharsis volcanoes at  $L_s = 150^\circ$ . Image from Smith [12].

loose surface material is moved and small dust particles are lifted from the surface to the Martian atmosphere. This is probably not unique the mechanism which rises up the particles from the Martian surface. Besides the wind stress,  $CO_2/H_2O$  out-gassing of the surface, pressure differences within dust devils or even meteorite impacts have been suggested as dust lifting processes on Mars [18, 19]. In addition, photophoresis and solid state greenhouse effects have been proposed as effective dust rising mechanisms [20, 21]. De Beule et al. [22], have recently shown that Martian soil can work as gas (Knudsen) pump injecting the particles into the atmosphere. In contrast to the Earth's atmosphere, where dust particles can remain unsettled for a large fraction of time, similarly-sized Martian dust can stay for a much shorter time [23]. However, on Earth, dust particles once on the surface get more efficiently trapped because of soil moisture, forming aggregates, or are directly removed by falling on the oceans. On Mars, the lack of a cleaning mechanism like rain or snow imply that these dust particles, once on the surface, can be injected again in the atmosphere.

The dust in the atmosphere is a barrier for thermal radiation, altering the energy budget of the atmosphere, and rising up its temperature. The atmospheric dust on Mars is a key radiative factor in the heating of the atmosphere and plays an important role in radiative and dynamical models of the Martian atmosphere. The study of the scattering properties of Martian dust analogs constitutes the main body of this Thesis.

## 1.2 Atmospheric Dust

Observations of atmospheric dust show that the Martian year can be divided into two distinct periods: a clear season during northern spring and summer, and a dust season, when great storms occur, during northern autumn and winter. In the clear season, storms are relatively few in number and in general, there is a small quantity of suspended dust in the atmosphere. During the Martian year typical small storms arise on similar dates and therefore quite similar quantities of airborne dust are observed. However, the global planet encircling storms that characterize the dust season vary from one year to another.

For security of future missions to Mars, especially the manned ones, it is necessary to study the dust, and the way it affects the weather conditions. Dust affects the energy budget of the atmosphere. Apart from scattering, it absorbs the solar radiation and re-radiates it at IR wavelengths, heating this way the

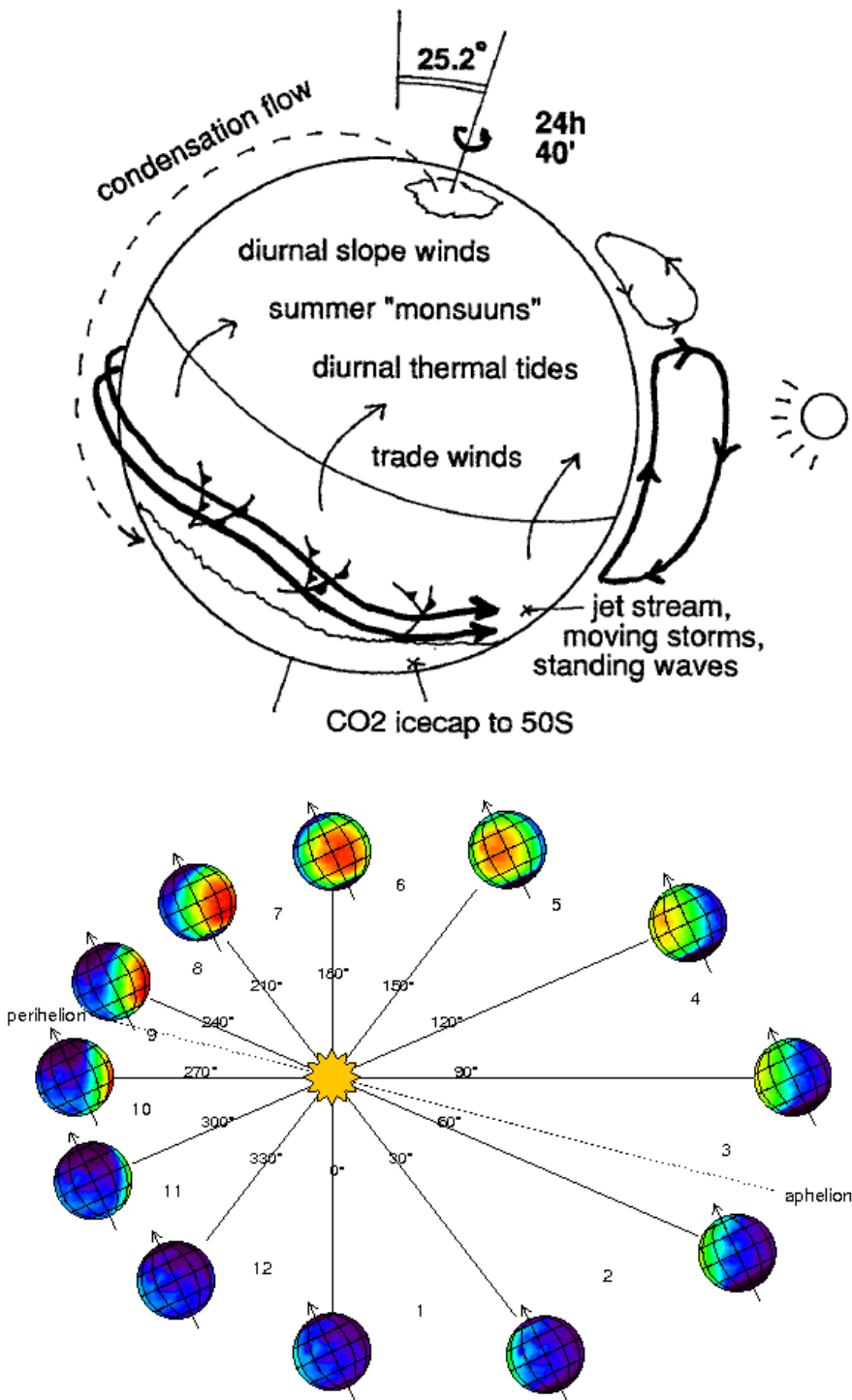


Figure 1.8: Top: The main wind systems of Mars during its northern hemisphere midsummer when the planet is in aphelion (Savijarvi, [17]), Bottom: The orbit of Mars with indicated Mars-Sun angles, the solar longitudes,  $L_s$ . The northern hemisphere spring equinox corresponds to  $L_s = 0$ , whereas beginning of the summer starts at  $L_s = 90$ . Credits: The Mars Climate Database Projects, [http://www-mars.lmd.jussieu.fr/mars/time/solar\\_longitude.html](http://www-mars.lmd.jussieu.fr/mars/time/solar_longitude.html).

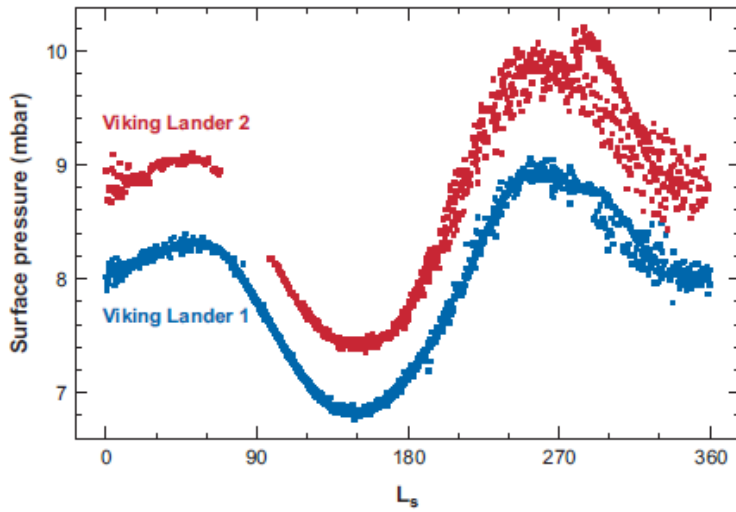


Figure 1.9: Daily averages of surface pressure (mbar) as recorded by the two Viking Lander spacecraft. Image from Smith [12].

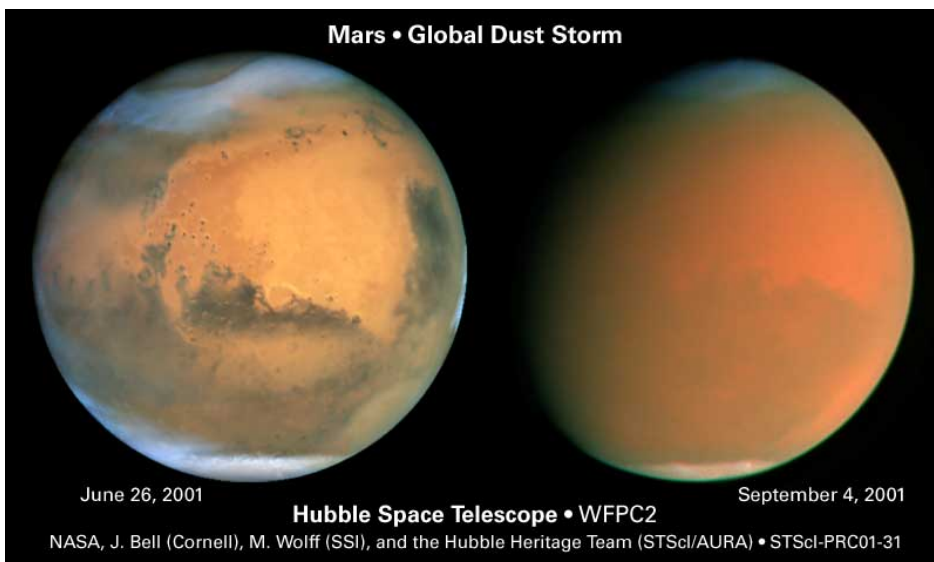


Figure 1.10: These Hubble Space Telescope images show the Red Planet before (left) and during (right) the great Martian dust storm of 2001. Credits: NASA.

Atmospheric composition:		
Major (by volume):	Carbon Dioxide ( $CO_2$ )	95.32%
	Nitrogen ( $N_2$ )	2.7%
	Argon (Ar)	1.6%
	Oxygen ( $O_2$ )	0.13%
	Carbon Monoxide (CO)	0.08%
Minor (ppm):	Water ( $H_2O$ )	210
	Nitrogen Oxide (NO)	100
	Neon (Ne)	2.5
	Hydrogen-Deuterium-Oxygen (HDO)	0.85
	Krypton (Kr)	0.3

Table 1.2: The major and minor components of Martian atmosphere [16]. One part per million (ppm) denotes one part per 1.000.000 parts.

atmosphere. The heating is very efficient especially under stormy conditions since there are enormous quantities of dust in the atmosphere. In Fig. 1.11 the schematic picture of transparent periods (a) and dust storm conditions (b) is displayed. In the first case we have single scattering regime, when the light is scattered only once by the dust particles, whereas under stormy conditions the light is scattered by the dust several times.

The radiative properties of the dust particles depends on their physical properties, namely, their size, composition (refractive index) and shape. Since dust plays crucial role in the radiative balance of the planet's atmosphere, the information of its physical properties is of high interest.

As expected, Martian dust is irregularly shaped, as revealed by the Martian regolith images from Phoenix microscope camera (see Fig. 1.12).

In this Section, a summary of retrievals of Martian airborne dust physical properties, as size and composition, with their short historical background is given.

### 1.2.1 Size.

The majority of authors, who are describing the size of Martian dust, uses the nomenclature of Hansen and Travis, [24]. Following this pioneering work, the aerosol particle size distribution function,  $n(r)$ , is expressed in terms of the first two moments of the distribution; the effective radius,  $r_{\text{eff}}$ , and the dimensionless effective variance,  $v_{\text{eff}}$ . They are given by the following formulae:

$$r_{\text{eff}} = \frac{\int_0^{\infty} r \pi r^2 n(r) dr}{\int_0^{\infty} \pi r^2 n(r) dr} \quad (1.1)$$

$$v_{\text{eff}} = \frac{\int_0^{\infty} (r - r_{\text{eff}})^2 \pi r^2 n(r) dr}{r_{\text{eff}}^2 \int_0^{\infty} \pi r^2 n(r) dr}, \quad (1.2)$$

where  $r$  is the radius and  $n(r)$  is the size distribution of the particles. Hansen and Travis [24] demonstrated that the exact form of the size distribution,  $n(r)$ , is not important for most problems as long as  $r_{\text{eff}}$  and  $v_{\text{eff}}$  are specified.

As previously explained, there are many physical processes affecting the dust environment on Mars. In addition, there are several (indirect) methods to retrieve size, shape, and composition of the dust particles. The physical dust properties can be inferred from photometric, polarimetric and spectroscopic observations, either from the ground or Earth-orbiting telescopes (HST), or from in-situ Mars orbiters and lander data. Tables 1.3 and 1.4 display compilations of retrieved sizes of the Martian dust during both clear sky and global dust storm conditions, where the retrieval methods and their limitations are also shown.

Ground-based observations performed under clear sky conditions are affected by the contribution of the reflection by the planet surface. In the case of polarimetric observations, however, if the observations are made at exactly the inversion angle for the scattering by the surface alone, which is near  $25^\circ$  for the Mars, the degree of polarization of the scattered light would be essentially due to the contribution of airborne dust. Some authors as Morozhenko e.g. [25] used that method, although in combination with assumption of spherical particles. In addition, as shown by Dlugach & Petrova [26], the retrieved

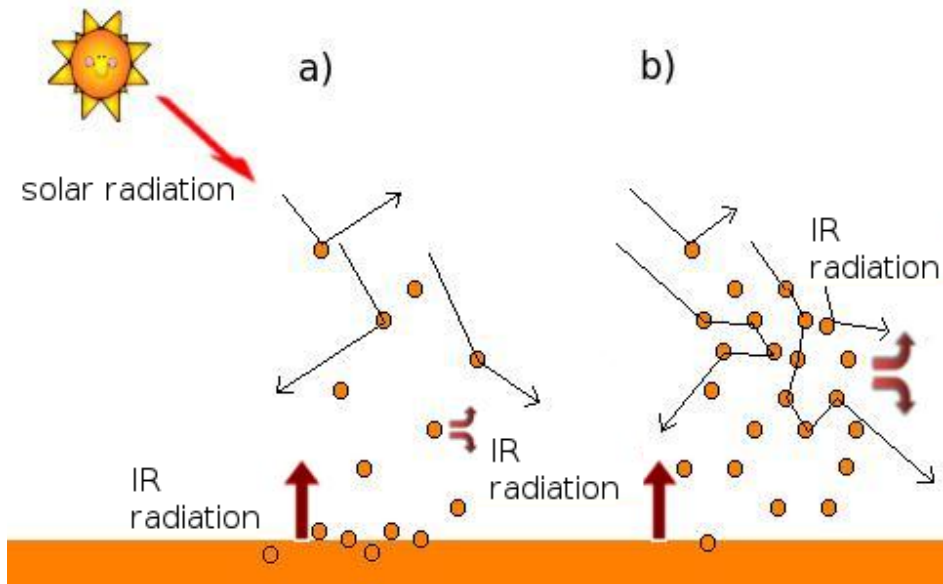


Figure 1.11: Schematic picture of scattering by dust in the Martian atmosphere under a) clear sky conditions, when the light is scattered only once (single scattering). Dust in the atmosphere re-radiates at IR wavelengths, however, the impact is much smaller than under dust storm conditions (b) in which multiple scattering processes occur.

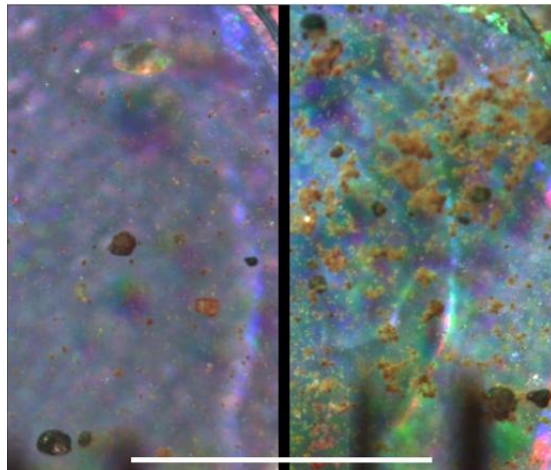


Figure 1.12: This pair of images taken by the Optical Microscope on NASA's Phoenix Mars Lander offers a side-by-side comparison of an air-fall dust sample collected on a substrate exposed during landing (left) and a soil sample scooped up from the surface of the ground beside the lander. Similar fine particles at the resolution limit of the microscope are seen in both samples, indicating that the soil has formed from settling of dust. The microscope took the image on the left during Phoenix's Sol 9 (3 June 2008). It took the image on the right during Sol 17 (11 June 2008). The scale bar is 1 millimeter. Credits: NASA, [http://www.nasa.gov/mission\\_pages/phoenix/images/press/DustFallSoilComparison\\_001.html](http://www.nasa.gov/mission_pages/phoenix/images/press/DustFallSoilComparison_001.html).

values depend on assumed refractive indices of the dust. Moreover, as Ebisawa & Dollfus [27] have shown, various events in the planet's atmosphere, such as hazes, clouds, dust devils, and storms might significantly affect the polarization of different areas on Mars. In consequence, this retrieval method is not accurate. The derived sizes in the spectral region  $0.225 - 0.434 \mu\text{m}$  are  $r_{\text{eff}}=0.05 - 0.065 \mu\text{m}$  and  $v_{\text{eff}} = 0.1$  [26] (see Tab. 1.3).

Spacecraft observations from an orbiter gave new possible solutions of the problem of reflection by the surface. For example, Drossart et al. [28] have used photometric profiles of the surface based on Phobos data at  $0.9 - 2.3 \mu\text{m}$ . The obtained results,  $r_{\text{eff}} = 1.2 \mu\text{m}$  and  $v_{\text{eff}} = 0.25$ , are close to ones obtained just recently. In addition, the authors accounted for irregular particles under multiple scattering regime. However, it is difficult to estimate the surface effect completely using this method. Furthermore, the measurements can also be influenced by ice particles.

The extensive coverage of the Emission Phase Function (EPF) is a much more qualitative approach. Such measurements firstly were carried out with the ultraviolet spectrometer UVS on board Mariner 9 in the  $25^\circ\text{-}85^\circ$  phase angle domain. Later that technique was widely used by e.g. TES (Thermal Emission Spectrometer)/MGS [29] or CRISM (Compact Reconnaissance Imaging Spectrometer for Mars)/MRO [30] that provided an extensive angular coverage of EPF sequences, Fig. 1.13. This method consists on viewing the same surface point through variable amounts of atmosphere, which can be used to determine the atmospheric properties. This procedure allows the separation of scattering by surface and by aerosols [31]. In addition, the EPF emission angle coverage induces significant scattering angle variations and the brightness variations are associated with the aerosol single scattering phase function. EPF sequences from TES/MGS were analyzed by Clancy et al. [29], with multiple scattering radiative transfer codes with the aim of obtaining for the first time seasonal/latitudinal distributions of aerosol visible optical depths, particle sizes, and single scattering phase functions. Clancy et al. [29] determined the aerosol particle sizes from visible/IR optical depth ratios, whereas Wolff & Clancy [32] performed IR spectral fitting analysis. Within their distinctive uncertainties, those two methods of aerosol particles size determination are equivalent.

The most commonly observed dust size obtained by Clancy et al. [29] is  $1.5 \pm 0.1 \mu\text{m}$ . However, airborne dust particle sizes clearly exhibit seasonal variations. In particular, very small dust particle sizes ( $r_{\text{eff}} = 1.0 \pm 0.2 \mu\text{m}$ ) appear commonly over northern latitudes for the seasonal ranges  $L_s = 40 - 200^\circ$  and  $320 - 340^\circ$ , and significantly larger dust particle sizes ( $r_{\text{eff}} = 1.8 - 2.5 \mu\text{m}$ ) were present at southern latitudes during the 2001 global dust storm. Wolff & Clancy [32] found that  $r_{\text{eff}} = 1.5 - 1.6 \mu\text{m}$  is quite representative for low and moderate dust loading epochs.

Another possibility to avoid surface reflection is the limb observational technique. Soviet Phobos spacecraft performed solar occultation observations of the Martian atmosphere, which resulted in nine vertical profiles of volume extinction coefficient at  $1.9$  and  $3.7 \mu\text{m}$  in the altitude range of  $12 - 35$  km. Korablev et al. [33] have obtained average  $r_{\text{eff}} = 1.3 \pm 0.2 \mu\text{m}$  at  $12 - 35$  km. However, there is a contribution of ice particles but they appear likely above  $20$  km. Moreover, the interpretation of observations was performed in terms of Mie scattering (spherical particles).

The MEx has performed a series of limb observations using occultation techniques and limb scattering photometric observations in the UV and near-IR spectral range with the SPICAM (Ultraviolet and Infrared Atmospheric Spectrometer) instrument. This has allowed systematical studies of the vertical structure of Martian aerosols. The retrieval method for the occultation technique is presented in Quemerais et al. [34], while the results for dust and clouds are discussed in [35, 36]. However, unlike Korablev et al. [33], they have used the semi-empirical model of Pollack and Cuzzi [37] for irregular particles in their radiative transfer model, retrieving particles sizes in the  $10 - 100$  nm range above  $20$  km. From this method, it is difficult to separate the ice and the dust contribution.

Finally, measurements carried out from the surface of Mars, are virtually free of the surface influence. The images obtained at several visible wavelengths by the Viking cameras [38], Mars Pathfinder [39, 40] MERs, Opportunity and Spirit [41] allowed the Martian sky brightness to be analyzed at various phase angles, and the angular dependence of intensity of light scattered in the atmosphere was obtained. Examples of the images taken by Pathfinder and Spirit are presented in Fig. 1.14. The observations have been modeled using Mie theory but adopted for non-spherical shapes using the semi empirical approach by Pollack and Cuzzi [37]. The sizes obtained with aero-optics experiments on landers or rovers are coherent between each other and vary from  $r_{\text{eff}} = 1.47 \mu\text{m} \pm 0.21$  for Spirit [41] to  $r_{\text{eff}} = 1.85 \mu\text{m} \pm 0.3$  for Viking [38]. The sizes retrieved from other surface missions are presented in Tab. 1.3.

When the observations are performed under storm conditions there is no surface reflection problem since the atmosphere can be considered semi-infinite. Under such conditions Dollfus et al. [42] have performed Earth-based observations of the degree of linear polarization. The best fits to the observations were obtained for particles radii  $> 8 \mu\text{m}$ . It is important to mention that non-absorbing spherical

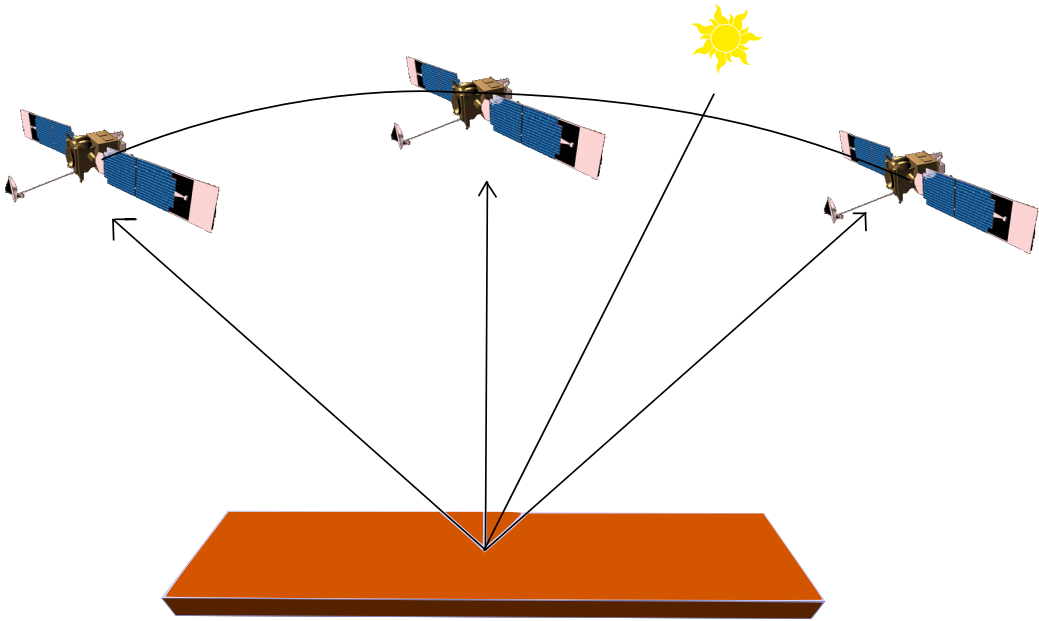


Figure 1.13: Schematic representation of an emission phase function (EPF) sequences, as observed from the MGS orbiter. The solar incidence angle is almost constant while the emission angle viewed from the orbiter varies from  $-75^\circ$  to  $75^\circ$ .

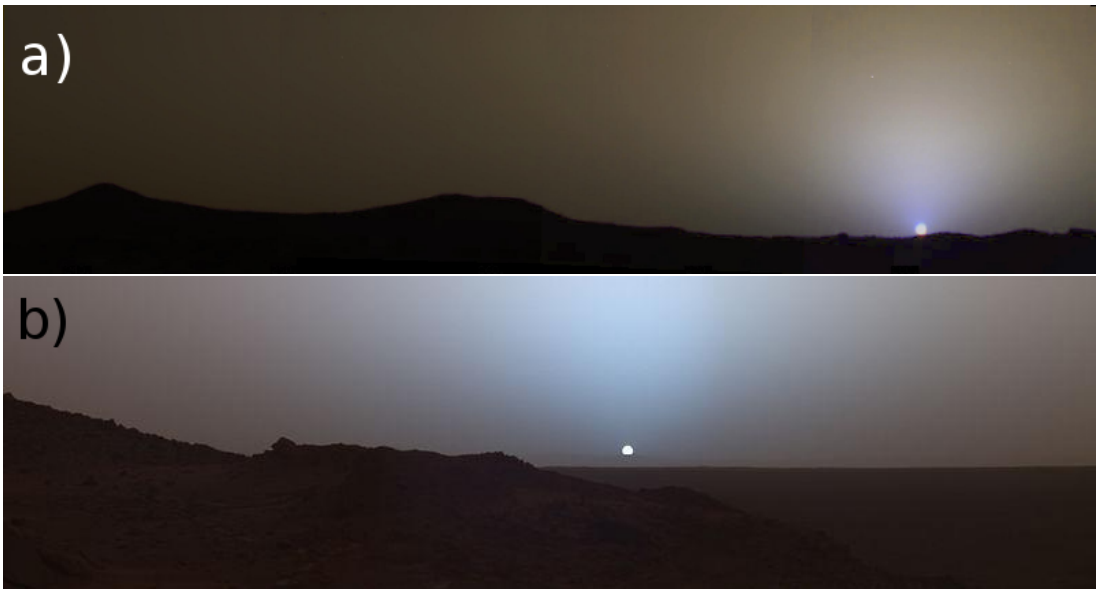


Figure 1.14: The twilights on Mars. a) Martian sunset by Pathfinder at Ares Vallis (July, 1997). b) Martian sunset by Spirit rover at Gusev crater (May, 2005). Credits: NASA.

particles were used in the model and that the obtained results are far from the actually expected.

Dlugach & Morozhenko [43], have simulated integral brightness for planetary disk. From this method the estimated particle size depends on the chosen imaginary part of refractive index,  $k$ . The  $k$  was set to 0.0001 that is close to the value of basalt glass at  $0.443 \mu\text{m}$ . To retrieve the size the dust particles are also assumed to be spheres. The results are  $r_{\text{eff}} = 4.5 - 7.5 \mu\text{m}$ ,  $v_{\text{eff}} = 0.2$ . Those sizes are also much larger than recent estimates for Martian dust.

Spacecraft observations at wide phase angle range gave more accurate methods to retrieve the Martian dust size and the refractive index of particles. Such measurements were carried out with the ultraviolet spectrometer UVS on board Mariner 9 during the 1971 global dust storm. The angular dependence of intensity of light diffusely scattered by the dust cloud layer by using both a model of spherical particles [44, 45] and a semi-empirical theory for randomly oriented particles [46] have been used to retrieve the dust size. The obtained sizes were  $r_{\text{eff}} = 0.8 - 1.8 \mu\text{m}$  by assuming spherical particles and  $r_{\text{eff}} = 0.2 \mu\text{m}$  for irregular ones. However, those retrievals are not considered reliable since multiple scattering was ignored in the radiative transfer calculations.

The EPF sequences can be used to retrieve dust sizes either during clear sky or dust storm conditions. During low transparency periods, Clancy et al. [29] have retrieved  $r_{\text{eff}} = 1.8 - 2.5 \mu\text{m}$ .

In Tabs. 1.3 and 1.4 the results that are considered more representative for Martian dust are marked by ♠.

Conditions:	clear sky		
Method:	size	Possible solutions of problem with reflected light by surface/ comments	reference
Ground based polarimetry observations	$r_{\text{eff}} = 0.05 - 0.065 \mu\text{m}$ $v_{\text{eff}} = 0.1$	There is a possible influence of inversion angle of radiation reflected by the surface. The influence of clouds and fogs unknown.	Dlugach & Petrova [26]
Spacecraft observations from the orbit:			
Phobos/ISM	$r_{\text{eff}} = 1.2 \mu\text{m}$ $v_{\text{eff}} = 0.25$	photometric profiles of the surface	Drossart et al. [28]
MGS/TES	♠ $r_{\text{eff}} = 1.5 \pm 0.1 \mu\text{m}$	- the extensive angular coverage of Emission Function (EPF) sequences: $1.5 \pm 0.1 \mu\text{m}$ is the most commonly observed dust size.	Clancy et al. [29]
MGS/TES	♠ $r_{\text{eff}} = 1.5 - 1.6 \mu\text{m}$	representative for low and moderate dust loading epochs.	Wolff & Clancy [32]
Phobos	$r_{\text{eff}} = 1.3 \pm 0.2 \mu\text{m}$	- limb measurements average at 12 - 35 km. There is a contribution of ice particles but they appear likely above 20 km. Moreover, the interpretation of observations was performed in terms of Mie scattering (spherical particles).	Korablev et al. [33]
SPICAM/Mars Express	♠ $r_{\text{eff}} = 0.01 - 0.1 \mu\text{m}$	above 20 km, semi-empirical model of [37] for irregular particles in radiative transfer model, difficult to separate ice and dust contribution.	Montmessin et al. [35], Rannou et al. [36]
Aero-optics experiments on lander/ rovers		Observations from the surface using TV cameras are virtually free from the surface influence. Measurements performed at visible/NIR wavelengths. In brightness modeling semi-empirical approach [37] used.	
Viking	♠ $r_{\text{eff}} = 1.52, 1.85 \pm 0.3 \mu\text{m}$	The values correspond to VL1 and VL2 landing sites, and dust storm and low dust loading conditions respectively.	Pollack et al. [38]
Pathfinder	♠ $r_{\text{eff}} = 1.6 \pm 0.15 \mu\text{m}$ , $r_{\text{eff}} = 1.71 +0.26/-0.29 \mu\text{m}$	The mean particle radius is almost independent of the assumed width (variance) of the size distribution.	Tomasko et al. [39], Markiewicz et al. [40]
MERs	♠ $r_{\text{eff}} = 1.52 \pm 0.21 \mu\text{m}$ (Opportunity) $r_{\text{eff}} = 1.47 \pm 0.21 \mu\text{m}$ (Spirit)	Retrievals from both sites averaged over about 100 sols	Lemmon et al. [41]

Table 1.3: The size of Martian atmospheric dust as retrieved by different methods general under clear sky conditions. In some cases, retrievals performed under stormy weather are also shown, if performed by the same authors under clear conditions for comparison purposes. The results which are nowadays considered the most representative for Martian dust are marked with ♠-symbol.



Conditions:	GDS	During GDS the planetary atmosphere can be considered as semi-infinite.	
Method:	size	comments	reference
Polarization Earth-based observations:	$r_{eff} > 8 \mu m$ $v_{eff} = 0.1$	The assumption on the spherical particles induces large errors in radiative transfer calculations.	Dollfus et al. [42]
Integral brightness for planetary disk	$r_{eff} = 4.5 - 7.5 \mu m$ , $v_{eff} = 0.2$	The particle size estimated depends on the chosen imaginary part of refractive index, $k$ . In this work the $k$ was set to 0.0001 what is close to value of basalt glass at $0.443 \mu m$ . The dust particles are assumed to be spheres to retrieve the size.	Dlugach & Morozhenko [43]
Spacecraft observations from Martian orbit:	$r_{eff} = 0.8 - 1.8 \mu m$	- model of spherical particles:	Pang & Ajello, 1977, Pang et al. [45, 44]
	$r_{eff} = 0.2 \mu m$	- the semi-empirical theory for randomly oriented irregular particles Those retrievals ([44, 45, 46]) are not considered reliable since multiple scattering was ignored.	Chylek & Grams [46]
	♠ $r_{eff} = 1.8 - 2.5 \mu m$	the extensive angular coverage of Emission Function (EPF) sequences	Clancy et al. [29]

Table 1.4: The size of Martian atmospheric dust as retrieved by some methods during GDS. The results which are nowadays considered the most representative for Martian dust are marked with ♠-symbol.

## 1.2.2 Composition.

Due to the common history of the Earth and Mars in the early Solar System, it can be assumed that they share mineral and rocks with very similar composition.

Nowadays, the knowledge about Martian surface chemistry, geology, mineralogy and lithology is mostly derived from remote sensing observations. In 2013, on the 10th anniversary of the launch of ESA's MEx the global maps of Mars were released tracing the history of water and volcanic activity on the Red Planet (see Fig. 1.15). This atlas is composed of maps showing the distribution of minerals which were formed in combination with water, by volcanic activity, and by weathering. The maps were built from ten years of data collected by the OMEGA (Observatoire pour la Minéralogie, l'Eau, les Glaces et l'Activité) on board MEx spacecraft. OMEGA is a Visible and Infrared Mineralogical Mapping Spectrometer, which determines mineral composition of the surface up to 100 m resolution. Some very valuable information about Martian airborne dust can be derived from those remote sensing observations of the surface. On the maps (Fig. 1.15) one can see that dust (d) which was created during weathering processes is presented in almost the same regions as reddish ferric oxides (e).

Remote sensing is a powerful tool for deriving the Martian dust physical properties. However, the composition of the regolith and lithology of rocks of the Martian surface can only be coarsely inferred from spectra. The measurements in situ provide much more detailed information about the regolith and rock composition. In addition, they provide more clues about the geological evolution of the surface. At the time this Thesis is written, seven successful missions took measurements on the Martian surface, chronologically, Viking 1, 2, Pathfinder, MER-A, MER-B, Phoenix and Curiosity. Currently, the MER-B: Opportunity and Curiosity are operating on the Martian surface.

Viking 1 landed on the rock-strewn plains of Chryse Planitia giving the first close-up views of the Martian surface, Fig. 1.16 a). The site has a mild topography partially covered by fine-grained materials, and pitted stones. Analysis of the soil are consistent with a basaltic composition. In addition, it has large fractions of sulfur. The sulfur comes from the crusty material just below the surface.

Viking 2 landed on a level plain at Utopia. This place is as well rocky, Fig. 1.16 b). The composition of the soil is similar to that at the Viking 1 site, what suggests that they are not true soils derived from weathering of the local rocks, but rather mineral that has been redistributed over the planet's surface. Detailed information about the soil composition of both landing sites can be found in [47, 48, 49].

Mars Pathfinder was the first mission to Mars to deploy a rover. It landed in Chrysa Planitia, 800 km southeast of the Viking 1 site. The brief overview of the site geology is described in [50] and for more details we refer to the three special issues of the Journal of Geophysical Research vols. 102(E2), 104(E4) and 105(E1). In the Mars Pathfinder surroundings were found pebbles, cobbles and dispositional surfaces produced in terrestrial catastrophic floods together with fine-grained wind-blown material, Fig. 1.16 c). Moreover, dune forms indicate the presence of sand-size material. Like in the case of Viking Landers sites, the Pathfinder soil shows a significant fraction of sulfur. The soil-free rocks have andesitic compositions. Pathfinder soils appear to be a mixture of basaltic material and volatiles rich in sulfur and chlorine derived from volcanic exhalations.

The MERs were destined to look for aqueous activity such as water-bearing materials, and minerals

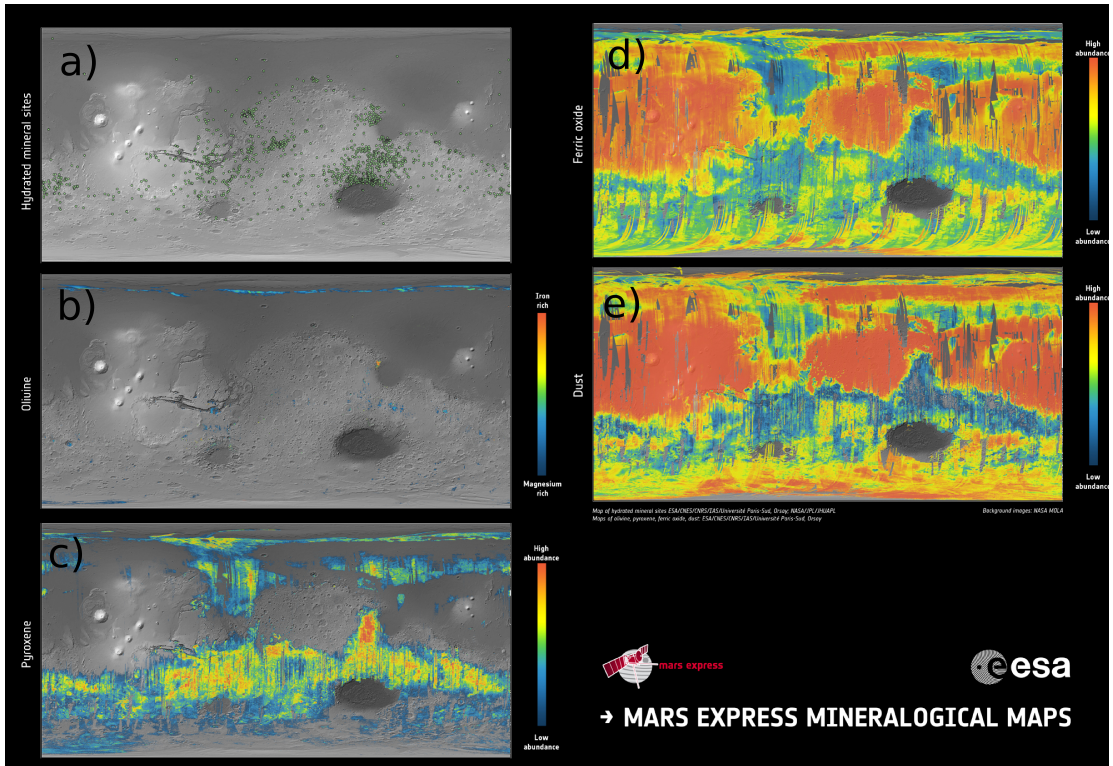


Figure 1.15: Maps showing the hydrated minerals, olivine, pyroxene, ferric oxide and dust. They are the keys to the history of Mars. The map of hydrated minerals indicates individual sites where a range of minerals that form only in the presence of water were detected. The maps of olivine and pyroxene tell the story of volcanism and the evolution of the planet’s interior. Ferric oxides, a mineral phase of iron, are present everywhere on the planet: within the bulk crust, lava outflows and the dust oxidized by chemical reactions with the Martian atmosphere, causing the surface to rust slowly over billions of years, giving Mars its distinctive red hue. The apparent data gap over the Hellas Basin, towards the lower right, is due to the unique atmospheric conditions in this 9 km-deep impact crater preventing robust detections from the crater floor to be made by OMEGA. Copyright ESA/CNES/CNRS/IAS/Universit Paris-Sud, Orsay; NASA/JPL/JHUAPL; Background images: NASA MOLA.

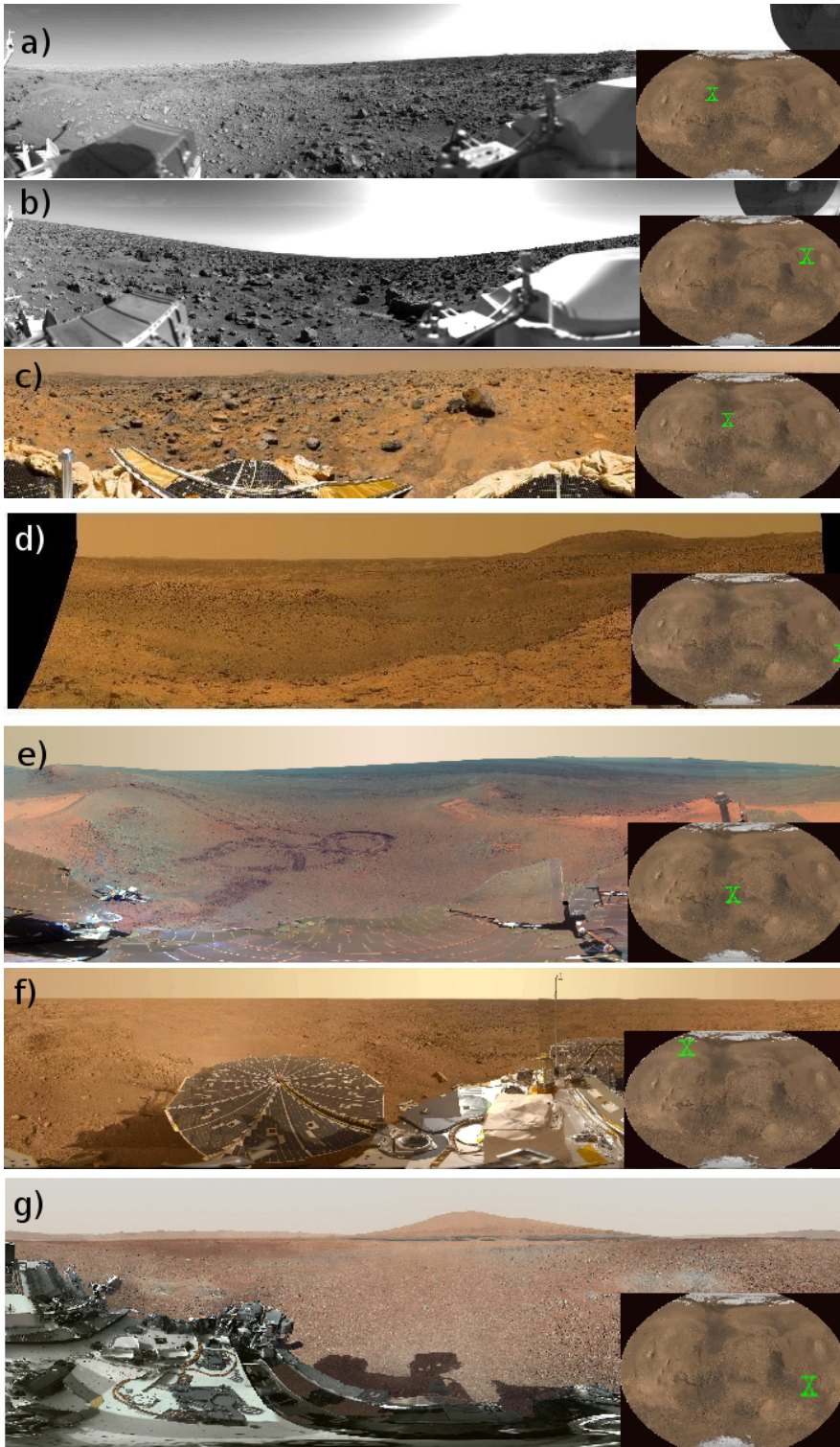


Figure 1.16: The images of landscapes provided by Martian-surface missions. Chronologically, from top to bottom, images taken by a) Viking 1, b) Viking 2, c) Pathfinder, MERs: d) Spirit and e) Opportunity, f) Phoenix Lander and g) Curiosity. On the right parts of the photographs the landing places are indicated where the images were taken. The Martian landscape is changing significantly with the locations of the spacecrafts, from extremely rocky surface, e.g. Viking 2 landing place to very "soft" Opportunity surroundings, where the tracks of the rover on the dusty surface are perfectly seen. The amount of reddish/ferric soil is changing being less on the rocks. The airborne dust is omnipresent at all locations never making the atmosphere absolutely clean. Panoramic photographs, credits: NASA.

deposited by precipitation, evaporation, sedimentation and hydrothermal activity. Both rovers found unequivocal evidence of the action of water e.g. [51, 52, 53].

Spirit landed on the rocky, cratered plain near the center of Gusev Crater, Fig. 1.16 d). It first characterized the materials in the immediate vicinity of the landing point, then traveled up to the Bonneville crater and finally, passed across the plains to the Columbia Hills. The surface material of plains consist of minimally altered basaltic rocks, whereas rocks on the hills are very different and highly variable in texture and composition. The soils at Gusev are similar in composition to those at the Viking and Pathfinder sites, which supports the hypothesis of the global mixing of fine grained materials by global dust storms. They are essentially basaltic in composition except for the higher concentrations of S and Cl elements. The main difference between the Gusev soils and those at the Pathfinder site is that the Gusev soils have less K and so do the rocks. This suggests that although dust seems to be globally mixed, the chemistry of soils is affected by local source materials. The iron mineralogy of the soils is still dominated by primary basaltic minerals such as olivine and pyroxene. The soils have a sulfur-rich component in addition to basalt and its oxidation products.

The Opportunity lander come to rest on dark, fine-grained soil at Maridiani Planum, one of the safest places for rovers on Mars, Fig. 1.16 e). Its scientific interest stemmed from abundant hematite at the surface detected by TES on Mars Global Surveyor, MGS [54]. Most of possible origins of this hematite involve liquid water, so this site had high potential for providing insights into aqueous processes. At Maridiani there are a lot of sediments partly covered with eolian deposits. Individual grains are composed by evaporate minerals, mostly sulfates and chlorides and silicic minerals, mostly basaltic alteration products. The sediments are mostly eolian, but include some of fluvial origin. Bedrocks found in the surroundings are sandstones composed of silicic clastic debris and chemical constituents dominated by evaporate minerals. The ferric sulfate mineral jarosite, was specifically identified. Moreover, calcium and magnesium sulfates are inferred from the chemical analysis. The soils are dominated by basaltic sands. In addition, there is dust derived locally from the sulfate rich out-crops and globally from air fall.

Phoenix landed in the north polar region, Fig. 1.16 f). One of its scientific goals was to obtain the data that would help to understand Mars' past climate. It looked for the secondary minerals that have been formed by reaction with volatile  $H_2O$  and  $CO_2$ . A wet, warmer climate during the early history of Mars with a denser atmosphere were the ideal conditions for the aqueous alteration of basaltic materials and the subsequent formation of carbonates. Carbonates are generally products of aqueous processes and may hold important clues about the history of liquid water on the surface of Mars. Calcium carbonate, in possible form of calcite, ikaite, aragonite, or ankerite, has been identified in the soils around the Phoenix landing site (approximately 3 to 5 weight percent) [55]. The amount of calcium carbonate found by Phoenix is consistent with its formation in the past by the interaction of atmospheric carbon dioxide with liquid water films on particle surfaces.

In addition, the Mg-rich carbonates have been suggested to be a component of the Martian global dust from orbital spectroscopy [56]. Similar features were observed in brighter, undistributed soils by the Mini-TES (The Miniature Thermal Emission Spectrometer)/Spirit at Gusev plains [51] and identified in the Nili Fossae region by the CRISM on board the MRO, prompting the idea that the carbonates in the dust might be due to the eolian redistribution of surface carbonates [57].

Curiosity, the newest rover, landed in Gale Crater, Fig. 1.16 g). The Rover is equipped with high-technology equipment that permitted to analyze the regolith with more details then previously. A complex chemistry of Martian soil was found. The small amount of water, about 1.5-3 % was found in Martian soil [58]. Moreover, sulfur, oxygen and chlorine containing substances among other ingredients. At the Rocknest, the site explored by Curiosity, the Rover examined the dust samples finding half of volcanic minerals and half, non-crystalline materials as glass. Curiosity suggested the presence of carbonate materials. In general, the chemical-element composition and textural appearance of soils found by the Rover is similar to sites visited by another rovers.

The chemical compositions obtained by Spirit, Opportunity and Curiosity soils are presented in Fig. 1.17. As shown, very similar results are found by the rovers. Small percentage differences in composition are found, however, the same elements are present. The ferric oxide retrievals are coherent with OMEGA retrievals Fig. 1.17.

The chemical composition of Martian soil and therefore the dust, is quite well known, but not the exact mineral composition. The mineral composition is particularly important in determining the refractive index of the material. Knowing the complex index of refraction of Martian atmospheric dust is of our special interest, since it is crucial in light scattering calculations.

The early choices of Earth spectral analogs to those observed in Mariner 9 IRIS thermal infrared spectra, were clay minerals as montmorillonite [60] and palagonite [61]. Both materials are commonly

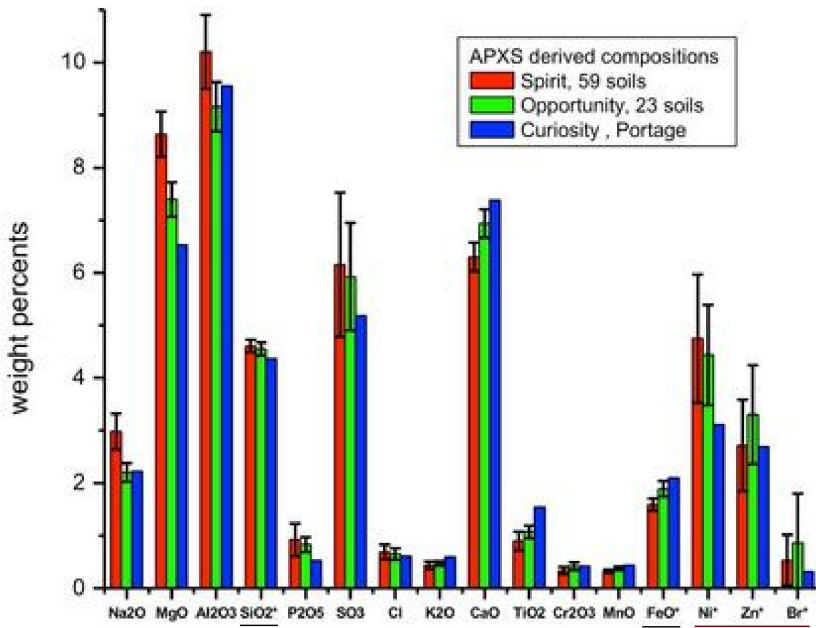


Figure 1.17: The elemental composition of typical soils at three landing sites on Mars: Gusev Crater (Spirit), Meridiani Planum (Opportunity) and Gale Crater (Curiosity). The data from the MERs are from several batches of soil, while the Curiosity data are from soil taken inside a wheel scuff mark called "Portage" and examined with its Alpha Particle X-ray Spectrometer (APXS). Error bars indicate the variations for the given number of soils measured for the Mars Exploration Rovers along the traverse. Note that concentrations of silicon dioxide and iron oxide were divided by 10, and nickel, zinc and bromine levels were multiplied by 100. Image Credit: Yen et al. [59]

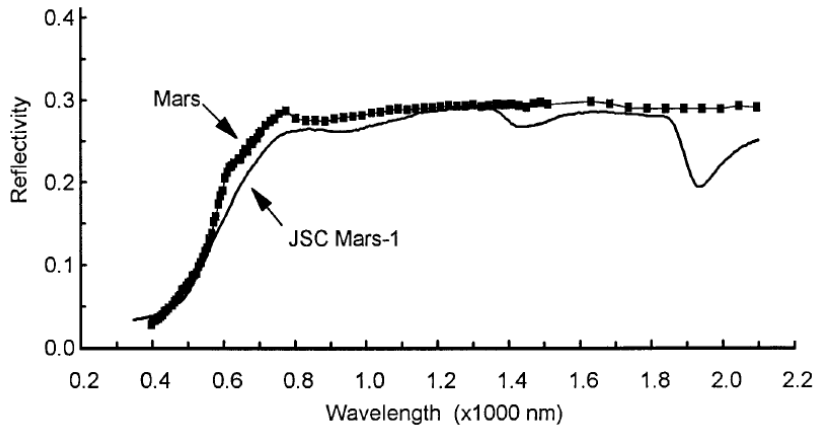


Figure 1.18: The VIS/NIR spectrum of the simulant and Martian bright region spectrum (atmospheric contributions removed) [71], [72]. Both spectra contain a relatively featureless ferric absorption edge through the visible, an indication of a ferric absorption band in the 800-900 nm region, and relatively flat absorption in the near-IR. Bands at 1400 and 1900 nm in the simulant spectrum result from higher levels of  $H_2O$  and  $OH$  in the simulant than on Mars.

used as terrestrial analogs for bright Martian soils e.g. [62, 63, 64, 65].

The clay reflectance spectra in the VIS and NIR are similar to the Martian spectra. Notwithstanding, it appears that the bright soils have dominant spectral characteristic for terrestrial weathering products of basaltic ash or glass, the palagonites [66, 67]. Palagonites are found to be better spectral Martian dust analogs. The montmorillonite spectrum has a greater number of spectral features and higher emissivity in contrast to the palagonite spectrum [68].

The VIS/NIR reflectance spectra of bright regions on Mars closely approximate the JSC Mars 1 simulant spectrum, Fig. 1.18. This sample is proposed by Johnson Space Center/NASA as simulant to the regolith of Mars for support of scientific research, engineering studies, and education. The JSC was collected from the slopes of Mauna Kea volcanoes on the Island of Hawaii, being dominated by amorphous palagonite. Nonetheless, amorphous palagonite simulant is not perfect. Ferric iron features near 600, 750 and 860 nm in the Martian spectrum imply higher levels of well crystallized red hematite in Martian dust than in the simulant. Moreover, the 1400 and 1900 nm bands, which indicate higher levels of  $H_2O$  and  $OH$  are present in the simulant but not in the Martian spectrum. This implies that the simulant is much wetter than the Martian regolith.

Bandfield & Smith [69] and Hamilton et al. [70] attempted to model dust aerosol composition by matching the shape of the observed spectral features against those expected from large libraries of mineral spectra. Bandfield & Smith [69] found a composition dominated by silicates with both primary and secondary minerals. Hamilton et al. [70], found that the dust is dominated also by silicates (probably feldspar), and that dust is largely the product of mechanical weathering of basaltic rocks with minor chemical alteration. It seems to be coherent with previous studies.

Spectral similarity cannot be used as the sole criterion for constraining Martian mineralogy since different minerals show similitude to the Martian spectra. Other properties need to be explored and combined to obtain a definitive identification. The final mineral composition of Martian dust will be determined in the future once the spacecrafts carrying Martian samples will return to the Earth.

In the absence of the exact compositional knowledge of Martian dust, an observationally derived refractive indices are valuable. Snook et al. [73], using IRIS (Infrared Interferometer Spectrometer)/Mariner 9 and Wolff & Clancy [32], using TES/MGS data attempted to directly solve radiative transfer equations for the dust's indices of refraction without identification of a specific composition.

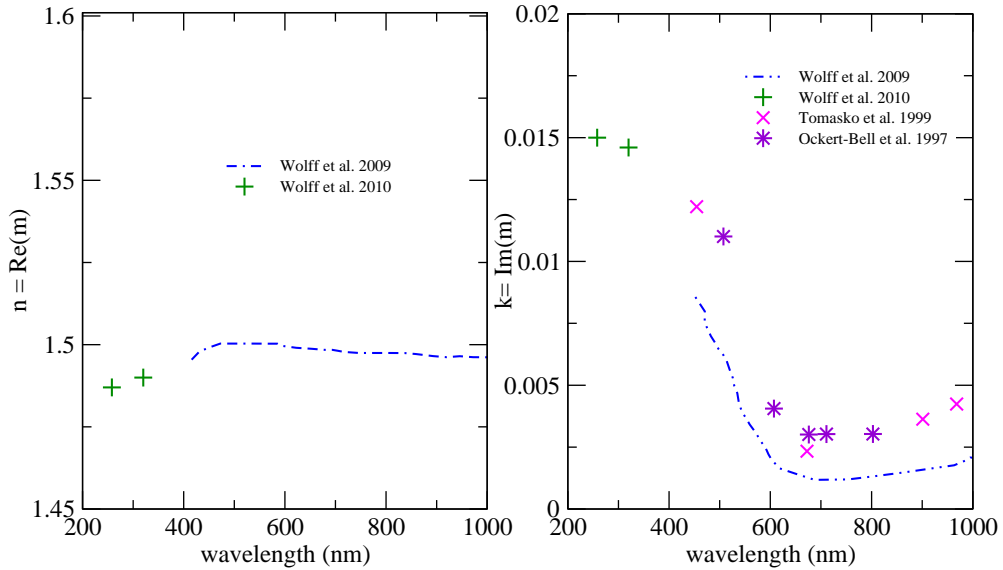


Figure 1.19: The refractive indices as derived for Martian dust. The values in the 440 - 1000 nm range are adopted from Wolff et al. [74] and retrieved for  $1.6 \mu\text{m}$  particles (represented by line), whereas for 258 and 320 nm are adopted from Wolff et al. [30] (crosses). The retrievals depend on the model assumptions as phase function or size of the particles. Therefore, for different sizes, slightly different refractive indices are obtained. The real part of the refractive index,  $n$ , is presented on the left side of the image, whereas on the right is presented the imaginary part,  $k$ . The derived imaginary parts of Wolff et al. are compared with previous work by Tomasko et al. [39] and Ockert-Bell et al. [75].

The goal was to be more accurate retrieving dust optical depth and particle sizes rather than composition information. Lately, Wolff et al. [30, 74] have determined the refractive indices of Martian dust in the UV and VIS/IR, respectively. Some of the obtained refractive indices are presented in Fig. 1.19 and compared with previous results from Tomasko et al. [39] and Ockert-Bell et al. [75].

## Objectives

Bohren and Huffman [76] clearly explain the two general classes of problems in the theory of the interaction of an electromagnetic wave with small particles. The first, direct problem, refers to the problem of determining the scattering pattern produced by one particle with given shape, size and composition which is illuminated by a beam of light. This is an "easy" problem and it corresponds to describing the tracks of the dragon on Fig. 2.1 a). The second, inverse problem, consists of suitable analysis of the scattered light in aim to describe the particles that are responsible for that scattering. This is the "hard" problem and consists on describing the dragon from its tracks Fig. 2.1 b).

The interpretation of photometric or polarimetric observations of Mars requires the solution of the inverse radiative transfer problem (allegory to the description of a dragon from its tracks). Unfortunately, at present, we still do not have the perfect tool for the interpretation of observations of Mars. To interpret observations of Mars, one has to resolve the radiative transfer equation, in which it is necessary to consider the scattering by dust particles. One of the possible ways to obtain the scattering by atmospheric particles is to simulate it. However, it brings some serious problems. In fact, the scattering pattern produced by a sphere of arbitrary radius and refractive index is the only exactly soluble problem theoretically. The solution to this problem, provided by Gustav Mie in 1908, is widely known as Mie theory [77], although strictly should be named Lorenz-Mie-Debye theory, because of independent work performed by those three authors [78, 79]. In the limiting case of electromagnetic scattering by particles whose size is much smaller than the wavelength of the incident light (e.g. gas molecules illuminated by visible light), the problem was solved much earlier by Lord Rayleigh in 1871, providing the explanation of the blue color of the sky. Mie theory naturally converges to the Rayleigh's limit when the size parameter, defined as  $x = 2\pi r/\lambda$ , is  $x \ll 1$ . The real problem arises in the calculation of the scattering matrix of natural dust (i.e. irregularly-shaped) particles, mainly if their sizes exceed that of the incident wavelength. Among the several methods that can be used to solve the problem, we will focus on the most popular, which are the T-matrix method, originally developed by Waterman [80], and the Discrete-Dipole Approximation (DDA) method, introduced by Draine [81]. Just for completeness, it is worth mentioning other methods such as the separation of variables for scattering by spheroidal particles [82], and the Finite Difference Time Domain (FDTD) technique, originally developed by Yee [83], applicable to non-spherical targets.

Despite the fact that natural particles, including Martian dust, are irregularly shaped, Mie theory has been commonly used to derive their properties. However, it has been proved by Mishchenko et al. [84] that moderately irregular terrestrial atmospheric particles treated with a conventional Mie theory for spherical particles could cause large errors in the optical thickness retrievals.

The T-matrix method allows to solve the scattering problem of rotationally symmetric particles, and clusters with rotationally symmetric monomers [85]. It has been employed in a number of problems, ranging from terrestrial aerosols to cometary dust (e.g.[86, 87]). In Mars, the T-matrix code developed by Mishchenko [85] has been used by Wolff et al [30, 74, 88] to simulate dust particles by a collection of cylinders of diameter-to-length ratio of unity ( $D/L=1$ ). However, that representation of non-spherical particles fails at scattering angles close to back-scattering, where the scattering function is clearly overestimated [30]. Very recently, the calculations by Pitman et al. [89] on Martian regolith by clusters of spheres and cubes using both the multisphere T-matrix code by Mackowski [90], and the DDA code DDSCAT by Draine and Flatau [91], constitute a much more realistic approximation to the problem



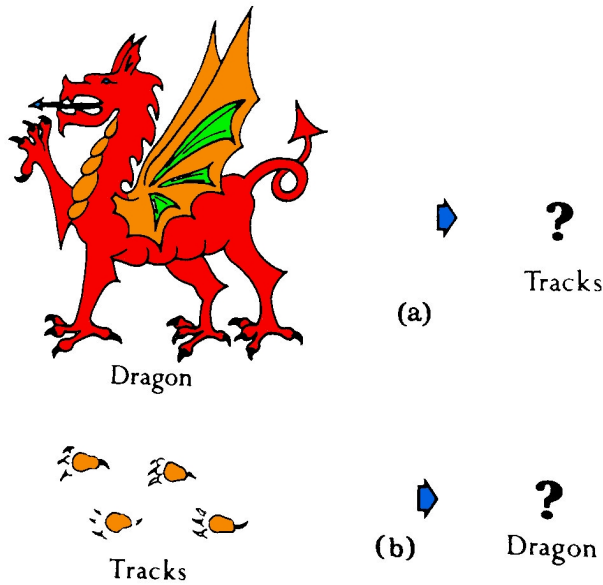


Figure 2.1: a) The direct problem: describe the tracks of the dragon. b) The inverse problem: Describe a dragon from its tracks. Figure modification from [76].

than that of the cylinders, with promising results regarding the back-scattering enhancement, but still needing improvements, as size average over the retrieved Martian dust size distribution. In this respect, it must be noted that the T-matrix method, as well as the DDA technique, or the other mentioned methods like FDTD, although in principle can be applied to any particle size, in practice requires large computer resources for large particle sizes, becoming impracticable for size parameters exceeding largely the unity, even for the most powerful computers, due to memory and CPU limitations. This is why laboratory measurements providing the full  $4 \times 4$  scattering matrix of Martian analog samples as a function of the scattering angle is, at present, the only way to face the problem. This constitutes the main objective of this Thesis, in which measurements of distinct Martian dust analog samples are performed at the IAA COsmic DUst LABoratory (CODULAB) [92]. The measurements are performed at 488 and 647 nm covering the scattering angle range from 3 to 177 degrees. The measured results provide a database for Martian aerosols studies. The results will be available upon publication at the Amsterdam-Granada Light-Scattering Database [1], [http : //www.iaa.es/scattering/](http://www.iaa.es/scattering/) together with other measurements, that can be freely downloaded by interested research groups.

As mentioned, remarkable progress in developing advanced numerical algorithms for computing electromagnetic light scattering by nonspherical particles has been achieved during the last decades. Even though, due to the complicated shapes of Martian dust, computations for realistic polydisperse irregular particles have to be replaced by simplified models such as cylinders [30], spheroids [93], ellipsoids [94], or clusters of spheres and cubes [89]. In this Thesis, we go one step further. We perform light scattering calculations for the actual shape of the particles of one of our Martian dust analogs, namely the calcite sample. The calculations are performed with the DDSCAT 7.1 code [3] for a mixture of flake- and rhomboidal-like shapes. One of the possible applications of the Database of Martian dust analogs is to check the validity of model particles in reproducing the scattering properties of natural particles. Thus, the DDA calculations haven compared with the measured scattering matrices for the calcite sample. Apart from its interest for atmospheric studies calcite is a very interesting material from a theoretical point of view. Calcite is a highly birefringent material. Therefore, we have performed a theoretical study of the impact of birefringence on the calculated scattering matrix elements. Further, we study whether the orientation of the optic axis actually has a significant impact on the calculated scattering matrix elements for irregularly shaped particles.

Finally, the study of Martian analogs is completed by a photophoresis experiment, with the aim to check whether this is an efficient dust lifting mechanism operating on the surface of Mars.

## Methodology

This chapter is devoted to set up the methodology to perform the experimental measurements of the Martian dust analog samples that are described in Dabrowska et al. [5, 7]. We start by giving a theoretical introduction on basic concepts of light scattering by small non-spherical particles. This section is followed by the description of the experimental setup, the IAA COsmic DUst LABoratory (CODULAB). The chapter continues with a section on theoretical simulations of the measured scattering matrix, and finally ends with a section on theory and experiments of photophoresis.

### 3.1 Theoretical description of the light scattering phenomenon: The scattering matrix

Light is electromagnetic radiation, consisting of oscillating electric and magnetic fields propagating through a medium. In 1852 George Gabriel Stokes introduced the parameters named after him to offer a handy way of describing light. The Stokes parameters for monochromatic light can be defined as functions of the components of the electric field vector,  $\mathbf{E}$  (Fig. 3.1):

$$I = E_l E_l^* + E_r E_r^* \quad (3.1)$$

$$Q = E_l E_l^* - E_r E_r^* \quad (3.2)$$

$$U = E_l E_r^* + E_r E_l^* \quad (3.3)$$

$$V = i(E_l E_r^* - E_r E_l^*) \quad (3.4)$$

Where  $E_r$  and  $E_l$  are the components of the electric field defined in Figure 3.1 and  $\mathbf{I} = (I, Q, U, V)^t$  denotes the transposed Stokes vector.

The frequency of the electromagnetic radiation associated to visible light is about  $5 \times 10^{14} \text{ s}^{-1}$ , becoming impractical to attempt to detect such oscillations experimentally. In addition, the detectors used to measure light intensity will have some finite bandwidth. Then, in practice, formulas (3.1) to (3.4) pertain to time and frequency averages. In this Stokes formalism, the flux is associated to the  $I$  component, while the linear polarization is given by the components  $Q$  and  $U$ , and the circular polarization is related to  $V$ . The incoherent addition of electric fields implies that the relation  $I^2 = Q^2 + U^2 + V^2$  no longer holds in general, but instead the inequality  $I^2 \geq Q^2 + U^2 + V^2$  [95, 96].

The degree of polarization of the light beam, DP, is defined as:

$$DP = \frac{\sqrt{Q^2 + U^2 + V^2}}{I}, \quad (3.5)$$

and degree of lineal polarization of the light beam, DLP is:

$$DLP = \frac{\sqrt{Q^2 + U^2}}{I}. \quad (3.6)$$

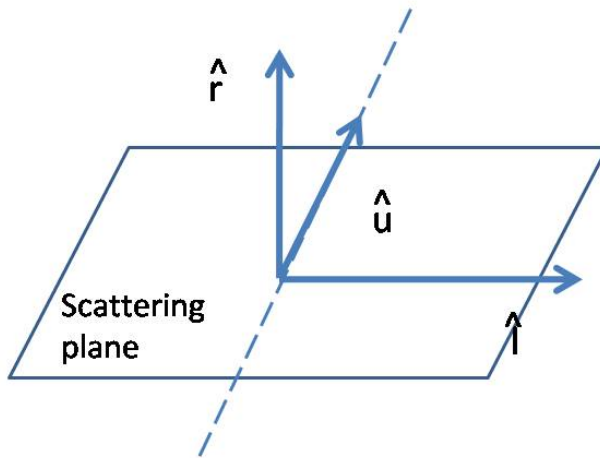


Figure 3.1: The orthogonal right-handed reference system used to describe the electric field. The system we assume is the one with plotted lines-  $\hat{l}, \hat{r}, \hat{u}$ , where  $\hat{u}$  is the direction and sense of propagation of light,  $\hat{r}$  is perpendicular to the scattering plane and  $\hat{l}$  is on the scattering plane in such way that  $\hat{r} \times \hat{l} = \hat{u}$ .

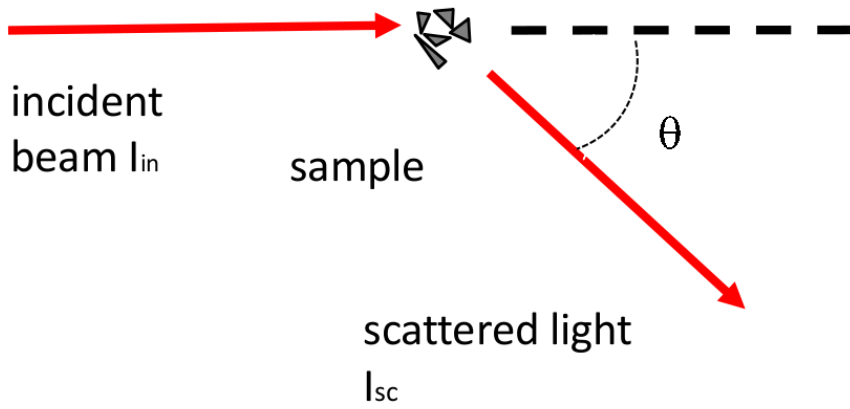


Figure 3.2: The incident beam  $I_{in}$  scattered  $I_{sc}$  on the sample with the scattering angle  $\theta$ .

The Stokes vector of the light passing through an optical component ( $\mathbf{I}_{sc}$ ) is proportional to the product of its 4 x 4 Mueller matrix by the Stokes vector of the incident light ( $\mathbf{I}_{in}$ ) (Fig. 3.2 and Equation 3.7).

$$\begin{pmatrix} I_{sc} \\ Q_{sc} \\ U_{sc} \\ V_{sc} \end{pmatrix} \propto \begin{pmatrix} F_{11} & F_{12} & F_{13} & F_{14} \\ F_{21} & F_{22} & F_{23} & F_{24} \\ F_{31} & F_{32} & F_{33} & F_{34} \\ F_{41} & F_{42} & F_{43} & F_{44} \end{pmatrix} \begin{pmatrix} I_{in} \\ Q_{in} \\ U_{in} \\ V_{in} \end{pmatrix} \quad (3.7)$$

The Mueller matrix of a collection of independent scatterers is called scattering matrix,  $\mathbf{F}$ . The elements of  $\mathbf{F}$  are written as  $F_{ij}$ , with  $i, j = 1, \dots, 4$ . The elements of the scattering matrix depend on the number and physical properties of the particles such as size, shape, structure and refractive index, as well as on the orientation of the particles, the wavelength of the incident light and the directions of incidence and scattering.

When the ensemble of particles are randomly oriented,  $\mathbf{F}$ , depends only on the scattering angle  $\theta$ , but not on the azimuthal angle. The scattering angle is defined by the directions of the incident and the scattered beams. When randomly oriented particles and their mirror particles are present in equal numbers in the cloud, the scattering matrix has the simple form [95]:

$$\mathbf{F}(\lambda, \theta) = \begin{pmatrix} F_{11} & F_{12} & 0 & 0 \\ F_{12} & F_{22} & 0 & 0 \\ 0 & 0 & F_{33} & F_{34} \\ 0 & 0 & -F_{34} & F_{44} \end{pmatrix} \quad (3.8)$$

This occurs in many practical cases, like measurements of scattering matrices of mineral dust samples in the IAA COsmic DUst LABoratory [92, 97].

## 3.2 The IAA COsmic DUst LABoratory (IAA-CODULAB)

The experimental measurements have been conducted at the IAA COsmic DUst LABoratory (CODULAB) [92]. The experiment is located at Instituto de Astrofísica in Granada, Spain. Figs. 3.3 and 3.4 show two images of the IAA-CODULAB. In the middle of the measuring ring we can see the aerosol beam produced by the aerosol generator (3.3) and the nebulizer that produces the water droplets cloud used for calibration purposes 3.4.

The design of this instrument is based on the Dutch instrument developed in the group of Hovenier in Amsterdam e.g. [98]. A schematic overview of the experimental apparatus is presented in Fig. 3.6. Light from a linearly polarized tunable Argon-Krypton laser (482, 488, 529, 568, 647 nm) passes through a polarizer, P, oriented at an angle  $\gamma_P$  and an electro-optic modulator, M oriented at an angle  $\gamma_M$  (angles of optical elements are angles between their optical axes and the horizontal plane, measured counterclockwise when looking in the direction of propagation of light). The modulated light is subsequently scattered by randomly oriented particles located in the jet stream produced by either an aerosol generator (Fig. 3.3) or nebulizer that produces water droplets (Fig. 3.4). In our experiment no vessel is needed to contain the sample at the point where the scattering takes place. This is a great advantage, since anything between the particles and the detector decreases the accuracy of the measurements and limits the angular range. The dust particles are brought into the jet stream as follows: Firstly, a compacted mass of powder is loaded into a cylindrical reservoir. A piston pushes the powder onto a rotating brush at a certain speed. An air stream carries the aerosol particles of the brush through a tube to a nozzle above the scattering volume. In Fig. 3.5 a schematic picture of the aerosol generator is presented.

A filter wheel, FW, equipped with gray filters of different density is located between the laser and polarizer (Fig. 3.6). It is operated from the computer so that the flux of the incident beam can be scaled to its most appropriate value for each scattering angle. The scattered light passes through a quarter-wave plate, Q, oriented at  $\gamma_Q$  and analyzer, A oriented at  $\gamma_A$  (both optional) and is detected by a photomultiplier tube, the detector (9828A Electron tubes). The A and Q are assembled to the photomultiplier by motorized rotating holders controlled from the computer. Another photomultiplier tube, the monitor, is located at a fixed position and it is used to correct from fluctuations in the aerosol stream. Detector and monitor are positioned on a ring with an outer diameter of 1 m with angular resolution of  $1/8^\circ$ . The detector can be programmed to move along the ring in steps even

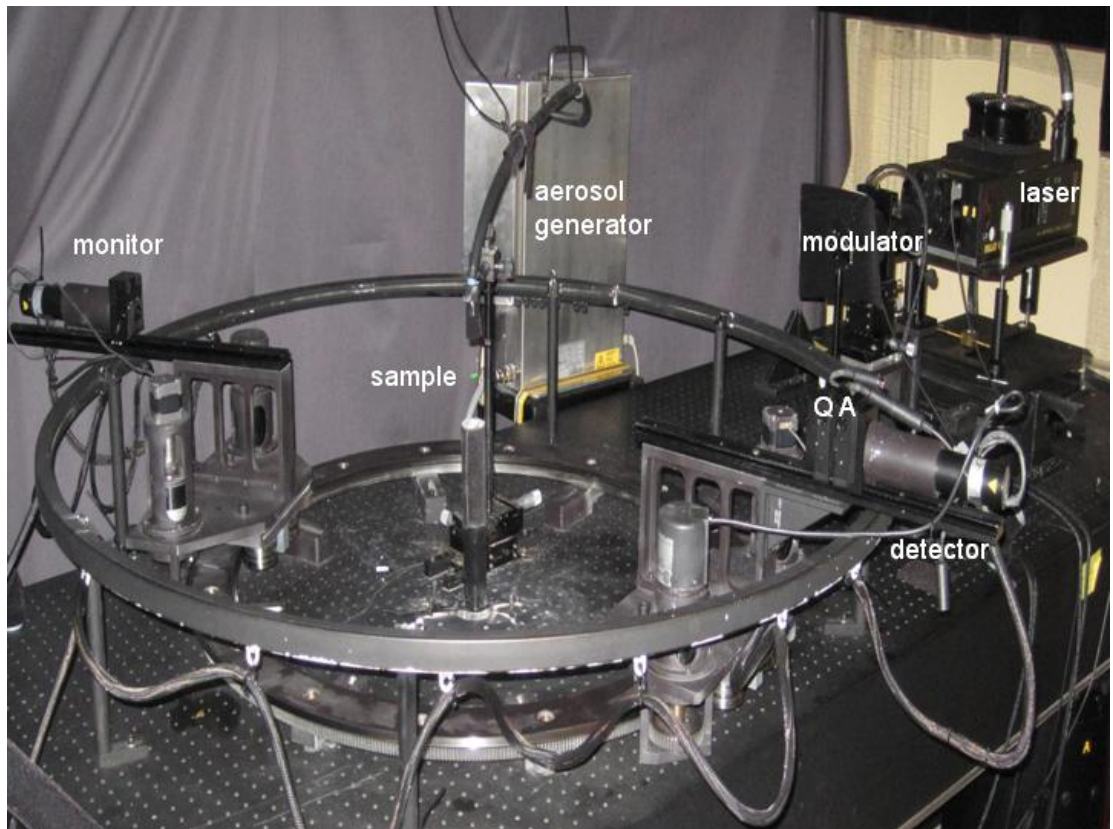


Figure 3.3: The photography of IAA Cosmic Dust Laboratory located at the Instituto de Astrofísica de Andalucía (IAA) in Granada prepared for measuring the scattering on dust particles. On the right we can see the detector that moves along the ring from 3 up to 177 deg. The ring is placed horizontally in the laboratory with an outer diameter of 1 m. At the other side is located the monitor. In the middle, we see the nozzle of the aerosol generator located vertically in the center of the ring. The green spot seen in the middle is where the laser interacts with the sample of dust. The quarter-wave plate, Q, and the analyzer A are located in front of the detector.

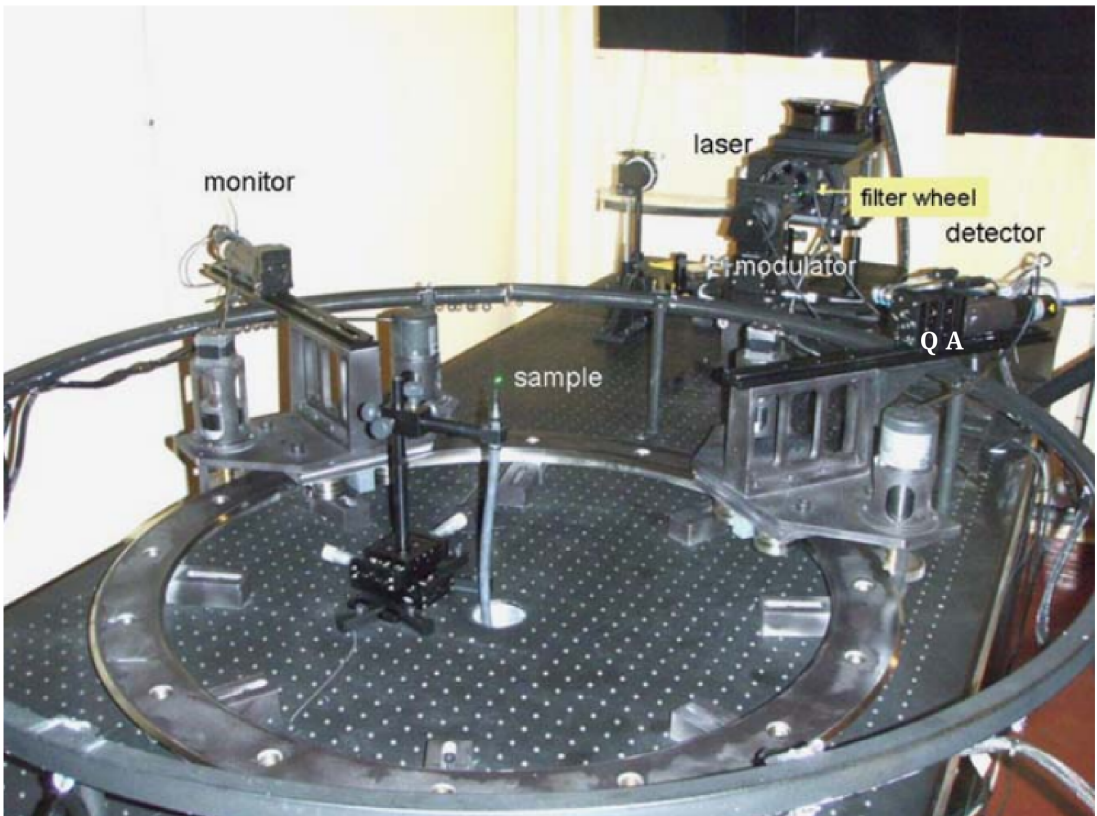


Figure 3.4: The same as Fig.3.3 but prepared for measuring the scattering on water droplets.

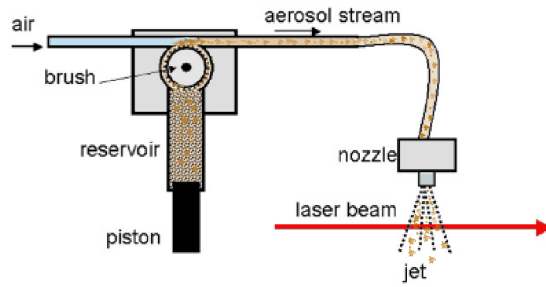


Figure 3.5: Schematic picture of the aerosol generator. A piston in the cylindrical feed stock reservoir with a diameter of 10 mm pushes powder onto a rotating brush at certain speed. An air stream carries the aerosol particles of the brush through the tube to a nozzle right above the scattering volume.

less than  $1^\circ$  covering the scattering angle range from  $3^\circ$  (nearly forward direction) to  $177^\circ$  (nearly backward direction). The measurements presented in this Thesis are performed in steps of 1 degree in the scattering angle range from  $3-10^\circ$  and  $170-177^\circ$  angle range, and in steps of 5 degrees from  $10$  to  $170$  degrees.

To avoid crossed contamination from ambient dust that could distort the measurements a special ceiling is installed over the experiment area. The ceiling produces a laminar airflow, which creates a constant over-pressure and preserving an exchange with dirty outside air.

The electro-optic modulator in combination with lock-in detection, increases the accuracy of the measurements and allows simultaneous determination of several elements of the scattering matrix from the detected signal. The electro-optic modulator consists of a birefringent crystal in which a certain birefringence can be induced by applying an electric field. This causes the parallel and perpendicular components of a polarized beam of light to emerge from the modulator with an induced phase difference (phase shifts). The phase shift is a linear function of the strength of the applied field. If the voltage over the crystal is varied sinusoidally in time, the induced phase shift,  $\phi$ , varies in time the same way:

$$\phi = \phi_m \sin \omega t, \quad (3.9)$$

where  $\phi_m$  is the maximum phase shift and  $\omega$  is the angular frequency of the voltage.

The Mueller matrix of a modulator with the orientation angle  $\gamma_M$  between the scattering plane and its principal axis is:

$$\mathbf{M}_{\gamma_M}(\phi) = \begin{bmatrix} 1 & 0 & 0 & 0 \\ 0 & C^2 + S^2 \cos \phi & SC(1 - \cos \phi) & -S \sin \phi \\ 0 & SC(1 - \cos \phi) & S^2 + C^2 \cos \phi & C \sin \phi \\ 0 & S \sin \phi & -C \sin \phi & \cos \phi \end{bmatrix}, \quad (3.10)$$

where  $C = \cos 2\gamma_M$  and  $S = \sin 2\gamma_M$ .

The Mueller matrices of the polarizer and quarter wave plate are given by:

$$\mathbf{P}_{\gamma_P} = 1/2 \begin{bmatrix} 1 & C & S & 0 \\ C & C^2 & SC & 0 \\ S & SC & S^2 & 0 \\ 0 & 0 & 0 & 0 \end{bmatrix}, \quad (3.11)$$

$$\mathbf{Q}_{\gamma_Q} = \begin{bmatrix} 1 & 0 & 0 & 0 \\ 0 & C^2 & SC & -S \\ 0 & SC & S^2 & C \\ 0 & S & -C & 0 \end{bmatrix}, \quad (3.12)$$



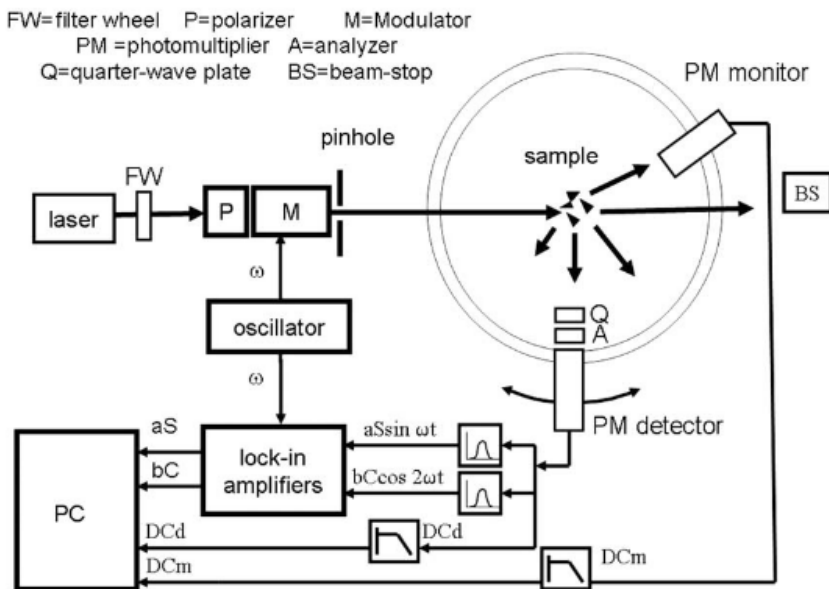


Figure 3.6: Schematic overview of the experimental light scattering apparatus as seen in Figs. 3.3 and 3.4. The detected signal is separated into its  $cDC$ ,  $aS\sin\omega t$  and  $bC\cos\omega t$ , where  $a=1.383$  and  $b=c0.8635$ .

Configuration	$\gamma_P$ (deg)	$\gamma_M$ (deg)	$\gamma_Q$ (deg)	$\gamma_A$ (deg)	DC( $\theta$ )	S( $\theta$ )	C( $\theta$ )
1	90	-45	-	-	$F_{11}$	$F_{14}$	$-F_{12}$
2	90	-45	-	0	$F_{11}+F_{21}$	$F_{14}+F_{24}$	$-F_{12}-F_{22}$
3	90	-45	-	45	$F_{11}+F_{31}$	$F_{14}+F_{34}$	$-F_{12}-F_{32}$
4	90	-45	0	45	$F_{11}+F_{41}$	$F_{14}+F_{44}$	$-F_{12}-F_{42}$
5	45	0	-	-	$F_{11}$	$-F_{14}$	$F_{13}$
6	45	0	-	0	$F_{11}+F_{21}$	$-F_{14}-F_{24}$	$F_{13}+F_{23}$
7	45	0	-	45	$F_{11}+F_{31}$	$-F_{14}-F_{34}$	$F_{13}+F_{33}$
8	45	0	0	45	$F_{11}+F_{41}$	$-F_{14}-F_{44}$	$F_{13}+F_{43}$

Table 3.1: Configurations of the orientation of polarizer P, modulator M, quarter-wave plate Q, and analyzer A used during the measurements.

Since  $\phi$  is itself a sinusoid, both  $\sin \omega$  and  $\cos \omega$  possess a complicated harmonic content which depends on the relative phase amplitude  $\phi_m$ . The strength of each harmonic can be expressed as Fourier series of Bessel functions ( $J_n$ ) as follows:

$$\sin \phi = \sin(\phi_m \sin \omega t) = 2 \sum_{k=1}^{\infty} J_{2k-1}(\phi_m) \sin(2k-1)\omega t, \quad (3.13)$$

$$\cos \phi = \cos(\phi_m \sin \omega t) = J_0(\phi_m) + 2 \sum_{l=1}^{\infty} J_{2l}(\phi_m) \cos 2l\omega t, \quad (3.14)$$

where only the terms of frequency  $2\omega$  and lower are of further interest.

The flux vector reaching the detector,  $\pi\Phi_{\text{dec}}(\lambda, \theta)$  is obtained by multiplying the flux vector of the incident light  $\pi\Phi_0(\lambda, \theta)$  by all Mueller matrices of the components of the optical train (Fig. 3.7). Thus we have:

$$\pi\Phi_{\text{dec}}(\lambda, \theta) = c_1 \mathbf{A}_{\gamma_A} \mathbf{Q}_{\gamma_Q} \mathbf{F}(\theta) \mathbf{M}_{\gamma_M} \mathbf{P}_{\gamma_P} \Phi_0(\lambda, \theta), \quad (3.15)$$

where  $c_1$  is a real constant, and  $\mathbf{A}$ ,  $\mathbf{Q}$ ,  $\mathbf{M}$  and  $\mathbf{P}$  are the Mueller matrices of the analyzer, quarter wave plate, modulator and polarizer, respectively.  $\mathbf{F}(\theta)$  is the scattering matrix of the ensemble of particles and  $\gamma_A$ ,  $\gamma_Q$ ,  $\gamma_M$  and  $\gamma_P$  are the orientations angles of the corresponding components. The amplitude of the sinusoidal signal applied to the modulator is adjusted so that the amplitude of the induced phase shift,  $\phi_m$ , is first zero of  $J_0$ , i.e.  $\phi_m = 2.404883$  rad. The flux reaching the detector is then given by

$$\Phi_{\text{det}}(\lambda, \theta) = c[DC(\theta) + 2J_1(\phi_m)S(\theta)\sin\omega t + 2J_2(\phi_m)C(\theta)\cos 2\omega t + \dots], \quad (3.16)$$

where the coefficients  $DC(\theta)$ ,  $C(\theta)$ , and  $S(\theta)$  contain elements of the scattering matrix,  $2J_1(\phi_m) = 1.0383$ ,  $2J_2(\phi_m) = 0.8635$ , and  $c$  is the constant that depends on the measuring conditions. By using lock-in amplifiers tuned to the first and second harmonic of  $\omega$  the  $2J_1(\phi_m)S(\theta)\sin\omega t$  and  $2J_2(\phi_m)C(\theta)\cos 2\omega t$  terms can be selected. In our apparatus these two components together with the DC part of the selected signal are sufficient to determine all elements of the scattering matrix as functions of the scattering angle. The detected signal is separated into  $cDC(\theta)$  and varying parts:  $c2J_1(\phi_m)S(\theta)$  and  $c2J_2(\phi_m)C(\theta)$ . The modulator voltage and the lock-in amplifiers are synchronized by using the same oscillator. Subsequently, we divide  $c2J_1(\phi_m)S(\theta)$  and  $c2J_2(\phi_m)C(\theta)$  by  $cDC$ , so the constant  $c$  is eliminated. By using different combinations for the orientation angles of the optical components we are able to determine all relevant scattering matrix elements (Tab. 3.1). As mentioned we cannot perform measurements between  $0^\circ$  and  $3^\circ$  and between  $177^\circ$  and  $180^\circ$ . Instead, we normalize the measured phase function to unity at an arbitrary scattering angle,  $30^\circ$ . We present the other scattering matrix elements divided by the original measured phase function.

### 3.3 Test measurements

The reliability of the measurements is tested by comparing results of (spherical) water droplets measurements to results of Lorenz-Mie calculations for a distribution of homogeneous spherical particles. The water droplets are produced by a nebulizer (Fig. 3.4). For the purpose of this Thesis we have constrained the calibration measurements to the wavelengths of 488 and 647 nm (Fig. 3.8). For the

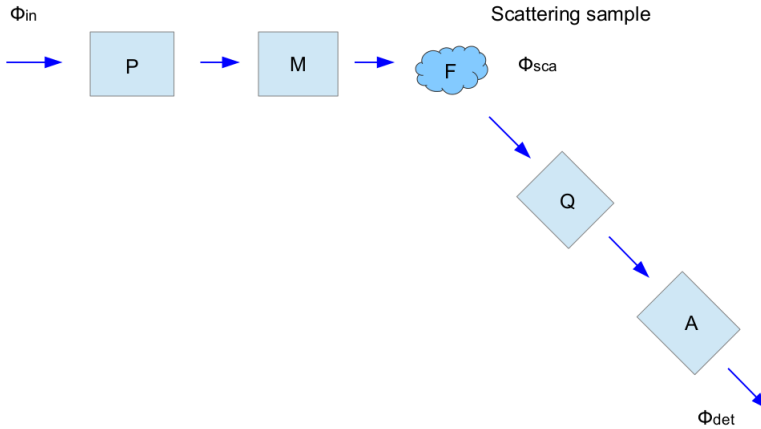


Figure 3.7: Schematic picture of the optical part of the light scattering experiment. P, M, Q and A are respectively a polarizer, modulator, quarter wave plate and analyzer with corresponding orientation  $\gamma$ .

Lorenz-Mie calculations, we assume a log-normal size distribution. In the fitting procedure, the refractive index of water is assumed as a fixed parameter at the studied wavelengths,  $m = 1.33 + 0.0i$ . The two parameters that define the size distribution,  $r_g$  and  $\sigma_g$  are defined as:

$$\ln r_g = \int_0^\infty \ln r n(r) dr \quad (3.17)$$

$$\sigma_g^2 = \int_0^\infty (\ln r - \ln r_g)^2 n(r) dr \quad (3.18)$$

where  $n(r)dr$  is the fraction of the total number of equivalent spheres with radii between  $r$  and  $r + dr$  per unit volume of space. They are chosen so that the differences between the measured and the calculated values for the  $F_{11}(\theta)$  and  $-F_{12}(\theta)/F_{11}(\theta)$  are minimized. The method to find the best-fitted values for  $r_g$  and  $\sigma_g$  is based on the downhill simplex method of Nelder and Mead [99], particularly the FORTRAN implementation described in the Numerical Recipes book [100], subroutine AMOEBA. The method is independently applied to fit the  $F_{11}(\theta)$  and  $-F_{12}(\theta)/F_{11}(\theta)$  at the studied wavelength. At studied wavelength the best fit we have obtained for  $\sigma_g=1.65$  and  $r_g=0.71 \mu m$ , Fig. 3.8. Muñoz et al. [92] have obtained have performed measurements at three wavelengths, 488, 520 and 647 nm and obtained the best fits for the six studied functions was  $\sigma_g=1.50 \pm 0.04$  and  $r_g=0.80 \pm 0.07 \mu m$ , what is in agreement with obtained by us results.

In Figs. 3.9 and 3.8, we present the measured and calculated scattering matrices as functions of the scattering angle for water droplets at 488 and 647 nm, respectively. The measured and the calculated  $F_{11}(\theta)$  are plotted on a logarithmic scale and normalized to 1 at  $30^\circ$ . The other matrix elements are plotted relative to  $F_{11}(\theta)$ . We refrain from showing the four element ratios  $F_{13}(\theta)/F_{11}(\theta)$ ,  $F_{14}(\theta)/F_{11}(\theta)$ ,  $F_{23}(\theta)/F_{11}(\theta)$  and  $F_{24}(\theta)/F_{11}(\theta)$ , since we verified that these ratios do not differ from zero by more than the error bars, in accordance with Lorenz-Mie theory. The measurements satisfy the Cloude coherency matrix test at all measured scattering angles. The reduction program verifies the reliability of the measurements by applying the Cloude coherency matrix test as suggested by Hovenier and van der Mee [2].

At both wavelengths the water droplets measurements show very good agreement with the Lorenz-Mie computations over the entire angle range. The small deviations may at least partly be due to

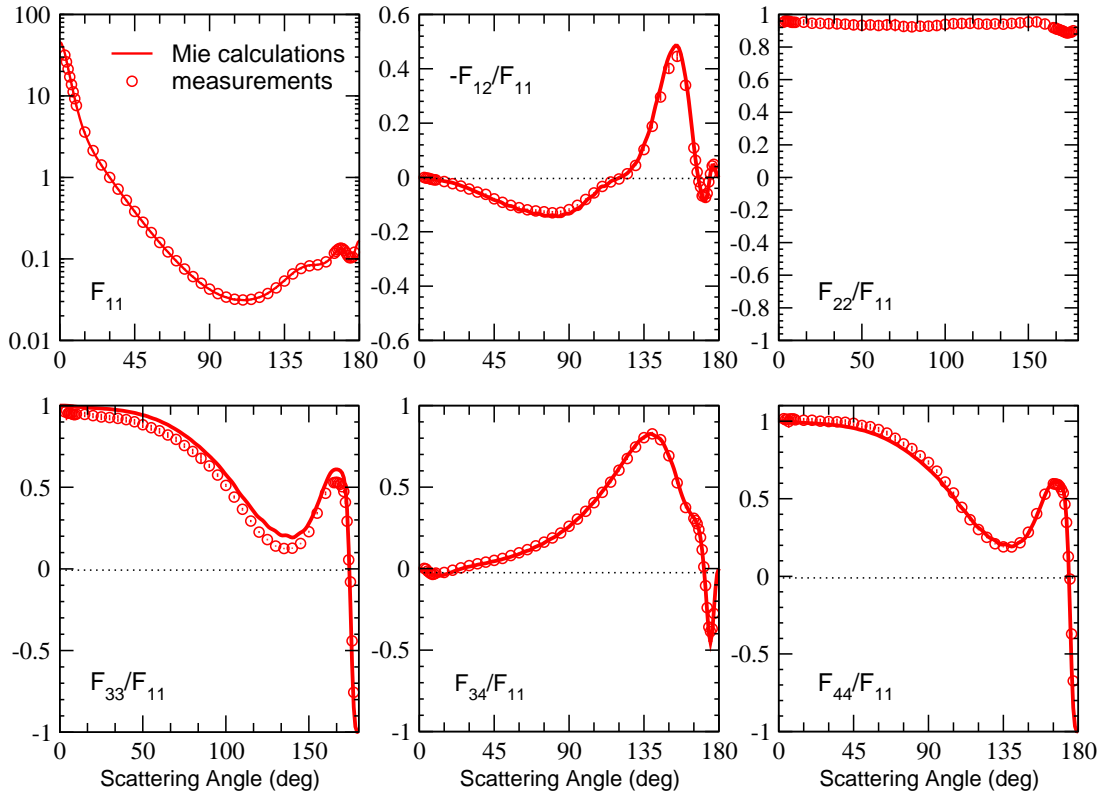
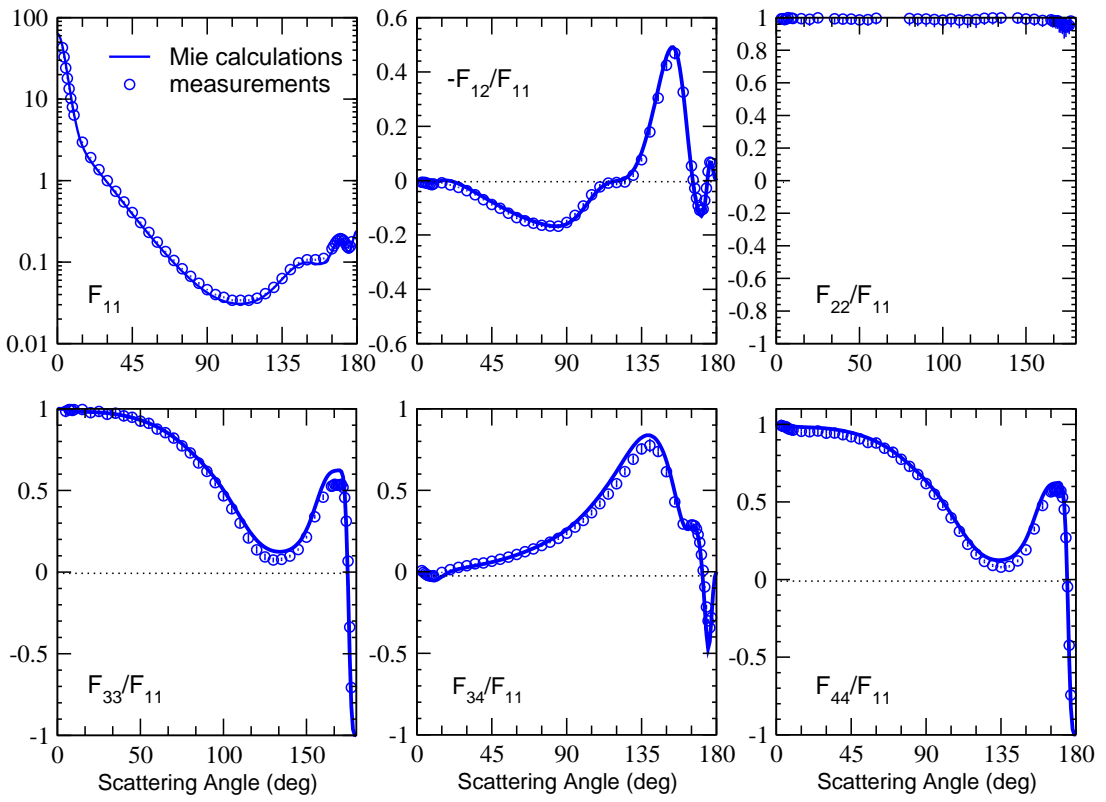


Figure 3.8: Non-zero scattering matrix elements for water droplets at  $\lambda = 647$  nm. Solid lines correspond to result of Lorentz-Mie calculations at 647 nm for a log-normal size distribution ( $r_g = 0.71 \mu\text{m}$  and  $\sigma_g = 1.65$ ). Error bars are presented with the measurements, however sometimes they are smaller than the size of the symbol of measurement.

differences in the size distributions and the not perfectly spherical shape of the water droplets used in the experiments.

### 3.4 Single or multiple scattering

Our measurements must be performed under single scattering conditions. We must have enough particles in the scattering volume to be representative for the ensemble of randomly oriented particles under study but not so many that multiple scattering may start playing a role. To check if multiple scattering effects can be neglected in our experiments a series of flux measurements with the detector in a fixed position are performed [101]. The speed of the piston that pushes the particles onto the rotating brush is then increased varying in this way the number of scattering particles. Since the number density of particles in the stream is proportional to the speed of the piston, the measured flux must increase linearly with the speed of the piston only under single scattering conditions, as the measured flux is proportional to the number density of particles in such conditions (see e.g. Van de Hulst [95]). In Fig. 3.10, the results of a multiple scattering test for a sample of white clay particles is presented. The measurements were performed at 647 nm, fixing the detector at  $10^\circ$  scattering angle. Since small fluctuations in particle density in the continuous aerosol jet stream occur, we integrated the signals over relatively long periods of time to get reasonable accuracy. During a normal light scattering measurement with a dust sample, the piston speed must be high enough to obtain a stable aerosol stream but not too high to avoid an unnecessary waste of sample. Thus, the piston speed usually ranges from 40 to 100 mm/h depending on the sample under study. In this multiple scattering test the piston speed was varied from 50 mm/h to 250 mm/h in steps of 50 mm/h. As shown, even at speeds as high as 250 mm/h we do not find any significant deviation from a linear behavior, which means that multiple scattering effects can be

Figure 3.9: The same as Fig. 3.8 but at  $\lambda = 488$  nm.

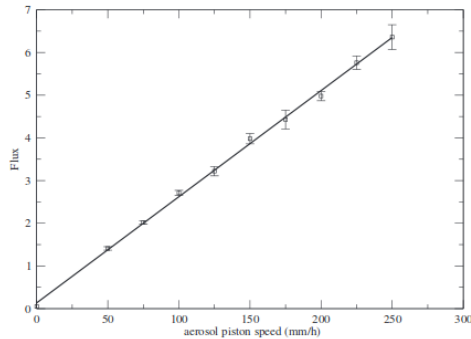


Figure 3.10: Flux of scattered light (in arbitrary units) versus aerosol generator speed for clay particles. The detector is placed at a scattering angle of  $10^\circ$ . No indication of multiple scattering is found. Image from Muñoz et al. [101].

neglected in our experiment.

### 3.5 Particle aggregation

One of the most common questions about light scattering experiments is if the aerosol beam may change the shape/size of the particles, either by breaking them up in smaller particles or by aggregating them into larger particles. To test this, we perform microscopy images for the sample under study as it is during the light scattering measurements. In particular we have taken Scanning Electron Microscope, SEM images. We collect particles directly in the jet stream holding the SEM slide briefly in the jet at the place where it intersects with the laser beam. A second SEM slide is prepared with particles taken directly from the container. In Fig. 3.11 (left panels) we present SEM images of the basalt, palagonite (JSC0), calcite, and montmorillonite samples directly collected from the container and from the aerosol jet (right panels) at similar scales. Comparison of the two set of images shows no evidence of a significant alteration of the particles due to the aerosol generator.

### 3.6 Simulations

The DDSCAT 7.1 code is an implementation of the discrete dipole approximation (DDA). DDSCAT 7.1 calculates scattering and absorption of electromagnetic waves by targets with arbitrary geometries and complex refractive index. In particular the DDSCAT 7.1 version allows calculations for birefringent particles [3]. The theory of DDA is presented in [91].

In the Discrete Dipole Approximation the target is replaced by an array of points. The points acquire dipole moment in response to the local electric field. The dipoles interact with one another via their electric fields. For the finite array of points the scattering problem is exactly solved. DDA is completely flexible regarding the geometry of the target, being limited only by the need to use 1) an interdipole separation,  $d$  and 2) the wavelength of incident light, both small compared to the size of the target. Numerical studies [81] indicate that the second criterion is adequately satisfied if  $|m|kd < 1$ , where  $m$  is the complex refractive index of the target material, and  $k \equiv 2\pi/\lambda$ , being  $\lambda$  the wavelength of the incident light beam.

Let  $V$  be the actual volume of solid material in the target. If the target is represented by an array of  $N$  dipoles, located on a cubic lattice with lattice spacing  $d$ , then

$$V = Nd^3. \quad (3.19)$$

We characterize the size of the target by the “DDA effective radius”:

$$a_{eff} \equiv (3V/4\pi)^{1/3}, \quad (3.20)$$

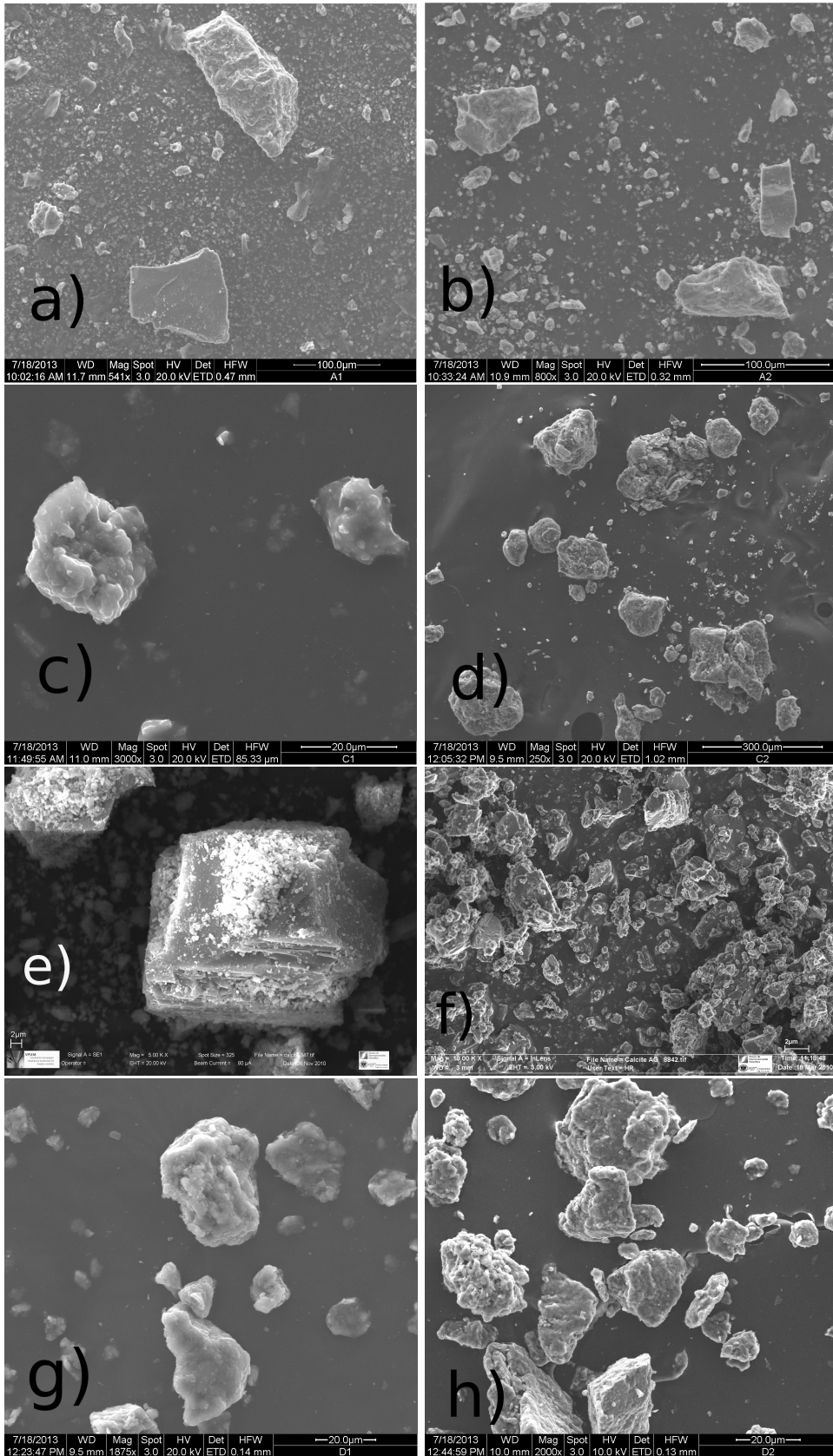


Figure 3.11: SEM images of a,b) basalt, c,d) palagonite (JSC0), e,f) calcite and g,h) montmorillonite. The 1st column (a,c,e,g) present samples collected from the container and 2nd column, directly from an aerosol jet n (b,d,f,h).

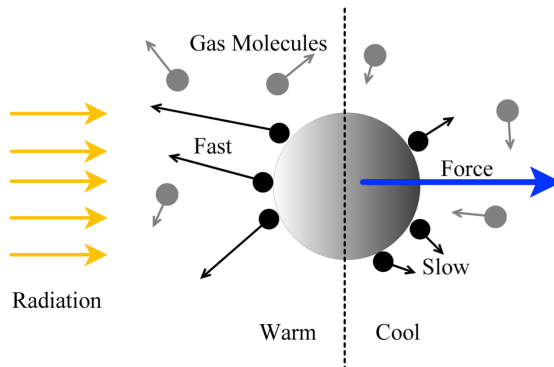


Figure 3.12: Schematic sketch of the principle of photophoresis. The illuminated surface heats up and transfer momentum to gas molecules, which finally leads to a net force in the direction of light (positive photophoresis). Image adopted from [103].

that is a radius of an equal volume sphere. A given scattering problem is then characterized by the dimensionless size parameter:

$$x \equiv 2\pi a_{eff}/\lambda. \quad (3.21)$$

To simulate the actual shape of the calcite particles we have used ten random flakes generated as described by Nousiainen et al. [102] and five new rhomboid-like shapes. Each irregular flake and rhomboid consists of about 50 000 and 100 000 dipoles, respectively. For each of the 15 mentioned shapes, scattering matrix computations for 14 different sizes from 0.1 to 1.2  $\mu m$  have been performed.

Simulations of such a large number of shapes and sizes is a challenge since they require a lot of memory and computing time. We have solved this problem using GRID technology that was available at the Instituto de Astrofísica de Andalucía (IAA). GRID permits simultaneous calculations on different cores and save a lot of time. In our work, we divide simulations into 540 different independent jobs that run at the same time on different cores. The cluster with 448 cores, that corresponds to 112 Intel Xeon Quad Core Processors (Model X7350 130W 2.93GHz 1066MHz 8MB L2) is used. One independent job is a calculation for one size, one shape and corresponding number of orientations. Each job needs from few hours up to 3 days depending on the parameters that are used. If we assume that the average calculation time for one job is about 1 day, all calculations presented in this work would have taken almost 2 years in a personal computer. By using GRID (540 cores), the calculations have been made in the same time that takes for the longest individual job. A detailed description on GRID is available at <http://grid.iaa.csic.es>.

### 3.7 Photophoresis: theory and experiment

Photophoresis is an interaction between particles and the surrounding gas in the medium with non-isotropic illumination. The illuminated particle is heated on its side that absorbs light. The other side stays cooler and a temperature gradient is formed along the particle. Gas molecules accommodate to the particle surface and adopt the surface temperature where they touch the dust particle. On the warm side of the grain, gas molecules gain more momentum than on cooler side. The velocity difference leads to a net momentum transfer from the gas molecules to the particle, which amounts to a net force in the direction of the temperature gradient. The principle of photophoresis is shown in the Fig. 3.12. Depending on the physical properties of the grain, we distinguish positive and negative photophoresis. Most of the cases are positive photophoresis, which results in movement with the same sense of direction of light photons. It occurs when the illuminated part corresponds to warm part of the particle. Nevertheless, in other case the light beam passes through the particle and becomes strongly absorbed by the back part of the particle. This results in movement towards the light source, what is called negative photophoresis, Fig. 3.13. The ideal case that causes negative photophoresis would be the glass particle, through which the beam passes with very absorbing, e.g. carbon-like back part.

Considering mineral samples the positive photophoresis is most probable mechanism.

Since photophoresis is pressure dependent, the number of affected particles should correlate with



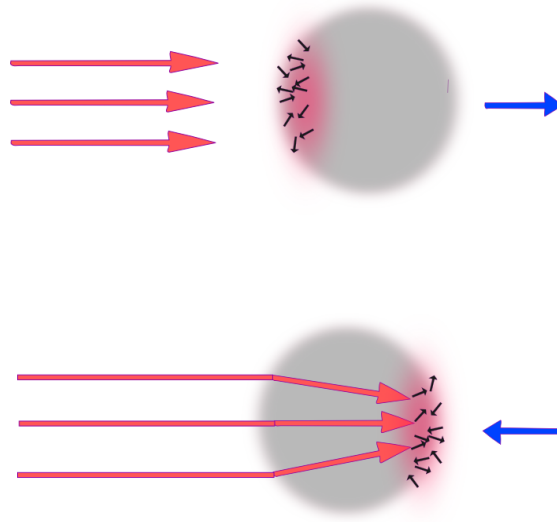


Figure 3.13: The positive (top) and negative photophoresis (bottom), which lead to movement according to light, and towards light source, respectively. In majority of cases the positive photophoresis is observed. The negative photophoresis case correspond to non-(poorly-)absorbing illuminated part of the particle.

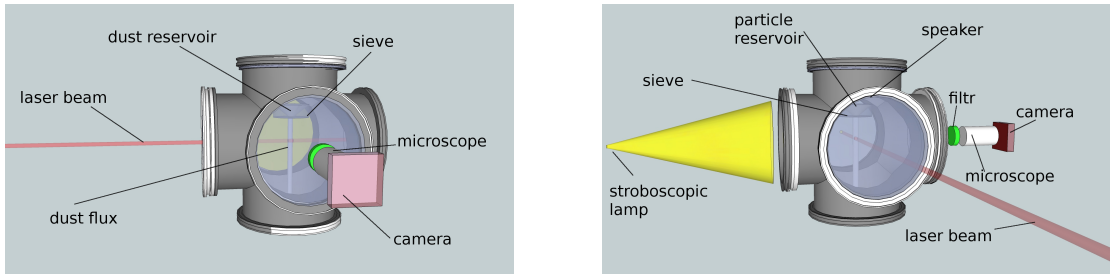


Figure 3.14: Schematic picture of the setup; left: front view; right: side view

this pressure dependence which is given by Rohatschek [4]:

$$F_{Ph} = \frac{(2 + \delta)F_{max}}{\frac{p}{p_{max}} + \frac{p_{max}}{p} + \delta}, \quad (3.22)$$

where  $p_{max}$  is the pressure where the maximum force  $F_{max}$  appears and  $\delta$  is the experimental constant to be determined. The maximum pressure can be found using following formula:

$$p_{max} = \frac{\eta}{a} \sqrt{12 \frac{RT}{\alpha \mu}}, \quad (3.23)$$

$$F_{max} = (\pi \sqrt{12 \frac{R}{3\mu T}} \eta a^2 I) (\sqrt{\alpha \frac{J}{k}}), \quad (3.24)$$

where  $\eta$  is the gas viscosity,  $k$  is the thermal conductivity of the dust,  $\alpha$  accommodation coefficient,  $J$  asymmetry parameter.  $I$  is the incoming radiation,  $T$  the gas temperature,  $a$  the particle radius,  $R$  the gas constant and  $\mu$  the molecular mass of gas. The gas viscosity  $\eta$  equals  $1.84 \times 10^{-5} \text{ kg/(ms)}$  and molecular mass of gas, in this case, air  $28.97 \text{ kg/kmol}$ .

Fig. 3.14 shows a schematic sketch of the experiment. For each series of experiments a preset pressure inside a vacuum chamber is set. Dust particles are generated through a sieve (mesh of  $63\text{-}\mu\text{m}$ ) loaded with a dust sample. A vertical dust flow occurs once vibrations are induced by an attached

speaker. The sieve aperture and therefore the particle beam diameter is about 1 cm. The particle enters the illuminated region of a horizontal laser beam ( $655 \pm 10$  nm). The cross section of the laser beam is about 0.8 cm and the intensity,  $I$ , is  $9280 \text{ W/m}^2$ .

The illuminated particles are observed with a long distance bright field microscopy with a mean spatial resolution of  $880 \times 900$  recorded by an attached camera at 500 fps. The spatial resolution slightly changes between the measurements of different samples. This allows the trajectories of the particles to be traced well while within the laser beam. The light scattered from the laser was removed by a filter in front of the camera.

The measurements are performed with a pressure range between 0.5 mbar to 100 mbar. For smaller pressure the photophoretic forces are too small to be resolved. At higher pressure convection can mask photophoretic motion. The mean free path,  $\lambda$ , of the gas molecules scales linearly with pressure and is  $68 \mu\text{m}$ ,  $14 \mu\text{m}$  and  $6.8 \mu\text{m}$  at 1, 5, and 10 mbar, respectively. Since the Knudsen number is defined by  $Kn = \lambda/a$ , where the  $a$  is the particle radius, and we have ten micrometer particles, the Knudsen number,  $Kn \sim 1$ . For this region the maximum photophoretic force should occur.



# Bibliography

- [1] O. Muñoz, F. Moreno, D. Guirado, D. D. Dabrowska, H. Volten, and J. W. Hovenier. The Amsterdam-Granada Light Scattering Database. *J. Quant. Spec. Radiat. Transf.*, 113:565–574, February 2012.
- [2] J. W. Hovenier and C. V. M. van der Mee. Testing scattering matrices: a compendium of recipes. *J. Quant. Spec. Radiat. Transf.*, 55:649–661, May 1996.
- [3] B. T. Draine and P. J. Flatau. User Guide for the Discrete Dipole Approximation Code DDSCAT 7.1. *ArXiv e-prints*, February 2010.
- [4] H. Rohatschek. Semi-empirical model of photophoretic forces for the entire range of pressures. *J. Aerosol Sci.*, 26:717–734, April 1995.
- [5] D. D. Dabrowska, O. Muñoz, F. Moreno, J. L Ramos, J. Martínez-Frías, and G. Wurm. Scattering matrices of Martian dust analogs at 488 nm 647 nm- under revision. *A&A*, 2014.
- [6] D. D. Dabrowska, O. Muñoz, F. Moreno, T. Nousiainen, and E. Zubko. Effect of the orientation of the optic axis on simulated scattering matrix elements of small birefringent particles. *Optics Letters*, 37:3252, August 2012.
- [7] D. D. Dabrowska, O. Muñoz, F. Moreno, T. Nousiainen, E. Zubko, and A. C. Marra. Experimental and simulated scattering matrices of small calcite particles at 647nm. *J. Quant. Spec. Radiat. Transf.*, 124:62–78, July 2013.
- [8] Schiaparelli. Observations de la Planete Mars en 1886. *Bulletin de la Societe Astronomique de France et Revue Mensuelle d’Astronomie, de Meteorologie et de Physique du Globe*, 12:112–120, 1898.
- [9] A. Dollfus, M. Deschamps, and L. V. Ksanfomaliti. The surface texture of the Martian soil from the Soviet spacecraft Mars-5 photopolarimeters. *A&A*, 123:225–237, July 1983.
- [10] R. Santer, M. Deschamps, L. V. Ksanfomaliti, and A. Dollfus. Photopolarimetric analysis of the Martian atmosphere by the Soviet MARS-5 orbiter. I - White clouds and dust veils. *A&A*, 150:217–228, September 1985.
- [11] R. Santer, M. Deschamps, L. V. Ksanfomaliti, and A. Dollfus. Photopolarimetry of Martian aerosols. II - Limb and terminator measurements. *A&A*, 158:247–258, April 1986.
- [12] M. D. Smith. Spacecraft Observations of the Martian Atmosphere. *Annual Review of Earth and Planetary Sciences*, 36:191–219, May 2008.
- [13] G. Di Achille and B. M. Hynek. Ancient ocean on Mars supported by global distribution of deltas and valleys. *Nature Geoscience*, 3:459–463, June 2010.
- [14] H. H. Kieffer, B. M. Jakosky, C. W. Snyder, and M. S. Matthews. *Mars*. 1992.
- [15] J. Bell, III. *The Martian Surface - Composition, Mineralogy, and Physical Properties*. July 2008.
- [16] N. Barlow. *Mars: An Introduction to its Interior, Surface and Atmosphere, by Nadine Barlow, Cambridge, UK: Cambridge University Press, 2008*. January 2008.

- [17] H. Savijärvi. Meteorology of the terrestrial planets. *Surveys in Geophysics*, 15:755–773, November 1994.
- [18] R. Greeley, N. Lancaster, S. Lee, and P. Thomas. *Martian aeolian processes, sediments, and features*, pages 730–766. Mars, 1992.
- [19] V. M. Khazins, V. A. Rybakov, R. Greeley, and M. Balme. The Dust Ejection Induced by a Meteoroid Impact as a Possible Initiator of Dust Devils on Mars: Laboratory Experiment and Numerical Simulation. *Solar System Research*, 38:12–20, January 2004.
- [20] G. Wurm and O. Krauss. Dust Eruptions by Photophoresis and Solid State Greenhouse Effects. *Physical Review Letters*, 96(13):134301, April 2006.
- [21] G. Wurm, J. Teiser, and D. Reiss. Greenhouse and thermophoretic effects in dust layers: The missing link for lifting of dust on Mars. *Geophys. Res. Lett.*, 35:10201, May 2008.
- [22] C. de Beule, G. Wurm, T. Kelling, M. Kupper, T. Jankowski, and J. Teiser. The martian soil as a planetary gas pump. *Nature physics*, 10:17–20, 2013.
- [23] B. A. Cantor. MOC observations of the 2001 Mars planet-encircling dust storm. *Icarus*, 186:60–96, January 2007.
- [24] J. E. Hansen and L. D. Travis. Light scattering in planetary atmospheres. *Space Science Reviews*, 16:527–610, October 1974.
- [25] A. V. Morozhenko. The Atmosphere of Mars According to Polarization Observations. *Soviet Astronomy*, 13:852, April 1970.
- [26] Z. M. Dlugach and E. V. Petrova. Polarimetry of Mars in High-Transparency Periods: How Reliable Are the Estimates of Aerosol Optical Properties? *Solar System Research*, 37:87–100, March 2003.
- [27] S. Ebisawa and A. Dollfus. Dust in the Martian Atmosphere: Polarimetric Sensing. *A&A*, 272:671–686, May 1993.
- [28] P. Drossart, J. Rosenqvist, M. Combes, S. Erard, Y. Langevin, and J. P. Bibring. Martian aerosol properties from the Phobos/ISM experiment. *Annales Geophysicae*, 9:754–760, November 1991.
- [29] R. T. Clancy, M. J. Wolff, and P. R. Christensen. Mars aerosol studies with the MGS TES emission phase function observations: Optical depths, particle sizes, and ice cloud types versus latitude and solar longitude. *Journal of Geophysical Research (Planets)*, 108:5098, September 2003.
- [30] M. J. Wolff, R. Todd Clancy, J. D. Goguen, M. C. Malin, and B. A. Cantor. Ultraviolet dust aerosol properties as observed by MARCI. *Icarus*, 208:143–155, July 2010.
- [31] R. T. Clancy and S. W. Lee. A new look at dust and clouds in the Mars atmosphere - Analysis of emission-phase-function sequences from global Viking IRTM observations. *Icarus*, 93:135–158, September 1991.
- [32] M. J. Wolff and R. T. Clancy. Constraints on the size of Martian aerosols from Thermal Emission Spectrometer observations. *Journal of Geophysical Research (Planets)*, 108:5097, September 2003.
- [33] O. I. Korablev, V. A. Krasnopolsky, A. V. Rodin, and E. Chassefiere. Vertical structure of Martian dust measured by solar infrared occultations from the PHOBOS spacecraft. *Icarus*, 102:76–87, March 1993.
- [34] E. Quémerais, J.-L. Bertaux, O. Korablev, E. Dimarellis, C. Cot, B. R. Sandel, and D. Fussen. Stellar occultations observed by SPICAM on Mars Express. *Journal of Geophysical Research (Planets)*, 111:9, September 2006.
- [35] F. Montmessin, E. Quémerais, J. L. Bertaux, O. Korablev, P. Rannou, and S. Lebonnois. Stellar occultations at UV wavelengths by the SPICAM instrument: Retrieval and analysis of Martian haze profiles. *Journal of Geophysical Research (Planets)*, 111:9, September 2006.
- [36] P. Rannou, S. Perrier, J.-L. Bertaux, F. Montmessin, O. Korablev, and A. Réberac. Dust and cloud detection at the Mars limb with UV scattered sunlight with SPICAM. *Journal of Geophysical Research (Planets)*, 111:9, September 2006.
- [37] J. B. Pollack and J. N. Cuzzi. Scattering by nonspherical particles of size comparable to wavelength - A new semi-empirical theory and its application to tropospheric aerosols. *Journal of Atmospheric Sciences*, 37:868–881, April 1980.

- [38] J. B. Pollack, M. E. Ockert-Bell, and M. K. Shepard. Viking Lander image analysis of Martian atmospheric dust. *J. Geophys. Res.*, 100:5235–5250, March 1995.
- [39] M. G. Tomasko, L. R. Doose, M. Lemmon, P. H. Smith, and E. Wegrzyn. Properties of dust in the Martian atmosphere from the Imager on Mars Pathfinder. *J. Geophys. Res.*, 104:8987–9008, April 1999.
- [40] W. J. Markiewicz, R. M. Sablotny, H. U. Keller, N. Thomas, D. Titov, and P. H. Smith. Optical properties of the Martian aerosols as derived from Imager for Mars Pathfinder midday sky brightness data. *J. Geophys. Res.*, 104:9009–9018, April 1999.
- [41] M. T. Lemmon, M. J. Wolff, M. D. Smith, R. T. Clancy, D. Banfield, G. A. Landis, A. Ghosh, P. H. Smith, N. Spanovich, B. Whitney, P. Whelley, R. Greeley, S. Thompson, J. F. Bell, and S. W. Squyres. Atmospheric Imaging Results from the Mars Exploration Rovers: Spirit and Opportunity. *Science*, 306:1753–1756, December 2004.
- [42] O. Dollfus, Z. M. Dlugach, A. V. Morozhenko, and É. G. Yanovitskii. Optical Parameters of the Atmosphere and Surface of Mars. II. Dust Strom. *Solar System Research*, 8:176, October 1974.
- [43] Z. M. Dlugach and A. V. Morozhenko. Parameters of Dust Particles in the Martian Atmosphere. *Solar System Research*, 35:421–430, November 2001.
- [44] K. Pang, J. M. Ajello, C. W. Hord, and W. G. Egan. Complex refractive index of Martian dust - Mariner 9 ultraviolet observations. *Icarus*, 27:55–67, January 1976.
- [45] K. Pang and J. M. Ajello. Complex refractive index of Martian dust - Wavelength dependence and composition. *Icarus*, 30:63–74, January 1977.
- [46] P. Chylek and G. W. Grams. Scattering by nonspherical particles and optical properties of Martian dust. *Icarus*, 36:198–203, November 1978.
- [47] A. B. Binder, R. E. Arvidson, E. A. Guinness, K. L. Jones, T. A. Mutch, E. C. Morris, D. C. Pieri, and C. Sagan. The geology of the Viking Lander 1 site. *J. Geophys. Res.*, 82:4439–4451, September 1977.
- [48] T. A. Mutch, R. E. Arvidson, E. A. Guinness, A. B. Binder, and E. C. Morris. The geology of the Viking Lander 2 site. *J. Geophys. Res.*, 82:4452–4467, September 1977.
- [49] A. Banin, B. C. Clark, and H. Waenke. *Surface chemistry and mineralogy*, pages 594–625. Mars, 1992.
- [50] M. P. Golombek, N. T. Bridges, H. J. Moore, S. L. Murchie, J. R. Murphy, T. J. Parker, R. Rieder, T. P. Rivellini, J. T. Schofield, A. Seiff, R. B. Singer, P. H. Smith, L. A. Soderblom, D. A. Spencer, C. R. Stoker, R. Sullivan, N. Thomas, S. W. Thurman, M. G. Tomasko, R. M. Vaughan, H. Wänke, A. W. Ward, and G. R. Wilson. Overview of the Mars Pathfinder Mission: Launch through landing, surface operations, data sets, and science results. *J. Geophys. Res.*, 104:8523–8554, April 1999.
- [51] P. R. Christensen, S. W. Ruff, R. L. Fergason, A. T. Knudson, S. Anwar, R. E. Arvidson, J. L. Bandfield, D. L. Blaney, C. Budney, W. M. Calvin, T. D. Glotch, M. P. Golombek, N. Gorelick, T. G. Graff, V. E. Hamilton, A. Hayes, J. R. Johnson, H. Y. McSween, G. L. Mehall, L. K. Mehall, J. E. Moersch, R. V. Morris, A. D. Rogers, M. D. Smith, S. W. Squyres, M. J. Wolff, and M. B. Wyatt. Initial Results from the Mini-TES Experiment in Gusev Crater from the Spirit Rover. *Science*, 305:837–842, August 2004.
- [52] D. W. Ming, D. W. Mittlefehldt, R. V. Morris, D. C. Golden, R. Gellert, A. Yen, B. C. Clark, S. W. Squyres, W. H. Farrand, S. W. Ruff, R. E. Arvidson, G. Klingelhöfer, H. Y. McSween, D. S. Rodionov, C. Schröder, P. A. de Souza, and A. Wang. Geochemical and mineralogical indicators for aqueous processes in the Columbia Hills of Gusev crater, Mars. *Journal of Geophysical Research (Planets)*, 111:2, January 2006.
- [53] J. Kula and S. L. Baldwin. On hematite as a target for dating aqueous conditions on Mars. *Planetary and Space Science*, 67:101–108, July 2012.
- [54] P. R. Christensen, J. L. Bandfield, R. N. Clark, K. S. Edgett, V. E. Hamilton, T. Hoefen, H. H. Kieffer, R. O. Kuzmin, M. D. Lane, M. C. Malin, R. V. Morris, J. C. Pearl, R. Pearson, T. L. Roush, S. W. Ruff, and M. D. Smith. Detection of crystalline hematite mineralization on Mars by the Thermal Emission Spectrometer: Evidence for near-surface water. *J. Geophys. Res.*, 105:9623–9642, April 2000.

- [55] W. V. Boynton, D. W. Ming, B. Sutter, R. E. Arvidson, J. Hoffman, P. B. Niles, P. Smith, and Phoenix Science Team. Evidence for Calcium Carbonate at the Phoenix Landing Site. In *Lunar and Planetary Science Conference*, volume 40 of *Lunar and Planetary Science Conference*, page 2434, March 2009.
- [56] J. L. Bandfield, T. D. Glotch, and P. R. Christensen. Spectroscopic Identification of Carbonate Minerals in the Martian Dust. *Science*, 301:1084–1087, August 2003.
- [57] B. L. Ehlmann, J. F. Mustard, G. A. Swayze, R. N. Clark, J. L. Bishop, F. Poulet, D. J. Des Marais, L. H. Roach, R. E. Milliken, J. J. Wray, O. Barnouin-Jha, and S. L. Murchie. Identification of hydrated silicate minerals on Mars using MRO-CRISM: Geologic context near Nili Fossae and implications for aqueous alteration. *Journal of Geophysical Research (Planets)*, 114:0, October 2009.
- [58] L. A. Leshin, P. R. Mahaffy, C. R. Webster, M. Cabane, P. Coll, P. G. Conrad, P. D. Archer, S. K. Atreya, A. E. Brunner, A. Buch, and et al. Volatile, Isotope, and Organic Analysis of Martian Fines with the Mars Curiosity Rover. *Science*, 341, September 2013.
- [59] A. S. Yen, R. Gellert, B. C. Clark, D. W. Ming, P. L. King, M. E. Schmidt, L. A. Leshin, R. V. Morris, S. W. Squyres, J. Spray, and J. L. Campbell. Evidence for a Global Martian Soil Composition Extends to Gale Crater. In *Lunar and Planetary Science Conference*, volume 44 of *Lunar and Planetary Science Conference*, page 2495, March 2013.
- [60] O. B. Toon, J. B. Pollack, and C. Sagan. Physical properties of the particles composing the Martian dust storm of 1971-1972. *Icarus*, 30:663–696, April 1977.
- [61] R. T. Clancy, S. W. Lee, G. R. Gladstone, W. W. McMillan, and T. Rousch. A new model for Mars atmospheric dust based upon analysis of ultraviolet through infrared observations from Mariner 9, Viking, and PHOBOS. *J. Geophys. Res.*, 100:5251–5263, March 1995.
- [62] A. Banin. The soils of Mars. In M. J. Drake, R. Greeley, G. A. McKay, D. P. Blanchard, M. H. Carr, J. Gooding, C. P. McKay, P. D. Spudis, and S. W. Squyres, editors, *Mars Sample Return Science*, pages 35–36, 1988.
- [63] A. Banin, L. Margulies, T. Ben-Shlomo, G. C. Carle, L. M. Coyne, J. B. Orenberg, and T. W. Scattergood. Constraining Mars Soil Mineralogical Composition: Palagonite vs. Iron Enriched Smectite Clays. In *Lunar and Planetary Science Conference*, volume 19 of *Lunar and Planetary Science Conference*, page 27, March 1988.
- [64] A. Banin, G. C. Carle, S. Chang, L. M. Coyne, J. B. Orenberg, and T. W. Scattergood. Laboratory investigations of mars: Chemical and spectroscopic characteristics of a suite of clays as Mars Soil Analogs. *Origins of Life*, 18:239–265, September 1988.
- [65] J. Orenberg and J. Handy. Reflectance spectroscopy of palagonite and iron-rich montmorillonite clay mixtures - Implications for the surface composition of Mars. *Icarus*, 96:219–225, April 1992.
- [66] J. Crisp and M. J. Bartholomew. Mid-infrared spectroscopy of Pahala ash palagonite and implications for remote sensing studies of Mars. *J. Geophys. Res.*, 97:14691, September 1992.
- [67] J. F. Bell, R. V. Morris, and J. B. Adams. Thermally altered palagonitic tephra - A spectral and process analog to the soil and dust of Mars. *J. Geophys. Res.*, 98:3373–3385, February 1993.
- [68] T. L. Roush and J. B. Orenberg. Estimated detectability limits of iron-substituted montmorillonite clay on Mars from thermal emission spectra of clay-palagonite physical mixtures. *J. Geophys. Res.*, 101:26111–26118, 1996.
- [69] J. L. Bandfield and M. D. Smith. Multiple emission angle surface-atmosphere separations of thermal emission spectrometer data. *Icarus*, 161:47–65, January 2003.
- [70] V. E. Hamilton, H. Y. McSween, and B. Hapke. Mineralogy of Martian atmospheric dust inferred from thermal infrared spectra of aerosols. *Journal of Geophysical Research (Planets)*, 110:12006, December 2005.
- [71] J. F. Mustard and J. F. Bell. New composite reflectance spectra of Mars from 0.4 to 3.14 micron. *Geophys. Res. Lett.*, 21:353–356, March 1994.
- [72] C. C. Allen, R. V. Morris, K. M. Jager, D. C. Golden, D. J. Lindstrom, M. M. Lindstrom, and J. P. Lockwood. Martian Regolith Simulant JSC Mars-1. In *Lunar and Planetary Science Conference*, volume 29 of *Lunar and Planetary Science Conference*, page 1690, March 1998.

- [73] K. J. Snook, J. L. Bandfield, F. Forget, and C. P. McKay. Derivation of Infrared Optical Properties of Dust Suspended in the Martian Atmosphere from MGS-TES Data. In *AAS/Division for Planetary Sciences Meeting Abstracts #32*, volume 32 of *Bulletin of the American Astronomical Society*, page 1094, October 2000.
- [74] M. J. Wolff, M. D. Smith, R. T. Clancy, R. Arvidson, M. Kahre, F. Seelos, S. Murchie, and H. Savijärvi. Wavelength dependence of dust aerosol single scattering albedo as observed by the Compact Reconnaissance Imaging Spectrometer. *Journal of Geophysical Research (Planets)*, 114:0, June 2009.
- [75] M. E. Ockert-Bell, J. F. Bell, J. B. Pollack, C. P. McKay, and F. Forget. Absorption and scattering properties of the Martian dust in the solar wavelengths. *J. Geophys. Res.*, 102:9039–9050, April 1997.
- [76] C. F. Bohren and D. R. Huffman. *Absorption and scattering of light by small particles*. 1983.
- [77] G. Mie. Beiträge zur Optik trüber Medien, speziell kolloidaler Metallösungen. *Annalen der Physik*, 330:377–445, 1908.
- [78] H. A. Lorentz. Ueber die Beziehung zwischen der Fortpflanzungsgeschwindigkeit des Lichtes und der Körperdichte. *Annalen der Physik*, 245:641–665, 1880.
- [79] P. Debye. Der Lichtdruck auf Kugeln von beliebigem Material. *Annalen der Physik*, 335:57–136, 1909.
- [80] P. C. Waterman. Symmetry, Unitarity, and Geometry in Electromagnetic Scattering. *Phys. Rev. D*, 3:825–839, February 1971.
- [81] B. T. Draine. *The Discrete Dipole Approximation for Light Scattering by Irregular Targets*, page 131. *Light Scattering by Nonspherical Particles : Theory, Measurements, and Applications*, January 2000.
- [82] I. R. Ciric and F. R. Cooray. *Separation of Variables for Electromagnetic Scattering by Spheroidal Particles*, page 90. *Light Scattering by Nonspherical Particles : Theory, Measurements, and Applications*, January 2000.
- [83] K. Yee. Numerical solution of initial boundary value problems involving maxwell’s equations in isotropic media. *IEEE Transactions on Antennas and Propagation*, 14:302–307, May 1966.
- [84] M. I. Mishchenko, A. A. Lacis, B. E. Carlson, and L. D. Travis. Nonsphericity of dust-like tropospheric aerosols: Implications for aerosol remote sensing and climate modeling. *Geophys. Res. Lett.*, 22:1077–1080, May 1995.
- [85] M. I. Mishchenko, L. D. Travis, and A. Macke. *T-Matrix Method and Its Applications*, page 147. *Light Scattering by Nonspherical Particles : Theory, Measurements, and Applications*, January 2000.
- [86] D. Guirado, J. W. Hovenier, and F. Moreno. Circular polarization of light scattered by asymmetrical particles. *J. Quant. Spec. Radiat. Transf.*, 106:63–73, July 2007.
- [87] L. Kolokolova and D. Mackowski. Polarization of light scattered by large aggregates. *J. Quant. Spec. Radiat. Transf.*, 113:2567–2572, December 2012.
- [88] M. J. Wolff, M. D. Smith, R. T. Clancy, N. Spanovich, B. A. Whitney, M. T. Lemmon, J. L. Bandfield, D. Banfield, A. Ghosh, G. Landis, P. R. Christensen, J. F. Bell, and S. W. Squyres. Constraints on dust aerosols from the Mars Exploration Rovers using MGS overflights and Mini-TES. *Journal of Geophysical Research (Planets)*, 111:12, December 2006.
- [89] K. M. Pitman, M. J. Wolff, and E. A. Cloutis. Building More Realistic Grain Shapes in Radiative Transfer Models of Mars Regolith. In *Lunar and Planetary Science Conference*, volume 45 of *Lunar and Planetary Science Conference*, page 2627, March 2014.
- [90] D. W. Mackowski and M. I. Mishchenko. Calculation of the T matrix and the scattering matrix for ensembles of spheres. *Journal of the Optical Society of America A*, 13:2266–2278, November 1996.
- [91] B. T. Draine. The discrete-dipole approximation and its application to interstellar graphite grains. *Astrophys. Journal*, 333:848–872, October 1988.
- [92] O. Muñoz, F. Moreno, D. Guirado, J. L. Ramos, A. López, F. Girela, J. M. Jerónimo, L. P. Costillo, and I. Bustamante. Experimental determination of scattering matrices of dust particles at visible wavelengths: The IAA light scattering apparatus. *J. Quant. Spec. Radiat. Transf.*, 111:187–196, January 2010.



- [93] E. V. Petrova. Mars aerosol optical thickness retrieved from measurements of the polarization inversion angle and the shape of dust particles. *J. Quant. Spec. Radiat. Transf.*, 63:667–676, December 1999.
- [94] S. Merikallio, T. Nousiainen, M. Kahnert, and A.-M. Harri. Light scattering by the Martian dust analog, palagonite, modeled with ellipsoids. *Optics Express*, 21:17972–17985, July 2013.
- [95] H. C. van de Hulst. *Light scattering by small particles*. New York: Dover, 1981, 1981.
- [96] J. W. Hovenier. Scattering matrix elements. Technical report, January 2004.
- [97] J. W. Hovenier. *Measuring Scattering Matrices of Small Particles at Optical Wavelengths*, page 355. *Light Scattering by Nonspherical Particles : Theory, Measurements, and Applications*, January 2000.
- [98] H. Volten, O. Muñoz, E. Rol, J. F. de Haan, W. Vassen, J. W. Hovenier, K. Muinonen, and T. Nousiainen. Scattering matrices of mineral aerosol particles at 441.6 nm and 632.8 nm. *J. Geophys. Res.*, 106:17375–17402, August 2001.
- [99] J. Nelder and R. Mead. A simplex method for function minimization. *Computer Journal*, 7:308313, 1965.
- [100] W. H. Press, S. A. Teukolsky, W. T. Vetterling, and B. P. Flannery. *Numerical recipes in FORTRAN. The art of scientific computing*. 1992.
- [101] O. Muñoz, F. Moreno, D. Guirado, J. L. Ramos, H. Volten, and J. W. Hovenier. The IAA cosmic dust laboratory: Experimental scattering matrices of clay particles. *Icarus*, 211:894–900, January 2011.
- [102] T. Nousiainen, E. Zubko, J. V. Niemi, K. Kupiainen, M. Lehtinen, K. Muinonen, and G. Videen. Single-scattering modeling of thin, birefringent mineral-dust flakes using the discrete-dipole approximation. *Journal of Geophysical Research (Atmospheres)*, 114:7207, April 2009.
- [103] G. Wurm, M. Trieloff, and H. Rauer. Photophoretic Separation of Metals and Silicates: The Formation of Mercury-like Planets and Metal Depletion in Chondrites. *Astrophys. Journal*, 769:78, May 2013.

## ”Scattering matrices of Martian dust analogs at 488 nm and 647 nm”

D.D. Dabrowska, O. Muñoz, F. Moreno, J.L. Ramos, J. Martínez-Frías, G. Wurm, *Scattering matrices of Martian dust analogs at 488 nm and 647 nm*, submitted to *Astronomy & Astrophysics*

**Abstract** The modeling of atmospheric radiative transfer on Mars is strongly affected by aerosol particles. We present measurements of the complete scattering matrix as a function of the scattering angle of five Martian dust analogs, namely montmorillonite, two palagonite (JSC-1) samples, basalt, and calcite. To facilitate the use of the experimental matrices for multiple-scattering calculations with polarization included, we present the corresponding synthetic scattering matrices based on the measurements and the assumption that the forward diffraction peak is mainly dependent on the size of the particles. The synthetic scattering matrices are available in the full range from 0 to 180 degrees. The measurements are performed at 448 and 647 nm covering the scattering angle range from 3 to 177 degrees. The experimental scattering matrices are compared with results of Lorenz-Mie calculations performed for the same size distributions and refractive indices as our analog samples. Scattering matrices of realistic polydispersions a dust particles are poorly represented by Lorenz-Mie theory. Moreover, the agreement between retrieved phase functions for Martian dust and our experimental phase functions is remarkable. Martian analogs closely mimic the phase functions retrieved using space-borne instrumentation [1, 2]. Further, spectro-polarimetric observations from Martian surface appear to be a powerful diagnostic tool to infer the composition of the dust in the Martian atmosphere.

## 4.1 Introduction

Martian atmospheric dust plays a crucial role in the planet's radiative transfer budget. Dust particles can modify the temperature, dynamics, and chemical composition of the atmosphere. To estimate the influence of atmospheric dust on Martian climate, the quantification of size-dependent optical properties of the dust particles is essential. Indeed, the importance of the studies of the spatial and temporal distribution of dust, its optical properties, and its influence on climate on Mars, have motivated a number of space missions to the planet.

The problem is far from trivial. In the first place, the dust distribution is highly variable in time and location on the planet, owing to the occurrence of a variety of transport phenomena, ranging from small-scale thermal eddies to global dust storms. In addition to strong winds lifting up dust particles from the surface, another mechanisms, such as solid state greenhouse effects or photophoresis have been proposed as rising dust mechanisms from the Martian surface (e.g. [3, 4]). In addition, de Baule et al. [5] have recently shown that Martian soil can work as a gas (Knudsen) pump injecting the particles into the atmosphere. Second, dust grains are irregular in shape, as confirmed by Phoenix Lander microscope images (e.g.[6]). This introduces a serious difficulty in the radiative transfer modeling. While the treatment of the scattering processes from spherical dust particles is straightforward using Mie theory, it is extremely tedious, or even impossible, for realistic polydispersions of non-spherical particles. One reason is the large memory and CPU needed by the available light scattering codes to compute the scattering matrix for individual irregular particles with sizes of the order or larger than the wavelength of the incident light (e.g. [7, 8, 9, 10, 11, 12, 13, 14]). Another reason is the difficulty in properly representing the internal structure and surface roughness of those particles as seen in nature [13]. In many cases, in radiative transfer calculations the vector nature of light is replaced by its intensity or flux, i.e. polarization is ignored. We might note that under multiple scattering conditions (as is the case during large dust storms on Mars) even in the cases when only the radiance need to be computed, adopting a scalar representation of light induces significant, wavelength dependent, errors in the calculated planetary phase functions and geometric albedos [15, 16]. Thus, an appropriate representation of the scattering matrix of dust particles is mandatory under multiple scattering conditions. All in all, measurements of the full scattering matrices (including polarization) of realistic polydispersions of dust particles in the laboratory remain an extremely valuable tool.

The light scattering properties of Martian dust have been so far estimated from analysis of the light scattered or emitted by the atmosphere or by the contribution of atmosphere plus surface (e.g.[1, 2, 17, 18, 19]). In this paper, we report on measurements of the full 4x4 scattering matrix as a function of the scattering angle of five Martian dust analogs. The measurements are performed at the IAA COsmic DUst LABoratory (CODULAB) [20], at two different wavelengths (448 and 647 nm) covering the scattering angle range from 3 to 177 degrees. In section 4.2 we present an outline of the current known properties of the Martian dust, and introduce the terrestrial analogs. Section 4.3 is devoted to the description of the light scattering setup CODULAB. Results and discussion of our experiments, comparison with Lorenz-Mie theory calculations, and the construction of the "synthetic" scattering matrices are given in section 4.4. In section 4.5, we compare our measurements with Martian dust observations. Finally, the conclusions of the paper are drawn in section 4.6.

## 4.2 Physical properties of Martian dust and its terrestrial analogues

### 4.2.1 Martian dust properties

Martian dust is a surface layer of chemically altered, the most fine-grained component of soil. It appears in bright reddish regions of the Planet. It has been largely homogenized by winds. Mars Exploration Rovers (MER) Microscopic Imager observations have shown that surface dust

occurs as fragile, low-density, sand-sized (200-300  $\mu\text{m}$ ) aggregates [21]. In contrast, atmospheric dust is much finer, but probably similar in form to loose material on the surface. The Phoenix microscopic images confirmed the irregular shapes of the airborne dust.

Space-based observations with OMEGA, a visible and infrared mineralogical mapping spectrometer on board Mars Express Orbiter, have shown a high abundance of iron oxides in the dusty bright regions of the planet [22]. The typical soil (Gusev Crater, Meridiani Planum and Gale Crater) is dominated by silicon dioxide  $\text{SiO}_2$  and ferric oxide  $\text{FeO}$  [23]. Results from Mars Pathfinder mission indicate that the dust is composed of micron-sized silicate particles composed in part of poorly crystalline or nanophase ferric materials, sometimes mixed with small but varying degrees of well-crystalline ferric and ferrous phase. Moreover, different surface missions present slightly different soil composition [23]. This indicates that the dust has been largely homogenized but there is still a small influence of underlying geologic units. Because of past volcanic activity on Mars there are many basaltic rocks. Therefore, the Martian dust could be composed by basalt or its weathering product. Minor components of the dust have also been identified in the soils around the Phoenix landing site, such as calcium carbonate, which is a possible form of calcite, ikaite, aragonite, or ankerite [24].

A crucial parameter of the dust is the complex refractive index,  $m$ , which is intimately related to the composition. Estimates of  $m$  have been given by e.g. Wolff et al., Tomasko et al., Ockert-Bell et al., Wolff et al. [1, 2, 25, 26]. Their results approximately agree with each other (see Fig. 4.1). The real part,  $n$ , remains more or less constant from UV to IR having values ranging from 1.47 to 1.5. The imaginary part displays a severe decrease from values around  $k = 0.014$  at UV to 0.001-0.002 at red and near-IR wavelengths. At longer wavelengths  $k$  increases moderately up to 0.006 at 2500 nm increasing drastically up to 0.05 at 2900 nm [1]. The exact retrieved values depend on model assumption, namely particle size distributions and phase functions used.

Regarding particle size in the Martian atmosphere, early results and retrieval methods were reviewed by Dlugach et al. [27]. They gave sizes retrieved from polarimetric observations ranging from very small particles ( $r_{\text{eff}}$  around 0.05  $\mu\text{m}$ ) during a high-transparency period to  $r_{\text{eff}} > 9 \mu\text{m}$  during Global Dust Storm (GDS) conditions. Estimates of Martian aerosol properties are obtained from sky images taken from the Martian surface [2] and from emission phase function (EPF) observations by the Mars Global Surveyor (MGS) Thermal Emission Spectrometer (TES) [17, 28]. Whereas those observations from the orbit give valuable overview of the dust in the entire atmosphere around the planet, the measurements made from the Mars surface represent the local dust properties of the lower atmosphere. In general, those models of Martian dust from such measurements are consistent with 1 - 2.5  $\mu\text{m}$  sized particles (being 1.8 - 2.5  $\mu\text{m}$  the typical values for the GDS of 2001, whereas 1  $\mu\text{m}$  is typical for quiet periods [17], the size distribution being rather poorly constrained. The size of airborne Martian dust depends on altitude as well. At high altitude, over 20 km, very fine particles of  $r_{\text{eff}} = 0.01$ - 0.1  $\mu\text{m}$  are found [29]. In contrast, strong winds near the surface tend to catch large dust particles. Therefore, a variety of dust size distributions can be actually found in the atmosphere.

Under moderate dust loading conditions [2, 18, 19, 30], have retrieved middle size airborne dust close to 1.5 - 1.6  $\mu\text{m}$  from surface-based observations at different visible wavelengths. As a representative example in Tab. 4.2) we present the size distribution (effective radii and effective variance) retrieved by Tomasko et al. [2] at Mars Pathfinder surroundings.

## 4.2.2 Martian dust analogs

### Origin and refractive indices

In our experiments five different analog samples have been analyzed, namely, two palagonites (JSC0, JSC200), montmorillonite, basalt, and calcite.

Since Mars and the Earth probably were formed at the same time and region of the Solar System, it is logical to find the same elements and minerals on both planets. Therefore, and since there is no available Martian dust to perform a laboratory study on Earth, dust analogs must be used. Early choices of Earth spectral analogs showed a predominantly montmorillonite

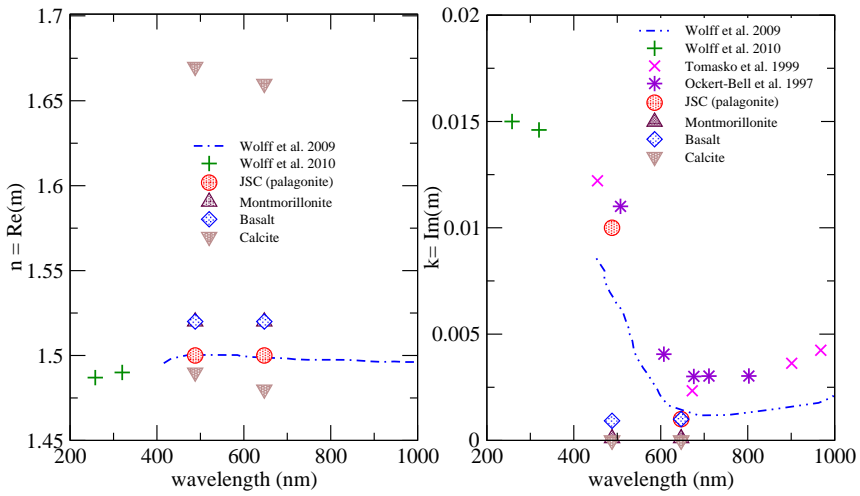


Figure 4.1: Wavelength dependence of the real (left panel) and imaginary (right panel) parts of the refractive index for Martian dust. The values in the 440 to 1000 nm range are adopted from Wolff et al. [26]. The 258 to 320 nm dependence is taken from Wolff et al. [1]. The values derived by Wolff et al. [26] for the imaginary part of the refractive index are compared with previous work by Tomasko et al. [2] and Ockert-Bell et al. [25]. The retrievals of Martian dust are presented together with the refractive indices of our samples of Martian dust analogs (Tab. 4.1).

composition [31]. The clay reflectance spectra in the VIS and NIR are similar to the Martian spectra. Notwithstanding, it appears that the bright soils have a dominant spectral characteristic for terrestrial weathering products of basaltic ash or glass, the palagonites [32, 33]. Palagonites are found to be better spectral Martian dust analogs. The montmorillonite spectrum has a greater number of spectral features and higher emissivity in contrast to the palagonite spectrum [34]. Both materials are commonly used as terrestrial analogs for bright Martian soils e.g. [35, 36, 37, 38].

The palagonite sample used in this study is JSC Mars-1 (JSC stands for Johnson Space Center), which is a Martian regolith simulant [39], the  $< 1$  mm size fraction of a palagonitic tephra (glassy volcanic ash altered at low temperatures) [40]. Allen et al. [40] have shown the VIS/NIR spectrum of the simulant and Martian bright regions with removed atmospheric contribution, where the bands at 1400 and 1900 nm in the simulant spectrum indicate a higher level of  $H_2O$  in the simulant than on Mars. Then, the original sample was first sieved with a 200  $\mu\text{m}$  sieve to remove the millimeter-sized particles. Subsequently, part of the sample was heated up to 200°C and left in the oven for 24h to get rid of the volatile components. To distinguish the heated and no-heated JSC samples, we call them JSC200 and JSC0, respectively.

Montmorillonite is the dominant clay mineral in bentonite, an altered volcanic ash. The montmorillonite sample used in this work is commercially available from WARD's Science, USA.

Apart from the palagonites and montmorillonite we also present measurements for a basalt sample collected at Tenerife Island (Canary archipelago), which corresponds to the Güimar volcanic eruption. The lava flow is recent and fresh (last historical eruption of the Black Sand Mountain of Arafo, 1704) and is defined as olivinic-pyroxenic basalt.

Although calcite is not a major component of the Martian surface, it is commonly considered to be particularly important for its link with climate evolution and water resources on Mars [41, 42]. The calcite sample studied in this work was obtained from limestone bulk material collected near Lecce, Italy [43] and was previously studied by Dabrowska et al. [44].

The approximate complex refractive indices of the studied samples are given in Tab. 4.1. Both the real and imaginary parts of the refractive indices remain essentially constant at visible wavelengths, except for the orange/brown colored JSC0 and JSC200 samples, for which the imaginary part is significantly higher in the blue than in the red region of the spectrum. This is possibly linked to the high iron content of the JSC samples. According to the measured optical constants of silicates of variable iron content, the imaginary part of refractive index increases as the iron content increases [45]. The high absorption at blue in comparison with red wavelengths of the JSC samples mimics perfectly the behavior of the Martian dust in the visible (see Tab. 4.1 and Fig. 4.1, right panel).

Basalt is black/grey colored having low iron content compared to that found in the JSC samples. In contrast, calcite and montmorillonite show white and light grey colors, respectively. Calcite is an uni-axial birefringent material, so it has one optic axis and, instead of one refractive index, it has a dielectric tensor specified by two principal dielectric functions, the ordinary and extraordinary refractive indices. In Tab. 4.1 we present the single effective refractive index  $m_{\text{eff}} = ((n_e^2 + n_o^2)/2)^{1/2}$  at the corresponding wavelength [46]. The imaginary part of the refractive index,  $k$ , is assumed to be zero since pure calcite is very weakly absorbing in the visible.

## Shapes

Fig. 4.2 displays the SEM images of basalt (a), palagonite samples JSC0 (b), and JSC200 (c), montmorillonite (d), and calcite (e). At microscopic scales, a variety of geometric forms are present. In particular, the calcite and montmorillonite particles present rhomboidal- and flake-like structures with layered structures typical of sedimentary minerals. We might note that the SEM images are not necessarily representative of the size distribution of the samples. For that purpose we refer the reader to next subsection.

Sample	Refractive index:	[488 nm]	[647 nm]	color	Source
Basalt		$1.52 + 0.00092i$	$1.52 + 0.001i$	dark gray	[49]
JSC0/JSC200		$1.5 + 0.01i$	$1.5 + 0.001i$	orange/brown	[50] [51]
Montmorillonite		$1.52 + 0.0001i$	$1.52 + 0.0001i$	light gray	[52]
Calcite	effective refractive index	$1.6 + 0i$	$1.6 + 0i$	white	[46]
Martian dust		$1.495 + 0.012-0.008$	$1.5 + 0.002-0.001^*$	orange/brown	[26]

Table 4.1: Refractive indices of the studied samples compared with refractive indices of Martian dust as retrieved by Wolff et al. [26].

### Determination of the size distribution of the dust analogs

The size distribution of the Martian analog samples is measured using the commercially available Mastersizer2000 particle sizer from Malvern Instruments. The Mastersizer measures the phase function of the samples paying special attention to the forward diffraction peak. It uses either Lorenz-Mie or Fraunhofer diffraction theories to retrieve the volume distributions that best fit the measurements. The retrievals from both methods are simplifications based on the assumption that the particles are spherical. Further studies are required to clarify which size distribution is more representative for our samples. Accordingly, we present the size distributions based on both Lorenz-Mie (Mie) or Fraunhofer (Fr) theories so that the reader can choose which one is more appropriate for his/her purposes or take the average. Fig. 4.3 depicts the retrieved number distributions as functions of radius for our samples from both, Fraunhofer (left panel) and Mie (right panel) theories. In those panels,  $r$  represents the radius of a sphere having the same volume as the particle (volume equivalent sphere). The transformation equations to obtain  $n(r)$ , from the measured volume size distribution,  $v(r)$  are given in the Amsterdam-Granada Light Scattering Database [http://www.iaa.es/scattering/site\\_media/sizedistributions.pdf](http://www.iaa.es/scattering/site_media/sizedistributions.pdf) (see also [47]). The size distribution of the calcite sample was previously presented in [44].

From the measured size distributions we calculate the values of the effective radii  $r_{\text{eff}}$  and effective variances  $v_{\text{eff}}$  as defined by Hansen and Travis [48]:

$$r_{\text{eff}} = \frac{\int_0^{\infty} r\pi r^2 n(r) dr}{\int_0^{\infty} \pi r^2 n(r) dr} \quad (4.1)$$

$$v_{\text{eff}} = \frac{\int_0^{\infty} (r - r_{\text{eff}})^2 \pi r^2 n(r) dr}{r_{\text{eff}}^2 \int_0^{\infty} \pi r^2 n(r) dr}, \quad (4.2)$$

In Tab. 4.2 we present the calculated  $r_{\text{eff}}$  and  $v_{\text{eff}}$  for our samples. For a direct comparison with Martian dust we also include in Tab. 4.2 the values retrieved by Tomasko et al. [2]. As shown, our samples are characterized by a broad range of sizes, having, in many cases,  $r_{\text{eff}}$  and  $v_{\text{eff}}$  higher than those retrieved by Tomasko et al. [2] for Martian dust. However, it must be noted that the dust size distribution in the Martian atmosphere surely depends strongly on the weather conditions and altitude as already stated. In addition, our goal is to determine how the different physical parameters of our Martian dust analogs might affect the measured scattering matrices.

## 4.3 Experimental Apparatus

The scattering matrices of our samples are measured at the IAA COsmic DUst LABoratory (CODULAB) located at the Instituto de Astrofísica de Andalucía, Granada, Spain. In this section we give a brief description of the experimental apparatus. For a detailed description of the experimental apparatus, calibration process, and data acquisition we refer to Muñoz et al. [20].

The IAA CODULAB is designed to study dust particles in the size range between 0.1 micron and 100 micron (in radius). We use an Argon-Krypton laser as light source that can emits at five different wavelengths. In this work we present measurements at two wavelengths, namely: 448 and 647 nm. The laser beam passes through a polarizer and an electro-optic modulator. The

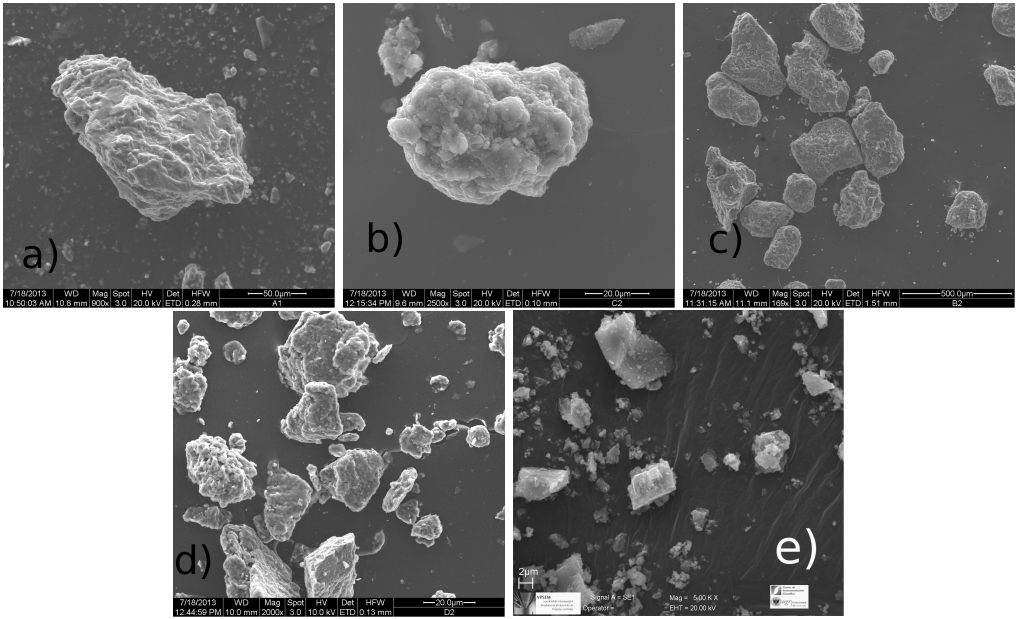


Figure 4.2: Scanning Electron Microscope images of (a) basalt, (b) JSC0, (c) JSC200, (d) montmorillonite, and (e) calcite. White bars at the bottom right corner of panels (a), (b), (c) , and (d) and left bottom corner (e) denote the scale of the images.

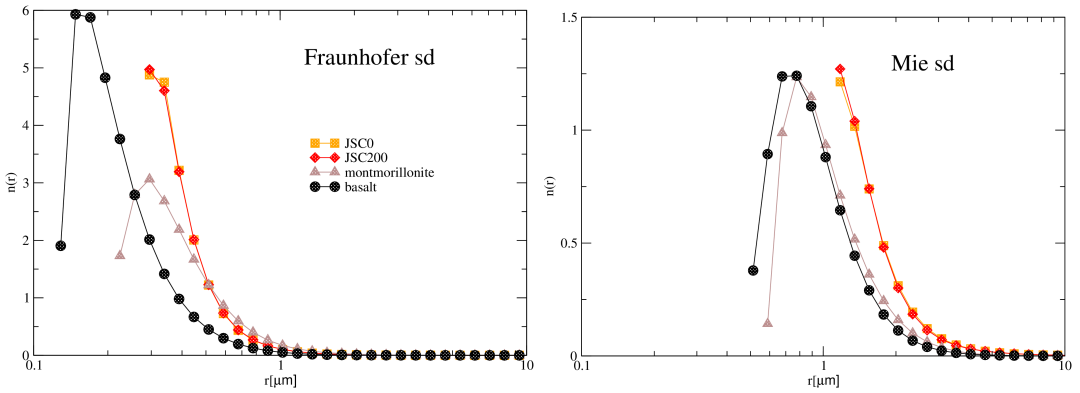


Figure 4.3: The number  $n(r)$  distributions of the basalt (black circles), JSC0 (red squares), JSC200 (green diamonds) and montmorillonite (blue triangles) samples as measured by MasterSizer 2000 from Malvern Instruments, based either on Fraunhofer (top) and Mie (bottom panels) theories.



Sample	Method	$r_{\text{eff}} [\mu\text{m}]$	$v_{\text{eff}}$
Basalt	Fraunhofer	2.9	15.1
	Mie	6.9	7.0
JSC0	Fraunhofer	17.2	2.4
	Mie	29.5	1.1
JSC200	Fraunhofer	15.5	2.8
	Mie	28.1	1.2
Calcite*	Fraunhofer	1.7	7.6
	Mie	3.3	4.9
Montmorillonite	Fraunhofer	1.8	1.6
	Mie	2.8	1.2
Martian dust	[2]	$1.6 \pm 0.15$	0.2-0.5 or more

Table 4.2: Effective radii  $r_{\text{eff}}$  and effective variances  $v_{\text{eff}}$  retrieved from the measured Fraunhofer and Mie size distributions.

modulated light is subsequently scattered by an ensemble of randomly oriented dust particles located in a jet stream produced by an aerosol generator. The scattered light passes through a quarter-wave plate and an analyzer (both optional) and is detected by a photomultiplier tube which moves along a ring. In this way a range of scattering angles from  $3^\circ$  to  $177^\circ$  is covered in the measurements. Another photomultiplier tube located at a fixed position is used to correct from fluctuations of the signal. We employ polarization modulation in combination with lock-in detection to obtain the entire four-by-four scattering matrix up to a constant. By using eight different combinations of the optical components and their orientations, and assuming the reciprocity of the sample (in particular  $F_{21}/F_{11} = F_{12}/F_{11}$ ,  $F_{31}/F_{11} = -F_{13}/F_{11}$  and  $F_{41}/F_{11} = F_{14}/F_{11}$ ), all scattering matrix elements are obtained as functions of the scattering angle [20, 53].

All matrix elements (except  $F_{11}$  itself) are normalized to  $F_{11}$ , that is, we consider  $F_{ij}/F_{11}$ , with  $i, j=1$  to 4 with the exception of  $i = j = 1$ . The values of  $F_{11}(\theta)$  are normalized so that they are equal to 1 at  $\theta=30^\circ$ . The function  $F_{11}(\theta)$ , normalized in this way, is called the phase function or scattering function in this paper.

The reliability of the apparatus has been tested by comparing measured scattering matrices of spherical water droplets at 488 nm, 520 nm and 647 nm with Lorenz-Mie computations [20]. In addition, special tests have been performed to ensure that our experiment is performed under the single scattering regime [54]. We also check that the measurements fulfill the Cloude coherency matrix test given in Hovenier et al. [55] within the experimental errors at all measured scattering angles.

## 4.4 Results

In section 4.4.1 we present the experimentally determined scattering matrices for the five Martian dust analog samples described in section 4.2. The measured scattering matrices are compared with Lorenz-Mie calculations for spheres with the same number distributions and refractive index as our sample have. In section 4.4.2 we describe how we construct a synthetic scattering matrix in the full range from 0 to 180 deg scattering angles, and derive the asymmetry parameters for our samples.

### 4.4.1 Measured scattering matrices.

In Figs. 4.4 to 4.8, we present the measured scattering matrix elements as functions of the scattering angle for the JSC0, JSC200, calcite, basalt (488 and 647 nm), and montmorillonite (488 nm) samples. The measurements cover the scattering angle range from 3 to 177 degrees.

We note that the measured scattering matrix at 647 nm for the calcite sample has been previously published by Dabrowska et al. [44]. We refrain from showing the elements  $F_{13}(\theta)/F_{11}(\theta)$ ,  $F_{14}(\theta)/F_{11}(\theta)$ ,  $F_{23}(\theta)/F_{11}(\theta)$ , and  $F_{24}(\theta)/F_{11}(\theta)$ , since they were found to be zero over the entire angle range within the accuracy of the measurements. This fact agrees with the assumption of randomly oriented particles with equal amounts of particles and their mirror particles [56]. As mentioned, all phase functions,  $F_{11}(\theta)$ , are arbitrarily normalized to 1 at 30 deg scattering angle, and always shown on a logarithmic scale. The experimental errors are indicated by error bars. When no error bar appears, this is because the experimental error is smaller than the symbol plotted. In general, the measurements for JSC samples show larger error bars than the measurements for all the other samples. This is predominantly due to the fact that those particles are relatively large so that relatively few particles are present in the scattering volume during the measurements, thereby decreasing the signal-to-noise ratio.

It is interesting to note that small differences in the physical properties of the JSC0 and JSC200 samples (e.g. size distribution) do not produce any significant effect on the measured scattering matrix elements.

In all studied cases, the measured phase function ( $F_{11}(\theta)$ ) presents the typical behavior for irregular mineral dust, i.e. it is a smooth function of scattering angle with steep forward peak and practically no structure at side- and back-scattering angles (see e.g. [57, 47, 58]).

The measured degree of linear polarization for incident unpolarized light,  $-F_{12}(\theta)/F_{11}(\theta)$ , displays the well-known bell shape in all cases, with a maximum at side-scattering angles, and a negative branch near back-scattering. Tab. 4.3 presents the measured main parameters in the region of minimum polarization ( $(-F_{12}/F_{11})_{min}, \theta_{min}$ ), inversion ( $\theta_{inv}$ ), and maximum polarization ( $(-F_{12}/F_{11})_{max}, \theta_{max}$ ), at the two studied wavelengths.

In Fig. 4.9, we compare the  $-F_{12}(\theta)/F_{11}(\theta)$  ratio at 488 nm (left) and 647 nm (right) for the 5 Martian dust analog samples. As shown, while for red wavelengths the maxima of the  $-F_{12}(\theta)/F_{11}(\theta)$  are similar for all samples, in the blue region the JSC samples are those having higher maxima relative to all the other samples. This is a very important result, coincidentally, those JSC samples are the ones having the largest effective radii. However, we conclude that it must be a consequence of the dominating effect of the much higher imaginary refractive index in those JSC samples as previous computations with irregular particles seem to indicate [59].

Moreover, it is interesting to note that the maximum of the  $-F_{12}(\theta)/F_{11}(\theta)$  ratio,  $(-F_{12}/F_{11})_{max}$ , for basalt, montmorillonite, and calcite samples, show higher values at 647 nm than at 488 nm i.e. they present a red polarization color. That seems to be also the color for silicate-type samples with low iron content as shown in many of the samples presented in the Amsterdam-Granada Light Scattering Database. As presented in Tab. 4.1, the imaginary part of the refractive index of the mentioned samples show a flat wavelength dependence. However, the JSC0 and JSC200 that present a significantly higher imaginary part of the refractive index at 488 nm than at 647 nm show a blue polarization color. Thus, since different Martian analogs have clearly different, wavelength-dependent polarimetric behavior, this could be used as a diagnostic tool to infer the composition of the dust.

The  $F_{22}(\theta)/F_{11}(\theta)$  ratio is often used as an indication of the non-sphericity of the particles, since for optically inactive spheres equals unity at all scattering angles. This ratio is affected by both the size distribution and refractive indices of the samples. In particular, we obtain, for the most absorbing samples (JSC0 and JSC200), the shallowest minimum in the  $F_{22}(\theta)/F_{11}(\theta)$  curve, and a dependence on wavelength opposite to all the other samples, which agrees with the results by Volten et al. [60].

The ratio  $F_{33}(\theta)/F_{11}(\theta)$ , is found to be different from the  $F_{44}(\theta)/F_{11}(\theta)$  at nearly all measured scattering angles, with  $F_{44}/F_{11}(\theta) > F_{33}(\theta)/F_{11}(\theta)$  at back-scattering angles. As indicated by Mishchenko et al. [7] and shown in many examples in the Amsterdam-Granada Light Scattering Database, this is a general property for irregular dust particles.

The pattern for the  $F_{34}(\theta)/F_{11}(\theta)$  ratio is very similar for all studied samples with a maximum at side-scattering angles and two negative branches at small and large scattering angles.

In Fig. 4.6 we compare the scattering matrices for montmorillonite and calcite samples at 488 nm. As shown in Tab. 4.1, the refractive index of both samples do not differ very much.

Sample	$\lambda$	$(-F_{12}/F_{11})_{min}$	$\theta_{min}$ (°)	$(-F_{12}/F_{11})_{max}$	$\theta_{max}$ (°)	$\theta_{inv}$ (°)
JSC0	488 nm	$-0.037 \pm 0.021$	$172 \pm 1$	$0.21 \pm 0.02$	$100 \pm 5$	$155 \pm 5$
	647 nm	$-0.036 \pm 0.017$	$174 \pm 1$	$0.14 \pm 0.01$	$90 \pm 5$	$155 \pm 5$
JSC200	488 nm	$-0.031 \pm 0.013$	$174 \pm 1$	$0.21 \pm 0.02$	$95 \pm 5$	$155 \pm 5$
	647 nm	$-0.054 \pm 0.09$	$172 \pm 1$	$0.159 \pm 0.015$	$90 \pm 5$	$160 \pm 5$
Montmorillonite	488 nm	$-0.024 \pm 0.018$	$172 \pm 1$	$0.104 \pm 0.001$	$70 \pm 5$	$15 \pm 5$
Basalt	488 nm	$-0.033 \pm 0.01$	$170 \pm 1$	$0.096 \pm 0.009$	$100 \pm 5$	$150 \pm 5$
	647 nm	$-0.03 \pm 0.008$	$170 \pm 1$	$0.12 \pm 0.01$	$95 \pm 5$	$155 \pm 5$
Calcite	488 nm	$-0.025 \pm 0.003$	$165 \pm 5$	$0.082 \pm 0.005$	$105 \pm 5$	$150 \pm 5$
	647 nm	$-0.034 \pm 0.008$	$169 \pm 1$	$0.155 \pm 0.021$	$100 \pm 5$	$150 \pm 5$
Martian yellow clouds*	590 nm	$-0.007$	$165$			$152$

Table 4.3: Measured maxima and minima of the degree of linear polarization for unpolarized incident light and the corresponding scattering angles at which they are obtained. We also present the inversion angle for all studied samples together with the inversion angle Martian (yellow) dust clouds as measured by Ebisawa et al. [62](<sup>\*</sup>).

Moreover their effective radii (see Tab. 4.2) and shapes are nearly identical (Section 4.2.2). However, the montmorillonite sample that shows the closest size distribution to Martian dust, presents a significantly lower effective variance ( $v_{eff}$ ), i.e. it shows the narrowest size distribution. Whereas the calcite sample has a  $v_{eff}$  equal to 1.6 (Fraunhofer theory), the montmorillonite shows a  $v_{eff}$  equal to 7.6 (Fraunhofer theory). Therefore, any differences in their scattering behavior are most likely due to the differences in the width of their size distributions.

In particular, the maximum of the  $-F_{12}(\theta)/F_{11}(\theta)$  ratio for montmorillonite is moved toward smaller scattering angles (see Tab. 4.3). Moreover, the  $F_{22}(\theta)/F_{11}(\theta)$ ,  $F_{33}(\theta)/F_{11}(\theta)$  and  $F_{44}(\theta)/F_{11}(\theta)$  for montmorillonite show significantly smaller values at forward- and side-scattering angles than those presented by the calcite sample.

#### 4.4.2 Lorenz-Mie calculations versus measured scattering matrices

In Figs. 4.4 to 4.8, we compare the measured scattering matrix elements as functions of the scattering angle with results of Lorenz-Mie theory for homogeneous optically non-active spherical particles. For the Lorenz-Mie calculations we employ the number distribution and refractive index of the corresponding sample. The calculated phase function are also normalized to 1 at 30 degrees. As it has been previously demonstrated (e.g. [61]), the scattering pattern for spherical particles cannot be used to represent the real behavior of natural, irregularly-shaped dust particles. In particular, the relative differences between calculated and experimental phase functions are quite strong at side- and back-scattering angles. Moreover, the measured degree of linear polarization for incident unpolarized light shows positive values at nearly all scattering angles with a maximum in the 90-100 degrees region and a negative branch at backward direction. As mentioned, that is a typical behavior for irregular mineral dust as shown in many examples at the Amsterdam-Granada Light scattering Database. In contrast, the calculated values tend to be negative at almost all scattering angles with exception of the JSC0 and JSC200 samples. Moreover, the  $F_{22}(\theta)/F_{11}(\theta)$  is equal to 1 at all scattering angles for spherical particles while the measured results for our Martian dust analogs strongly deviate from 1 at nearly all measured scattering angles. Significant differences between calculated and measured values are also found for the other elements of the scattering matrix.

#### 4.4.3 Synthetic scattering matrices

As mentioned, the experimental measurements do not cover either forward scattering or the exact backward scattering directions. Therefore, what we obtain is the relative phase function,  $F_{11}(\theta)/F_{11}(30^\circ)$ , where (see [63]),

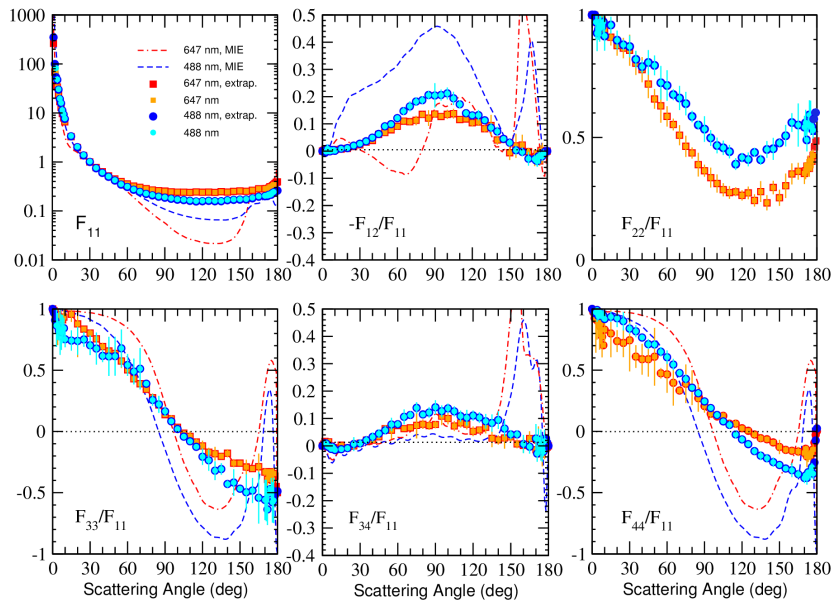


Figure 4.4: Measured scattering matrix elements as functions of the scattering angle at 448 (small circles) and 647 nm (small squares) for the JSC0 sample. Large circles and squares correspond to the synthetic scattering matrix elements based on the FR size distribution at 448 and 647 nm, respectively. The measurements are presented together with Lorenz-Mie calculations for spheres with the same size distribution (Mie) and refractive index as the JSC0 sample.

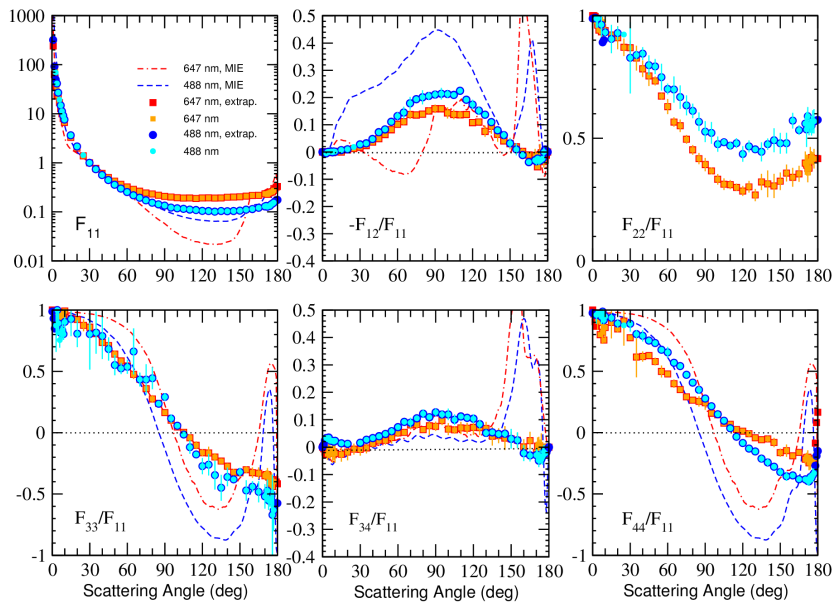


Figure 4.5: The same as Fig. 4.4 but for the JSC200 sample.

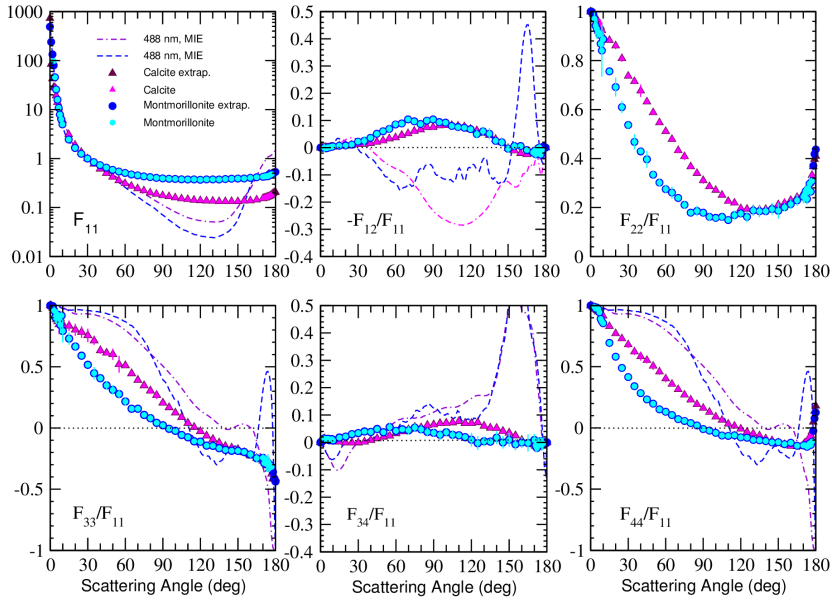


Figure 4.6: Measured scattering matrix elements as functions of the scattering angle at 448 nm for the montmorillonite sample (small circles) and calcite (small triangles). Large circles and triangles correspond to the synthetic scattering matrix elements for both samples, respectively. The measurements are presented together with Lorenz-Mie calculations for spheres with the same size distribution (FR) and refractive index as the corresponding sample.

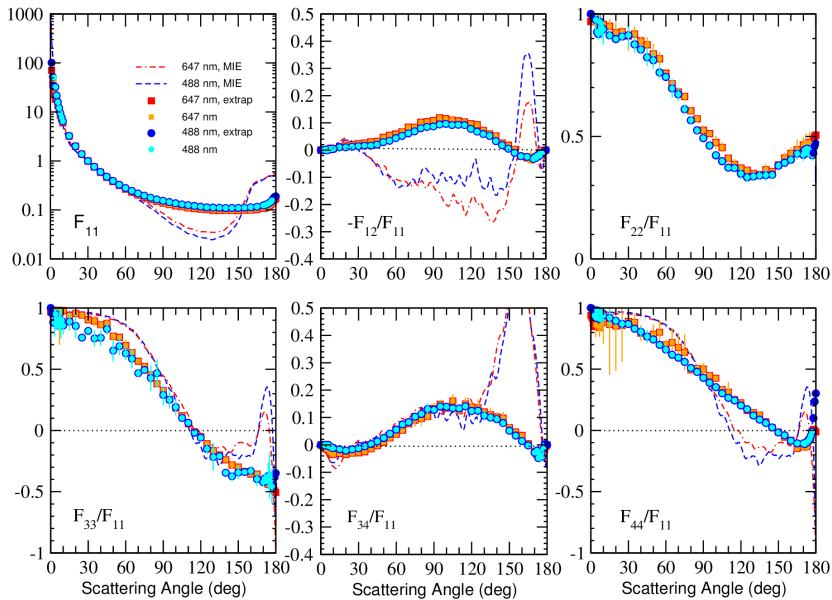


Figure 4.7: The same as Fig. 4.4 but for the basalt sample.

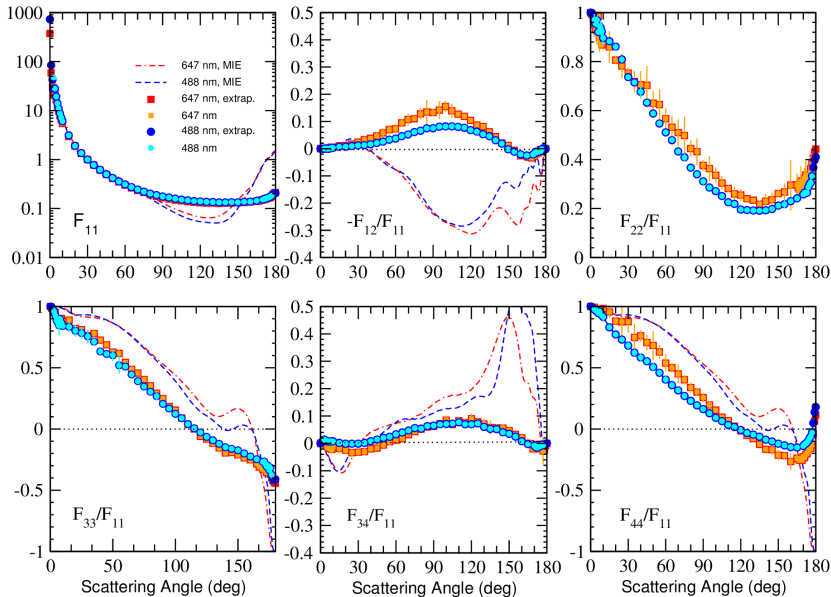


Figure 4.8: The same as Fig. 4.4 but for the calcite sample. The measurements at 647 nm have been previously published by Dabrowska et al. [44]

$$\frac{F_{11}(\theta)}{F_{11}(30^\circ)} = \frac{F_{11}^{au}(\theta)}{F_{11}^{au}(30^\circ)}. \quad (4.3)$$

The  $F_{11}^{au}(\theta)$  ratio is the auxiliary phase function which is normalized the way its average over all directions equals unity, i.e.,

$$1/2 \int_0^\pi d\theta \sin\theta F_{11}^{au}(\theta) = 1. \quad (4.4)$$

The lack of measurements at forward and back-scattering angles limits the use of the measured scattering matrix data for radiative transfer calculations. To facilitate the use of the experimental data we construct the so-called synthetic scattering matrices from our measurements. Then, the matrices are defined in the full scattering angle range, from 0 to 180 degrees.

The extrapolation of the phase function,  $F_{11}(\theta)$  is based on the assumption that the forward diffraction peak for randomly oriented particles with moderate aspect ratios mainly depends on the size of the particles [64] and is largely independent of their shape. Thus we merge the results of Lorenz-Mie calculations for projected-surface-area equivalent spheres between  $0^\circ$  and  $3^\circ$  with the corresponding measured phase function, which is scaled until the normalization condition (Eq.4.4) was satisfied. For the Lorenz-Mie computations we use the measured size distribution retrieved from both Fraunhofer and Lorenz-Mie theories (Fig. 4.3) and assuming the particles to have a refractive indices as given in Tab. 4.1. In the case of calcite, the effective refractive index,  $m_{\text{eff}} = 1.6 + 0.0i$  is considered [44]. The scaled phase function is then extrapolated to  $180^\circ$  assuming a smooth polynomial extrapolation. For the relative scattering matrix elements,  $F_{ij}(\theta)/F_{11}(\theta)$  (where  $i,j=1..4$ , and  $i \neq j \neq 1$ ), a polynomial extrapolation is used for both forward and backward scattering directions.

Values at exact forward and backward scattering were determined so that they satisfy the conditions given by Hovenier & van der Mee [65]. In addition, we make use of the fact that for each element of the scattering matrix the right-hand derivative at 0 degrees scattering angle and the left-hand derivative at 180 degrees must both vanish as described by Hovenier & Guirado [66]. Tables with the experimental data and the corresponding extrapolated

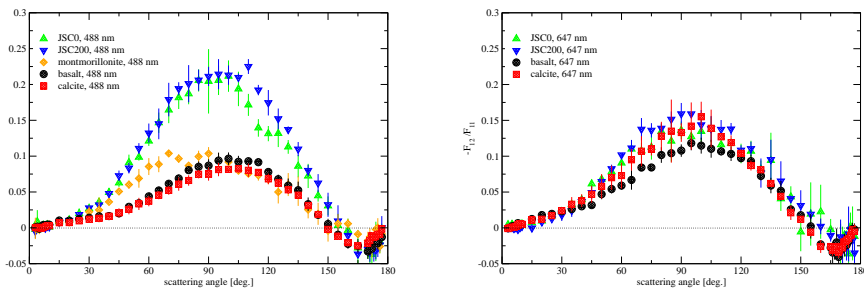


Figure 4.9: Measured degree of linear polarization as function of the scattering angle for the JSC0 (triangles), JSC200 (triangles down), montmorillonite (diamonds), basalt (circles), and calcite (squares) at 488 nm (left panel) and 647 nm (right panel).

Asymmetry parameter:				
Sample	[488 nm]		[647 nm]	
	Fr sd	Mie sd	Fr sd	Mie sd
Basalt	0.66	0.71	0.65	0.71
JSC0	0.66	0.80	0.54	0.64
JSC200	0.73	0.84	0.58	0.68
Calcite	0.61	0.65	0.60	0.63
Montmorillonite	0.44	0.55		
Martian dust	at visible(0.4-0.7 $\mu m$ )		0.84-0.65	Ockert-Bell et al. [25]

Table 4.4: The asymmetry parameter,  $g$ , retrieved from our measurements at 488 and 647 nm using both, the Fr and Mie sd presented in Section 4.2.

matrices for all samples are presented in the Amsterdam-Granada light scattering database <http://www.iaa.es/scattering/> [58].

From the extrapolated phase functions we compute the asymmetry parameter  $g$ , defined as the average cosine of the scattering angle  $\theta$ . The obtained values for our Martian dust analogs are presented in the Tab. 4.4.

## 4.5 Comparison with derived phase functions and degree of linear polarization in the Martian atmosphere.

In Fig. 4.10, left and right panels, we show the pseudo emission phase function retrieved from the Mars Colors Imager (MARCI band1) on board the Mars Reconnaissance Orbiter (MRO) observations [26] and data of the imager for Mars Pathfinder at 671 nm [2], respectively. In particular, we show the retrieved phase function at 671 nm, corresponding to a gamma size distributions with  $r_{\text{eff}}$  equal to 1.6  $\mu m$  and  $v_{\text{eff}}$  equal to 0.2. The observations for Martian dust are presented with single Henyey-Greenstein phase functions for the asymmetry parameters retrieved for Martian dust at the corresponding wavelengths, namely  $g = 0.65$  at blue wavelengths and  $g = 0.75$  at red wavelengths [25]. In Fig. 4.10 we also present Lorenz-Mie calculations for the same size distribution as retrieved by Tomasko et al. [2] and the refractive indices of the JSC sample (Tab. 4.1). In addition, a synthetic phase function calculated for cylinders with aspect ratio = 1 [26] is displayed. In all cases, the phase function is normalized at 30 deg to facilitate comparison with the laboratory measurements. In Fig. 4.11 we also present the experimental phase functions for basalt, montmorillonite, and JSC0 samples at the corresponding wavelengths.

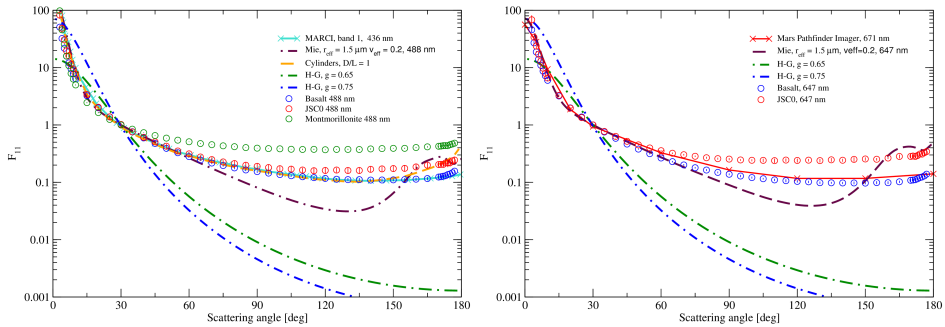


Figure 4.10: Pseudo Emission Phase Function constructed from MARCI band 1 by Wolff et al. [1] at 436 nm (blue line) (left) and phase function as derived by Tomasko et al. [2] at 671 nm (right). We also present analytical Henyey-Greestein phase functions for  $g=0.65$  (left) and  $g=0.75$  (right), and calculated phase functions for spheres (violet) and cylinders with the  $D/L=1$  [1] together with our measurements for basalt, JSC0, and montmorillonite.

As can be seen, none of the computed phase functions reproduce the observations for Mars. The phase function for cylinders gives the closest match, but differs substantially at back-scattering directions. On the contrary, despite the differences in the size distributions of the Martian dust derived by Tomasko et al. [2] and our Martian dust analogs, the agreement between observed and experimental phase functions for the Martian dust analogs at both wavelengths is remarkable. The main discrepancies are related to the forward diffraction peak that is highly dependent on the size of the particles.

In addition to the  $F_{11}(\theta)$  element, some observations of the degree of linear polarization for incident unpolarized light have also been performed on Mars. A recent review on polarimetry of terrestrial planets has been reported by Kaydash et al. [67]. The limitation of the observations, particularly related to remote measurements from Earth (e.g. [62]), or near-Earth orbiters like HST [68], is that the phase angles available are always restricted to the range 0-45 deg. Moreover, all the observations refer to the atmosphere plus surface system. In case the observations are performed during a dust storm, the contribution of the surface becomes negligible. However, in that case, the contribution of multiple scattering becomes important.

An important characteristic of the  $-F_{12}(\theta)/F_{11}(\theta)$  curve is the inversion angle, which is the scattering angle at which the  $-F_{12}/F_{11} = 0$ , changing from a positive to a negative value. It is generally found in the 150-160 degrees scattering angle range. As an illustrative example, in Fig. 4.11 we present our measured  $-F_{12}(\theta)/F_{11}(\theta)$  for basalt at 488 and 647 nm together with Martian polarimetric observations described in Ebisawa & Dollfus [62] at 590 nm, from previous works of [69, 70], corresponding to dust storm conditions. It is seen that the inversion angles of the Martian analog samples (see Table 3) closely agree with the Martian dust observations indicating an inversion at 28 deg phase angle. However, the negative branch is much deeper for the laboratory measurements. That seems to be a multiple scattering effect as previous comparative measurements of the phase angle dependence of the degree of linear polarization of particulate surfaces and particles in air show [71, 72].

## 4.6 Conclusions

We present measurements of the full  $4 \times 4$  scattering matrices as functions of the scattering angle of five Martian dust analogs: Basalt, two JSC-1 Martian simulants, montmorillonite, and calcite. To facilitate the use of the experimental scattering matrices for multiple-scattering calculations, we have obtained synthetic scattering matrices based on the measurements in the full scattering angle range from 0 to 180 degrees. Tables of the measured and synthetic scattering matrices are available in the Amsterdam-Granada Light Scattering Database ([www.iaa.es/scattering](http://www.iaa.es/scattering)). The



data are freely available under request of citation of this paper and [58].

The measured scattering matrices are compared with results of Lorenz-Mie calculations for the same number distribution and refractive indices as given for our Martian dust analogs. The experimental scattering matrices are poorly represented by the Lorenz-Mie calculations, showing strong differences between measured and calculated values at all measured scattering angles. Further, our measured phase functions have been compared with the retrieved phase functions for Martian dust from MARCI [1] and Mars Pathfinder [2], analytical Henyey-Greenstein phase functions, and computations for cylinders. The measured phase functions at blue and red wavelengths of the Martian analogs closely mimic the phase functions retrieved using spaceborne instrumentation [1, 2]. The measured  $-F_{12}(\theta)/F_{11}(\theta)$  ratio show a similar behavior to that observed in Mars during a Martian dust storm [62].

The scattering pattern of the Martian analogs follows generally the trend found in previous analysis of other mineral samples (e.g. [60]). Further, the polarimetric color might be an indication of the composition of Martian dust. The measured degree of linear polarization seems to be sensitive to the width of the size distribution. Therefore, spectro-polarimetric observations from Martian surface appear to be a powerful diagnostic tool to infer information on the physical properties of Martian dust.

Due to the complicated shapes of Martian dust, computations for realistic polydisperse irregular particles have to be replaced by simplified models such as cylinders [1, 73], spheroids [74], ellipsoids [75], or more sophisticated particles as aggregates of spheres and cubes [76]. Our experimental data can be used to check the validity of such model particles.

In particular, as our measurements indicate:

- Phase functions must be smooth functions of the scattering angle with strong forward peaks and nearly no structure at side- and back-scattering angles.
- The polarization color is directly dependent on the refractive index of the particles showing a red polarization color those particles with a flat dependence of the imaginary part of the refractive index at visible wavelengths and blue polarization color if it is significantly higher at blue than at red wavelengths.
- The maximum of the degree of linear polarization is also strongly dependent on the imaginary part of the refractive index showing highest values for those samples with a higher imaginary part of the refractive index (see e.g. [77]).
- Differences in the effective variance of the size distribution of the sample may have a significant effect in the scattering matrix elements.

Once the model is tested, further calculations can be performed at different wavelengths or physical parameters of the particles are which the measurements are not possible.

#### **Acknowledgements**

The SEM pictures were taken at the Scientific Instrumentation Center of the University of Granada. We are indebted to I. Guerra-Tschuschke for her support with the SEM. This work has been supported by the Plan Nacional de Astronomía y Astrofísica under Contracts AYA2009-08190 and AYA2012-39691, and Junta de Andalucía under Contract P09-FMQ-455.

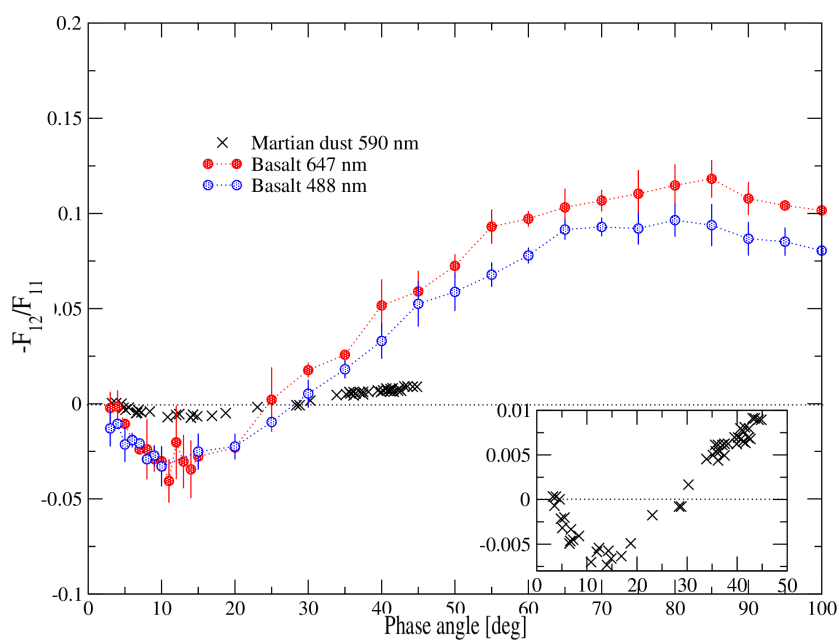


Figure 4.11: The negative polarization branch of Martian dust clouds as observed by Ebisawa & Dollfus [62] at 590 nm (crosses) presented together with the measured degree of linear polarization for basalt at 448 and 647 nm.



# Bibliography

- [1] M. J. Wolff, R. Todd Clancy, J. D. Goguen, M. C. Malin, and B. A. Cantor. Ultraviolet dust aerosol properties as observed by MARCI. *Icarus*, 208:143–155, July 2010.
- [2] M. G. Tomasko, L. R. Doose, M. Lemmon, P. H. Smith, and E. Wegryn. Properties of dust in the Martian atmosphere from the Imager on Mars Pathfinder. *J. Geophys. Res.*, 104:8987–9008, April 1999.
- [3] G. Wurm and O. Krauss. Dust Eruptions by Photophoresis and Solid State Greenhouse Effects. *Physical Review Letters*, 96(13):134301, April 2006.
- [4] G. Wurm, J. Teiser, and D. Reiss. Greenhouse and thermophoretic effects in dust layers: The missing link for lifting of dust on Mars. *Geophys. Res. Lett.*, 35:10201, May 2008.
- [5] C. de Beule, G. Wurm, T. Kelling, M. Kupper, T. Jankowski, and J. Teiser. The martian soil as a planetary gas pump . *Nature physics*, 10:17–20, 2014.
- [6] P. H. Smith.  $H_2O$  at the Phoenix Landing Site. *Science*, 325:58–61, 2009.
- [7] M. I. Mishchenko, L. D. Travis, and A. Macke. *T-Matrix Method and Its Applications*, page 147. Light Scattering by Nonspherical Particles : Theory, Measurements, and Applications, January 2000.
- [8] M. I. Mishchenko, L. D. Travis, and D. W. Mackowski. T-matrix computations of light scattering by nonspherical particles: a review. *J. Quant. Spec. Radiat. Transf.*, 55:535–575, May 1996.
- [9] B. T. Draine and P. J. Flatau. User Guide for the Discrete Dipole Approximation Code DDSCAT.6.0. *ArXiv Astrophysics e-prints*, September 2003.
- [10] M. Kahnert. Numerical methods in electromagnetic scattering theory. *J. Quant. Spec. Radiat. Transf.*, 79:775, September 2003.
- [11] A. Taflove and S. Hagness. *Computational Electrodynamics: The Finite-Difference Time-Domain Method*. 2005.
- [12] M. A. Yurkin and A. G. Hoekstra. The discrete dipole approximation: An overview and recent developments. *J. Quant. Spec. Radiat. Transf.*, 106:558–589, July 2007.
- [13] K. Muinonen, T. Nousiainen, H. Lindqvist, O. Muñoz, and G. Videen. Light scattering by Gaussian particles with internal inclusions and roughened surfaces using ray optics. *J. Quant. Spec. Radiat. Transf.*, 110:1628–1639, September 2009.
- [14] T. Wriedt. Light scattering theories and computer codes. *J. Quant. Spec. Radiat. Transf.*, 110:833–843, July 2009.
- [15] F. Moreno, O. Muñoz, J. J. López-Moreno, A. Molina, and J. L. Ortiz. A Monte Carlo Code to Compute Energy Fluxes in Cometary Nuclei. *Icarus*, 156:474–484, April 2002.
- [16] D. M. Stam and J. W. Hovenier. Errors in calculated planetary phase functions and albedos due to neglecting polarization. *A&A*, 444:275–286, December 2005.

- [17] R. T. Clancy, M. J. Wolff, and P. R. Christensen. Mars aerosol studies with the MGS TES emission phase function observations: Optical depths, particle sizes, and ice cloud types versus latitude and solar longitude. *Journal of Geophysical Research (Planets)*, 108:5098, September 2003.
- [18] J. B. Pollack, M. E. Ockert-Bell, and M. K. Shepard. Viking Lander image analysis of Martian atmospheric dust. *J. Geophys. Res.*, 100:5235–5250, March 1995.
- [19] M. T. Lemmon, M. J. Wolff, M. D. Smith, R. T. Clancy, D. Banfield, G. A. Landis, A. Ghosh, P. H. Smith, N. Spanovich, B. Whitney, P. Whelley, R. Greeley, S. Thompson, J. F. Bell, and S. W. Squyres. Atmospheric Imaging Results from the Mars Exploration Rovers: Spirit and Opportunity. *Science*, 306:1753–1756, December 2004.
- [20] O. Muñoz, F. Moreno, D. Guirado, J. L. Ramos, A. López, F. Girela, J. M. Jerónimo, L. P. Costillo, and I. Bustamante. Experimental determination of scattering matrices of dust particles at visible wavelengths: The IAA light scattering apparatus. *J. Quant. Spec. Radiat. Transf.*, 111:187–196, January 2010.
- [21] R. Sullivan, R. Arvidson, J. F. Bell, R. Gellert, M. Golombek, R. Greeley, K. Herkenhoff, J. Johnson, S. Thompson, P. Whelley, and J. Wray. Wind-driven particle mobility on Mars: Insights from Mars Exploration Rover observations at “El Dorado” and surroundings at Gusev Crater. *Journal of Geophysical Research (Planets)*, 113:6, June 2008.
- [22] F. Poulet, C. Gomez, J.-P. Bibring, Y. Langevin, B. Gondet, P. Pinet, G. Belluci, and J. Mustard. Martian surface mineralogy from Observatoire pour la Minéralogie, l’Eau, les Glaces et l’Activité on board the Mars Express spacecraft (OMEGA/MEEx): Global mineral maps. *Journal of Geophysical Research (Planets)*, 112:8, July 2007.
- [23] A. S. Yen, R. Gellert, B. C. Clark, D. W. Ming, P. L. King, M. E. Schmidt, L. A. Leshin, R. V. Morris, S. W. Squyres, J. Spray, and J. L. Campbell. Evidence for a Global Martian Soil Composition Extends to Gale Crater. In *Lunar and Planetary Science Conference*, volume 44 of *Lunar and Planetary Science Conference*, page 2495, March 2013.
- [24] W. V. Boynton, D. W. Ming, B. Sutter, R. E. Arvidson, J. Hoffman, P. B. Niles, P. Smith, and Phoenix Science Team. Evidence for Calcium Carbonate at the Phoenix Landing Site. In *Lunar and Planetary Science Conference*, volume 40 of *Lunar and Planetary Science Conference*, page 2434, March 2009.
- [25] M. E. Ockert-Bell, J. F. Bell, J. B. Pollack, C. P. McKay, and F. Forget. Absorption and scattering properties of the Martian dust in the solar wavelengths. *J. Geophys. Res.*, 102:9039–9050, April 1997.
- [26] M. J. Wolff, M. D. Smith, R. T. Clancy, R. Arvidson, M. Kahre, F. Seelos, S. Murchie, and H. Savijärvi. Wavelength dependence of dust aerosol single scattering albedo as observed by the Compact Reconnaissance Imaging Spectrometer. *Journal of Geophysical Research (Planets)*, 114:0, June 2009.
- [27] Z. M. Dlugach, O. I. Korablev, A. V. Morozhenko, V. I. Moroz, E. V. Petrova, and A. V. Rodin. Physical Properties of Dust in the Martian Atmosphere: Analysis of Contradictions and Possible Ways of Their Resolution. *Solar System Research*, 37:1–19, January 2003.
- [28] M. J. Wolff and R. T. Clancy. Constraints on the size of Martian aerosols from Thermal Emission Spectrometer observations. *Journal of Geophysical Research (Planets)*, 108:5097, September 2003.
- [29] P. Rannou, S. Perrier, J.-L. Bertaux, F. Montmessin, O. Korablev, and A. Réberac. Dust and cloud detection at the Mars limb with UV scattered sunlight with SPICAM. *Journal of Geophysical Research (Planets)*, 111:9, September 2006.
- [30] W. J. Markiewicz, R. M. Sablotny, H. U. Keller, N. Thomas, D. Titov, and P. H. Smith. Optical properties of the Martian aerosols as derived from Imager for Mars Pathfinder midday sky brightness data. *J. Geophys. Res.*, 104:9009–9018, April 1999.
- [31] O. B. Toon, J. B. Pollack, and C. Sagan. Physical properties of the particles composing the Martian dust storm of 1971-1972. *Icarus*, 30:663–696, April 1977.
- [32] J. Crisp and M. J. Bartholomew. Mid-infrared spectroscopy of Pahala ash palagonite and implications for remote sensing studies of Mars. *J. Geophys. Res.*, 97:14691, September 1992.
- [33] J. F. Bell, R. V. Morris, and J. B. Adams. Thermally altered palagonitic tephra - A spectral and process analog to the soil and dust of Mars. *J. Geophys. Res.*, 98:3373–3385, February 1993.

- [34] T. L. Roush and J. B. Orenberg. Estimated detectability limits of iron-substituted montmorillonite clay on Mars from thermal emission spectra of clay-palagonite physical mixtures. *J. Geophys. Res.*, 101:26111–26118, 1996.
- [35] A. Banin. The soils of Mars. In M. J. Drake, R. Greeley, G. A. McKay, D. P. Blanchard, M. H. Carr, J. Gooding, C. P. McKay, P. D. Spudis, and S. W. Squyres, editors, *Mars Sample Return Science*, pages 35–36, 1988.
- [36] A. Banin, L. Margulies, T. Ben-Shlomo, G. C. Carle, L. M. Coyne, J. B. Orenberg, and T. W. Scattergood. Constraining Mars Soil Mineralogical Composition: Palagonite vs. Iron Enriched Smectite Clays. In *Lunar and Planetary Science Conference*, volume 19 of *Lunar and Planetary Science Conference*, page 27, March 1988.
- [37] A. Banin, G. C. Carle, S. Chang, L. M. Coyne, J. B. Orenberg, and T. W. Scattergood. Laboratory investigations of mars: Chemical and spectroscopic characteristics of a suite of clays as Mars Soil Analogs. *Origins of Life*, 18:239–265, September 1988.
- [38] J. Orenberg and J. Handy. Reflectance spectroscopy of palagonite and iron-rich montmorillonite clay mixtures - Implications for the surface composition of Mars. *Icarus*, 96:219–225, April 1992.
- [39] C. C. Allen, R. V. Morris, K. M. Jager, D. C. Golden, D. J. Lindstrom, M. M. Lindstrom, and J. P. Lockwood. Martian Regolith Simulant JSC Mars-1. In *Lunar and Planetary Science Conference*, volume 29 of *Lunar and Planetary Science Conference*, page 1690, March 1998.
- [40] C. C. Allen, R. V. Morris, D. J. Lindstrom, M. M. Lindstrom, and J. P. Lockwood. JSC Mars-1 - Martian regolith simulant. In *Lunar and Planetary Science Conference*, volume 28 of *Lunar and Planetary Science Conference*, page 27, March 1997.
- [41] M. C. Booth and H. H. Kieffer. Carbonate formation in Marslike environments. *J. Geophys. Res.*, 83:1809–1815, April 1978.
- [42] J. L. Gooding. Chemical weathering on Mars - Thermodynamic stabilities of primary minerals /and their alteration products/ from mafic igneous rocks. *Icarus*, 33:483–513, March 1978.
- [43] V. Orofino, A. Blanco, S. Fonti, R. Proce, and A. Rotundi. The infrared optical constants of limestone particles and implications for the search of carbonates on Mars. *Planetary and Space Science*, 46:1659–1669, December 1998.
- [44] D. D. Dabrowska, O. Muñoz, F. Moreno, T. Nousiainen, E. Zubko, and A. C. Marra. Experimental and simulated scattering matrices of small calcite particles at 647nm. *J. Quant. Spec. Radiat. Transf.*, 124:62–78, July 2013.
- [45] J. Dorschner, B. Begemann, T. Henning, C. Jaeger, and H. Mutschke. Steps toward interstellar silicate mineralogy. II. Study of Mg-Fe-silicate glasses of variable composition. *A&A*, 300:503, August 1995.
- [46] G. Ghosh. Dispersion-equation coefficients for the refractive index and birefringence of calcite and quartz crystals. *Optics Communications*, 163:95–102, May 1999.
- [47] H. Volten, O. Munoz, J. W. Hovenier, J. F. de Haan, W. Vassen, W. J. van der Zande, and L. B. F. M. Waters. WWW scattering matrix database for small mineral particles at 441.6 and 632.8nm. *J. Quant. Spec. Radiat. Transf.*, 90:191–206, January 2005.
- [48] J. E. Hansen and L. D. Travis. Light scattering in planetary atmospheres. *Space Science Reviews*, 16:527–610, October 1974.
- [49] J. B. Pollack, O. B. Toon, and B. N. Khare. Optical properties of some terrestrial rocks and glasses. *Icarus*, 19:372–389, July 1973.
- [50] R. T. Clancy, S. W. Lee, G. R. Gladstone, W. W. McMillan, and T. Rousch. A new model for Mars atmospheric dust based upon analysis of ultraviolet through infrared observations from Mariner 9, Viking, and PHOBOS. *J. Geophys. Res.*, 100:5251–5263, March 1995.
- [51] E. C. Laan, H. Volten, D. M. Stam, O. Muñoz, J. W. Hovenier, and T. L. Roush. Scattering matrices and expansion coefficients of martian analogue palagonite particles. *Icarus*, 199:219–230, January 2009.
- [52] I. N. Sokolik and O. B. Toon. Incorporation of mineralogical composition into models of the radiative properties of mineral aerosol from UV to IR wavelengths. *J. Geophys. Res.*, 104:9423–9444, April 1999.

- [53] J. W. Hovenier. *Measuring Scattering Matrices of Small Particles at Optical Wavelengths*, page 355. *Light Scattering by Nonspherical Particles : Theory, Measurements, and Applications*, January 2000.
- [54] O. Muñoz, F. Moreno, D. Guirado, J. L. Ramos, H. Volten, and J. W. Hovenier. The IAA cosmic dust laboratory: Experimental scattering matrices of clay particles. *Icarus*, 211:894–900, January 2011.
- [55] J. W. Hovenier, H. C. van de Hulst, and C. V. M. van der Mee. Conditions for the elements of the scattering matrix. *A&A*, 157:301–310, March 1986.
- [56] H. C. van de Hulst. *Light scattering by small particles*. New York: Dover, 1981, 1981.
- [57] O. Muñoz, H. Volten, J. F. de Haan, W. Vassen, and J. W. Hovenier. Experimental determination of scattering matrices of olivine and Allende meteorite particles. *A&A*, 360:777–788, August 2000.
- [58] O. Muñoz, F. Moreno, D. Guirado, D. D. Dabrowska, H. Volten, and J. W. Hovenier. The Amsterdam–Granada Light Scattering Database. *J. Quant. Spec. Radiat. Transf.*, 113:565–574, February 2012.
- [59] E. Zubko, G. Videen, Y. Shkuratov, K. Muinonen, and T. Yamamoto. The Umov effect for single irregularly shaped particles with sizes comparable with wavelength. *Icarus*, 212:403–415, March 2011.
- [60] H. Volten, O. Muñoz, E. Rol, J. F. de Haan, W. Vassen, J. W. Hovenier, K. Muinonen, and T. Nousiainen. Scattering matrices of mineral aerosol particles at 441.6 nm and 632.8 nm. *J. Geophys. Res.*, 106:17375–17402, August 2001.
- [61] O. Muñoz, H. Volten, J. W. Hovenier, B. Veihelmann, W. J. van der Zande, L. B. F. M. Waters, and W. I. Rose. Scattering matrices of volcanic ash particles of Mount St. Helens, Redoubt, and Mount Spurr Volcanoes. *Journal of Geophysical Research (Atmospheres)*, 109:16201, August 2004.
- [62] S. Ebisawa and A. Dollfus. Dust in the Martian Atmosphere: Polarimetric Sensing. *A&A*, 272:671–686, May 1993.
- [63] H. Volten, O. Muñoz, J. W. Hovenier, and L. B. F. M. Waters. An update of the Amsterdam Light Scattering Database. *J. Quant. Spec. Radiat. Transf.*, 100:437–443, July 2006.
- [64] L. Liu, M. I. Mishchenko, J. W. Hovenier, H. Volten, and O. Muñoz. Scattering matrix of quartz aerosols: comparison and synthesis of laboratory and Lorenz-Mie results. *J. Quant. Spec. Radiat. Transf.*, 79:911–920, 2003.
- [65] J. W. Hovenier and C. V. M. van der Mee. *Basic Relationships for Matrices Describing Scattering by Small Particles*, page 61. *Light Scattering by Nonspherical Particles : Theory, Measurements, and Applications*, January 2000.
- [66] J. W. Hovenier and D. Guirado. Zero slopes of the scattering function and scattering matrix for strict forward and backward scattering by mirror symmetric collections of randomly oriented particles. *J. Quant. Spec. Radiat. Transf.*, 133:596–602, January 2014.
- [67] V. Kaydash, Y. Shkuratov, M. Wolff, and G. Videen. *Polarimetry of terrestrial planets*. Polarization of stars and Planetary Systems (in press), 2014.
- [68] Y. Shkuratov, M. Kreslavsky, V. Kaydash, G. Videen, J. Bell, M. Wolff, M. Hubbard, K. Noll, and A. Lubenow. Hubble Space Telescope imaging polarimetry of Mars during the 2003 opposition. *Icarus*, 176:1–11, July 2005.
- [69] A. Dollfus, S. Ebisawa, and E. Bowell. Polarimetric analysis of the Martian dust storms and clouds in 1971. *A&A*, 131:123–136, February 1984.
- [70] A. Dollfus, E. Bowell, and S. Ebisawa. The Martian dust storms of 1973 - A polarimetric analysis. *A&A*, 134:343–353, May 1984.
- [71] Y. Shkuratov, A. Ovcharenko, E. Zubko, H. Volten, O. Munoz, and G. Videen. The negative polarization of light scattered from particulate surfaces and of independently scattering particles. *J. Quant. Spec. Radiat. Transf.*, 88:267–284, September 2004.
- [72] Y. Shkuratov, S. Bondarenko, V. Kaydash, G. Videen, O. Muñoz, and H. Volten. Photometry and polarimetry of particulate surfaces and aerosol particles over a wide range of phase angles. *J. Quant. Spec. Radiat. Transf.*, 106:487–508, July 2007.

- 
- [73] M. J. Wolff, M. D. Smith, R. T. Clancy, N. Spanovich, B. A. Whitney, M. T. Lemmon, J. L. Bandfield, D. Banfield, A. Ghosh, G. Landis, P. R. Christensen, J. F. Bell, and S. W. Squyres. Constraints on dust aerosols from the Mars Exploration Rovers using MGS overflights and Mini-TES. *Journal of Geophysical Research (Planets)*, 111:12, December 2006.
- [74] E. V. Petrova. Mars aerosol optical thickness retrieved from measurements of the polarization inversion angle and the shape of dust particles. *J. Quant. Spec. Radiat. Transf.*, 63:667–676, December 1999.
- [75] S. Merikallio, T. Nousiainen, M. Kahnert, and A.-M. Harri. Light scattering by the Martian dust analog, palagonite, modeled with ellipsoids. *Optics Express*, 21:17972–17985, July 2013.
- [76] K. M. Pitman, M. J. Wolff, and E. A. Cloutis. Building More Realistic Grain Shapes in Radiative Transfer Models of Mars Regolith. In *Lunar and Planetary Science Conference*, volume 45 of *Lunar and Planetary Science Conference*, page 2627, March 2014.
- [77] E. Zubko, K. Muinonen, O. Muñoz, T. Nousiainen, Y. Shkuratov, W. Sun, and G. Videen. Light scattering by feldspar particles: Comparison of model agglomerate debris particles with laboratory samples. *J. Quant. Spec. Radiat. Transf.*, 131:175–187, December 2013.



## ”The effect of the orientation of the optic axis on simulated scattering matrix elements of small birefringent particles”

D.D. Dabrowska, O.Muñoz, F.Moreno, T. Nousiainen, E. Zubko, *Effect of the orientation of the optic axis on simulated scattering matrix elements of small birefringent particles*, OPTICS LETTERS, **35**, No. 14 (2012), 3252-3254

**Abstract** We study how the orientation of the optic axis affects single scattering properties for small, birefringent calcite particles simulated using DDSCAT 7.1.1. We consider two irregular model particles, a flake and a rhomboid, either in a (i) fixed or (ii) random orientation. Simulations are performed for three volume-equivalent radii of  $0.1 \mu\text{m}$ ,  $0.45 \mu\text{m}$  and  $1.0 \mu\text{m}$ . For each target, we repeat the computations for three sets of orientations of the optic axis. When a fixed spatial orientation of the target is considered, the simulations are significantly affected by the orientation of the optic axis. However, the effect is considerably weaker when assuming the same targets in random spatial orientation.

The study of light scattering by small irregular dielectric particles is of interest for different scientific disciplines. For example, the Earth's radiation budget is significantly affected by scattering of solar radiation by cloud and aerosol particles. Mineral dust is one of most important aerosol types in the Earth's atmosphere [1]. Some of those mineral dust particles are composed of strongly birefringent materials [2]. Moreover, small airborne particles can be absorbed by human pulmonary airways causing some diseases such as talcosis or silicosis. Birefringent particles visualized under a polarized light microscope lead to a proper diagnosis of these and, for example, some skin diseases (e.g. [3]).

In addition to their birefringent composition, small dust particles present quite complex shapes, making the numerical light-scattering simulations a challenging task. To properly account for the birefringence in the simulations, one has to replace the complex refractive index by a dielectric tensor, and second, establish the orientation of the optic axis (or axes) relative to the particle. The latter is straightforward for regular crystals and other shapes where specific crystal faces can be readily identified, but anything but for irregular particles without well-defined faces. In this paper we focus on studying whether the orientation of the optic axis actually has a significant impact on the computed scattering matrix elements for irregularly shaped particles. As examples, we consider irregular calcite particles.

Calcite is a strongly birefringent material, that can be found as a component of desert dust [4] and Mars surface [5]. It belongs to a trigonal system of crystal symmetries and thus has a single optic axis [6]. For such particles, waves propagating parallel to the optic axis are subject to an extraordinary refractive index, whereas, waves traveling normal to the optic axis experience an ordinary refractive index.

The single-scattering simulations have been carried out using DDSCAT 7.1.1, developed by Draine and Flatau [7, 8], which is an implementation of the Discrete Dipole Approximation. The model computes scattering and absorption of electromagnetic waves for targets with arbitrary geometries, discretized to a set of evenly spaced volume elements or dipoles, and allows them to be composed of birefringent materials. When computing light scattering by birefringent targets, one needs to establish both the orientation of the target, and the orientation of the optic axis relative to the target. In DDSCAT, both of these are described by a set of three Euler rotation angles. One set specifies the relation of the target coordinate system (target frame; TF) and the scattering coordinate system (laboratory frame; LF), and the other the relation of the target frame and a coordinate system where the dielectric tensor is diagonal (dielectric frame; DF).

As was mentioned, airborne particles often present quite complex morphologies. For example, calcite particles can have flake- and rhomboidal-like shapes [2, 9]. For our computations, one irregular flake and one irregular rhomboid are generated with approximately 50.000 and 100.000 dipoles, respectively (Fig.5.1). An oblate spheroid is used as a initial shape for the flake. The generation process is described in detail by [2]. The irregular rhomboid is generated similarly, starting with an ideal rhomboid. Then, seed cells of calcite and void, respectively, are randomly located close to the surface of the rhomboid, and all the surface cells turned either into void or calcite, depending on which type of seed cell is the closest.

In our computations the wavelength is fixed at 647 nm, where the real parts of the ordinary and extraordinary refractive indices are 1.655 and 1.485, respectively [10]. The imaginary part of the refractive index,  $k$ , is assumed to be zero since pure calcite is practically non-absorbing in the visible.

There are some indications of preferentially oriented dust particles in the atmosphere of the Earth [11]. Consequently, we first consider our particles in a fixed spatial orientation, defined as  $lf_1$  in Table 5.1. For both shapes, we consider three different particle sizes,  $r = 0.1 \mu\text{m}$ ,  $0.45 \mu\text{m}$  and  $1.00 \mu\text{m}$ , where  $r$  is the radius of the equal-volume sphere. The computations are performed for three different orientations for the dielectric frame, specified by the rotation angles  $\theta_{DF}$ ,  $\phi_{DF}$  and  $\beta_{DF}$  as given in Table 5.2. The second one,  $df_2$ , actually corresponds to the real orientation of the optic axis for the flake [2]. For simplicity, in Figs. 5.2, and 5.3, we only present results for  $r = 1.0 \mu\text{m}$  flake and rhomboid, respectively. All  $F_{11}(\theta)$  functions are plotted on a logarithmic scale. The other elements are shown relative to the corresponding  $F_{11}(\theta)$ . It is clear from the figures that all scattering matrix elements are significantly affected by the orientation of DF. In

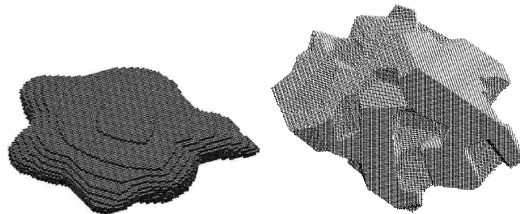


Figure 5.1: Computer-generated particle shapes considered. An irregular flake (left; approx. 50.000 dipoles), and an irregular rhomboid (right; approx. 100.000 dipoles).

Table 5.1: Spatial orientation of the particles with respect to the laboratory frame LF;  $lf_1$ ,  $lf_2$ ,  $lf_3$ , used in our computations.

	$\beta_{LF} [^\circ]$	$\theta_{LF} [^\circ]$	$\phi_{LF} [^\circ]$
$lf_1$	45	31.4	45
$lf_2$	135	69.3	135
$lf_3$	270	120	270

addition, the effect is stronger for the flake than for the rhomboid. This is most likely to be due to the large aspect ratio of the flake which, together with the rotation of the optic axis, allows different refractive indices for short and long propagation paths through the particle. Indeed, additional tests with rectangular prisms of varying aspect ratios show that the effect increases with increasing aspect ratio. While confirming our hypothesis, it is nevertheless noted that contributions of other geometrical factors cannot be ruled out. To check whether the results also depend on the orientation of the particle, the computations are repeated for two additional spatial orientations ( $lf_2$ ,  $lf_3$ , see Table 1). All computed scattering matrices (not shown here) are significantly affected by the orientation of the DF showing a different dependence for each LF. For both studied shapes, the effect of the orientation of the optic axis on the scattering matrix elements becomes weaker when the size of the particles is decreased.

In many applications, particles are generally assumed to be randomly oriented (e.g.[1] and references therein). To simulate this, we compute the scattering matrix of our target particles in many different orientations (varying  $\beta_{LF}$ ,  $\theta_{LF}$  and  $\phi_{LF}$  rotations in DDSCAT) and average over them. We have verified that 512 different orientations provide an accurate convergence for the orientation average for 0.1- $\mu\text{m}$  radius particles, while 1485 orientations are needed for 1- $\mu\text{m}$  radius particles. Again, for simplicity, in Fig. 5.4 we only show the computed results for 1- $\mu\text{m}$  radius flake and rhomboid. As is seen, the scattering matrix depends much less on the orientation of the optic axis when averaging over spatial orientations. This is because the effect of rotating the optic axis can be small or large, or even negative at different scattering angles and in different matrix elements for fixed spatial orientations. The averaging thus largely reduces the impact, and indeed, the computed phase functions,  $F_{11}(\theta)$ , and  $F_{12}(\theta)/F_{11}(\theta)$  ratio, for  $df_1$ ,  $df_2$ , and  $df_3$ , are nearly on top of each other for both model particles. Somewhat stronger effects are found for the  $F_{22}(\theta)/F_{11}(\theta)$ , and  $F_{44}(\theta)/F_{11}(\theta)$  ratios. Similar to our findings with fixed orientations, the computed scattering matrix element ratios seem more sensitive to the orientation of the optic axis for the flake than for the rhomboid.

In summary, we have studied how the orientation of the optic axis affects the computed scattering matrix elements of small calcite particles. The computations have been carried out for three different sizes and two model particles (irregular flake and rhomboid). Our simulations demonstrate that when our model particles are in a fixed spatial orientation, the computed scattering matrix elements are significantly affected by the choice of the orientation of the optic axis. In contrast, when averaging over particle orientations, the effect is significantly reduced. The effect appears to be stronger for strongly elongated particles as compared to nearly equi-

Table 5.2: Orientations of the optic axis in the dielectric frame DF;  $df_1$ ,  $df_2$ ,  $df_3$ , used in our computations.

	$\beta_{DF} [^\circ]$	$\theta_{DF} [^\circ]$	$\phi_{DF} [^\circ]$
$df_1$	30	60	30
$df_2$	44.6	0.0	0.0
$df_3$	30	60	0.0

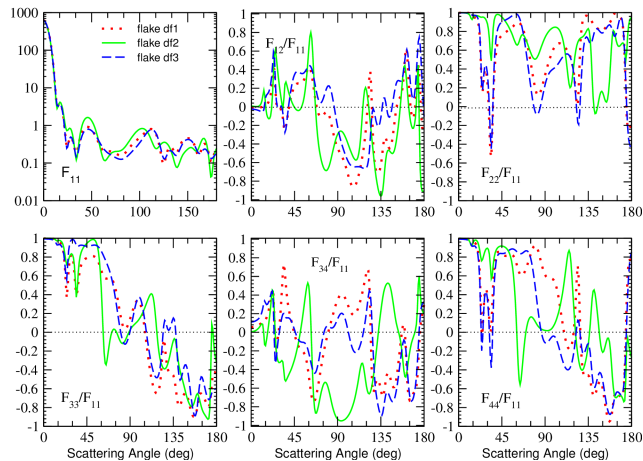


Figure 5.2: Computed scattering matrix elements as a function of the scattering angle ( $\theta$ ) for an irregular  $1\text{-}\mu\text{m}$  radius calcite flake in the fixed spatial orientation  $lf_1$  (Table 5.1) and different dielectric frame orientations labeled as  $df_1$ ,  $df_2$  and  $df_3$  (Table 5.2). The computations are performed at  $647\text{ nm}$ . Different colors refer to different DF orientations.

dimensional particles. Finally, the effect is weaker for smaller particles. It is expected that the effects would be further reduced by averaging over an ensemble of shapes. Therefore, in many applications, it may not be necessary to correctly orient the optic axis to obtain reasonable light-scattering results for birefringent particles. This is good news, because for many real particles the correct orientation of the optic axis would be difficult to establish due to the lack of easily identifiable crystal faces.

This work has been supported by the Plan Nacional de Astronomía y Astrofísica under contract AYA2009-08190, and Junta de Andalucía, contract P09-FMQ-4555, the Academy of Finland (contracts 125180 and 127461) and NASA program for Outer Planets Research (grant NNX10AP93G). We are grateful to anonymous referees for their constructive remarks.

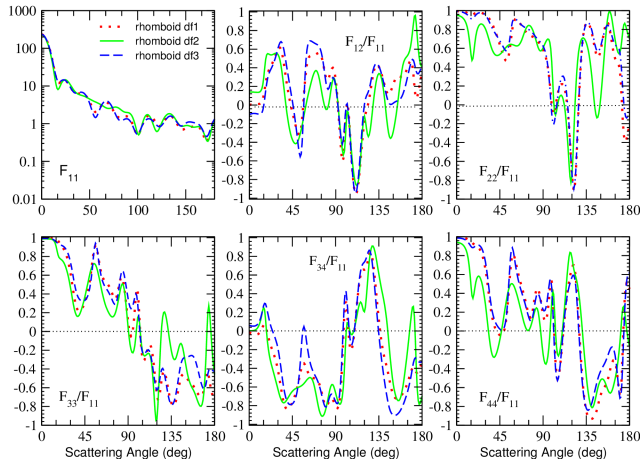


Figure 5.3: As Fig. 5.2 but for an irregular  $1\text{-}\mu\text{m}$  radius calcite rhomboid.

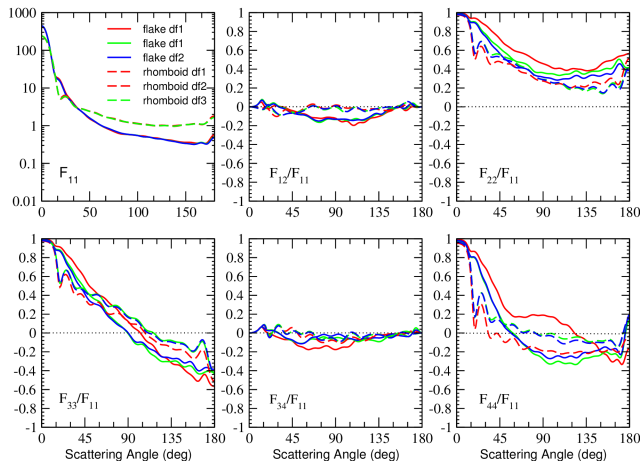


Figure 5.4: Computed orientation-averaged scattering matrix elements as functions of the scattering angle ( $\theta$ ) for irregular  $1\text{-}\mu\text{m}$  calcite flake (solid lines) and rhomboid (dashed lines). 1485 spatial orientations have been used, and the computations are performed at 647 nm wavelength. Different colors refer to DF orientations  $df_1$ ,  $df_2$  and  $df_3$  (see Table 5.2).

# Bibliography

- [1] M. I. Mishchenko, L. D. Travis, and A. Macke. Light Scattering by Nonspherical Particles : Theory, Measurements, and Applications, January 2000.
- [2] T. Nousiainen, E. Zubko, J. V. Niemi, K. Kupiainen, M. Lehtinen, K. Muinonen, and G. Videen. Single-scattering modeling of thin, birefringent mineral-dust flakes using the discrete-dipole approximation. *Journal of Geophysical Research (Atmospheres)*, 114:7207, April 2009.
- [3] E. Marchiori, S. Lourenço, F. Davaus Gasperetto, G. Zanetti, C. Mauro Mano, and L. F. Nobre. Pulmonary Talcosis: Imaging Findings. *Lung*, 188:165–171, 2010.
- [4] T. Claquin, M. Schulz, and Y. J. Balkanski. Modeling the mineralogy of atmospheric dust sources. *J. Geophys. Res.*, 104:22243, September 1999.
- [5] V. Orofino, A. Blanco, S. Fonti, R. Proce, and A. Rotundi. The infrared optical constants of limestone particles and implications for the search of carbonates on Mars. *Planetary and Space Science*, 46:1659–1669, December 1998.
- [6] D. McKie and C. McKie. *Crystalline solids*. 1974.
- [7] B. T. Draine and P. J. Flatau. User Guide for the Discrete Dipole Approximation Code DDSCAT 7.1. *ArXiv e-prints*, February 2010.
- [8] B. T. Draine and P. J. Flatau. Discrete-dipole approximation for scattering calculations. *Journal of the Optical Society of America A*, 11:1491–1499, April 1994.
- [9] D. D. Dabrowska, O. Munoz, T. Nousiainen, E. Zubko, and A. C Marra. Scattering matrix measurements and light-scattering calculations of calcite particles. *Atti della Accademia Peloritana dei Pericolanti. Classe di Scienze Fisiche, Matematiche e Naturali, vol. 89, Suppl No 1, p. C1V89S1P024-1 - C1V89S1P024-5*, 89:67–1, September 2011.
- [10] G. Ghosh. Dispersion-equation coefficients for the refractive index and birefringence of calcite and quartz crystals. *Optics Communications*, 163:95–102, May 1999.
- [11] Z. Ulanowski, J. Bailey, P. W. Lucas, J. H. Hough, and E. Hirst. Alignment of atmospheric mineral dust due to electric field. *Atmospheric Chemistry & Physics*, 7:6161–6173, December 2007.

## ” Experimental and simulated scattering matrices of small calcite particles at 647 nm”

D.D. Dabrowska, O.Muñoz, F.Moreno, T. Nousiainen, E. Zubko, A.C. Marra, *Experimental and simulated scattering matrices of small calcite particles at 647 nm*, Journal of Quantitative Spectroscopy & Radiative Transfer, **124**, (2013), 62-78

**Abstract** We present measurements of the complete scattering matrix as a function of the scattering angle of a sample of calcite particles. The measurements are performed at 647 nm in the scattering angle range from  $3^\circ$  to  $177^\circ$ . To facilitate the use of the experimental data we present a synthetic scattering matrix based on the measurements and defined in the full range from  $0^\circ$  to  $180^\circ$ . The scattering matrix of the calcite sample is modeled using the discrete-dipole approximation. Two sets of shapes, flake-like and rhomboid-like particles giving a total of 15 different targets are considered since both type of shapes have been found in our calcite sample. In our computations we use the measured size distribution of the calcite sample truncated at 1.2 micrometers. We present a theoretical study of the impact of birefringence on the computed scattering matrix elements for both sets of shapes. Four different cases regarding the composition of the calcite particles are considered: two isotropic cases corresponding to the ordinary and extraordinary refractive index of calcite, respectively; one equivalent isotropic case analogous to internal mixing; and birefringence fully accounted for. Numerical simulations are compared with the experimental data. We find that birefringence has little impact on the calculated phase functions but it has a significant effect on the polarization-related elements of the scattering matrix. Moreover, we conclude that the shape of the targets (flakes or irregular rhomboids) has a much stronger effect on the computed scattering matrix elements than birefringence.

## 6.1 Introduction

The study of light scattering by small particles is of interest for different scientific disciplines, from medicine to astrophysics. Dust grains exist in a wide variety of cosmic environments ranging from the diffuse interstellar medium, molecular clouds, and disks around new stellar objects [1, 2, 3], to cometary [4] and planetary atmospheres (e.g. [5, 6, 7]). Those dust particles play an important role in the radiative balance and dynamics of the atmosphere. Moreover, small particles can be absorbed by human pulmonary airways causing some diseases such as talcosis or silicosis [8].

In this paper we present measurements of the complete scattering matrix as a function of the scattering angle of a calcite sample. The measurements are performed in the  $3^\circ$  to  $177^\circ$  scattering angle range at the wavelength of 647 nm. The lack of experimental data at very small and very large scattering angles [ $0^\circ - 3^\circ$ ], and [ $177^\circ - 180^\circ$ ] limits the use of the experimental data. Therefore, we also present the extrapolated scattering matrix that is defined in the entire angle range from  $0^\circ$  to  $180^\circ$  [9]. The extrapolation of the phase function is performed using the procedure suggested by Liu et al. [10] and subsequently adopted by e.g. Kahnert and Nousiainen [11] and Muñoz et al. [9].

Although calcite is not a major component of the Martian surface, it is commonly considered to be particularly important for its link with climate evolution and water resources on Mars [12, 13]. Moreover, calcite is also found in the Earth's atmosphere. Desert dust is rich in calcite [14, 15], the Saharan desert being one of the main sources of mineral dust in our atmosphere [6].

In addition to its relevance for atmospheric applications, calcite is also very interesting from the light scattering modeling point of view due to its high birefringence. In this work we use the DDSCAT 7.1 code [16] to perform a theoretical study of the impact of birefringence on the computed scattering matrix elements. The computations are compared with the experimentally determined scattering matrix for the calcite sample. A detailed physical characterization of our sample is presented in Section 6.2. In Section 6.3, we describe the experimental apparatus used in this work together with the experimental scattering matrix of our calcite sample. Simulations of the scattering matrix elements as functions of the scattering angle are discussed in Section 6.4. Summary and conclusions are given in Section 6.5.

## 6.2 The Calcite Sample

### 6.2.1 Origin of the calcite sample and size distribution

The calcite sample is obtained from a limestone bulk sample collected near Lecce, Italy [17]. Limestone is a very abundant mineral on the Earth, calcite being its main component (98%). We ground the bulk limestone sample with an Agatha ball-miller to obtain fine powder. The size distribution of the resulting sample is measured using a Mastersizer 2000 from Malvern Instruments. The Mastersizer measures the phase function of the sample at 633 nm in a certain scattering-angle range with special attention to the forward-diffraction region. Subsequently, it uses either Lorenz-Mie or Fraunhofer diffraction theory to retrieve the volume distribution that best fits the measurements. It is important to note that the retrievals from both methods are simplifications based on the assumption that the particles are spherical (see [18]). Further studies are required to clarify which SD is more representative for our samples of irregular particles. Accordingly, we present the size distributions based on both Fraunhofer and Lorenz-Mie theories so that the reader can choose which one is more appropriate for his/her purposes or take the average.

In Fig. 6.1, we plot the number,  $n(r)$ , projected-surface-area  $S(\log r)$  and volume  $V(\log r)$  distributions for the calcite sample retrieved from both, the Fraunhofer and Lorenz-Mie theories. Here,  $r$  represents the radius of a sphere having the same volume as the particle (volume-equivalent sphere). The transformation equations to obtain  $n(r)$ ,  $S(\log r)$  and  $V(\log r)$  from the measured  $v(r)$  are given in the Amsterdam-Granada Light Scattering Database [http://www.iaa.es/scattering/site\\_media/sizedistributions.pdf](http://www.iaa.es/scattering/site_media/sizedistributions.pdf) (see also [19]). In the database



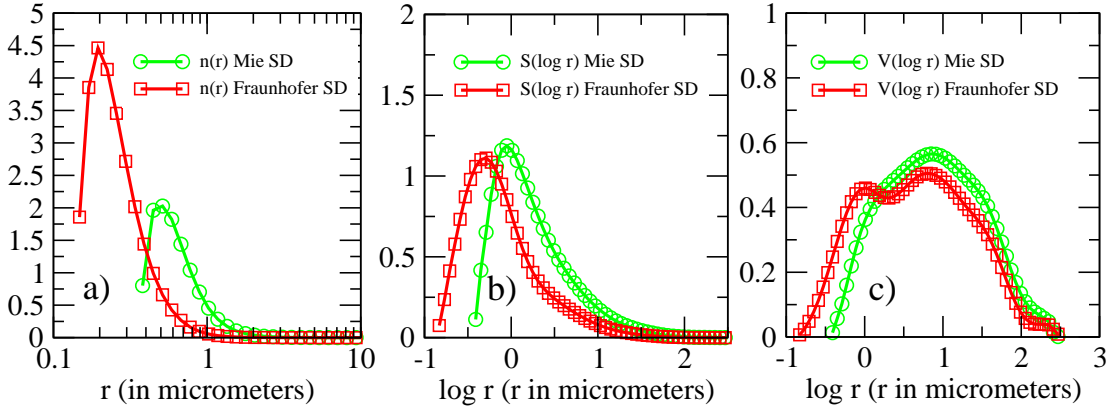


Figure 6.1: a) Normalized number, b) projected-surface-area and c) volume distributions of the calcite sample as a function of  $r$  and  $\log r$  as measured by a Mastersizer 2000 from Malvern Instruments, based on using either Fraunhofer and Lorenz-Mie theories.

[20] we present tables of  $N(\log r)$ ,  $S(\log r)$  and  $V(\log r)$ , as well as the corresponding  $n(r)$ ,  $s(r)$  and  $v(r)$  based on both the Fraunhofer and Lorenz-Mie theories. As can be seen from Fig. 6.1, the use of Lorenz-Mie theory in the size retrieval results in larger particle sizes than the Fraunhofer theory. This can be seen for  $V(\log r)$  and  $S(\log r)$ , but is especially pronounced in  $n(r)$ . Interestingly, the Fraunhofer retrieval results in a bimodal  $V(\log r)$ , the small-particle mode being less prominent in the Mie-based retrieval. This bi-modality may be an artifact. From the measured size distributions we also calculate the values of the effective radius  $r_{eff}$  and effective variance  $v_{eff}$  as defined by Hansen and Travis [21]:

$$r_{eff} = \frac{\int_0^\infty r \pi r^2 n(r) dr}{\int_0^\infty \pi r^2 n(r) dr} \quad (6.1)$$

$$v_{eff} = \frac{\int_0^\infty (r - r_{eff})^2 \pi r^2 n(r) dr}{r_{eff}^2 \int_0^\infty \pi r^2 n(r) dr}, \quad (6.2)$$

The resulting values for the calcite sample are presented in Table 6.1.

Table 6.1

Method	$r_{eff}$ ( $\mu\text{m}$ )	$v_{eff}$
Fraunhofer	1.7	7.6
Lorenz-Mie	3.3	4.9

Table 6.2: The effective radii  $r_{eff}$  and effective variances  $v_{eff}$  retrieved from the Fraunhofer and Lorenz-Mie size distributions.

## 6.2.2 Refractive Index

Calcite is an uni-axial birefringent material, so it has one optic axis and, instead of one refractive index, it has a dielectric tensor specified by two principal dielectric functions, the ordinary and extraordinary refractive indices. These refractive indices are dependent on the wavelength, the real part of the ordinary refractive index,  $n_o$  varying roughly between 1.57 and 1.47, while the extraordinary refractive index,  $n_e$ , varies between 1.88 and 1.62 in the 0.2–3.3  $\mu\text{m}$  wavelength range [22]. At the wavelength of the measurements and simulations, 647 nm,  $n_o = 1.655$  and

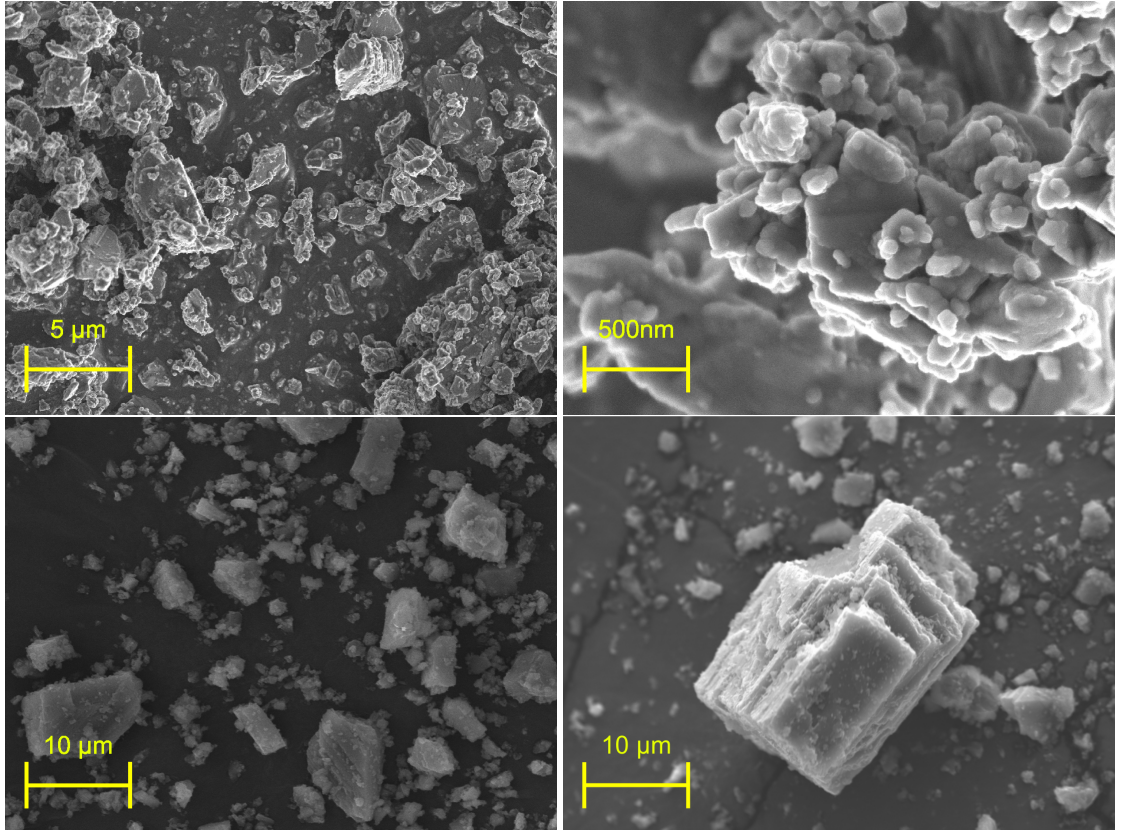


Figure 6.2: Top panels: FESEM images of the calcite sample. Bottom: SEM images of the calcite sample. The bars at the left bottom corners denote the scale of the images. Note that the scale bars differ among panels.

$n_e = 1.485$  [22]. The imaginary part of the refractive index,  $k$ , is assumed to be zero since pure calcite is very weakly absorbing in the visible.

### 6.2.3 Shapes

In Fig. 6.2, we show Field Emission Scanning Electron Microscope (FESEM; top panels), and Scanning Electron Microscope (SEM; bottom panels) images arbitrarily chosen to show the shape of our calcite particles. It should be noted that the microscope images are not necessarily representative of the size distribution (for that purpose, we refer the reader to Fig. 6.1). As mentioned, the original sample is ball-milled to produce smaller particles. After this artificial procedure, two kinds of shapes are found. In addition to the typical flake-like shapes of calcite particles, many rhomboidal structures are also present (Fig. 6.2, bottom panels). Both types of shapes have also been found in natural samples [15].

## 6.3 Experimental data

### 6.3.1 Experimental apparatus

The flux and state of polarization of a beam of quasi-monochromatic light can be described by means of a so-called flux vector. If such a beam of light is scattered by a sample of randomly oriented particles with equal amounts of particles and their mirror particles, the flux vectors of the incident beam,  $\pi\Phi_0$  and scattered beam,  $\pi\Phi_{\text{det}}$ , are related by the  $4\times 4$  scattering matrix,  $\mathbf{F}$ , for each scattering angle  $\theta$ , as follows [23, 24]:

$$\Phi_{\text{det}}(\lambda, \theta) = \frac{\lambda^2}{4\pi^2 D^2} \begin{pmatrix} F_{11} & F_{12} & 0 & 0 \\ F_{12} & F_{22} & 0 & 0 \\ 0 & 0 & F_{33} & F_{34} \\ 0 & 0 & -F_{34} & F_{44} \end{pmatrix} \Phi_{\mathbf{o}}(\lambda) \quad (6.3)$$

where the first elements of the column vectors are fluxes divided by  $\pi$  and the other elements describe the state of polarization of the beams by means of Stokes parameters. Furthermore,  $\lambda$  is the wavelength, and  $D$  is the distance from the sample to the detector. The matrix  $\mathbf{F}$  with elements  $F_{i,j}$  is called the scattering matrix of the sample and refers to light that has been scattered once. The elements of the scattering matrix are dimensionless and depend on the physical properties of the particles (size, shape, and refractive index), the number of the scattering particles that contribute to the detected radiation, the wavelength of the incident light, and the direction of the scattered light, which, for randomly oriented particles, is sufficiently described by means of the scattering angle  $\theta$ . The scattering angle,  $\theta$ , is defined by the directions of the incident and scattered light.

The scattering matrix of our sample of calcite particles is measured at the IAA COsmic DUst LABoratory (CODULAB) [25]. In Fig. 6.3, we present a photograph of the experimental apparatus. In our experiment we use an Argon-Krypton laser as a light source. It emits linearly polarized light at one of the five possible wavelengths, namely, 483 nm, 488 nm, 520 nm, 568 nm, and 647 nm. The light passes through a polarizer and an electro-optic modulator. The light is subsequently scattered by randomly oriented particles located in a jet stream produced by an aerosol generator, so no vessel is needed to contain the sample. This is a big advantage since any object containing the sample may cause undesirable reflections. Subsequently, the scattered light passes through a quarter wave plate, Q, and an analyzer, A, (both optional) and is detected by a photomultiplier tube which moves in steps along a ring around the ensemble of particles, the detector. In this way a range of scattering angles from  $3^\circ$  to  $177^\circ$  is covered in the measurements. All matrix elements (except  $F_{11}$  itself) are normalized to  $F_{11}$ , that is, we consider  $F_{ij}/F_{11}$ , with  $i, j=1$  to 4 with the exception of  $i = j = 1$ . Due to the lack of measurements between  $0^\circ$  and  $3^\circ$  and  $177^\circ$  and  $180^\circ$ , we cannot measure the absolute dependence of the  $F_{11}(\theta)$  element. Instead, we normalize the measured  $F_{11}(\theta)$  to 1 at 30 degrees. The function  $F_{11}(\theta)$ , normalized in this way, is called the phase function or scattering function in this paper. Another photomultiplier tube, the monitor, is located in a fixed position and is used to correct for fluctuations in the aerosol cloud. By using eight different combinations of the optical components and their orientations, and assuming the reciprocity of the sample (in particular  $F_{21} = F_{12}$ ,  $F_{31} = -F_{13}$  and  $F_{41} = F_{14}$ ), all scattering matrix elements are obtained as functions of the scattering angle [26]. A detailed description of the instrument is given by Muñoz et al. [25].

The reliability of the apparatus has been tested by comparing measured scattering matrices of spherical water droplets at 488 nm, 520 nm, and 647 nm with Lorenz-Mie computations [25]. Special tests have been performed to ensure that our experimental results are not significantly contaminated by multiple scattering [18]. In addition, we check that the measured scattering matrices fulfill the Cloude coherency matrix test [27] within the experimental errors at all measured scattering angles.

### 6.3.2 Experimental scattering matrix

In Fig. 6.4, we present the measured scattering matrix as a function of the scattering angle for our sample of randomly oriented calcite particles. The measurements have been performed in the scattering angle range  $3^\circ$ - $177^\circ$  at a wavelength of 647 nm. As mentioned in Section 6.3.1, all matrix elements (except  $F_{11}$  itself) are normalized to  $F_{11}$ . The scattering function or phase function,  $F_{11}(\theta)$ , is shown on a logarithmic scale and is normalized to 1 at  $30^\circ$ . Due to the limited amount of sample we avoid measuring the  $F_{32}(\theta)/F_{11}(\theta)$  and  $F_{42}(\theta)/F_{11}(\theta)$  ratios. As shown in Fig. 6.4, the measured  $F_{13}(\theta)/F_{11}(\theta)$ ,  $F_{14}(\theta)/F_{11}(\theta)$  and  $F_{24}(\theta)/F_{11}(\theta)$  are zero within the experimental errors in the full scattering angle range i.e., the measured scattering matrix

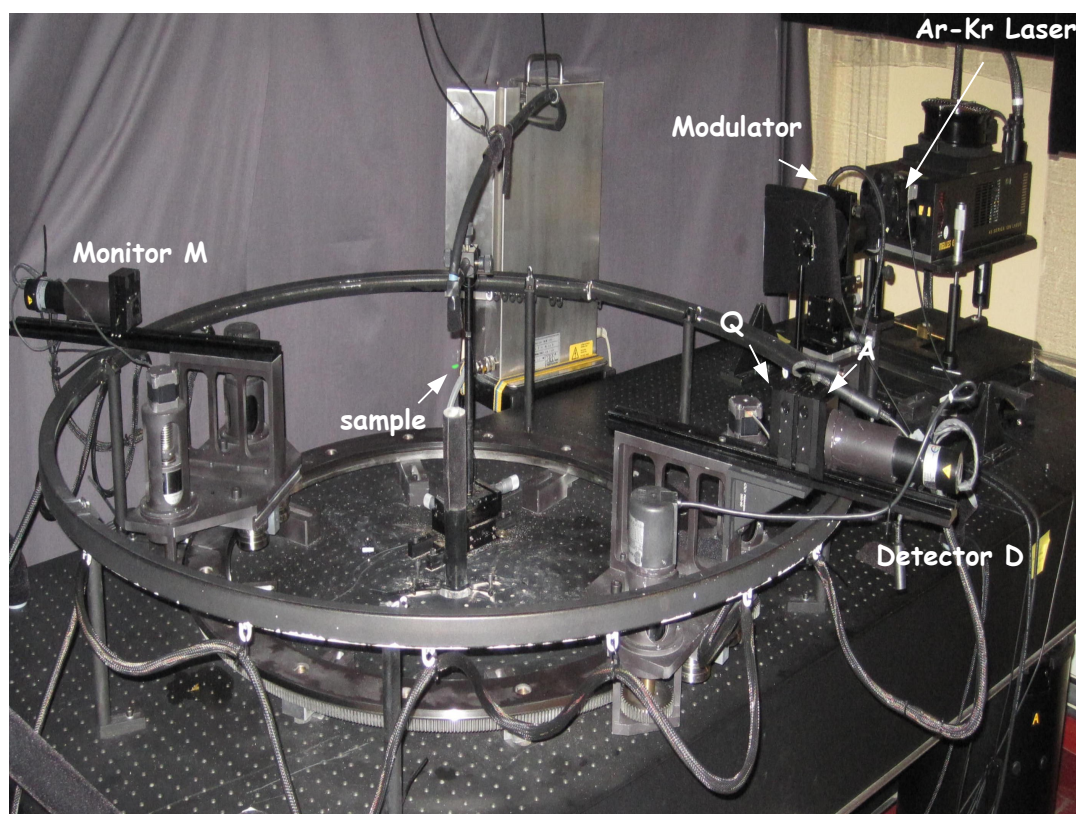


Figure 6.3: Photograph of the experimental apparatus. On the right we can see the detector that moves along the ring. The ring is placed horizontally in the laboratory with an outer diameter of 1 m. The monitor is located on the left. In the middle, we see the nozzle of the nebulizer located vertically in the center of the ring, and the green spot is where the laser beam interacts with the aerosol cloud.

has the form presented in Eq. (6.3). That is a good indication that the aerosol cloud during the measurements can be considered a macroscopically isotropic medium with mirror symmetry even though strictly speaking the assumption of mirror symmetry is not satisfied in a finite sample. In this case, the  $-F_{12}(\theta)/F_{11}(\theta)$  ratio is the degree of linear polarization for incident unpolarized light.

In general, the scattering matrix for the calcite sample looks very typical for irregularly shaped mineral particles. For example, the  $F_{11}(\theta)$  has a strong forward peak with almost no structure at side- and back- scattering angles. In addition, a slight increase at backward direction is present. The degree of linear polarization for unpolarized incident light,  $-F_{12}(\theta)/F_{11}(\theta)$ , shows a typical bell shape with a maximum of about 16% at  $100^\circ$  and a negative branch near back-scattering direction. Moreover, the  $F_{44}(\theta)/F_{11}(\theta)$  is larger than the  $F_{33}(\theta)/F_{11}(\theta)$  at side and back-scattering angles, whereas the  $F_{22}(\theta)/F_{11}(\theta)$  deviates from unity at nearly all measured scattering angles.

### 6.3.3 Synthetic Scattering Matrix for the calcite sample

As mentioned, the experimental data do not cover either the exact forward or the exact backward direction. Therefore, what we obtain is the relative phase function,  $F_{11}(\theta)/F_{11}(30^\circ)$  with (see [28]),

$$\frac{F_{11}(\theta)}{F_{11}(30^\circ)} = \frac{F_{11}^{au}(\theta)}{F_{11}^{au}(30^\circ)}, \quad (6.4)$$

where  $F_{11}^{au}(\theta)$  is the auxiliary phase function which is normalized so that its average over all directions equals unity, i.e.,

$$1/2 \int_0^\pi d\theta \sin\theta F_{11}^{au}(\theta) = 1. \quad (6.5)$$

To facilitate the use of the experimental data we construct a synthetic scattering matrix from our measurements that is defined in the full scattering angle range, from 0 to 180 degrees. The extrapolation of the phase function  $F_{11}(\theta)$  is based on the assumption that the forward diffraction peak for randomly oriented particles with moderate aspect ratios mainly depends on the size of the particles ([9], [10] and references therein). The procedure consists of scaling the measured phase function until its value at 3 degrees matches the Lorenz-Mie computations for the corresponding projected surface area equivalent spheres. For the Lorenz-Mie computations we use the measured size distribution retrieved from both Fraunhofer and Lorentz-Mie theories (Fig. 6.1) assuming the calcite particles to have a single effective refractive index  $m_{eff} = ((n_e^2 + n_o^2)/3)^{(1/2)} = 1.60$  corresponding to the internal mixing of  $n_e$  and  $n_o$ . The imaginary part of the refractive index is fixed to 0. This is a reasonable assumption, as birefringence does not significantly affect the forward scattering peak [15]. The scaled phase function was then extrapolated to 180 degrees assuming a smooth polynomial extrapolation. Once the scattering function is defined in the complete scattering angle range from 0 to 180 degrees, we check whether our extrapolated phase function fulfills Eq. (6.5). If this conditions is not met, the measured point at the overlap angle (in this case  $\theta = 3^\circ$ ) is iteratively adjusted until the normalization condition is satisfied.

For the other scattering matrix elements,  $F_{ij}(\theta)/F_{11}(\theta)$  (where  $i,j=1..4$ , and  $i \neq j \neq 1$ ), a polynomial extrapolation is used for both forward and backward directions, with the constraints at the exact forward and backward directions as given by Hovenier et al. [24]:

$$F_{12}(\theta)/F_{11}(\theta) = F_{34}(\theta)/F_{11}(\theta) = 0 \quad (\theta = 0^\circ, 180^\circ) \quad (6.6)$$

$$F_{22}(0^\circ)/F_{11}(0^\circ) = F_{33}(0^\circ)/F_{11}(0^\circ) \quad (6.7)$$

$$1 \geq |F_{22}(0^\circ)/F_{11}(0^\circ)| \quad (6.8)$$

$$1 \geq |F_{44}(0^\circ)/F_{11}(0^\circ)| \quad (6.9)$$

$$F_{44}(0^\circ)/F_{11}(0^\circ) \geq 2|F_{22}(0^\circ)/F_{11}(0^\circ)| - 1 \quad (6.10)$$

$$F_{22}(180^\circ)/F_{11}(180^\circ) = -F_{33}(180^\circ)/F_{11}(180^\circ) \quad (6.11)$$

$$1 \geq |F_{22}(180^\circ)/F_{11}(180^\circ)| \geq 0 \quad (6.12)$$

$$F_{44}(180^\circ)/F_{11}(180^\circ) \geq 1 - 2|F_{22}(180^\circ)/F_{11}(180^\circ)| \quad (6.13)$$

In addition we verify that the extrapolated points satisfy the Cloude coherency matrix test as described by Hovenier et al. [27]. In Tables 6.4 and 6.5, we present the synthetic scattering matrices for the calcite sample obtained for both measured size distributions. The experimental data and the corresponding extrapolated matrix are freely available in digital form in the Amsterdam-Granada light scattering database [20].

## 6.4 Computations for Calcite Particles

### 6.4.1 DDSCAT 7.1

The DDSCAT 7.1 code is a freely available open-source Fortran-90 software package based on the "Discrete Dipole Approximation" (DDA). It computes scattering and absorption of electromagnetic waves by targets with arbitrary shape and complex refractive index. In particular the DDSCAT 7.1 version allows computations for birefringent particles [16]. The theory of DDA is presented in [29].

In the Discrete Dipole Approximation the target is replaced by an array of points. The points acquire dipole moment in response to the local electric field. The dipoles interact electromagnetically with one another. For the finite array of points the scattering problem is exactly solved. DDA is completely flexible regarding the shape of the target, being limited only by the need to use an inter-dipole separation,  $d$ , that must be small compared with 1) the size of the particle and 2) the wavelength of the incident light. Although there is no restriction on the relationship between the wavelength and the target size, in practice small size parameters ( $x = 2\pi r/\lambda$ ) are much faster to compute than the large ones. Numerical studies [30] indicate that the second criterion is adequately satisfied for non-spherical targets if  $|m|kd < 1$ , where  $m$  is the complex refractive index of the target material  $k \equiv 2\pi/\lambda$  is the wave number, and  $\lambda$  the wavelength of the incident light.

r( $\mu\text{m}$ )	Orientations
0.10	512
0.15	512
0.20	512
0.25	512
0.30	576
0.35	576
0.40	729
0.45	729
0.60	810
0.65	900
0.75	1485
1.00	1485
1.10	1728
1.20	1728

Table 6.3: Number of orientations used in our computations for flakes and rhomboids as a function of volume-equivalent radius.

### 6.4.2 Simulations of Calcite Particles

As we have seen in Section 6.2, the calcite sample presents a broad size distribution with particles from the sub-micrometer scale to hundreds of micrometers in radius. A good accuracy in the

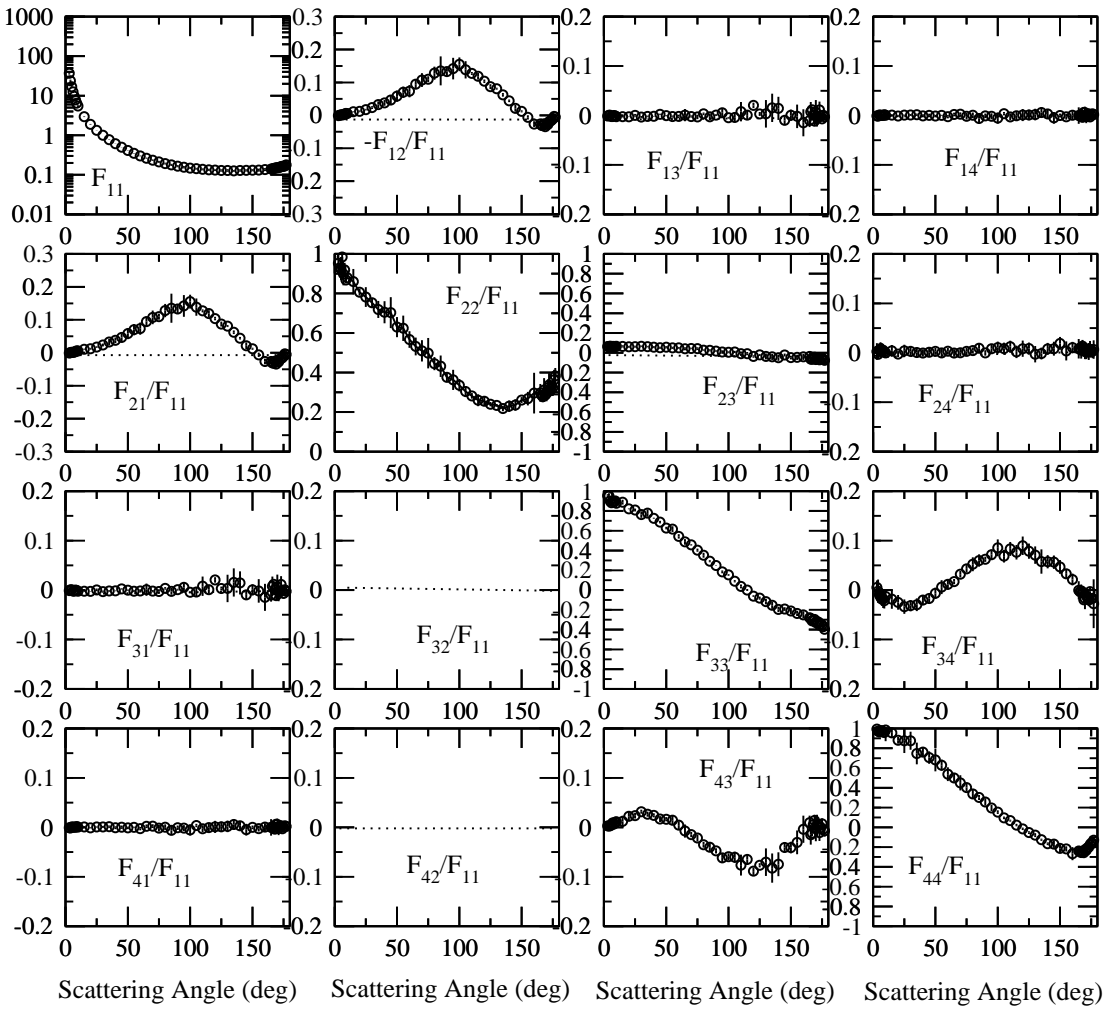


Figure 6.4: Measured scattering matrix elements as functions of the scattering angle at 647 nm wavelength. Circles correspond to the measurements that are presented together with their error bars.

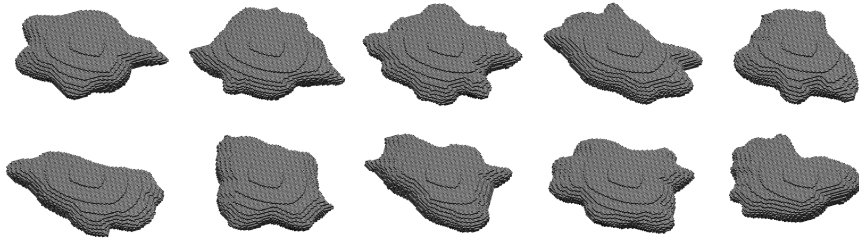


Figure 6.5: Modeled flake-like shapes used in our simulations. Each shape consists of about 50000 dipoles.

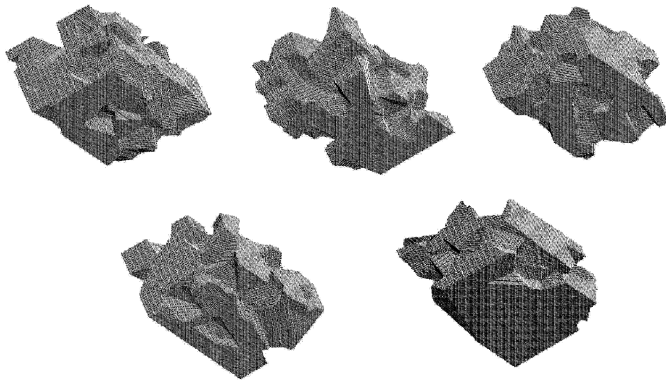


Figure 6.6: Modeled rhomboid-like shapes used in our simulations. Each shape consists of about 100000 dipoles.

computations requires the use of a large amount of dipoles for the largest targets. The number of dipoles is directly related to the computational time that increases very quickly as the number of dipoles (size of the target) increases. For a detailed description and limitations of the code we refer to [16]. Due to this limitation, in our computations we cannot take into account the complete size distributions derived from Fraunhofer and Lorenz-Mie theories (hereafter Fraunhofer SD, and Mie SD, respectively) as presented in Section 6.2.1. Instead, we have to truncate the size distributions at  $r=1.2 \mu\text{m}$ . The effective radii,  $r_{eff}$ , for the truncated Fraunhofer SD and Mie SD are equal to  $0.6$  and  $0.8 \mu\text{m}$ , respectively. For the Fraunhofer SD a 74% of the total scattering cross section of the original distribution is included in the truncated distribution whereas only 55% is included if we use the Mie SD.

Owing to the limited size range we can cover with the simulations, we do not attempt to obtain a perfect fit with the measured scattering matrix elements. Instead, we consider the behavior of the computed scattering matrix elements as a function of particle size, shape, and refractive index. For simplicity, for computations involving size averaging we use the Fraunhofer SD unless it is otherwise noted. Since we do not know which of the two size distributions is more accurate, the choice is based on the simple reason that a larger fraction of the Fraunhofer SD can be simulated with our truncated SD. Notwithstanding this, size-averaged computations based on the Mie SD are also reported for comparison (see Section 6.4.5).

In our computations we only consider orientation-averaged results, the number of orientations used depending on the particle size as shown in Table 6.3. In order to compare the experimental scattering matrix elements for the calcite sample, all computations presented in this paper have been performed at  $647 \text{ nm}$ .

As we mention in Section 6.2, the composition of calcite is defined by a dielectric tensor



specified by two principal dielectric functions, ordinary and extraordinary refractive indices. To study the impact of birefringence on the simulations, we have considered four cases regarding the composition of calcite particles:

1. The particles of the sample are assumed to be composed of an isotropic material with a refractive index  $m_1 = 1.655 + 0.0i$ , corresponding to the ordinary refractive index of calcite.
2. The particles of the sample are assumed to be composed of an isotropic material with a refractive index  $m_2 = 1.485 + 0.0i$ , corresponding to the extraordinary refractive index of calcite.
3. The particles of the sample are considered to be composed of calcite, but its birefringence is approximated by assuming a mixture of particles in such a way that 1/3 are isotropic particles with refractive index  $m_2$ , and 2/3 of the particles with refractive index  $m_1$ . This is known as the "1/3-2/3 approximation" [29].
4. The particles of the sample are considered to be composed of calcite, its birefringence fully accounted for.

When fully accounting for the birefringence, one needs to specify the orientation of the optic axes relative to the particle. This is straightforward for regular crystals where different crystal faces can be readily identified, but far from trivial for irregular particles without well-defined faces. It is therefore fortunate that the orientation of the optic axis has much reduced effect when averaging over particle orientation [31] as we do here. Further, the effect depends on the particle shape such that large-aspect-ratio particles show larger effect than the more equidimensional particles. This is also fortunate, because the orientation of the optic axis is easier to guess at least for calcite when the particles are very thin [15]. Accordingly, for flakes, we use the orientation suggested by [15] and, for simplicity, use the same orientation also for our irregular rhombohedra. For light-scattering simulations for flake-like particles, we use existing model shapes from [15]. Ten such random flakes are used and their ensemble-averaged light-scattering properties considered here. The generation of these shapes is described in detail by [15] and is not repeated here. Moreover, five new rhomboid-like shapes have been generated (see Fig. 6.6). Each irregular rhomboid presented in the figure consists of about 100 000 dipoles. Rhomboid-like structures are generated in a similar way, but starting with an ideal rhomboid. Later, seed cells of calcite and void are randomly located close to the surface of the rhomboid, and all the surface cells are turned into either void or calcite, depending on which type of seed is the closest.

For each of the 15 mentioned shapes, scattering matrix computations for 14 different sizes from 0.1 to 1.2  $\mu\text{m}$  have been performed (see Table 6.3). The DDSCAT uses the time factor  $\exp(-i\omega t)$  to define the Stokes parameters, causing the sign of the computed  $F_{34}(\theta)/F_{11}(\theta)$  to be opposite to that measured. For consistency, the computed  $F_{34}(\theta)/F_{11}(\theta)$  are thus multiplied by  $-1$  in the comparison.

### 6.4.3 Flake particles

In our computations, for each flake presented in Fig. 6.5, we consider the 14 size bins shown in Table 6.3. The computations are averaged over a sufficient amount of orientations to provide a meaningful average (Table 6.3). Moreover, the simulations for four different compositions as described in Section 6.4.2 are considered. In practice we only perform computations for three of them, namely cases 1, 2, and 4, since case 3 is obtained by combining results from 1 and 2. In Fig. 6.7, we present results for the non-zero elements of the scattering matrix computed for the isotropic case 1 ( $m_1=1.655 + 0.0i$ ). In the figure, the results for five different sizes namely 0.10, 0.45, 0.75, 1.0 and 1.2  $\mu\text{m}$  are displayed, each an average of the ten shapes. As shown, the computed scattering matrix elements are highly dependent on the size of the particles. As the size increases, some scattering matrix elements, such as the  $F_{11}(\theta)$  or  $-F_{12}(\theta)/F_{11}(\theta)$  ratio,

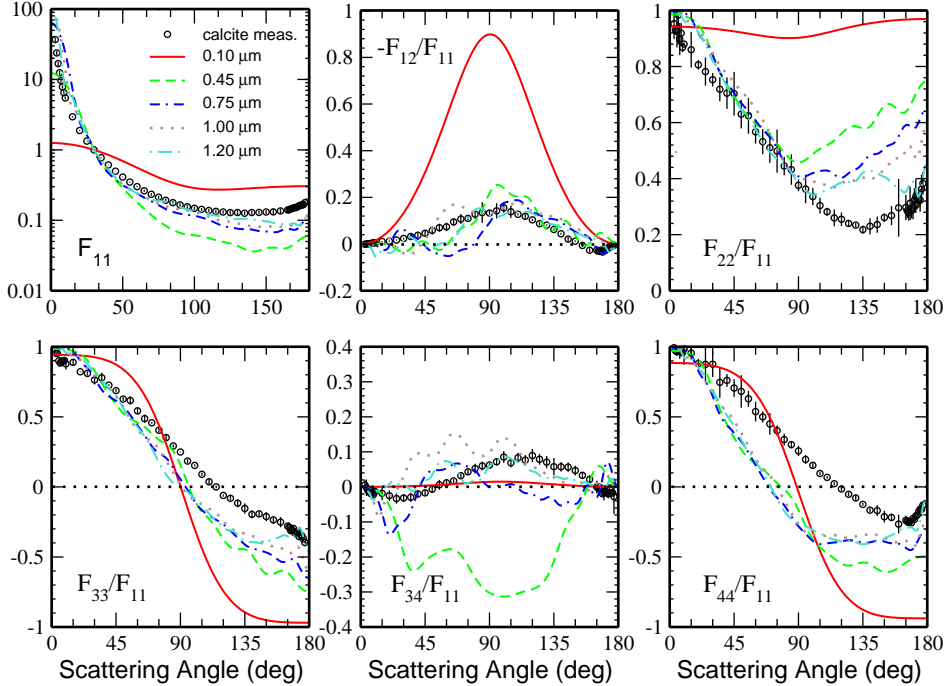


Figure 6.7: Computed scattering matrix elements for different volume equivalent radii. The results are averaged over ten flake-like shapes fixing the refractive index to  $m_1=1.655 + 0.0i$ . Circles correspond to the measurements that are presented together with their error bars. Computations and measurements have been performed at 647 nm.

tend to converge towards the measured values. This is also the case with the  $F_{22}(\theta)/F_{11}(\theta)$  and  $F_{33}(\theta)/F_{11}(\theta)$  ratios at forward and side scattering angles. A strong dependence of the scattering matrix elements on the particle size is also seen for the other three studied cases referred above regarding the composition. It is good to notice that in some cases the simulations agree well with the measurements already for 1.2  $\mu\text{m}$  particles even though the effective radius of the sample is 1.7  $\mu\text{m}$  containing particles even larger than 200  $\mu\text{m}$  (Fraunhofer SD).

In Fig. 6.8, we present the scattering matrix elements for the four studied compositions considering averages over all ten flakes and the Fraunhofer SD truncated at 1.2  $\mu\text{m}$ . As it can be seen, the  $F_{11}(\theta)$  element computed for the isotropic case 2 ( $m_2 = 1.485 + 0i$ ) substantially differs from the other three cases. Strong differences are also found for the  $-F_{12}(\theta)/F_{11}(\theta)$ , and  $F_{22}(\theta)/F_{11}(\theta)$  ratios when comparing with the results obtained for cases 1, 3 and 4.

The computed phase functions for the isotropic cases 1 ( $m_1=1.655 + 0.0i$ ) and 3 (“1/3-2/3 approximation”) are nearly on top of that obtained for the birefringent case 4. Therefore, it seems like birefringence does not significantly affect  $F_{11}(\theta)$ . However, that is not the case for the polarization-related elements of the scattering matrix. These results are in agreement with previous studies on the impact of birefringence on the computed scattering matrix elements [15]. When comparing the computed  $-F_{12}(\theta)/F_{11}(\theta)$ ,  $F_{22}(\theta)/F_{11}(\theta)$  and  $F_{44}(\theta)/F_{11}(\theta)$  ratios for case 3 (“1/3-2/3 approximation”) with those obtained for the birefringent case 4, we find significant differences at nearly all computed scattering angles. In contrast, the computed  $-F_{12}(\theta)/F_{11}(\theta)$  at all scattering angles and the  $F_{22}(\theta)/F_{11}(\theta)$  at side- and back-scattering angles for the isotropic case 1 ( $m_1=1.655 + 0.0i$ ) are very similar to those obtained for the birefringent case 4, constituting a better approximation to the birefringent case than the “1/3-2/3 approximation” as far as the mentioned ratios are concerned.

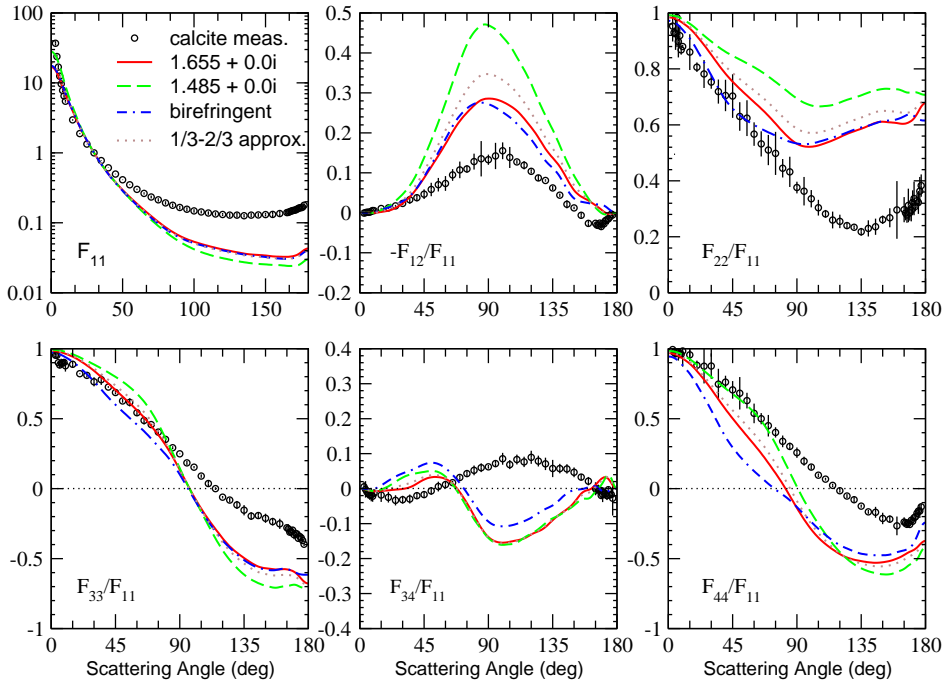


Figure 6.8: Computed scattering matrix elements for different refractive indices. The results are averaged over ten flake-like shapes and the Fraunhofer SD up to  $1.2 \mu\text{m}$ . Circles correspond to the measurements that are presented together with their error bars. Computations and measurements have been performed at  $647 \text{ nm}$ .

#### 6.4.4 Rhomboid-like particles

In analogy with flakes, for each rhomboid-like particle presented in Fig. 6.6, we consider 14 different sizes as shown in Table 6.3. The computations are averaged over a sufficient number of orientation in order to provide a meaningful average. Then, the four compositions described in Section 6.4.2 are considered. In Fig. 6.9, we show results for the non-zero elements of the scattering matrix computed for the isotropic case 1 ( $m_1 = 1.655 + 0i$ ). We present results for five different sizes:  $0.10, 0.45, 0.75, 1.00$  and  $1.20 \mu\text{m}$ . Each of those sizes has been averaged over the five rhomboid-like particles. We find that the computed scattering matrix elements are highly dependent on the size of the particles. Moreover, a slight increase at backward direction for the  $F_{11}(\theta)$  element appears as the size of the particles increases (particles larger than  $0.45 \mu\text{m}$ ). In general, we do not find any clear tendency to approach the measurements for any of the studied sizes. The only exception is found for the  $F_{22}(\theta)/F_{11}(\theta)$  and  $F_{33}(\theta)/F_{11}(\theta)$  ratios that for the largest radius ( $1.2 \mu\text{m}$ ) show a reasonably agreement to the measurements. Similar size dependence is found for the other three studied cases regarding the composition referred in Section 6.4.2.

In Fig. 6.10, we present the scattering matrix elements for the four considered compositions averaged over the five irregular rhomboids. The computations are averaged over the Fraunhofer SD truncated at  $1.2 \mu\text{m}$ . As shown, the  $F_{11}(\theta)$  element computed for the isotropic case 2 ( $m_2 = 1.485 + 0i$ ) shows significant differences when comparing to the computed values for cases 1, 3, and 4. The computed  $F_{11}(\theta)$  show very similar results for the isotropic cases 1 and 3, and those obtained for birefringent rhomboidal particles, case 4. Therefore, it seems that birefringence has little impact on the computed  $F_{11}(\theta)$ . Moreover, the  $-F_{12}(\theta)/F_{11}(\theta)$  ratio for the “1/3-2/3 approximation” seems to be a good approximation for the birefringent case. The other polarization-related elements show a significant dependence on birefringence.

In general the computed scattering for the birefringent case (4) agrees better with the mea-

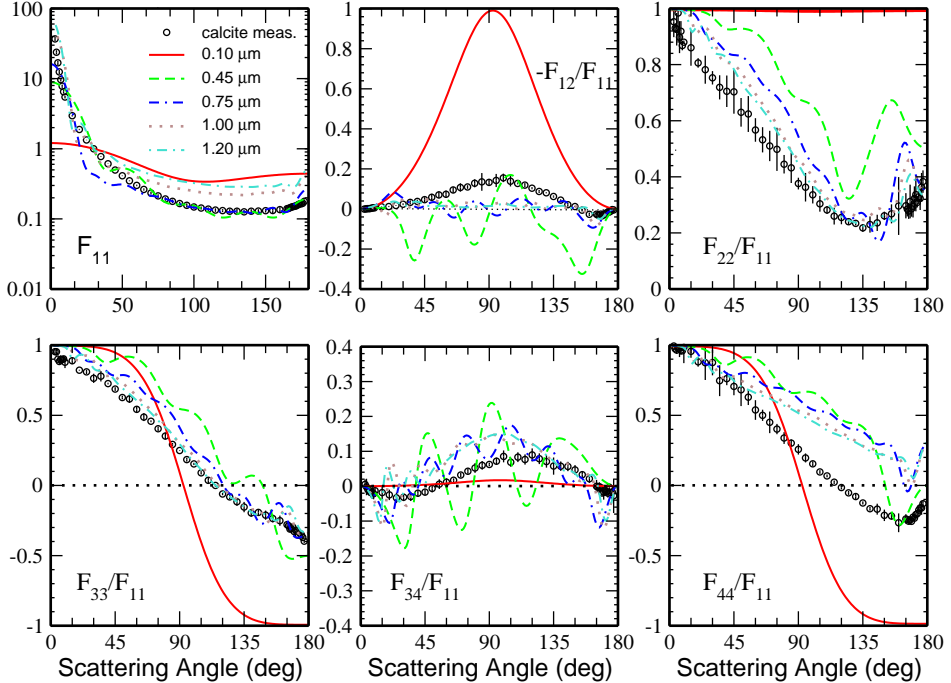


Figure 6.9: Computed scattering matrix elements for different volume equivalent radii. The results are averaged over five rhomboid-like shapes fixing the refractive index to  $m_1 = 1.655 + 0.0i$ . Circles correspond to the measurements that are presented together with their error bars. Computations and measurements have been performed at 647 nm.

sured values than the other 3 studied cases. The only exception is related to the  $-F_{12}(\theta)/F_{11}(\theta)$  ratio for which the isotropic refractive index  $m_2 = 1.485 + 0.0i$  produces an excellent fit to the measured  $-F_{12}(\theta)/F_{11}(\theta)$  from 3 to 95 degrees scattering angle.

#### 6.4.5 Combination of Flake-like and Rhomboid-like particles

In this section we study the effect of particle shape on the scattering matrix by comparing the computed scattering matrix elements for flakes and rhomboid-like particles. For simplicity, we only consider size-average results. Further, we only consider the birefringent case. The results of the comparison are shown in Fig. 6.11 for the Fraunhofer SD. It is clear that all calculated scattering matrix elements are significantly affected by the shape of the particles. When we compare e.g. the  $-F_{12}(\theta)/F_{11}(\theta)$  ratio for both types of shapes we see the change from the bell shape in the case of flakes to a negative branch at large scattering angles, typical for cubes. At this point it is interesting to see whether this behavior would be different by considering the Mie SD. In Fig. 6.12 we compare the computed scattering matrix elements for flakes and rhomboids averaged over the Mie SD truncated at  $1.2 \mu\text{m}$ . Again, all calculated scattering matrix elements are significantly affected by the shape of the particles. It is important to note that the computed  $F_{11}(\theta)$ ,  $F_{22}(\theta)/F_{11}(\theta)$ ,  $F_{33}(\theta)/F_{11}(\theta)$ , and  $F_{34}(\theta)/F_{11}(\theta)$  for rhomboid-like particles averaged over the Mie SD produce nearly perfect fits to the measurements. Moreover, the measured  $-F_{12}(\theta)/F_{11}(\theta)$  ratio presents values within the domains defined by the computed  $-F_{12}(\theta)/F_{11}(\theta)$  for flakes and rhomboid-like particles. That is also the case for the calculated  $-F_{12}(\theta)/F_{11}(\theta)$ ,  $F_{33}(\theta)/F_{11}(\theta)$ ,  $F_{34}(\theta)/F_{11}(\theta)$ ,  $F_{44}(\theta)/F_{11}(\theta)$  ratios for flakes and rhomboid-like particles averaged over the Fraunhofer SD at nearly the complete scattering angle range. This seems to indicate that a combination of flake- and rhomboid-like particles could provide better fits with the measurements than either shape on its own, consistent with the presence of both types of shapes in the sample.

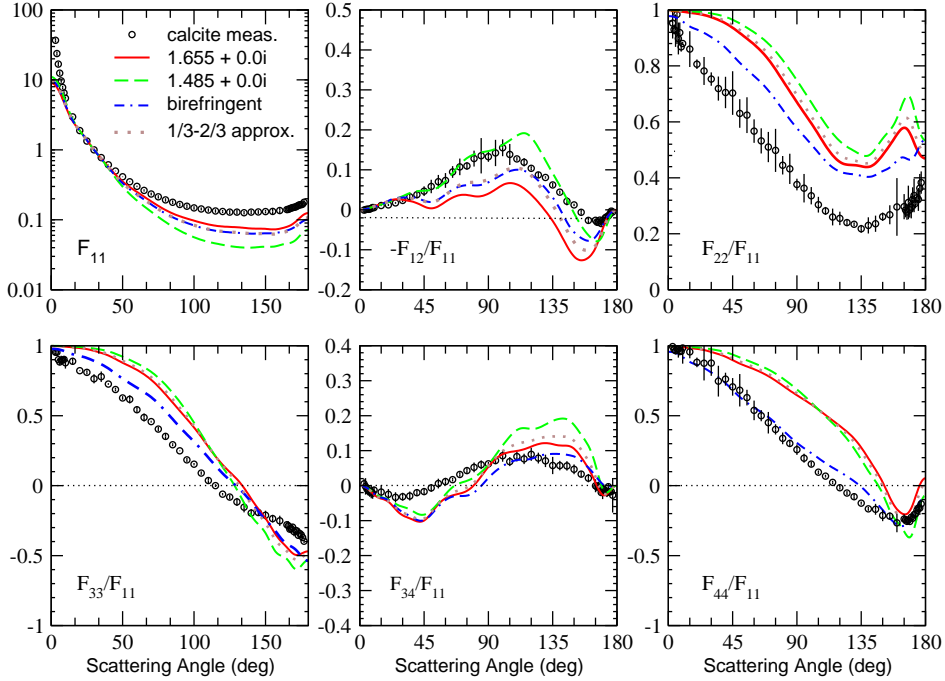


Figure 6.10: Computed scattering matrix elements for different refractive indices. The results are averaged over five rhomboid-like shapes and the Fraunhofer SD up to  $1.2 \mu\text{m}$ . Circles correspond to the measurements that are presented together with their error bars. Computations and measurements have been performed at  $647 \text{ nm}$ .

As illustrative examples, we have computed the scattering matrix considering a varying percentage of flakes and rhomboid-like particles. Figure 6.13 presents the results obtained for three different mixtures, namely 80% of flakes and 20% of irregular rhomboids; 50% of flakes and 50% of irregular rhomboids; and 20% of flakes and 80% of irregular rhomboids. All computations correspond to the birefringent case (4) averaged over the Fraunhofer SD. As shown in the figure, a better agreement with the measurements is reached with those mixtures. In Fig. 6.14, we present the computed scattering matrix elements for the same three mixtures of flakes and rhomboids just mentioned but averaged over the Mie SD. As shown, a good approximation to the measured scattering matrix elements is also obtained. In the case of the Fraunhofer SD (Fig. 6.13) a combination of 20% of flakes and 80% of rhomboids gives the closest approach to the measurements. That is also the case for Mie SD with the exception of the  $-F_{12}(\theta)/F_{11}(\theta)$  ratio which is better represented by the 80% of flakes and 20% rhomboids combination. It is remarkable how similar the computed  $F_{11}(\theta)$ ,  $F_{22}(\theta)/F_{11}(\theta)$ , and  $F_{33}(\theta)/F_{11}(\theta)$  by assuming the Mie SD and a mixture of 20% flakes-80% rhomboids are to the measured ones. Moreover, reasonably good fits are obtained for the  $-F_{12}(\theta)/F_{11}(\theta)$  and  $F_{44}(\theta)/F_{11}(\theta)$  ratios by assuming the Fraunhofer SD. This seems to indicate that a kind of averaged size distribution out of the Fraunhofer and Mie SDs could give a more adequate representation of the measured scattering matrix elements. In any case, we must point out that the mandatory truncation of the size distributions in the computations prevent us from knowing the effect of larger sized particles. The best fit to the measurements which are found for the 20% flakes- 80% rhomboids combination might change by the inclusion of such particles.

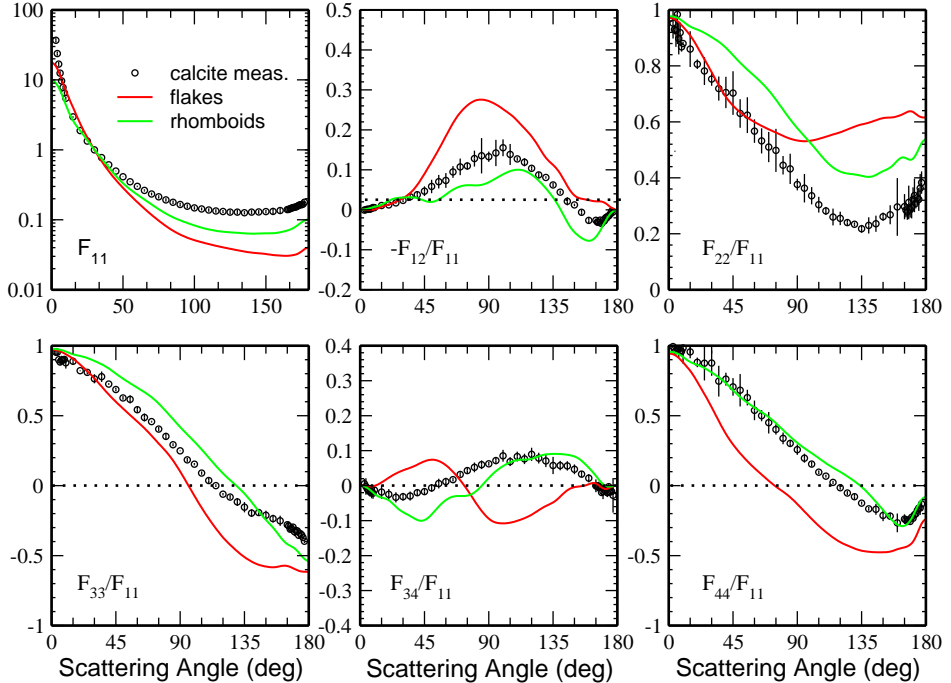


Figure 6.11: Computed scattering matrix elements for birefringent flake- and rhomboid-like particles. The results are averaged over shapes and the Fraunhofer SD up to  $1.2 \mu\text{m}$ . Circles correspond to the measurements that are presented together with their error bars. Computations and measurements have been performed at  $647 \text{ nm}$ .

## 6.5 Summary and Conclusions

In this work, we present the experimental scattering matrix as a function of the scattering angle of a calcite sample. The measurements are performed in the  $3^\circ - 177^\circ$  scattering angle range. To facilitate the use of the measured scattering matrix of the sample for multiple scattering computations we also present a synthetic scattering matrix based on the measured scattering matrix covering the full angle range from 0 to 180 degrees. The measured and synthetic scattering matrices for the calcite sample are available in the Amsterdam-Granada Light Scattering database at [www.iaa.es/scattering](http://www.iaa.es/scattering). They are freely available under request of citation of this paper and [20].

Since calcite is a birefringent material, the measurements for the calcite sample are used to test the effect of birefringence on the computed scattering matrix elements. We present single scattering computations that have been performed using DDSCAT 7.1 [16]. In our computations, four cases are considered: 1. Calcite is considered an isotropic material with refractive index  $m_1 = 1.655 + 0.0i$ , corresponding to the ordinary refractive index of calcite; 2. Calcite is considered an isotropic material with refractive index  $m_2 = 1.485 + 0.0i$ , corresponding to the extraordinary refractive index of calcite; 3. The “1/3-2/3 approximation” [29], where calcite is considered a mixture of particles such that 1/3 are isotropic particles with refractive index  $m_2$ , and 2/3 of the particles with refractive index  $m_1$ ; 4. The birefringence of calcite is fully accounted for by replacing the refractive index by a dielectric tensor. All computations are performed at  $647 \text{ nm}$ . For each of the four mentioned cases, 14 sizes from  $0.1 \mu\text{m}$  up to  $1.2 \mu\text{m}$  with a number of orientations ranging from 512 up to 1728, are considered. In addition, the scattering matrix elements are modeled for two sets of shapes: flake-like and rhomboid-like particles, giving together 15 different shapes. Due to computational limitations we can only perform computations for particles up to  $1.2 \mu\text{m}$  in radii, i.e we cannot cover the entire

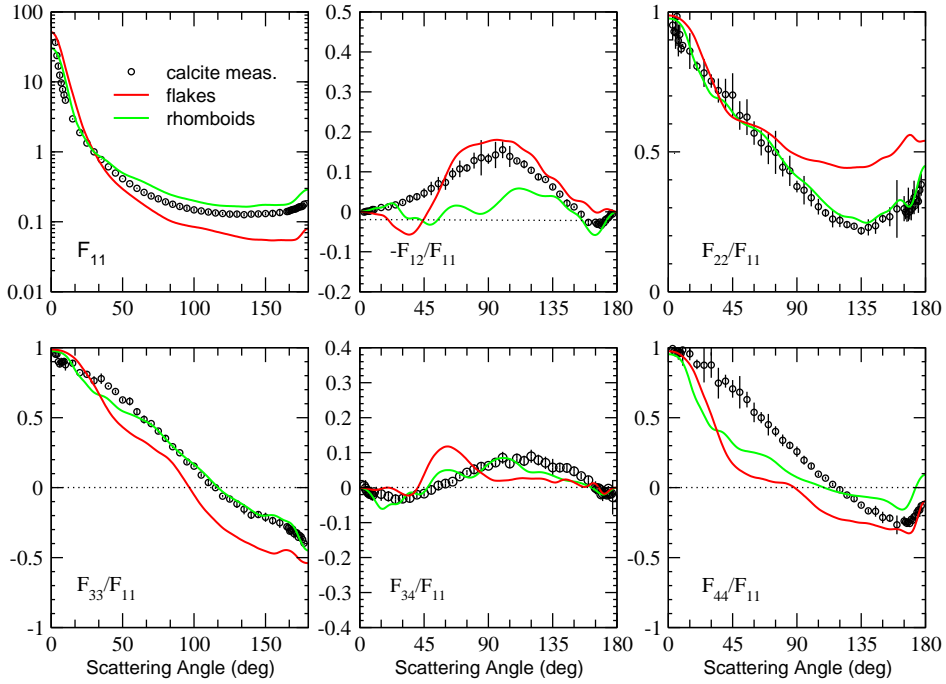


Figure 6.12: Computed scattering matrix elements for birefringent flake- and rhomboid-like particles. The results are averaged over shapes and the Mie SD up to  $1.2 \mu\text{m}$ . Circles correspond

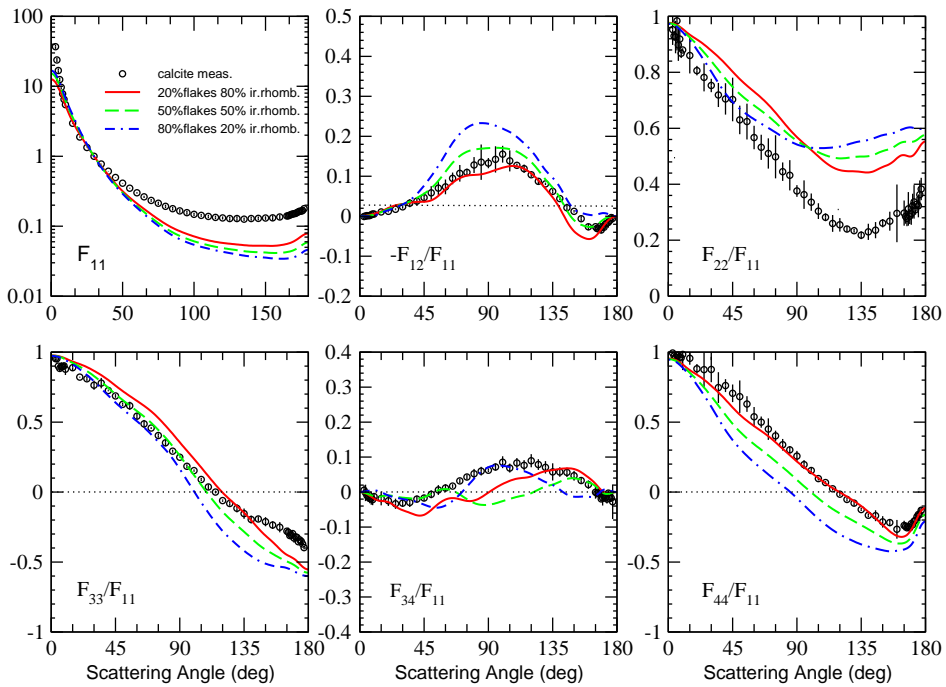


Figure 6.13: Computed scattering matrix elements for different percentages of birefringent flake- and rhomboid-like particles. The results are averaged over shapes and the Fraunhofer SD up to  $1.2 \mu\text{m}$ . Circles correspond to the measurements that are presented together with their error bars. Computations and measurements have been performed at  $647 \text{ nm}$ .

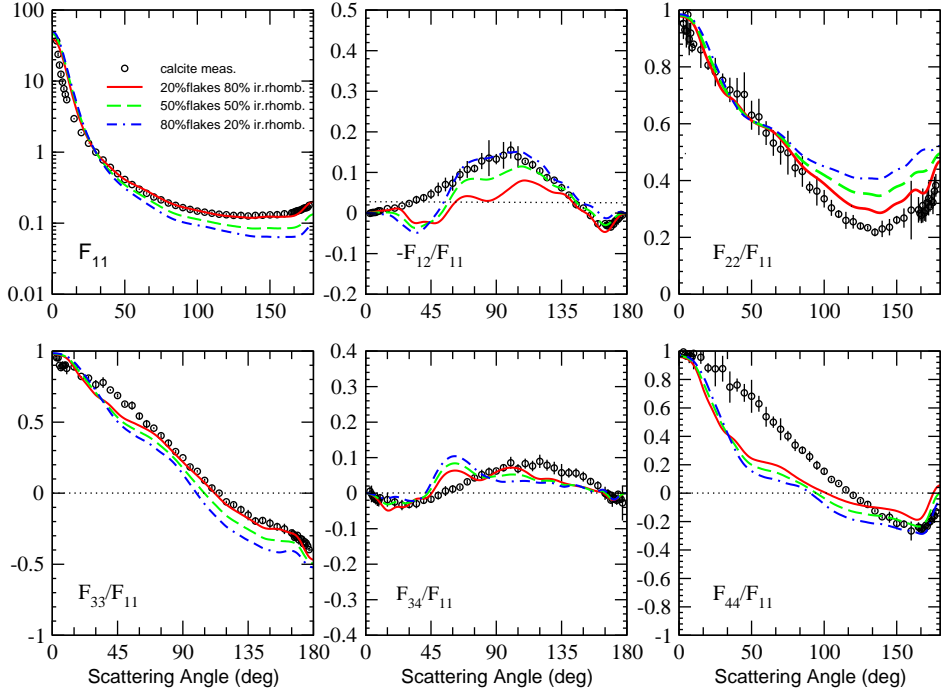


Figure 6.14: Computed scattering matrix elements for different percentage of birefringent flake- and rhomboid-like particles. The results are averaged over shapes and the Mie SD up to 1.2  $\mu\text{m}$ . Circles correspond to the measurements that are presented together with their error bars. Computations and measurements have been performed at 647 nm.

range of sizes of our calcite sample. Therefore, instead of looking for a perfect fitting to the measurements, the experimental scattering matrix is used as qualitative reference to which we can compare our computations to study a) the effect of birefringence on the computed scattering matrix elements and b) the validity of our shape models to reproduce the scattering behavior of our calcite sample.

Firstly, we analyze the effect of birefringence on the computed scattering matrix elements. In general, the simulated scattering matrices show a strong dependence on the particle sizes. For both flakes and irregular rhomboids, we have found that the isotropic cases 1 ( $m_1 = 1.655$ ), and 3 (1/3-2/3 approximation), provide quite similar values for the  $F_{11}(\theta)$  element to those obtained by assuming birefringent particles (case 4). Therefore, for the studied shapes and sizes, birefringence has little impact on the computed phase functions. In contrast, birefringence produces a significant effect on the polarization-related scattering matrix elements. The obtained conclusions are in agreement with [15]. In the case of flakes, the isotropic refractive index  $m_1$  provides a good approximation to the birefringent case for the  $-F_{12}(\theta)/F_{11}(\theta)$  ratio. In contrast, for irregular rhomboids, the "1/3-2/3" approximation provides closest values to the computed  $-F_{12}(\theta)/F_{11}(\theta)$  for birefringent particles.

Secondly, the simulations are compared with the experimental scattering matrix for the calcite sample. It is interesting to note that the shape of the targets (flakes or irregular rhomboids) has a much stronger effect on the computed scattering matrix elements than birefringence. Significant differences in the simulated scattering matrices are found between those two types of particles. Since our sample consists of two types of particles, we compare the matrices obtained for different percentages of flakes and irregular rhomboids.

We find that varying the percentage of flakes and irregular rhomboids in the sample, we get a significantly better approximation to the measurements than for flakes or irregular rhomboids alone. For the Fraunhofer SD computations, we find that a particle shape distribution having



20% of flakes and 80% of irregular rhomboids gives a better approximation to the measurements. The agreement with the measurements is even better in the case of the Mie SD even considering that the calculated cross section in the former case is 74% of the total scattering cross section while in the Mie SD it is only 55%. That is probably due to the fact that the resulting  $r_{eff}$  of the Mie SD after the truncation at 1.2 micron is closer to the  $r_{eff}$  of any of the two size distributions (Mie and Fraunhofer) before truncation. The limitations of the computations due to the extreme difficulties in dealing with large particle sizes prevent us from drawing firm conclusions on the relative percentages of different particle shapes that exist in the calcite sample. We hope, however, that further computations including particles in geometric optics domain will shed more light on the issue.

### Acknowledgements

J.R. Rodon and A. Benitez from IAA GRID team are hearty acknowledged for their support. Furthermore we are indebted to A. Gonzalez and I. Guerra Tschuschke from The Scientific Instrumentation Center of the University of Granada, who took the FESEM and SEM images of the calcite samples. Bob West and two anonymous referee are acknowledged by their reviews on a previous version of this paper. This work has been supported by the Plan Nacional de Astronomia y Astrofisica under contract AYA2009-08190, and Junta de Andalucia, contract P09-FMQ-455. Timo Nousiainen and Evgenij Zubko acknowledge the Academy of Finland (contracts 125180 and 127461) for its financial support. Evgenij Zubko acknowledges also NASA program for Outer Planets Research (grant NNX10AP93G).

## 6.6 Appendix

Synthetic scattering matrix elements as functions of the scattering angle by assuming the Fraunhofer SD (6.4), and the Mie SD (6.5), respectively.

Angle, deg	$F_{11}^{uu}$	$-F_{12}/F_{11}$	$F_{22}/F_{11}$	$F_{33}/F_{11}$	$F_{34}/F_{11}$	$F_{44}/F_{11}$
0.0	8.61E2	0.00E0	1.00E0	1.00E0	0.00E0	1.00E0
1.0	1.34E2	-3.75E-4	9.93E-1	9.87E-1	2.17E-3	1.00E0
2.0	7.01E1	-9.72E-4	9.75E-1	9.64E-1	5.45E-3	1.00E0
3.0	4.74E1	-1.00E-3	9.53E-1	9.54E-1	5.00E-3	9.94E-1
4.0	5.47E1	0.00E0	9.30E-1	9.53E-1	-2.00E-3	9.74E-1
5.0	3.86E1	1.00E-3	9.26E-1	9.00E-1	-1.00E-2	9.65E-1
6.0	2.87E1	1.00E-3	9.84E-1	8.84E-1	-1.40E-2	9.77E-1
7.0	2.22E1	2.00E-3	8.98E-1	8.97E-1	-1.80E-2	9.78E-1
8.0	1.79E1	4.00E-3	9.19E-1	8.97E-1	-1.80E-2	9.65E-1
9.0	1.49E1	6.00E-3	8.68E-1	9.02E-1	-2.20E-2	9.60E-1
10.0	1.26E1	5.00E-3	8.80E-1	8.78E-1	-1.30E-2	9.84E-1
15.0	6.79E0	1.10E-2	8.60E-1	8.89E-1	-1.80E-2	9.56E-1
20.0	4.33E0	1.20E-2	8.06E-1	8.21E-1	-2.50E-2	8.81E-1
25.0	3.06E0	1.70E-2	7.82E-1	8.10E-1	-3.40E-2	8.75E-1
30.0	2.30E0	2.40E-2	7.53E-1	7.64E-1	-3.20E-2	8.76E-1
35.0	1.78E0	3.30E-2	7.19E-1	7.79E-1	-3.00E-2	7.47E-1
40.0	1.40E0	3.80E-2	7.05E-1	7.26E-1	-2.00E-2	7.61E-1
45.0	1.14E0	4.70E-2	7.03E-1	6.87E-1	-1.70E-2	7.06E-1
50.0	9.46E-1	5.80E-2	6.30E-1	6.27E-1	-6.00E-3	6.82E-1
55.0	8.02E-1	7.00E-2	6.24E-1	6.17E-1	6.00E-3	6.29E-1
60.0	6.91E-1	7.30E-2	5.67E-1	5.43E-1	1.20E-2	5.38E-1
65.0	6.04E-1	9.50E-2	5.32E-1	4.87E-1	1.70E-2	5.00E-1
70.0	5.37E-1	1.07E-1	5.10E-1	4.57E-1	3.20E-2	4.50E-1
75.0	4.89E-1	1.10E-1	4.98E-1	4.04E-1	4.30E-2	4.02E-1
80.0	4.43E-1	1.28E-1	4.45E-1	3.52E-1	5.20E-2	3.38E-1
85.0	4.09E-1	1.35E-1	4.32E-1	2.92E-1	6.00E-2	3.02E-1
90.0	3.81E-1	1.33E-1	3.76E-1	2.49E-1	6.20E-2	2.57E-1
95.0	3.58E-1	1.42E-1	3.63E-1	1.84E-1	7.20E-2	1.96E-1
100.0	3.40E-1	1.55E-1	3.36E-1	1.54E-1	8.50E-2	1.54E-1
105.0	3.28E-1	1.39E-1	3.04E-1	9.00E-2	6.90E-2	9.60E-2
110.0	3.17E-1	1.27E-1	2.82E-1	3.60E-2	8.30E-2	6.80E-2
115.0	3.08E-1	1.19E-1	2.60E-1	0.00E0	7.60E-2	2.30E-2
120.0	3.01E-1	1.04E-1	2.55E-1	-6.10E-2	9.00E-2	-1.50E-2
125.0	2.96E-1	8.70E-2	2.40E-1	-8.20E-2	7.90E-2	-5.30E-2
130.0	2.96E-1	8.10E-2	2.34E-1	-1.16E-1	7.10E-2	-7.90E-2
135.0	2.89E-1	6.20E-2	2.18E-1	-1.54E-1	5.80E-2	-1.25E-1
140.0	2.96E-1	4.40E-2	2.30E-1	-1.96E-1	5.70E-2	-1.66E-1
145.0	2.96E-1	2.10E-2	2.36E-1	-1.92E-1	5.60E-2	-1.69E-1
150.0	3.01E-1	1.20E-2	2.61E-1	-2.12E-1	4.70E-2	-2.13E-1
155.0	3.03E-1	-6.00E-3	2.68E-1	-2.36E-1	3.30E-2	-2.18E-1
160.0	3.12E-1	-2.60E-2	2.96E-1	-2.51E-1	2.10E-2	-2.66E-1
165.0	3.22E-1	-2.60E-2	2.97E-1	-2.80E-1	-0.00E0	-2.39E-1
166.0	3.24E-1	-3.10E-2	2.85E-1	-2.87E-1	-3.00E-3	-2.44E-1
167.0	3.31E-1	-3.10E-2	2.78E-1	-3.11E-1	-1.00E-3	-2.55E-1
168.0	3.38E-1	-2.60E-2	3.12E-1	-3.08E-1	-4.00E-3	-2.46E-1
169.0	3.42E-1	-3.40E-2	2.86E-1	-2.97E-1	-2.00E-2	-2.56E-1
170.0	3.47E-1	-2.60E-2	2.95E-1	-3.29E-1	-1.70E-2	-2.26E-1
171.0	3.49E-1	-2.80E-2	3.23E-1	-3.20E-1	-1.20E-2	-2.33E-1
172.0	3.58E-1	-1.90E-2	3.37E-1	-3.23E-1	-1.50E-2	-2.08E-1
173.0	3.68E-1	-1.70E-2	3.09E-1	-3.55E-1	-2.00E-2	-2.01E-1
174.0	3.77E-1	-1.50E-2	3.29E-1	-3.42E-1	-3.00E-3	-1.76E-1
175.0	3.77E-1	-1.10E-2	3.23E-1	-3.52E-1	-1.80E-2	-1.60E-1
176.0	3.84E-1	-3.00E-3	3.63E-1	-3.71E-1	-1.70E-2	-1.60E-1
177.0	4.09E-1	-5.00E-3	3.83E-1	-3.97E-1	-2.80E-2	-1.30E-1
178.0	4.43E-1	-4.98E-3	4.06E-1	-4.21E-1	-2.42E-2	-3.92E-2
179.0	4.72E-1	-1.94E-3	4.31E-1	-4.37E-1	-8.98E-3	6.45E-2
180.0	4.85E-1	0.00E0	4.43E-1	-4.43E-1	0.00E0	1.14E-1

Table 6.4: The synthetic scattering matrix elements obtained with Fraunhofer distribution, as functions of the scattering angle for calcite sample at 647 nm.

Angle, deg	$F_{11}^{00}$	$-F_{12}/F_{11}$	$F_{22}/F_{11}$	$F_{33}/F_{11}$	$F_{34}/F_{11}$	$F_{44}/F_{11}$
0.0	2.68E3	0.00E0	1.00E0	1.00E0	0.00E0	1.00E0
1.0	3.22E2	-3.75E-4	9.93E-1	9.87E-1	2.17E-3	1.00E0
2.0	1.55E2	-9.72E-4	9.75E-1	9.64E-1	5.45E-3	1.00E0
3.0	9.56E1	-1.00E-3	9.53E-1	9.54E-1	5.00E-3	9.94E-1
4.0	5.03E1	0.00E0	9.30E-1	9.53E-1	-2.00E-3	9.77E-1
5.0	3.55E1	1.00E-3	9.26E-1	9.00E-1	-1.00E-2	9.65E-1
6.0	2.63E1	1.00E-3	9.84E-1	8.84E-1	-1.40E-2	9.77E-1
7.0	2.05E1	2.00E-3	8.98E-1	8.97E-1	-1.80E-2	9.78E-1
8.0	1.65E1	4.00E-3	9.19E-1	8.97E-1	-1.80E-2	9.65E-1
9.0	1.37E1	6.00E-3	8.68E-1	9.02E-1	-2.20E-2	9.60E-1
10.0	1.16E1	5.00E-3	8.80E-1	8.78E-1	-1.30E-2	9.84E-1
15.0	6.24E0	1.10E-2	8.60E-1	8.89E-1	-1.80E-2	9.56E-1
20.0	3.98E0	1.20E-2	8.06E-1	8.21E-1	-2.50E-2	8.81E-1
25.0	2.82E0	1.70E-2	7.82E-1	8.10E-1	-3.40E-2	8.75E-1
30.0	2.11E0	2.40E-2	7.53E-1	7.64E-1	-3.20E-2	8.76E-1
35.0	1.63E0	3.30E-2	7.19E-1	7.79E-1	-3.00E-2	7.47E-1
40.0	1.29E0	3.80E-2	7.05E-1	7.26E-1	-2.00E-2	7.61E-1
45.0	1.05E0	4.70E-2	7.03E-1	6.87E-1	-1.70E-2	7.06E-1
50.0	8.70E-1	5.80E-2	6.30E-1	6.27E-1	-6.00E-3	6.82E-1
55.0	7.37E-1	7.00E-2	6.24E-1	6.17E-1	6.00E-3	6.29E-1
60.0	6.36E-1	7.30E-2	5.67E-1	5.43E-1	1.20E-2	5.38E-1
65.0	5.55E-1	9.50E-2	5.32E-1	4.87E-1	1.70E-2	5.00E-1
70.0	4.94E-1	1.07E-1	5.10E-1	4.57E-1	3.20E-2	4.50E-1
75.0	4.50E-1	1.10E-1	4.98E-1	4.04E-1	4.30E-2	4.02E-1
80.0	4.08E-1	1.28E-1	4.45E-1	3.52E-1	5.20E-2	3.38E-1
85.0	3.76E-1	1.35E-1	4.32E-1	2.92E-1	6.00E-2	3.02E-1
90.0	3.51E-1	1.33E-1	3.76E-1	2.49E-1	6.20E-2	2.57E-1
95.0	3.29E-1	1.42E-1	3.63E-1	1.84E-1	7.20E-2	1.96E-1
100.0	3.13E-1	1.55E-1	3.36E-1	1.54E-1	8.50E-2	1.54E-1
105.0	3.02E-1	1.39E-1	3.04E-1	9.00E-2	6.90E-2	9.60E-2
110.0	2.91E-1	1.27E-1	2.82E-1	3.60E-2	8.30E-2	6.80E-2
115.0	2.83E-1	1.19E-1	2.60E-1	0.00E0	7.60E-2	2.30E-2
120.0	2.77E-1	1.04E-1	2.55E-1	-6.10E-2	9.00E-2	-1.50E-2
125.0	2.72E-1	8.70E-2	2.40E-1	-8.20E-2	7.90E-2	-5.30E-2
130.0	2.72E-1	8.10E-2	2.34E-1	-1.16E-1	7.10E-2	-7.90E-2
135.0	2.66E-1	6.20E-2	2.18E-1	-1.54E-1	5.80E-2	-1.25E-1
140.0	2.72E-1	4.40E-2	2.30E-1	-1.96E-1	5.70E-2	-1.66E-1
145.0	2.72E-1	2.10E-2	2.36E-1	-1.92E-1	5.60E-2	-1.69E-1
150.0	2.77E-1	1.20E-2	2.61E-1	-2.12E-1	4.70E-2	-2.13E-1
155.0	2.79E-1	-6.00E-3	2.68E-1	-2.36E-1	3.30E-2	-2.18E-1
160.0	2.87E-1	-2.60E-2	2.96E-1	-2.51E-1	2.10E-2	-2.66E-1
165.0	2.96E-1	-2.60E-2	2.97E-1	-2.80E-1	-0.00E0	-2.39E-1
166.0	2.98E-1	-3.10E-2	2.85E-1	-2.87E-1	-3.00E-3	-2.44E-1
167.0	3.04E-1	-3.10E-2	2.78E-1	-3.11E-1	-1.00E-3	-2.55E-1
168.0	3.10E-1	-2.60E-2	3.12E-1	-3.08E-1	-4.00E-3	-2.46E-1
169.0	3.15E-1	-3.40E-2	2.86E-1	-2.97E-1	-2.00E-2	-2.56E-1
170.0	3.19E-1	-2.60E-2	2.95E-1	-3.29E-1	-1.70E-2	-2.26E-1
171.0	3.21E-1	-2.80E-2	3.23E-1	-3.20E-1	-1.20E-2	-2.33E-1
172.0	3.29E-1	-1.90E-2	3.37E-1	-3.23E-1	-1.50E-2	-2.08E-1
173.0	3.38E-1	-1.70E-2	3.09E-1	-3.55E-1	-2.00E-2	-2.01E-1
174.0	3.46E-1	-1.50E-2	3.29E-1	-3.42E-1	-3.00E-3	-1.76E-1
175.0	3.46E-1	-1.10E-2	3.23E-1	-3.52E-1	-1.80E-2	-1.60E-1
176.0	3.53E-1	-3.00E-3	3.63E-1	-3.71E-1	-1.70E-2	-1.60E-1
177.0	3.76E-1	-5.00E-3	3.83E-1	-3.97E-1	-2.80E-2	-1.30E-1
178.0	4.07E-1	-4.98E-3	4.06E-1	-4.21E-1	-2.42E-2	-3.92E-2
179.0	4.34E-1	-1.94E-3	4.31E-1	-4.37E-1	-8.98E-3	6.45E-2
180.0	4.46E-1	0.00E0	4.43E-1	-4.43E-1	0.00E0	1.14E-1

Table 6.5: The synthetic scattering matrix elements obtained with Mie size distribution, as functions of the scattering angle for calcite sample at 647 nm.

# Bibliography

- [1] Planck Collaboration, A. Abergel, P. A. R. Ade, N. Aghanim, M. Arnaud, M. Ashdown, J. Aumont, C. Baccigalupi, A. Balbi, A. J. Banday, and et al. Planck early results. XXIV. Dust in the diffuse interstellar medium and the Galactic halo. *A&A*, 536:A24, December 2011.
- [2] H. Kirk, D. Johnstone, and J. Di Francesco. The Large- and Small-Scale Structures of Dust in the Star-forming Perseus Molecular Cloud. *Astrophys. Journal*, 646:1009–1023, August 2006.
- [3] J. C. Weingartner and B. T. Draine. Dust Grain-Size Distributions and Extinction in the Milky Way, Large Magellanic Cloud, and Small Magellanic Cloud. *Astrophys. Journal*, 548:296–309, February 2001.
- [4] F. Moreno, L. M. Lara, O. Muñoz, J. J. López-Moreno, and A. Molina. Dust in Comet 67P/Churyumov-Gerasimenko. *Astrophys. Journal*, 613:1263–1269, October 2004.
- [5] M. I. Mishchenko, L. D. Travis, and A. A. Lacis. *Scattering, absorption, and emission of light by small particles*. 2002.
- [6] T. Nousiainen. Optical modeling of mineral dust particles: A review. *J. Quant. Spec. Radiat. Transf.*, 110:1261–1279, September 2009.
- [7] J. B. Pollack, D. S. Colburn, F. M. Flasar, R. Kahn, C. E. Carlston, and D. G. Pidek. Properties and effects of dust particles suspended in the Martian atmosphere. *J. Geophys. Res.*, 84:2929–2945, June 1979.
- [8] E. Marchiori, S. Lourenço, F. Davaus Gasperetto, G. Zanetti, C. Mauro Mano, and L. F. Nobre. Pulmonary Talcosis: Imaging Findings. *Lung*, 188:165–171, 2010.
- [9] O. Muñoz, H. Volten, J. W. Hovenier, T. Nousiainen, K. Muinonen, D. Guirado, F. Moreno, and L. B. F. M. Waters. Scattering matrix of large Saharan dust particles: Experiments and computations. *Journal of Geophysical Research (Atmospheres)*, 112:13215, July 2007.
- [10] L. Liu, M. I. Mishchenko, J. W. Hovenier, H. Volten, and O. Muñoz. Scattering matrix of quartz aerosols: comparison and synthesis of laboratory and Lorenz-Mie results. *J. Quant. Spec. Radiat. Transf.*, 79:911–920, 2003.
- [11] M. Kahnert and T. Nousiainen. Uncertainties in measured and modelled asymmetry parameters of mineral dust aerosols. *J. Quant. Spec. Radiat. Transf.*, 100:173–178, July 2006.
- [12] M. C. Booth and H. H. Kieffer. Carbonate formation in Marslike environments. *J. Geophys. Res.*, 83:1809–1815, April 1978.
- [13] J. L. Gooding. Chemical weathering on Mars - Thermodynamic stabilities of primary minerals /and their alteration products/ from mafic igneous rocks. *Icarus*, 33:483–513, March 1978.
- [14] T. Clauquin, M. Schulz, and Y. J. Balkanski. Modeling the mineralogy of atmospheric dust sources. *J. Geophys. Res.*, 104:22243, September 1999.
- [15] T. Nousiainen, E. Zubko, J. V. Niemi, K. Kupiainen, M. Lehtinen, K. Muinonen, and G. Videen. Single-scattering modeling of thin, birefringent mineral-dust flakes using the discrete-dipole approximation. *Journal of Geophysical Research (Atmospheres)*, 114:7207, April 2009.

- [16] B. T. Draine. *The Discrete Dipole Approximation for Light Scattering by Irregular Targets*, page 131. *Light Scattering by Nonspherical Particles : Theory, Measurements, and Applications*, January 2000.
- [17] V. Orofino, A. Blanco, S. Fonti, R. Proce, and A. Rotundi. The infrared optical constants of limestone particles and implications for the search of carbonates on Mars. *Planetary and Space Science*, 46:1659–1669, December 1998.
- [18] O. Muñoz, F. Moreno, D. Guirado, J. L. Ramos, H. Volten, and J. W. Hovenier. The IAA cosmic dust laboratory: Experimental scattering matrices of clay particles. *Icarus*, 211:894–900, January 2011.
- [19] H. Volten, O. Muñoz, J. W. Hovenier, J. F. de Haan, W. Vassen, W. J. van der Zande, and L. B. F. M. Waters. WWW scattering matrix database for small mineral particles at 441.6 and 632.8nm. *J. Quant. Spec. Radiat. Transf.*, 90:191–206, January 2005.
- [20] O. Muñoz, F. Moreno, D. Guirado, D. D. Dabrowska, H. Volten, and J. W. Hovenier. The Amsterdam-Granada Light Scattering Database. *J. Quant. Spec. Radiat. Transf.*, 113:565–574, February 2012.
- [21] J. E. Hansen and L. D. Travis. Light scattering in planetary atmospheres. *Space Science Reviews*, 16:527–610, October 1974.
- [22] G. Ghosh. Dispersion-equation coefficients for the refractive index and birefringence of calcite and quartz crystals. *Optics Communications*, 163:95–102, May 1999.
- [23] H. C. van de Hulst. *Light scattering by small particles*. New York: Dover, 1981, 1981.
- [24] J. W. Hovenier, C. Van Der Mee, and H. Domke. *Transfer of polarized light in planetary atmospheres : basic concepts and practical methods*. Dordrecht: Kluwer, Springer, 2004.
- [25] O. Muñoz, F. Moreno, D. Guirado, J. L. Ramos, A. López, F. Girela, J. M. Jerónimo, L. P. Costillo, and I. Bustamante. Experimental determination of scattering matrices of dust particles at visible wavelengths: The IAA light scattering apparatus. *J. Quant. Spec. Radiat. Transf.*, 111:187–196, January 2010.
- [26] J. W. Hovenier. *Measuring Scattering Matrices of Small Particles at Optical Wavelengths*, page 355. *Light Scattering by Nonspherical Particles : Theory, Measurements, and Applications*, January 2000.
- [27] J. W. Hovenier, H. C. van de Hulst, and C. V. M. van der Mee. Conditions for the elements of the scattering matrix. *A&A*, 157:301–310, March 1986.
- [28] H. Volten, O. Muñoz, J. W. Hovenier, and L. B. F. M. Waters. An update of the Amsterdam Light Scattering Database. *J. Quant. Spec. Radiat. Transf.*, 100:437–443, July 2006.
- [29] B. T. Draine. The discrete-dipole approximation and its application to interstellar graphite grains. *Astrophys. Journal*, 333:848–872, October 1988.
- [30] E. Zubko, D. Petrov, Y. Grynko, Y. Shkuratov, H. Okamoto, K. Muinonen, T. Nousiainen, H. Kimura, T. Yamamoto, and G. Videen. Validity criteria of the discrete dipole approximation. *Applied Optics*, 49:1267, March 2010.
- [31] D. D. Dabrowska, O. Muñoz, F. Moreno, T. Nousiainen, and E. Zubko. Effect of the orientation of the optic axis on simulated scattering matrix elements of small birefringent particles. *Optics Letters*, 37:3252, August 2012.

## Chapter 7

# ”The Amsterdam-Granada Light Scattering Database”

O. Muñoz, F. Moreno, D. Guirado, D.D. Dabrowska, H. Volten, J.W. Hovenier *The Amsterdam-Granada Light Scattering Database*, Journal of Quantitative Spectroscopy and Radiative Transfer, **113** (2012), 565-574

**Abstract** The Amsterdam Light Scattering Database proved to be a very successful way of promoting the use of the data obtained with the Amsterdam Light Scattering apparatus at optical wavelengths. Many different research groups around the world made use of the experimental data. After the closing down of the Dutch scattering apparatus, a modernized and improved descendant, the IAA Cosmic Dust Laboratory (CoDuLab), has been constructed at the Instituto de Astrofísica de Andalucía (IAA) in Granada, Spain. The first results of this instrument for water droplets and for two samples of clay particles have been published. We would now like to make these data also available to the community in digital form by introducing a new light scattering database, the Amsterdam-Granada Light Scattering Database ([www.iaa.es/scattering](http://www.iaa.es/scattering)). By combining the data from the two instruments in one database we ensure the continued availability of the old data, and we prevent fragmentation of important data over different databases. In this paper we present the Amsterdam-Granada Light Scattering Database.

## 7.1 Introduction

In the last few decades, the Amsterdam light scattering setup [1] fulfilled a unique position in producing a significant amount of experimental scattering matrices as functions of the scattering angle of samples of small irregular particles relevant for astronomy, and studies of the atmosphere, as well as coastal and inland waters of the Earth (see e.g. [2, 3, 4, 5, 6, 7, 8]). The measurements of aerosols were performed at two different wavelengths (441.6 and 632.8 nm) in the scattering angle range from 3-5 degrees (depending on the sample) to 174 degrees. The hydrosol measurements were done at 632.8 nm in the scattering angle range from 20 to 160 degrees. These experimental data are a powerful tool for properly interpreting space- and ground-based observations or for testing different computational approaches devoted to obtain the scattering behavior of small irregular particles (e.g. [9, 10, 11, 12, 13, 14, 15, 16]). In addition, the light scattering results may also be applicable in the paper and paint industry, or in the fields of chemistry and biology.

Since September 2003, the Dutch experimental data are freely available in digital form in the Amsterdam Light Scattering Database [17, 18]. The success of this database is clearly demonstrated by the increasing number of different research groups (see e.g. [19, 20, 21, 22, 23, 24, 25, 26, 27, 28, 29, 30, 31, 32, 33, 34, 35, 36, 37]) that make use of the data. The Amsterdam Light scattering setup was closed in 2007, but a modernized and improved descendant of the Dutch scattering apparatus, the IAA Cosmic Dust Laboratory (CoDuLab), has been constructed at the Instituto de Astrofísica de Andalucía (IAA) in Granada, Spain [38]. In the new apparatus the scattering angle range at which the measurements are performed is  $3^{\circ}$ - $177^{\circ}$  degrees. The measurements can be performed at five different wavelengths namely, 483, 488, 520, 568, and 647 nm. The first results of this instrument for water droplets and for a sample of green clay particles, that had also been studied in Amsterdam, demonstrate the excellent performance of the Granadian instrument [39]. We proceed to make these data also available for the community in tabular form by constructing a new light scattering database, the Amsterdam-Granada Light Scattering Database (AGLSD), available at the website ([www.iaa.es/scattering](http://www.iaa.es/scattering)). This database consists of two branches, one with experimental data from Amsterdam and the other one with experimental data from Granada. By combining the data from the two instruments in one database we ensure the continued availability of the old data, and we prevent fragmentation of scattering data over different databases.

The purpose of this paper is to introduce the new Amsterdam-Granada Light Scattering Database, and to explain the improvements made to this database with respect to the old Amsterdam Light Scattering Database. The main improvements pertain to the user-friendliness of the database. By way of example we demonstrate the usefulness of the database by applying it to dust in the Martian atmosphere.

## 7.2 Amsterdam-Granada Light Scattering Database

In Fig. 7.1 we present the main page of the website of the Amsterdam-Granada Light Scattering Database (AGLSD). It consists of two branches from which experimental data from Amsterdam (Fig. 7.2) and Granada (Fig. 7.3) can be selected by clicking at the corresponding buttons. All measurements presented in the database have been previously published in peer-reviewed scientific journals predominantly in graphical form. References and access to the full text of those papers are also provided. Data in this database are freely available under the request of citation of this paper and the paper in which the used data were published. As in the Amsterdam branch, the heart of the AGLSD is the collection of tables and plots of the measured scattering matrix elements listed as functions of the scattering angle at different wavelengths. The database also includes information on the sample under study such as, size distribution, composition, origin, optical and/or scanning microscope images, and refractive indices of the particles. In addition, a detailed theoretical basis is provided to facilitate the correct use of the experimental data. Although the Amsterdam light scattering setup was closed in 2007 some of its experimental data have not been published yet. We update the AGLSD regularly with new

data from Amsterdam and Granada. As shown in Fig. 7.1, new measurements included in the AGLSD will be high-lighted in the main page as "Latest News". In this section we present the contents of the AGLSD, which hereafter will be referred to as the database.

## 7.2.1 Samples

The particle samples included in the database comprise a wide range in origin and composition, and have relevance for different subjects. Light scattering by particles with typical diameters (or volume-equivalent diameters) ranging from sub-micron to about 200 micron were measured with the experimental setups in Amsterdam and Granada. In Figs. 7.4 and 7.5, we present a complete table of samples included in the database at the time of writing this paper, together with some relevant information such as wavelengths, scattering angle range at which the measurements have been performed, and effective radii,  $r_{\text{eff}}$ , and variance,  $v_{\text{eff}}$ , as defined by Hansen and Travis [40]:

$$r_{\text{eff}} = \frac{\int_0^{\infty} r \pi r^2 n(r) dr}{\int_0^{\infty} \pi r^2 n(r) dr} \quad (7.1)$$

$$v_{\text{eff}} = \frac{\int_0^{\infty} (r - r_{\text{eff}})^2 \pi r^2 n(r) dr}{r_{\text{eff}}^2 \int_0^{\infty} \pi r^2 n(r) dr}, \quad (7.2)$$

where  $r$  is the radius and  $n(r)$  is the size distribution of volume equivalent spheres. The values for  $r_{\text{eff}}$  and  $v_{\text{eff}}$  presented in the complete table of samples are retrieved from the size distribution measurements based on the Fraunhofer diffraction theory (see Sect. 7.2.1). This table is available at the main page of the database under the "summary of samples" link (Fig. 7.1). Within the table, by clicking at the sample of interest the user is re-directed to the part of the database where the complete description of the sample and measurements are available. As shown in Figs. 7.4 and 7.5, a high percentage of the data presented in the database correspond to aerosol measurements although some measurements on hydrosols are also presented. Moreover, measurements on spherical water droplets that are used as test particles at different wavelengths are provided. For the water droplets measurements at 488, 520, and 647 nm we provide, instead of the effective radii and variance, the  $r_g$  and  $\sigma_g$  parameters corresponding to a log-normal size distribution as defined by Hansen and Travis [40].

## General information

Once you are in any of the two branches by clicking on the name of a certain sample, general information concerning the sample is provided on a fact sheet. For instance, the origin of the sample is given together with qualitative estimates of its main constituents. They may give an indication of the refractive index of the bulk sample. For cases where the refractive index is not accurately known, we provide an estimate of the real part of the refractive index,  $\text{Re}(m)$ , based on values found in the literature for the constituent minerals. Less information is usually available for the imaginary part of the refractive index,  $\text{Im}(m)$ , because the natural variability within a mineral can be quite large. An indication of whether the value of  $\text{Im}(m)$  is relatively high or low is given by the color of the powdered sample, since white looking powders absorb little. The colors of the powders are mentioned or shown on photographs. For example, by clicking on the green clay sample you will see that its main constituent minerals are illite, kaolinite, montmorillonite, and quartz. Based on literature values [41, 42, 43, 44], we may assume that the real part of the refractive index of green clay lies between 1.5 and 1.7, while the imaginary part likely lies in the range between  $10^{-5}$  and  $10^{-3}$  at visual wavelengths.

As mentioned, the scattering matrices of some of the samples presented in the database might be useful for various applications. As an example, clay particles are believed to occur on different Solar System bodies such as Mars, satellites, and asteroids. Clay is also an important component of mineral aerosols in the Earth atmosphere. This type of information will be provided for the new samples in the corresponding fact sheet under the *practical significance* item.



To give an indication of the shapes of the grains we provide one or more scanning electron microscope and/or optical images in the database for each sample. In order to check if the aerosol jet may change the shape/size of the particles during the measurements, either by breaking them up into smaller particles or by aggregating them into larger particles, we made several special test images. Field Emission Scanning Electron Microscope (FESEM) images were made for the sample under study as it was during the light scattering measurements, i.e. particles directly collected from the aerosol jet [39, 45]. Comparison of images of the sample directly taken from the container and that taken from the jet stream showed no evidence of a significant alteration of the particles produced by the aerosol generator. This is illustrated in Fig. 7.6, which shows FESEM images of some green clay particles directly collected from the container (left panel) and from the aerosol jet stream (right panel). The FESEM/SEM images presented in the Granada branch (unless indicated otherwise) are taken from a glass slide briefly held in the aerosol jet at the place where it intersects with the laser beam.

It is important to note that the FESEM/SEM images in the database are not suited to infer detailed information about the sizes of the particles, mainly because they range over several orders of magnitude in most cases, so that images with lower magnification will be biased towards showing only larger particles, and viceversa.

Figures of the measured size distributions (Sect. 7.2.1) and scattering matrices (Sect. 7.2.2) are also provided, as well as the PDF file of the paper in which the data were published.

### Size distributions

Apart from shape and composition, size is a key property in determining the light scattering properties of small particles. In a collection of randomly oriented nonspherical particles we can replace each particle by a sphere with radius,  $r$ , having the same average (over all rotations) projected surface area or volume. In this way we can obtain size distributions. In the database we provide tables for normalized number, projected-surface-area, and volume size distributions. To plot these three size distributions in a convenient way a change of variables from  $r$  to  $\log r$  is often performed, so that three different types of size distributions are formed, the normalized number distribution  $N(\log r)$ , the normalized projected-surface-area distribution  $S(\log r)$ , and the normalized volume distribution  $V(\log r)$ . In this way, equal areas under parts of the curve obtained by plotting  $N(\log r)$  versus  $\log r$ , means equal relative number of particles per unit volume in the ranges considered. A similar property holds for plots of  $S(\log r)$  and  $V(\log r)$  versus  $\log r$ .

Size distributions as functions of radii,  $r$ , are common in the literature and often required for numerical applications. Thus, in addition to the mentioned  $N(\log r)$ ,  $S(\log r)$ , and  $V(\log r)$ , the corresponding  $n(r)$ ,  $s(r)$ , and  $v(r)$  distributions for the new samples presented in the database will be also provided. Detailed information on how to transform one size distribution into another can be found in the database at [www.iaa.es/scattering/site\\_media/sizedistributions.pdf](http://www.iaa.es/scattering/site_media/sizedistributions.pdf) and in [17]. It is often useful to characterize the sizes of the particles of a sample with two parameters: the effective radius  $r_{\text{eff}}$ , and effective standard variance  $v_{\text{eff}}$ . In the database we provide the calculated effective radius,  $r_{\text{eff}}$ , and the effective variance,  $v_{\text{eff}}$  as defined in [40] (see Eqs. 7.1 and 7.2) for all our samples.

The projected-surface-area size distributions of the samples studied in Amsterdam were measured by using a Fritsch laser particle sizer [46] that employs the Fraunhofer diffraction theory for spheres. The particle sizer used in Granada is a Mastersizer2000 from Malvern instruments. The Mastersizer measures the phase function of the sample at 633 nm in a certain scattering angle range with special attention to the forward scattering peak. Once it is measured it uses either Lorenz-Mie theory or Fraunhofer theory for spheres to retrieve the volume distribution that best fits the measured scattering pattern. It is clear that the retrievals from both methods are simplifications based on the assumption that the particles of the sample under study are spherical. Moreover, the Fraunhofer method has the restriction that the particles must be large compared to the wavelength of the incident light. However, at this moment this is the best that can be done as far as particle sizing for broad distributions of irregular particles is concerned. At the Granada branch we present the size distributions retrieved from both Fraunhofer and

Lorenz-Mie theory so that the reader can choose which one is more appropriate for her/his purposes or take the average. As an example, Fig. 7.7 shows the measured  $V(\log r)$  as a function of  $\log r$  obtained from both, Fraunhofer and Lorenz-Mie theory for the green clay sample [4, 39]. For comparison purposes we also present the  $V(\log r)$  for a sample of Saharan dust collected in Libya (Sahara sand, Libya) [47]. In general, increasing the size of a particle with a certain shape promotes diffraction and the shapes of diffraction peaks of collections of randomly oriented particles are similar for different particle shapes as confirmed by various computations [48]. Thus, as shown in Fig. 7.7, results of both sizing methods tend to converge as the particles become larger, as is the case for the Sahara sand (Libya) sample that consists of particles larger than the wavelength of the incident light. In Tab. 7.1. we present the values of the effective radius,  $r_{\text{eff}}$ , and effective variance,  $v_{\text{eff}}$ , obtained from the measured size distributions in Amsterdam and Granada, respectively for the green clay and Sahara sand (Libya) samples. As shown, the values retrieved for  $r_{\text{eff}}$  and  $v_{\text{eff}}$  based on Fraunhofer theory in Amsterdam and Granada are very similar to each other even though the measurements have been performed far away in time ( $\simeq 10$  years) and with completely different devices.

## 7.2.2 Measured scattering matrix elements

The flux and state of linear and circular polarization of a quasi-monochromatic beam of light can be described by means of the so-called flux vector whose elements are Stokes parameters [49, 50]. If such a beam of light is singly scattered by an ensemble of particles and is observed from a distance much greater than the maximal linear dimension of the ensemble (far-field approximation [51]), the flux vectors of the incident beam  $\pi\Phi_0$  and scattered beam  $\pi\Phi$  are, for each scattering direction, related by the so called  $4 \times 4$  scattering matrix,  $\mathbf{F}$ , with elements  $F_{i,j}$ . For randomly oriented particles, all scattering planes are equivalent. Thus, the scattering direction is fully described by the scattering angle  $\theta$ , i.e. the angle between the directions of propagation of the incident and the scattered beams. Moreover, when randomly oriented irregular particles and their mirror particles are present in equal numbers in the ensemble, as is the case in our experiments, the scattering matrix has only six independent elements that are not identically equal to zero. A detailed description of the scattering matrix measured during the experiments can be found in the database at [www.iaa.es/scattering/site\\_media/scatteringmatrix.pdf](http://www.iaa.es/scattering/site_media/scatteringmatrix.pdf).

As mentioned, the measurements of our experimental apparatus must be performed under single scattering conditions. Therefore, we must have enough particles in the scattering volume to be representative for the ensemble of randomly oriented particles under study, but not so many that multiple scattering might start playing a role. Special test experiments were performed which show that our experimental results for scattering matrices are not significantly contaminated by multiple scattering [39, 45].

It is important to remark that the measured values of  $F_{11}(\theta)$  for the aerosol samples in the database are normalized so that they are equal to 1 at  $\theta = 30$  degrees [5]. The function  $F_{11}(\theta)$ , normalized in this way, is proportional to the flux of the scattered light for unpolarized incident light and called the *phase function* or *scattering function* throughout the database. Furthermore, all scattering matrix elements, except  $F_{11}(\theta)$  itself are given relative to  $F_{11}(\theta)$ , i.e., we present  $F_{ij}(\theta)/F_{11}(\theta)$ , with  $i, j=1$  to 4 except for  $i=j=1$ . Also, for unpolarized incident light, the ratio  $-F_{12}(\theta)/F_{11}(\theta)$  coincides with the *degree of linear polarization* of the scattered light. A detailed description of the scattering matrix elements tabulated in the database and the way they are normalized can be found in the database at [www.iaa.es/scattering/site\\_media/normalization.pdf](http://www.iaa.es/scattering/site_media/normalization.pdf) and in [18]. In addition to each measured matrix element (ratio) value, the experimental errors are also given. We refrain from listing the four element ratios  $F_{13}(\theta)/F_{11}(\theta)$ ,  $F_{14}(\theta)/F_{11}(\theta)$ ,  $F_{23}(\theta)/F_{11}(\theta)$ , and  $F_{24}(\theta)/F_{11}(\theta)$ , since we verified that these ratios never differ from zero by more than the experimental errors. This is consistent with scattering samples consisting of randomly oriented particles with equal amounts of particles and their mirror particles [49].

Different conventions are used for Stokes parameters and, in particular for the sign of the ratio of scattering matrix elements  $F_{34}(\theta)/F_{11}(\theta)$ . The convention employed here is in accordance with [49] and [50]. The scattering matrices given in the database satisfy the Cloude coherency matrix test as suggested by Hovenier et al. [50] within the accuracy of the measurements.

### 7.2.3 Average and Synthetic matrices

The high similarity of the measured scattering matrices for different samples of irregular mineral compact particles induced us to construct an Average Aerosol Scattering matrix [5]. The Average is obtained from the measured scattering matrices of seven samples of irregular compact particles: feldspar, red clay, quartz, Pinatubo volcanic ash, loess, Lokon volcanic ash, and Sahara sand at two different wavelengths, 441.6 and 632.8 nm. The Average Aerosol Scattering Matrix is obtained as follows. First, the Average Aerosol phase function,  $F_{11}(\theta)$ , is determined by averaging the 14 phase functions measured at both wavelengths. Since no scattering cross sections are available, the phase functions are averaged giving them equal weights. As mentioned in Sect. 7.2.2, the 14 measured phase functions are all normalized to one at 30 degrees and this is also the case for the Average phase function. Second, each measured element ratio is multiplied by its corresponding normalized phase function, thus yielding elements instead of element ratios. Third, for each pair of indices (i,j) the elements  $F_{i,j}(\theta)$  of the Average Aerosol Scattering Matrix are obtained by averaging the 14 corresponding elements. Finally, division by the Average phase function yields the element ratios of the Average Aerosol Scattering Matrix. The resulting Average Matrix satisfies the Cloude test at each measured scattering angle.

A similar average scattering matrix was obtained for volcanic ash particles [6]. The average scattering matrices can be used, for example, in remote sensing studies for which the specific properties of the mineral aerosols or the volcanic ash are often not known (e.g. [11, 16]). Moreover, using various computational techniques the average volcanic scattering matrix as well as the measured matrices for Sahara sand (Libya) [47], and the Martian analog (palagonite) particles [52] were extrapolated to cover the full range of scattering angles from  $0^\circ$  to  $180^\circ$  (e.g. [6, 21]). These are called synthetic scattering matrices.

Tables of the Average Aerosol Scattering matrix and Synthetic Average Volcanic Scattering Matrix, as well as the mentioned synthetic scattering matrices for Sahara sand (Libya) and a Martian analog (palagonite) sample, are available in the database and can be directly accessible through the “summary of samples” table at the main page of the database (see Fig. 7.5).

## 7.3 Applications

The experimental data can be used in a direct manner, e.g. by comparison with astronomical observations of light scattered in single scattering conditions. Further, experimental scattering matrices are used to check the validity of advanced computational techniques devoted to simulate the scattering behavior of realistic polydisperse irregular particles e.g. [12, 13, 25, 31, 33, 36, 37, 53, 54, 55]. Also the data can be used in an indirect manner if a method is applied to extrapolate the measured angular distributions of the scattering matrix elements to the full scattering angle range, including forward and backward scattering [21, 47, 56], the extrapolated functions can be used to perform multiple scattering calculations in scattering media such as planetary atmospheres and circumstellar disks of dust particles [9, 10, 19, 21, 53]. Apart from that, measuring all elements of the scattering matrix instead of one or two helps us in identifying errors in the electronics or in the alignment of the optics involved in the experiment since all theoretical relationships valid for the elements of the scattering matrix [50, 57] can be applied for tests.

### 7.3.1 An example: Martian atmosphere

Dust from the Martian surface is regularly swept up by winds and becomes suspended in the atmosphere of Mars. These airborne dust particles scatter and absorb solar radiation thereby playing a key role in determining the thermal structure of the thin Martian atmosphere. Thus, quantifying the effect of such particles in the atmosphere has been and still is a hot topic in Martian studies. This task is obviously far from trivial. This is not only due to the limitations of computational techniques to reproduce the scattering behavior of natural polydisperse irregular particles. In addition, astronomers have to face the lack of measurements of various input

parameters needed for their radiative transfer codes (see e.g. [58, 59, 60, 61], and references therein). The scattering function at a certain wavelength of Martian dust particles has been often derived by using the semi-empirical theory for nonspherical particles developed by Pollack and Cuzzi [62]. It is based on the use of Mie theory for spheres for the scattering function of particles smaller than a certain size parameter combined with results of approximate formulae for larger particles. Lately, the efforts have been focused on the use of more sophisticated model particles, namely cylinders, to calculate the phase function of Martian dust particles [61, 63, 64, 65, 66]. Even so, as pointed out by Wolff et al. [65], the calculated phase functions for a size distribution of cylinders produce a considerable overestimation of the phase function near backscattering direction when comparing with the Tomasko et al. [59] empirically derived phase functions of Martian dust. Therefore, the calculated phase functions require an empirical correction to remove the artificial backscattering enhancement that is not found either in the experimental phase functions for ensembles of randomly oriented irregular compact particles presented in the AGLSD (see e.g. Sect. 7.2.3).

As an example of the use of the AGLSD in Fig. 7.8, we show one of the four phase functions presented by Tomasko et al. [59] for Martian aerosols based on data of the Imager for Mars Pathfinder (IMP). In particular, we show the retrieved phase function at 671 nm corresponding to a gamma size distribution [40] with  $r_{\text{eff}}$  equal to  $1.6 \mu\text{m}$  and  $v_{\text{eff}}$  equal to 0.2. In Fig. 7.8, we also present the experimental phase function for a palagonite sample [52] considered as a Martian dust analogue [67], the so called Martian analog (palagonite) sample. The palagonite sample has a real part of the refractive index,  $\text{Re}(m)=1.5$  and an imaginary part,  $\text{Im}(m)$ , in the range  $10^{-3}$  to  $10^{-4}$  at visible wavelengths [68]. The  $r_{\text{eff}}$  and  $v_{\text{eff}}$  of the palagonite sample equal  $4.5 \mu\text{m}$  and 7.3, respectively. The phase functions presented in Fig. 7.8 are normalized to unity at 30 degrees scattering angle. Despite the differences in the size distributions of the Martian dust derived by Tomasko et al. [59] and the Martian analog (palagonite) sample, the agreement between both phase functions is remarkable. The main discrepancies are related to the forward diffraction peak that is highly dependent on the size of the particles. This direct comparison suggests that the measured scattering function of the Martian analog (palagonite) sample may be considered a good approximation for Martian dust at the mentioned wavelengths.

## 7.4 Discussion and conclusion

A large collection of scattering matrices as functions of the scattering angle for irregular mineral particles is available in the Amsterdam-Granada light scattering database. To ensure the reliability of these data only data that have been previously published in peer-reviewed scientific journals have been included in the AGLSD. To facilitate the correct use of the experimental data detailed theoretical information is also provided in the database e.g. on size distributions and scattering matrices. Data in this database are freely available under request of citation of this paper and the paper in which the used data were published. We plan to update this database regularly with new light scattering matrices for various samples of particles. We would appreciate to be informed about new works in which the experimental data presented in the AGLSD are used. That information would help us to obtain a realistic view on which samples are of major interest for the scientific community.

	Sample	Fraun. Ams	Fraun. Gr	Mie Gr
$r_{\text{eff}}$	Green Clay	$1.55 \mu\text{m}$	$1.62 \mu\text{m}$	$2.24 \mu\text{m}$
$v_{\text{eff}}$	Green Clay	1.40	1.57	1.08
$r_{\text{eff}}$	Sahara sand, Libya	$124.75 \mu\text{m}$	$130.22 \mu\text{m}$	$130.90 \mu\text{m}$
$v_{\text{eff}}$	Sahara sand, Libya	0.15	0.11	0.11

Table 7.1: Effective radius and effective variance obtained from the measured size distributions of green clay and Sahara sand (Libya) in Amsterdam and Granada.

**Amsterdam-Granada light scattering database**

Data in this database are freely available under the request of citation of [this paper](#) and the paper in which the used data were published.

In the last decades, the **experimental setup located in Amsterdam**, The Netherlands, has produced a significant number of experimental scattering matrices as functions of the scattering angle of randomly oriented small particles. The Dutch setup was closed in 2007. An improved descendant of the Dutch experimental setup has been recently constructed at the Instituto de Astrofísica de Andalucía, CSIC, the **IAA cosmic dust laboratory**. To provide an incentive for further research and applications all published Dutch and Spanish experimental data are accessible through this database.

**Summary of samples in the Amsterdam-Granada Light Scattering Database.**

AMSTERDAM LIGHT SCATTERING DATABASE (1989-2007)

GRANADA LIGHT SCATTERING DATABASE (2008-2011)

**LATEST NEWS**

**First measurements of the IAA Cosmic Dust Laboratory available**

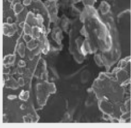
 **Nov 16th, 2010** The first results of measurements on solid particles (white and green clay) performed at the Instituto de Astrofísica de Andalucía (IAA) Cosmic Dust Laboratory (Granada, Spain) are available. The laboratory apparatus measures the complete scattering matrix as a function of the scattering angle of aerosol particles. [Read more](#)

Figure 7.1: Main page of the Amsterdam-Granada Light Scattering Database available at [www.iaa.es/scattering](http://www.iaa.es/scattering).

Data in this database are freely available under the request of citation of [this paper](#) and the paper in which the used data were published.

**The Amsterdam Light Scattering Database**

Hester Volten\*, Olga Muñoz<sup>†</sup>, Joop Hovenier\*, Rens Waters\*

\*Astronomical Institute "Anton Pannekoek", University of Amsterdam, Netherlands

<sup>†</sup>Instituto de Astrofísica de Andalucía, CSIC, Granada, Spain

Last update: October 2011

**Table of content**

- [Aerosol particles](#)
- [Hydrosol particles](#)
- [Organization of the database](#)
- [Amsterdam Light Scattering Database Tables](#)
- [Articles and background information](#)
- [Questions or comments?](#)

Figure 7.2: Amsterdam branch of Amsterdam-Granada Light Scattering Database.

Figure 7.3: Granada branch of Amsterdam-Granada Light Scattering Database.

Sample	$r_{\text{eff}}$ (micron)	$v_{\text{eff}}$	Wavelengths (nm)	Angle range (deg.)
<b>AEROSOLS</b>				
Aggregates (fluffy) Sample 1	--	--	632.8	[5,174]
Aggregates (fluffy) Sample 2	--	--	632.8	[5,174]
Aggregates (fluffy) Sample 3	--	--	632.8	[5,174]
Aggregates (fluffy) Sample 4	--	--	632.8	[5,174]
Aggregates (fluffy) Sample 5	--	--	632.8	[5,174]
Aggregates (fluffy) Sample 6	--	--	632.8	[5,174]
Aggregates (fluffy) Sample 7	--	--	632.8	[5,174]
Allende Meteorite	0.8	3.3	632.8, 441.6	[5,173]
Clay Green (Amsterdam)	1.55	1.4	632.8, 441.6	[5,173]
Clay Green (Granada)	1.6	1.6	647	[3,177]
Clay Red	1.5	1.6	632.8, 441.6	[5,173]
Clay White	1.6	1.4	488, 647	[3,177]
Feldspar	1.0	1.0	632.8, 441.6	[5,173]
Fly Ash	3.65	10.9	632.8, 441.6	[5,173]
Forsterite Initial	1.8	5.4	632.8	[5,173]
Forsterite Small	1.3	3.1	632.8	[5,173]
Forsterite Washed	3.3	4.7	632.8	[5,173]
Hematite	0.4	0.6	632.8	[5,174]
Loess	3.9	2.6	632.8, 441.6	[5,173]
Martian Analog (palagonite)	4.5	7.3	632.8	[3,174]
Olivine L	3.8	3.7	632.8, 441.6	[5,173]
Olivine M	2.6	5.0	632.8, 441.6	[5,173]
Olivine S	1.3	1.8	632.8, 441.6	[5,173]
Olivine XL	6.3	6.8	632.8, 441.6	[5,173]
Quartz	2.3	2.3	632.8, 441.6	[5,173]
Rutile	0.13	0.5	632.8	[5,173]
Sahara Sand	8.2	4.0	632.8, 441.6	[5,173]
Sahara Sand (Libya)	124.75	0.15	632.8	[4,174]
Volcanic Ash (el chichon)	3.2	5.4	632.8	[5,173]
Volcanic Ash (Lokon)	7.1	2.6	632.8, 441.6	[5,173]
Volcanic Ash (Mount St. Helens)	4.1	9.5	632.8	[3,173]
Volcanic Ash (Pinatubo)	3.0	12.3	632.8, 441.6	[5,173]
Volcanic Ash (Redoubt A)	4.1	9.7	632.8	[3,173]
Volcanic Ash (Redoubt B)	6.4	7.6	632.8	[3,173]
Volcanic Ash (Spurr Anchorage)	4.8	8.8	632.8	[3,174]
Volcanic Ash (Spurr Ashton)	2.7	4.9	632.8	[3,174]
Volcanic Ash (Spurr Gunsight)	3.5	8.2	632.8	[3,174]
Volcanic Ash (Spurr stop 33)	14.4	6.6	632.8	[3,174]

Figure 7.4: Summary of samples in the Amsterdam-Granada Light Scattering Database.

HYDROSOLS				
Anabaena flos aquae	3.09	0.012	632.8	[20,160]
Astrionella formosa	4.23	0.010	632.8	[20,160]
Emiliania huxleyi, no coccoliths	1.8	0.002	632.8	[35,145]
Emiliania huxleyi with coccoliths	1.8	0.07	632.8	[35,145]
Melosira granulata	3.74	0.004	632.8	[20,160]
Microcystis aeruginosa, no gas vacuoles	5.23	0.50	632.8	[20,160]
Microcystis aeruginosa with gas vacuoles	6.83	0.92	632.8	[20,160]
Microcystis sp.	1.87	0.063	632.8	[20,160]
Oscillatoria agardhii	1.64	0.044	632.8	[20,160]
Oscillatoria amoena	2.58	0.002	632.8	[20,160]
Phaeodactylum	16.4	0.23	632.8	[20,160]
Phaeocystis	12.2	0.43	632.8	[20,160]
Prochlorothrix hollandica	1.55	0.080	632.8	[20,160]
Selenastrum capricornutum	1.09	0.037	632.8	[20,160]
Volvox aureus	105	0.07	632.8	[20,160]
Westerschelde silt, 5-12 micron	5.93	0.00	632.8	[20,160]
Westerschelde silt, 3-5 micron	1.95	0.50	632.8	[20,160]
TEST PARTICLES				
Water Droplets	1.1	0.50	632.8, 441.6	[5, 173]
Water Droplets	rg=0.8 micron	sigmag=1.5	488, 520, 647	[3, 177]
AVERAGE AND SYNTHETIC SCATTERING MATRICES				
Average Aerosol Scattering Matrix	--	--	632.8 and 441.6 combined	[5,175]
Synthetic Average Volcanic Scattering Matrix	--	--	632.8	[0,180]
Synthetic Matrix Sahara Sand (Libya)	--	--	632.8	[0,180]
Synthetic Matrix Martian analog (palagonite) particles	--	--	632.8	[0,180]

Figure 7.5: Continued from Fig 7.4.

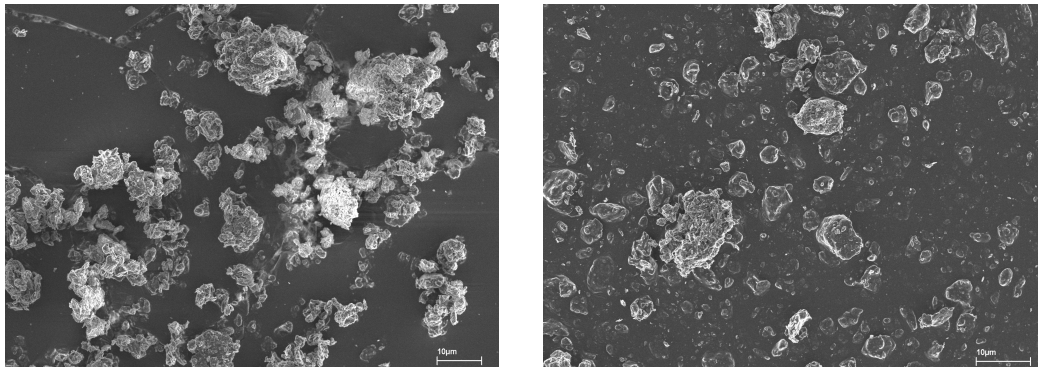


Figure 7.6: FESEM images of green clay particles directly collected from the container (left panel) and collected from the aerosol jet (right panel).

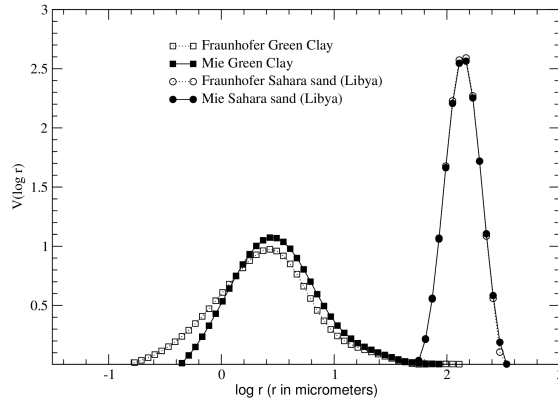


Figure 7.7: Normalized volume distributions as a function of  $\log r$  for the green clay and Sahara sand (Libya) samples. The volume distributions have been retrieved by assuming Lorenz-Mie (solid symbols) and Fraunhofer (empty symbols) theories.

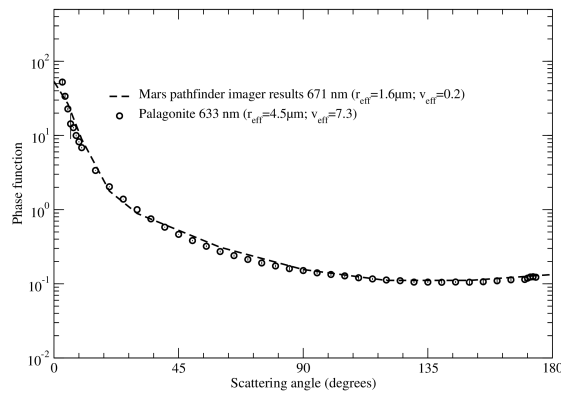


Figure 7.8: Measured phase function of the Martian analog (palagonite) sample compared to the phase function derived by Tomasko et al. [59] for Martian dust particles. Both phase functions are normalized to 1 at 30 degrees scattering angle.



**Acknowledgements**

Timo Nousiainen and Michael Kahnert are heartily acknowledged for their encouragement and constructive suggestions on a previous version of the Amsterdam-Granada Light Scattering Database. Comments of M. Wolff and an anonymous referee on an earlier version of this paper are gratefully acknowledged. We are indebted to A. González from the Scientific Instrumentation Center of the University of Granada who took the FESEM images of the green clay sample. This work has been supported by the Plan Nacional de Astronomía y Astrofísica under contract AYA2009-08190, and Junta de Andalucía, contract P09-FMQ-4555.



# Bibliography

- [1] J. W. Hovenier. *Measuring Scattering Matrices of Small Particles at Optical Wavelengths*, page 355. *Light Scattering by Nonspherical Particles : Theory, Measurements, and Applications*, January 2000.
- [2] H. Volten, J. F. de Haan, J. W. Hovenier, R. Schreurs, W. Vassen, A. G. Dekker, H. J. Hoogenboom, F. Charlton, and R. Wouts. Laboratory measurements of angular distributions of light scattered by phytoplankton and silt. *Limnology and Oceanography*, vol.43, pp. 1180-1197, 43:1180–1197, 1998.
- [3] O. Muñoz, H. Volten, J. F. de Haan, W. Vassen, and J. W. Hovenier. Experimental determination of scattering matrices of olivine and Allende meteorite particles. *A&A*, 360:777–788, August 2000.
- [4] O. Muñoz, H. Volten, J. F. de Haan, W. Vassen, and J. W. Hovenier. Experimental determination of scattering matrices of randomly oriented fly ash and clay particles at 442 and 633 nm. *J. Quant. Spec. Radiat. Transf.*, 106:22833, October 2001.
- [5] H. Volten, O. Muñoz, E. Rol, J. F. de Haan, W. Vassen, J. W. Hovenier, K. Muinonen, and T. Nousiainen. Scattering matrices of mineral aerosol particles at 441.6 nm and 632.8 nm. *J. Geophys. Res.*, 106:17375–17402, August 2001.
- [6] O. Muñoz, H. Volten, J. W. Hovenier, B. Veihelmann, W. J. van der Zande, L. B. F. M. Waters, and W. I. Rose. Scattering matrices of volcanic ash particles of Mount St. Helens, Redoubt, and Mount Spurr Volcanoes. *Journal of Geophysical Research (Atmospheres)*, 109:16201, August 2004.
- [7] H. Volten, O. Muñoz, J. R. Brucato, J. W. Hovenier, L. Colangeli, L. B. F. M. Waters, and W. J. van der Zande. Scattering matrices and reflectance spectra of forsterite particles with different size distributions. *J. Quant. Spec. Radiat. Transf.*, 100:429–436, July 2006.
- [8] H. Volten, O. Muñoz, J. W. Hovenier, F. J. M. Rietmeijer, J. A. Nuth, L. B. F. M. Waters, and W. J. van der Zande. Experimental light scattering by fluffy aggregates of magnesiosilica, ferrosilica, and alumina cosmic dust analogs. *A&A*, 470:377–386, July 2007.
- [9] F. Moreno, O. Muñoz, J. J. López-Moreno, A. Molina, and J. L. Ortiz. A Monte Carlo Code to Compute Energy Fluxes in Cometary Nuclei. *Icarus*, 156:474–484, April 2002.
- [10] M. Mishchenko, I. Geogdzhaev, L. Liu, A. Orgen, A. Lacis, W. Rossow, J. Hovenier, H. Volten, and O. Muñoz. Aerosol retrievals from AVHRR radiances: effects of particle nonsphericity and absorption and an updated long-term global climatology of aerosol properties. *J. Quant. Spec. Radiat. Transf.*, 79:953, September 2003.
- [11] M. Herman, J.-L. Deuzé, A. Marchand, B. Roger, and P. Lallart. Aerosol remote sensing from POLDER/ADEOS over the ocean: Improved retrieval using a nonspherical particle model. *Journal of Geophysical Research (Atmospheres)*, 110:10, May 2005.
- [12] T. Nousiainen, K. Muinonen, and P. Räisänen. Scattering of light by large Saharan dust particles in a modified ray optics approximation. *Journal of Geophysical Research (Atmospheres)*, 108:4025, January 2003.
- [13] O. Dubovik, A. Sinyuk, T. Lapyonok, B. N. Holben, M. Mishchenko, P. Yang, T. F. Eck, H. Volten, O. Muñoz, B. Veihelmann, W. J. van der Zande, J.-F. Leon, M. Sorokin, and I. Slutsker. Application of spheroid models to account for aerosol particle nonsphericity in remote sensing of desert dust. *Journal of Geophysical Research (Atmospheres)*, 111:11208, June 2006.
- [14] M. Kahnert and T. Rother. Modeling optical properties of particles with small-scale surface roughness: combination of group theory with a perturbation approach. *Optics Express*, 19:11138, June 2011.

- [15] A. García Muñoz, E. Pallé, M. R. Zapatero Osorio, and E. L. Martín. The impact of the Kasatochi eruption on the Moon's illumination during the August 2008 lunar eclipse. *Geophys. Res. Lett.*, 38:14805, July 2011.
- [16] A. Miffre, G. David, B. Thomas, and P. Rairoux. Atmospheric non-spherical particles optical properties from UV-polarization lidar and scattering matrix. *Geophys. Res. Lett.*, 38:16804, August 2011.
- [17] H. Volten, O. Muñoz, J. W. Hovenier, J. F. de Haan, W. Vassen, W. J. van der Zande, and L. B. F. M. Waters. WWW scattering matrix database for small mineral particles at 441.6 and 632.8nm. *J. Quant. Spec. Radiat. Transf.*, 90:191–206, January 2005.
- [18] H. Volten, O. Muñoz, J. W. Hovenier, and L. B. F. M. Waters. An update of the Amsterdam Light Scattering Database. *J. Quant. Spec. Radiat. Transf.*, 100:437–443, July 2006.
- [19] C. J. Braak, J. F. de Haan, C. V. M. van der Mee, J. W. Hovenier, and L. D. Travis. Parameterized scattering matrices for small particles in planetary atmospheres. *J. Quant. Spec. Radiat. Transf.*, 69:585–604, June 2001.
- [20] M. I. Mishchenko, L. D. Travis, and A. A. Lacis. *Scattering, absorption, and emission of light by small particles*. 2002.
- [21] L. Liu, M. I. Mishchenko, J. W. Hovenier, H. Volten, and O. Muñoz. Scattering matrix of quartz aerosols: comparison and synthesis of laboratory and Lorenz-Mie results. *J. Quant. Spec. Radiat. Transf.*, 79:911–920, 2003.
- [22] E. Zubko, Y. Shkuratov, M. Hart, J. Eversole, and G. Videen. Backscattering and negative polarization of agglomerate particles. *Optics Letters*, 28:1504–1506, September 2003.
- [23] R. Vilaplana, F. Moreno, and A. Molina. Computations of the single scattering properties of an ensemble of compact and inhomogeneous rectangular prisms: implications for cometary dust. *J. Quant. Spec. Radiat. Transf.*, 88:219–231, September 2004.
- [24] B. Veihelmann, T. Nousiainen, M. Kahnert, and W. J. van der Zande. Light scattering by small feldspar particles simulated using the Gaussian random sphere geometry. *J. Quant. Spec. Radiat. Transf.*, 100:393–405, July 2006.
- [25] M. Min, J. W. Hovenier, and A. de Koter. Modeling optical properties of cosmic dust grains using a distribution of hollow spheres. *A&A*, 432:909–920, March 2005.
- [26] V. K. Rosenbush and N. N. Kiselev. Polarization opposition effect for the Galilean satellites of Jupiter. *Icarus*, 179:490–496, December 2005.
- [27] M. Kahnert and T. Nousiainen. Uncertainties in measured and modelled asymmetry parameters of mineral dust aerosols. *J. Quant. Spec. Radiat. Transf.*, 100:173–178, July 2006.
- [28] T. Nousiainen, M. Kahnert, and B. Veihelmann. Light scattering modeling of small feldspar aerosol particles using polyhedral prisms and spheroids. *J. Quant. Spec. Radiat. Transf.*, 101:471–487, October 2006.
- [29] A. M. Tafuro, F. Barnaba, F. De Tomasi, M. R. Perrone, and G. P. Gobbi. Saharan dust particle properties over the central Mediterranean. *Atmospheric Research*, 81:67–93, July 2006.
- [30] M. Kahnert, T. Nousiainen, and P. Räisänen. Mie simulations as an error source in mineral aerosol radiative forcing calculations. *Quarterly Journal of the Royal Meteorological Society*, 133:299–307, January 2007.
- [31] F. Moreno, O. Muñoz, D. Guirado, and R. Vilaplana. Comet dust as a size distribution of irregularly shaped, compact particles. *J. Quant. Spec. Radiat. Transf.*, 106:348–359, July 2007.
- [32] S. R. Cloude. Depolarization by aerosols: Entropy of the Amsterdam light scattering database. *J. Quant. Spec. Radiat. Transf.*, 110:1665–1676, September 2009.
- [33] K. Muinonen, T. Nousiainen, H. Lindqvist, O. Muñoz, and G. Videen. Light scattering by Gaussian particles with internal inclusions and roughened surfaces using ray optics. *J. Quant. Spec. Radiat. Transf.*, 110:1628–1639, September 2009.
- [34] Z. Meng, P. Yang, G.W. Kattawar, L. Bi, N.K. Liou, and I. Laszlo. Single-scattering properties of tri-axial mineral dust Aerosols: A database for application to radiative transfer calculations. *J. of Aerosol Science*, 41:501–512, 2010.
- [35] J. Tyynelä, E. Zubko, K. Muinonen, and G. Videen. Interpretation of single-particle negative polarization at intermediate scattering angles. *Applied Optics*, 49:5284, September 2010.

- [36] L. Bi, P. Yang, G. W. Kattawar, and R. Kahn. Modeling optical properties of mineral aerosol particles by using nonsymmetric hexahedra. *Applied Optics*, 49:334, January 2010.
- [37] H. Ishimoto, Y. Zaizen, A. Uchiyama, K. Masuda, and Y. Mano. Shape modeling of mineral dust particles for light-scattering calculations using the spatial Poisson-Voronoi tessellation. *J. Quant. Spec. Radiat. Transf.*, 111:2434–2443, November 2010.
- [38] O. Muñoz, F. Moreno, D. Guirado, J. L. Ramos, A. López, F. Girela, J. M. Jerónimo, L. P. Costillo, and I. Bustamante. Experimental determination of scattering matrices of dust particles at visible wavelengths: The IAA light scattering apparatus. *J. Quant. Spec. Radiat. Transf.*, 111:187–196, January 2010.
- [39] O. Muñoz, F. Moreno, D. Guirado, J. L. Ramos, H. Volten, and J. W. Hovenier. The IAA cosmic dust laboratory: Experimental scattering matrices of clay particles. *Icarus*, 211:894–900, January 2011.
- [40] J. E. Hansen and L. D. Travis. Light scattering in planetary atmospheres. *Space Science Reviews*, 16:527–610, October 1974.
- [41] F. P. Kerr. *Optical Mineralogy*. McGraw-Hill, New York.
- [42] W. G. Egan and T. W. Hilgeman. *Optical properties of inhomogeneous materials.-applications to geology, astronomy, chemistry, and engineering*. Optical properties of inhomogeneous materials.-applications to geology, astronomy, chemistry, and engineering., by Egan, W. G.; Hilgeman, T. W.. New York, NY (USA): Academic Press, 235 p., 1979.
- [43] H. E. Gerber and E. E. Hindman. Light absorption by aerosol particles: First international workshop. *Applied Optics*, 21:370, February 1982.
- [44] C. Klein and C. S. Hurlbut Jr. *Manual of Mineralogy*. John Wiley, New York, 1993.
- [45] J. W. Hovenier, H. Volten, O. Munoz, W. J. van der Zande, and L. B. Waters. Laboratory study of Scattering Matrices for Randomly Oriented Particles: Potentials, Problems, and Perspectives. *J. Quant. Spec. Radiat. Transf.*, 79:741, September 2003.
- [46] M. Konert and J. Vandenberghe. Comparison of laser grain size analysis with pipette and sieve analysis: a solution for the underestimation of the clay fraction. *Sedimentology*, 44:532, 1997.
- [47] O. Muñoz, H. Volten, J. W. Hovenier, T. Nousiainen, K. Muinonen, D. Guirado, F. Moreno, and L. B. F. M. Waters. Scattering matrix of large Saharan dust particles: Experiments and computations. *Journal of Geophysical Research (Atmospheres)*, 112:13215, July 2007.
- [48] M. I. Mishchenko. Electromagnetic scattering by nonspherical particles: A tutorial review. *J. Quant. Spec. Radiat. Transf.*, 110:808–832, July 2009.
- [49] H. C. van de Hulst. *Light scattering by small particles*. New York: Dover, 1981, 1981.
- [50] J. W. Hovenier, C. Van Der Mee, and H. Domke. *Transfer of polarized light in planetary atmospheres : basic concepts and practical methods*. Dordrecht: Kluwer, Springer, 2004.
- [51] M. I. Mishchenko, J. W. Hovenier, and D. W. Mackowski. Single scattering by a small volume element. *Journal of the Optical Society of America A*, 21:71–87, January 2004.
- [52] E. C. Laan, H. Volten, D. M. Stam, O. Muñoz, J. W. Hovenier, and T. L. Roush. Scattering matrices and expansion coefficients of martian analogue palagonite particles. *Icarus*, 199:219–230, January 2009.
- [53] B. Veihelmann, H. Volten, and W. J. van der Zande. Light reflected by an atmosphere containing irregular mineral dust aerosol. *Geophys. Res. Lett.*, 31:4113, February 2004.
- [54] T. Nousiainen and K. Vermeulen. Comparison of measured single-scattering matrix of feldspar with T-matrix simulations using spheroids. *J. Quant. Spec. Radiat. Transf.*, 79:1031, September 2003.
- [55] T. Nousiainen, O. Muñoz, H. Lindqvist, P. Mauno, and G. Videen. Light scattering by large Saharan dust particles: Comparison of modeling and experimental data for two samples. *J. Quant. Spec. Radiat. Transf.*, 112:420–433, February 2011.
- [56] M. Kahnert and T. Nousiainen. Variational data-analysis method for combining laboratory-measured light-scattering phase functions and forward-scattering computations. *J. Quant. Spec. Radiat. Transf.*, 103:27–42, January 2007.
- [57] J. W. Hovenier and C. V. M. van der Mee. Testing scattering matrices: a compendium of recipes. *J. Quant. Spec. Radiat. Transf.*, 55:649–661, May 1996.

- [58] W. J. Markiewicz, R. M. Sablotny, H. U. Keller, N. Thomas, D. Titov, and P. H. Smith. Optical properties of the Martian aerosols as derived from Imager for Mars Pathfinder midday sky brightness data. *J. Geophys. Res.*, 104:9009–9018, April 1999.
- [59] M. G. Tomasko, L. R. Doose, M. Lemmon, P. H. Smith, and E. Wegryn. Properties of dust in the Martian atmosphere from the Imager on Mars Pathfinder. *J. Geophys. Res.*, 104:8987–9008, April 1999.
- [60] J. L. Bandfield. Global mineral distributions on Mars. *Journal of Geophysical Research (Planets)*, 107:5042, June 2002.
- [61] M. J. Wolff, M. D. Smith, R. T. Clancy, N. Spanovich, B. A. Whitney, M. T. Lemmon, J. L. Bandfield, D. Banfield, A. Ghosh, G. Landis, P. R. Christensen, J. F. Bell, and S. W. Squyres. Constraints on dust aerosols from the Mars Exploration Rovers using MGS overflights and MINITES. *Journal of Geophysical Research (Planets)*, 111:12, December 2006.
- [62] J. B. Pollack and J. N. Cuzzi. Scattering by nonspherical particles of size comparable to wavelength - A new semi-empirical theory and its application to tropospheric aerosols. *Journal of Atmospheric Sciences*, 37:868–881, April 1980.
- [63] M. J. Wolff, M. D. Smith, R. T. Clancy, R. Arvidson, M. Kahre, F. Seelos, S. Murchie, and H. Savijärvi. Wavelength dependence of dust aerosol single scattering albedo as observed by the Compact Reconnaissance Imaging Spectrometer. *Journal of Geophysical Research (Planets)*, 114:0, June 2009.
- [64] M. Vincendon, Y. Langevin, F. Poulet, A. Pommerol, M. Wolff, J.-P. Bibring, B. Gondet, and D. Jouglet. Yearly and seasonal variations of low albedo surfaces on Mars in the OMEGA/MEX dataset: Constraints on aerosols properties and dust deposits. *Icarus*, 200:395–405, April 2009.
- [65] M. J. Wolff, R. Todd Clancy, J. D. Goguen, M. C. Malin, and B. A. Cantor. Ultraviolet dust aerosol properties as observed by MARCI. *Icarus*, 208:143–155, July 2010.
- [66] J.-B. Madeleine, F. Forget, E. Millour, L. Montabone, and M. J. Wolff. Revisiting the radiative impact of dust on Mars using the LMD Global Climate Model. *Journal of Geophysical Research (Planets)*, 116:11010, November 2011.
- [67] T. L. Roush and J. F. Bell, III. Thermal emission measurements 2000–400/cm (5–25 micrometers) of Hawaiian palagonitic soils and their implications for Mars. *J. Geophys. Res.*, 100:5309–5317, March 1995.
- [68] R. T. Clancy, S. W. Lee, G. R. Gladstone, W. W. McMillan, and T. Rousch. A new model for Mars atmospheric dust based upon analysis of ultraviolet through infrared observations from Mariner 9, Viking, and PHOBOS. *J. Geophys. Res.*, 100:5251–5263, March 1995.

# The photophoresis experiment for Martian dust analogs at 655 nm - work in progress

Particles in the range 20 (montmorillonite) / 30 (basalt, JSC)- 400 *pixel*<sup>2</sup> corresponding to a radius of about 20-90  $\mu\text{m}$  of the equal area disk particles, were analyzed. In this analysis we set the following parameters: maximum velocity to 110 pixels/frame, maximum area change to 40 % and the minimum track length to 5 frames. Some examples of particle trajectories are shown in Fig. 8.1. In addition to the trajectories of these particles and thus, the photophoretic acceleration, we obtained the mean cross section (size) of each particle. The bulk density of the samples considering spheres of equivalent cross section was  $3\text{g}/\text{cm}^3$ ,  $1.91\text{g}/\text{cm}^3$ ,  $2.35\text{g}/\text{cm}^3$  for basalt, JSC- Mars 1 and montmorillonite, respectively. This gives an approximate mass of each particle and, therefore, the photophoretic force.

In the Fig. 8.2 the examples of obtained photophoretic accelerations are presented for three different pressures in range 1-10 mbar for the samples.

The particles with zero photophoretic acceleration, thus, photophoretic force  $F_{ph} = 0$  are rejected because it is impossible to distinguish them from the non-illuminated particles (as we removed the scattered laser light). Tab. 8.1 summarizes the number of particles analyzed for different samples and pressures. Fig. 8.3 shows an example of a normalized photophoretic force distributions at 5 mbar and 6 mbar.

Table 8.1: Number of particles analyzed for given sample and pressure.

pressure [mbar]	0.5	1	2	4	5	6	7	8	10	15	20	25	30	40	50	75	100
Basalt	119	169	-	-	336	-	313	-	278	-	-	-	-	-	47	27	24
JSC	-	216	-	-	205	-	219	-	189	99	99	40	42	86	29	-	44
Montmorillonite	-	-	73	323	-	164	-	178	160	159	106	100	-	87	-	-	-

The strong differences in the photophoretic strength for particles of similar size seems to be related to their physical properties (e.g. to particles shapes or the refractive index,  $m$ ). All samples are characterized by irregular particles (Fig. 3.11). In addition, some grains tend to form aggregates larger than sieve mesh (63  $\mu\text{m}$ ) e.g. in Fig 8.1 the large basalt particle has about 200  $\mu\text{m}$  of diameter. The structures of the particle can be very important, since the geometry affects the distribution of the surface temperature and, thus, induced photophoretic force.

The montmorillonite has the lowest imaginary part of the refractive index at the red wavelength (i.e.  $m = 1.52 + 0.0001i$  for montmorillonite [8], in comparison to  $m = 1.52 + 0.001i$  basalt [9], and  $m = 1.5 + 0.001i$  JSC [10]). This indicates that the amount of absorption loss when the electromagnetic wave propagates through the material is smaller than for the other two samples, in agreement with its lowest photophoretic forces.

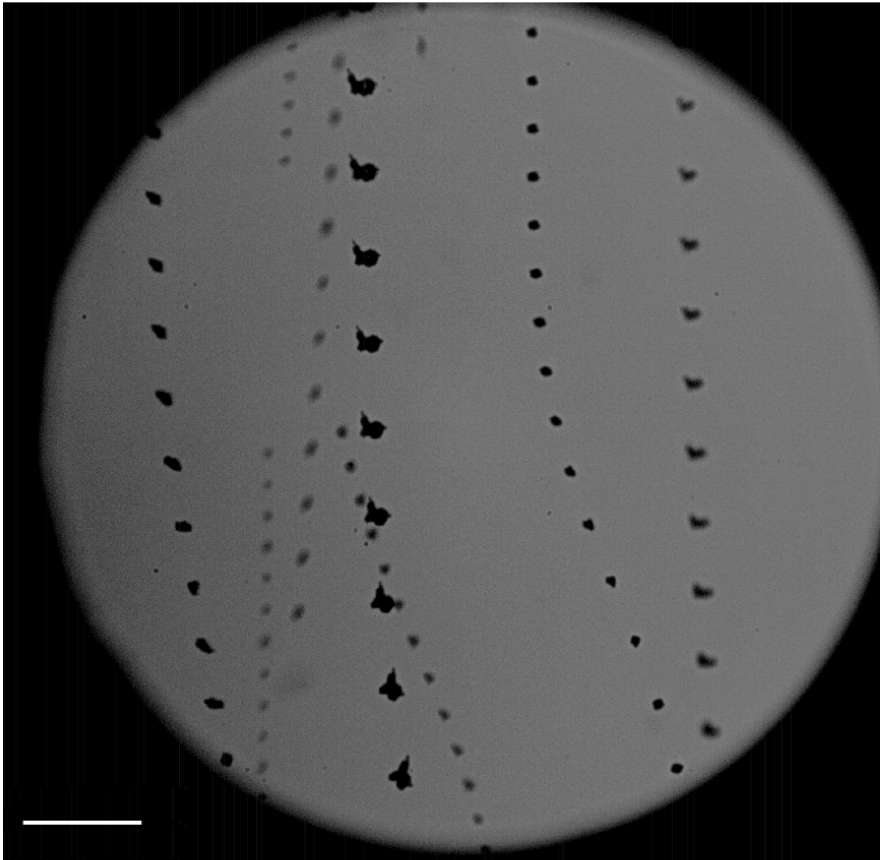


Figure 8.1: Sample trajectories of illuminated particles (basalt, 5 mbar). The light passes through the dust stream at approximately half of the image, exactly where some particles deviate their trajectories. The image is constructed from 17 independent images with 880 x 900 spatial resolution. The white bar indicates scale bar of 1 mm.



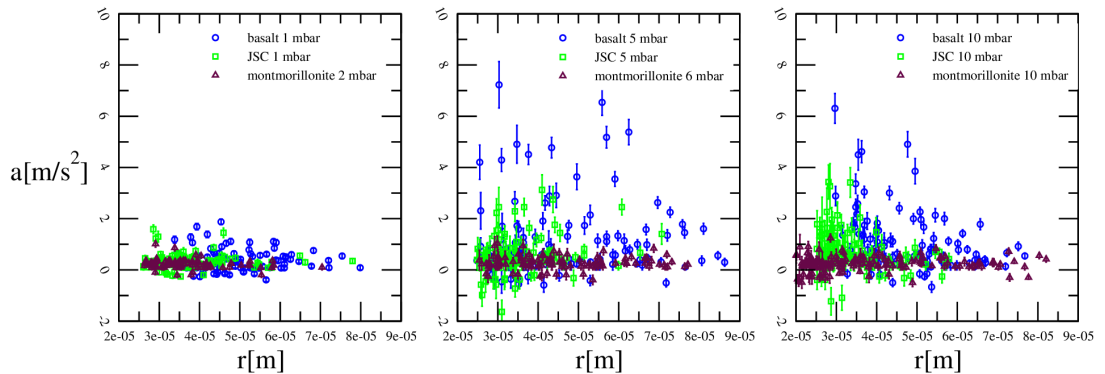


Figure 8.2: The photophoretic acceleration  $a$  in the function of radius at different pressures (1-10 mbar) for 100 first analyzed basalt (blue circles), JSC (green squares) and montmorillonite (violet triangles) particles. Please note, that the left and middle panels present the results at 1, 5 mbar for basalt and JSC, whereas for montmorillonite at 2, 6 mbar. At 2 mbar only 72 montmorillonite particles are presented because of lack of the measurements.

Although at studied wavelength basalt and JSC have similar refractive indices, the obtained forces seem to vary. This is probably because the samples are characterized by different mean particle radii (Tab. 8.2). Therefore, the obtained results can not be directly compared.

In Eqs. 3.22 - 3.24 we see that the photophoretic force depends on thermal conductivity,  $k$ , the asymmetry parameter,  $J$ , and the accommodation coefficient,  $\alpha$ . The thermal conductivity,  $k$ , is the property of a material to conduct heat and here is assumed to be a scalar value. The thermal accommodation coefficient,  $\alpha$ , refers to the interaction of gas molecules with the particles surface. It is often close to 1 and depends on the gas and the surface properties of the particle. The asymmetry parameter,  $J$ , summarizes the interaction of the particle with the radiation. The determination of  $J$  is, in general, a complex problem. Particles perfectly absorbing with the surface of the front side has  $J = 0.5$ .

None of the three parameters,  $J$ ,  $k$  and  $\alpha$ , can be not easily determined for small irregular and inhomogeneous particles. However, they can be deduced from our measurements and the Eqs. 3.22 - 3.24.

Very small values of the photophoretic force are sensitive to disturbances, e.g. a small residual gas motion superimposed. Therefore, we decided to analyze the particles in the pressure range 1 - 50 mbar. In addition, force's number is also biased (decreased) as small values can result from sideward motion and such particles leave the focus of the microscope too early to determine accurate trajectories. To evade this problem we focus on a sample of the 20 particles most affected by positive photophoretic force in case of each sample and pressure, where the number 20 is artificially chosen as appropriate number where all particles still have appropriately large photophoretic forces. For those particles the mean radii, mean accelerations and mean photophoretic forces depending on pressure are calculated. The results are presented in Tab. 8.2. The pressure dependence of the photophoretic forces is presented in the Fig. 8.4. To determine the maximum pressure  $p_{max}$  we used Eqs. 3.22 - 3.24.

The pressure related to the maximum photophoretic force is related to the accommodation coefficient (Eq. 3.23). The obtained values are presented in the Tab. 8.3. Furthermore, knowing the maximum photophoretic force  $F_{max}$  occurring for  $p_{max}$  from the Eq. 3.24 we calculate  $J/k$ . Finally, to estimate the thermal coefficient  $k$ , we use the common value of the asymmetry coefficient  $J=0.5$ . The obtained  $J/k$  and estimated  $k$  are presented as well in the same Tab. 8.3.

- Basalt: The accommodation coefficient  $\alpha$  is constrained to a range of  $[0.3 - 0.5]$ . These values are rather low and imply that using the typical value of  $\alpha = 1$  might overestimate photophoretic forces by a factor of 2 to 3. Deduced values for the thermal conductivity are between  $k = 0.041 - 0.053 \text{ W/mK}$ .

- JSC: Here,  $\alpha$  is formally constrained to  $0.97 - 1.42$ , but as  $\alpha$  has to be smaller than 1 on physical arguments  $\alpha = 0.97 - 1$ . For  $J = 0.5$  the thermal conductivity is constrained to  $k = 0.35 \text{ W/mK}$ .

- Montmorillonite: Due to the small effects measurement errors are larger for this sample and the accommodation coefficient is only poorly constrained to  $\alpha = [0.3 - 1.13]$ . However, like in case of JSC,  $\alpha$  has to be smaller than 1, therefore  $\alpha = 0.3 - 1$ . For the thermal conductivity we find  $k = 0.36 - 0.66$

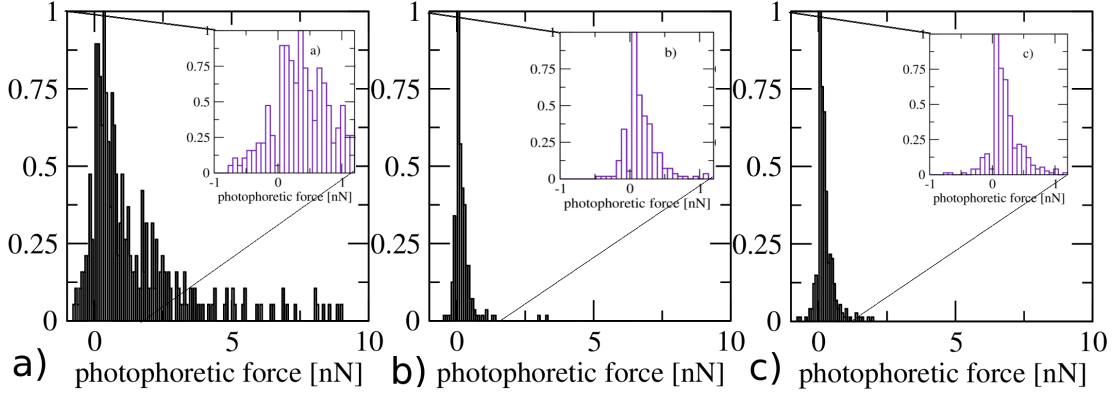


Figure 8.3: The normalized photophoretic force distribution at 5 mbar for a) basalt, b) JSC and c) montmorillonite (6 mbar) samples.

Table 8.2: Average properties measured for different pressure.

pressure [mbar]	mean radius [ $\mu\text{m}$ ]	mean photophoretic acceleration $a_{ph}$ [ $\text{m/s}^2$ ]	mean photophoretic force $F_{Ph}$ [nN]
Basalt			
1	64.3	$0.78 \pm 0.02$	$1.80 \pm 0.2$
5	64.9	$3.92 \pm 0.09$	$9.31 \pm 0.8$
7	62.7	$4.15 \pm 0.12$	$7.68 \pm 0.9$
10	60.6	$2.36 \pm 0.06$	$4.09 \pm 0.5$
50	42.7	$1.30 \pm 0.30$	$0.79 \pm 0.25$
JSC			
1	53.8	$1.05 \pm 0.03$	$0.60 \pm 0.09$
5	46.6	$1.69 \pm 0.08$	$0.98 \pm 0.18$
7	40.3	$2.28 \pm 0.12$	$0.74 \pm 0.15$
10	39.4	$2.19 \pm 0.17$	$0.63 \pm 0.13$
15	33.8	$2.36 \pm 0.12$	$0.51 \pm 0.11$
20	32.2	$2.19 \pm 0.12$	$0.43 \pm 0.11$
25	31.5	$1.47 \pm 0.13$	$0.24 \pm 0.06$
30	30.3	$0.96 \pm 0.07$	$0.16 \pm 0.04$
40	31.3	$0.93 \pm 0.07$	$0.16 \pm 0.04$
50	36.2	$1.00 \pm 0.20$	$0.23 \pm 0.07$
Montmorillonite			
2	46.1	$0.36 \pm 0.02$	$0.2 \pm 0.05$
4	63.3	$0.63 \pm 0.03$	$1.14 \pm 0.16$
6	67.1	$0.44 \pm 0.03$	$0.95 \pm 0.15$
8	62.1	$0.44 \pm 0.03$	$0.72 \pm 0.13$
10	64.3	$0.41 \pm 0.03$	$0.81 \pm 0.13$
15	52.9	$0.32 \pm 0.04$	$0.36 \pm 0.08$
20	44.3	$0.44 \pm 0.05$	$0.35 \pm 0.09$
30	41.6	$0.51 \pm 0.06$	$0.31 \pm 0.09$
40	44.5	$0.34 \pm 0.04$	$0.25 \pm 0.07$

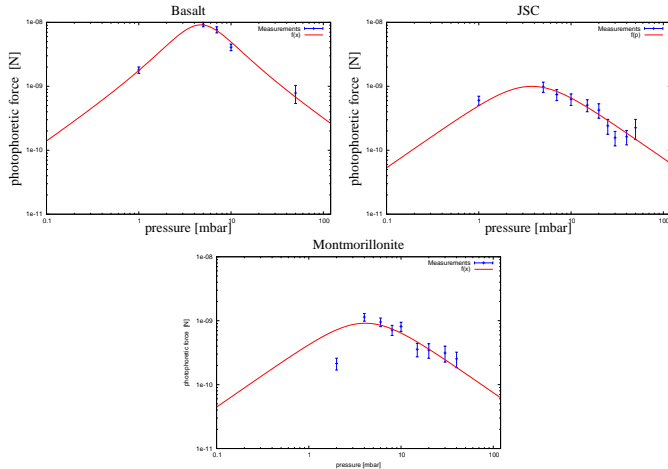


Figure 8.4: The pressure dependence of photophoretic force for Martian dust analogs, i.e. basalt, JSC and montmorillonite samples fitted with the Rohatschek formula, Eq. 3.22.

Table 8.3: The determined photophoretic parameters for Martian dust analogs. \* Please note that the values of  $\alpha > 1$  are not physically possible, therefore the upper range of  $\alpha$  was reduced to 1.

sample:	$F_{max}$ [nN]	$\delta$	$p_{max}$ [mbar]	$\alpha$	$J/k$	$k$ [W/mK]
Basalt, $r_{mean} = 64.8\mu m$	$9.13 \pm 0.7$	$1.3 \pm 0.26$	$4.7 \pm 0.6$	[0.3-0.5]	[12.2-9.47]	[0.041-0.053]
JSC, $r_{mean} = 48\mu m$	$0.997 \pm 0.08$	$0.001 \pm 0.407$	$3.75 \pm 0.38$	[0.97-1]*	[1.45-1.47]	0.35
Montmorillonite, $r_{mean} = 63\mu m$	$0.912 \pm 0.172$	$-1.3 \pm 1.33$	$4.1 \pm 1.3$	[0.3-1]*	[1.39-0.76]	[0.36-0.66]

W/mK.

## Conclusions

From these preliminary results it can be deduced that small particles of Martian dust analogs are affected by illumination at low pressures. Negative and positive photophoresis were observed and, as expected, the positive one was dominant. The strength of photophoretic force is related to the imaginary part of the refractive index of the illuminated material, i.e. the more absorbing particles are the more affected by photophoresis, in agreement with the results. The obtained forces are as well strongly related with shapes and sizes of the particles.

For Martian dust analogs with sizes of tens of microns, the maximum photophoretic force occurs at 4-5 mbar, i.e. Mars-like pressures. Therefore, the photophoresis can be a very effective mechanism to inject small particles in the Martian atmosphere.

In addition, an innovative method to obtain accommodation coefficient  $\alpha$  and  $J/k$  ratio was introduced. Better approximations of these parameters can be obtained with more measurements, especially in the 2-5 mbar pressure range. Then maximum pressure and maximum force should be more determined with more accuracy.



# Bibliography

- [1] O. Muñoz, F. Moreno, D. Guirado, D. D. Dabrowska, H. Volten, and J. W. Hovenier. The Amsterdam-Granada Light Scattering Database. *J. Quant. Spec. Radiat. Transf.*, 113:565–574, February 2012.
- [2] J. W. Hovenier and C. V. M. van der Mee. Testing scattering matrices: a compendium of recipes. *J. Quant. Spec. Radiat. Transf.*, 55:649–661, May 1996.
- [3] B. T. Draine and P. J. Flatau. User Guide for the Discrete Dipole Approximation Code DDSCAT 7.1. *ArXiv e-prints*, February 2010.
- [4] H. Rohatschek. Semi-empirical model of photophoretic forces for the entire range of pressures. *J. Aerosol Sci.*, 26:717–734, April 1995.
- [5] D. D. Dabrowska, O. Muñoz, F. Moreno, J. L Ramos, J. Martínez-Frías, and G. Wurm. Scattering matrices of Martian dust analogs at 488 nm 647 nm- under revision. *A&A*, 2014.
- [6] D. D. Dabrowska, O. Muñoz, F. Moreno, T. Nousiainen, and E. Zubko. Effect of the orientation of the optic axis on simulated scattering matrix elements of small birefringent particles. *Optics Letters*, 37:3252, August 2012.
- [7] D. D. Dabrowska, O. Muñoz, F. Moreno, T. Nousiainen, E. Zubko, and A. C. Marra. Experimental and simulated scattering matrices of small calcite particles at 647nm. *J. Quant. Spec. Radiat. Transf.*, 124:62–78, July 2013.
- [8] I. N. Sokolik and O. B. Toon. Incorporation of mineralogical composition into models of the radiative properties of mineral aerosol from UV to IR wavelengths. *J. Geophys. Res.*, 104:9423–9444, April 1999.
- [9] J. B. Pollack, O. B. Toon, and B. N. Khare. Optical properties of some terrestrial rocks and glasses. *Icarus*, 19:372–389, July 1973.
- [10] E. C. Laan, H. Volten, D. M. Stam, O. Muñoz, J. W. Hovenier, and T. L. Roush. Scattering matrices and expansion coefficients of martian analogue palagonite particles. *Icarus*, 199:219–230, January 2009.

## Conclusions and future work

This Thesis deals mainly with the study of the scattering properties of several Martian dust analog samples, with direct applications in radiative transfer modeling of the atmosphere of Mars, and serving also as a test for electromagnetic and light scattering codes applied to irregularly shaped targets. In addition, for completeness, studies of the role of photophoresis on the injection of small dust particles in the Martian atmosphere, have also been performed.

The main conclusions of this work are as follows:

The dust samples studied are palagonite-JSC Mars-1 (one sample heated at  $200^{\circ}\text{C}$ , meaning different volatile content), montmorillonite, basalt, and calcite. Among the samples studied, the calcite sample has the peculiarity of being a birefringent material, giving us information on the impact (both experimentally and theoretically) of birefringence on the scattering matrix elements.

Measurements continue to be the only way to obtain the full scattering matrix for dust samples. Even the existing largest-sized computer arrays are unable to obtain their light scattering properties through simulations because of the huge memory and CPU time needed to perform the calculations when the size of the particles exceeds significantly that of the incident wavelength.

The measurements of the full  $4\times 4$  scattering matrix elements were performed at the IAA-CODULAB, a world-wide reference setup for the experimental acquisition of the complete scattering matrix of mineral dust samples, completely developed at the IAA, and based on the design of the Dutch setup built by Prof. J.W. Hovenier and colleagues during the early 80's. The experimental Apparatus is capable of performing measurements at several wavelengths in the visible using a tunable laser. In this work, all measurements have been done at 488 and 647 nm. The dust size distribution of the samples are measured by a commercially available Mastersizer 2000. The published results are available at the Amsterdam-Granada light scattering database for interested researchers.

Regarding all the dust samples analyzed, the first immediate conclusion is that Mie theory for spherical particles constitutes only a poor approximation of the real dependence of the scattering matrix elements as a function of the scattering angle. This agrees with the results of previous measurements of other mineral samples (e.g. [1, 2, 3]), which display a similar behavior as a function of the scattering angle.

The retrieved phase functions for Martian dust from space-borne instruments are very close to the scattering functions measured at the laboratory, especially for the basalt sample. In contrast, analytical functions, such as the synthetic Henyey-Greenstein phase function, do not provide a good fit either. Simulations of scattering by cylinders based on the T-matrix do not provide good fit at backscattering. However, some recent simulations (T-matrix and DDA techniques) of scattering by non-spherically shaped particles, such as aggregate of spheres/cubes have provided much more promising results, especially at backscattering. On the other hand, the dependence of  $-F_{12}(\theta)/F_{11}(\theta)$  observed in Mars during a dust storm is similar to that displayed

by the laboratory measurements of the analogs, particularly in that they have a similar value in the inversion angle.

The polarimetric color has been found as a powerful diagnostic tool to detect compositionally different materials of the Martian dust, as it is dependent on the variation of refractive index with wavelength. For a given wavelength, the maximum in the  $-F_{12}(\theta)/F_{11}(\theta)$  ratio is higher for particles having higher imaginary part of the refractive index. This is important regarding the possibility of having a polarimeter on board an orbiter/lander on Mars.

The calcite sample studied has a special interest because of its birefringence. In that case, the influence of birefringence on the scattering matrix has been studied both experimentally and theoretically, with the use of the DDA code, which is specially suited for that purpose. SEM images showed the particles as having flake-like and rhomboid-like shapes, that were also generated theoretically as input of the DDA code. For both flakes and irregular rhomboids, we have found that the isotropic cases 1 ( $m_1 = 1.655$ ), and 3 (1/3-2/3 approximation), provide quite similar values for the  $F_{11}(\theta)$  element to those obtained by assuming birefringent particles. Therefore, for the studied shapes and sizes, birefringence has little impact on the computed phase functions. In contrast, birefringence produces a significant effect on the polarization-related scattering matrix elements. In the case of flakes, the isotropic refractive index  $m_1$  provides a good approximation to the birefringent case for the  $-F_{12}(\theta)/F_{11}(\theta)$  ratio. In contrast, for irregular rhomboids, the "1/3-2/3" approximation provides the closest values to the computed  $-F_{12}(\theta)/F_{11}(\theta)$  for birefringent particles.

Concerning the simulations of the calcite sample, it has been found that the shape of the targets (flakes or irregular rhomboids) has a much stronger effect on the computed scattering matrix elements than birefringence. On the other hand, significant differences in the simulated scattering matrices are found between those two types of particles. We find that varying the percentage of flakes and irregular rhomboids in the sample, we get a significantly better approximation to the measurements than for flakes or irregular rhomboids alone. In particular, for the Fraunhofer SD computations, we find that a particle shape distribution having 20% of flakes and 80% of irregular rhomboids gives a better approximation to the measurements. The agreement with the measurements is even better in the case of the Mie SD even considering that the calculated cross section in the former case is 74% of the total scattering cross section while in the Mie SD it is only 55%. The limitations of the computations due to the extreme difficulties in dealing with large particle sizes prevent us from drawing firm conclusions on the relative percentages of different particle shapes that exist in the calcite sample. We hope, that further computations including particles in the geometric optics domain will shed more light on the issue.

Another aspect that has been investigated concerning birefringent calcite particles is the effect of the orientation of the optical axis on the computation of the scattering matrix. This was performed for two model particles, rhomboid and flake-like. For a fixed spatial orientation, the scattering matrix is affected strongly by variations in the orientation of the optical axis. In contrast, the effect is significantly reduced by orientational averaging. In general, the effect is stronger for elongated as compared to nearly equi-dimensional particles, and is weaker the smaller the particles. It is expected that the effect would be further reduced by averaging over an ensemble of shapes. Therefore, in many applications, it might not be necessary to correctly orient the optical axis to obtain reasonable light-scattering results for birefringent particles

Last but not least, the photophoretic forces on Martian dust analogs have been investigated. This work was performed as a collaboration with a research group at Duisburg-Essen University. Under Mars-like conditions, the photophoretic force on dust particles with sizes of tens of microns is comparable or even greater than the gravitational force. Therefore, photophoresis is likely a very effective mechanism injecting small particles into the Martian atmosphere. In fact, the Martian dust analogs studied experience a maximum of photophoretic force at similar pressures prevailing on Mars, i.e., at about 4-5 mbars. The effect is seen to increase in strength for absorbing particles compared to non-absorbing particles. Thus, the photophoretic force is about an order of magnitude stronger for basalt than for montmorillonite particles of same size. The pressure dependence of the photophoretic force has been shown to be compatible

with semi-empirical studies. This study allowed us to estimate additional physical parameters of the samples, such as the so-called accommodation coefficient, and the ratio of the asymmetry parameter to the thermal conductivity. The results obtained are within the range of the expected values, but still more measurements are needed in order to determine them with increased accuracy.



# Bibliography

- [1] H. Volten, O. Muñoz, E. Rol, J. F. de Haan, W. Vassen, J. W. Hovenier, K. Muinonen, and T. Nousiainen. Scattering matrices of mineral aerosol particles at 441.6 nm and 632.8 nm. *J. Geophys. Res.*, 106:17375–17402, August 2001.
- [2] O. Muñoz, F. Moreno, D. Guirado, J. L. Ramos, H. Volten, and J. W. Hovenier. The IAA cosmic dust laboratory: Experimental scattering matrices of clay particles. *Icarus*, 211:894–900, January 2011.
- [3] E. C. Laan, H. Volten, D. M. Stam, O. Muñoz, J. W. Hovenier, and T. L. Roush. Scattering matrices and expansion coefficients of martian analogue palagonite particles. *Icarus*, 199:219–230, January 2009.

